History-Dependent Changes to the Structure, Properties, and Function of the Cartilaginous Endplate

by

Jackie Doreen Zehr

A thesis

presented to the University of Waterloo

in fulfillment of the

thesis requirement for the degree of

Doctor of Philosophy

in

Kinesiology

Waterloo, Ontario, Canada, 2023

Examining Committee Membership

The following served on the Examining Committee for this thesis. The decision of the Examining Committee is by majority vote.

External Examiner:	**Dr. Gregory N. Kawchuk**, PhD Professor, Dept. of Physical Therapy Faculty of Rehabilitation Medicine, University of Alberta
Supervisor:	**Dr. Jack P. Callaghan**, PhD Professor, Dept. of Kinesiology and Health Sciences Faculty of Health, University of Waterloo
Internal-External Member:	**Dr. Stewart D. McLachlin**, PhD Asst Professor, Dept. of Mechanical & Mechatronics Engineering Faculty of Engineering, University of Waterloo
Internal Member:	**Dr. Andrew C. Laing**, PhD Assoc Professor, Dept. of Kinesiology and Health Sciences Faculty of Health, University of Waterloo
Internal Member:	**Dr. Chad E. Gooyers**, PhD Adjunct Appointment, Dept. of Kinesiology and Health Sciences Faculty of Health, University of Waterloo

Author's Declaration

This thesis consists of materials all of which I authored or co-authored: see Statement of Contributions included in this thesis. This is a true copy of the thesis, including any required final revisions, as accepted by my examiners.

I understand that my thesis may be made electronically available to the public.

Statement of Contributions

I hereby declare that my contribution to each journal publication that was produced from my thesis (currently in press, accepted, and submitted) was my own work, and for each study, I was responsible for the conception and/or design, preparation, collection and analysis of the data, and the writing and editing of the manuscripts.

I hereby declare that the contribution of Dr. Jack Callaghan on each manuscript was conception and/or design, editing of the manuscripts, assisting with instrumentation, providing laboratory reagents/materials/analysis tools, and securing external funding for the research.

Chapter 3.2: I hereby declare that the contribution of Jessa Buchman-Pearle was the preparation of some experimental specimens and editing of the manuscript.

Chapter 3.3: I hereby declare that the contribution of Fasih Rahman was assistance with data collection, assistance with analyses of experimental data, and editing of the manuscript. I hereby declare that the contribution of Dr. Joe Quadrilatero was conception and/or design, contribution of reagents/materials/analysis tools, and editing of the manuscript.

Chapter 5: I hereby declare that the contribution of Dr. Jeff Barrett was assisting with instrumentation and editing of the manuscript.

Chapter 6: I hereby declare that the contribution of Dr. Joe Quadrilatero was contribution of reagents/materials/analysis tools and editing of the manuscript.

Chapter 7: I hereby declare that the contribution of Dr. Joe Quadrilatero was contribution of reagents/materials/analysis tools, and editing of the manuscript.

Chapter 8: I hereby declare that the contribution of Michael Watson was the preparation of some experimental specimens and editing of the manuscript.

Abstract

The performance of manual lifting is associated with 33-51% of incidental low back injuries in work, leisure, and sport/exercise contexts. To effectively prevent low back injuries and evaluate the risk of occurrence, knowledge on the fundamental pathways of microscopic damage accumulation in lumbar spine tissues is required and lacking in the literature. This thesis broadly explored this knowledge gap in the cartilaginous endplate (CEP), which is a hypothesized origin for compression-induced low back injuries and degenerative changes to the intervertebral disc. Therefore, the global objectives of this dissertation included: 1) to quantify the effect of cyclic compression paradigms on the properties and microstructure of the cartilaginous endplate; 2) to examine the effect of cyclic loading parameters on microscopic and macroscopic injury patterns in the cartilaginous endplate; and 3) to characterize the cycle-dependent ultimate compression trajectories in response to acute loading histories. To address these objectives, *in vitro* mechanical testing and immunofluorescence staining techniques were developed and performed on intact spinal units and isolated CEP tissue.

The effects of joint posture, variation in peak compression force, and loading duration on cycle-dependent changes to spinal joint mechanics, isolated CEP properties, and the pathways of microstructural and constitutive damage were quantified. Compared to neutral joint postures, cyclic loading applied to flexed spinal joints reduced the ultimate strength and CEP stiffness at a given loading duration, irrespective of the peak compression variation. An effect of peak compression variation was observed only within neutral postures and beyond the approximate mid-point of the joint lifespan; a 40% variation reduced the joint strength and CEP stiffness compared to the 10% and 20% variation groups. These altered mechanical properties were supported by evidence of sub-surface microstructural void development followed by damage to native type II

collagen proteins within the central CEP region. Data obtained from these *in vitro* mechanical tests were then used to mathematically characterize the relationships between UCT and loading duration. The second-order polynomial functions demonstrated the depreciation of ultimate compression tolerance and altered safety margins for a given loading history. These data collectively highlighted the importance of spinal joint posture for mediating the damage cascade, which can inform the priorities of job (re)design, clinical intervention, and movement training.

The morphology of microstructural injury patterns was also driven by joint posture during sub-threshold cyclic loading, and the lesion size generally progressed as a function of loading duration. That is, cartilage microfractures were more common in neutrally positioned joints, while avulsion and node microinjuries were most common in flexed spinal units. However, on a macroscopic level, the failure morphology was less sensitive to posture and was attributed to the pace of damage accumulation in the sub-chondral bone relative to the hyaline cartilage surface. This notion was experimentally demonstrated by imposing targeted trabecular bone strength deficits within intact vertebrae and performing subsequent fatigue testing. Initially healthy spinal joints resulted in fracture lesions, while spinal joints with pre-existing strength deficits resulted in Schmorl's nodes over 50% of the time. This dissociation of macroscopic injury mechanisms provided new insights into their prevention, treatment, and diagnosis and ultimately improves the specificity of ergonomics tools that are developed from *in vitro* experimental data.

Overall, this research documents the effects of joint posture, variation in peak compression force, and loading duration on the pathways and time-course of microscopic damage in the cartilage endplate of the spine. These data will be used to broadly inform task design, load management, and injury prevention initiatives in many occupational sectors, specifically public protection (i.e., military, emergency response personnel), health care, manufacturing, and

professional/colligate sport where low back injuries are a common and costly cause of personal disability and lost work time. The work of this thesis further advanced the methodology used within the broader field of spine biomechanics and the experimental results represent a significant step to understanding the mechanisms and prevention of lifting-related overuse injuries in the lumbar spine.

Acknowledgments

To my supervisor and mentor, Dr. Jack Callaghan, my gratitude far exceeds these few words. The work of this dissertation simply would not be possible without his unwavering support and encouragement. Not only was he an exemplar scientist, but also a person that I look up to greatly and genuinely enjoyed working with. Thank you for providing a rigorous training experience and the resources to pursue new and unfamiliar lines of research; I learned more than I thought possible. I am very proud to have been a part of his research program and indebted for the many "mentoring moments" and opportunities.

Thank you to my examination committee members, Drs. Andrew Laing, Chad Gooyers, and Stewart McLachlin for their insights and detailed feedback. I also sincerely thank my external examiner, Dr. Greg Kawchuk, for attending my defence and for sharing his valuable perspectives.

To my collaborators, Dr. Joe Quadrilatero, Fasih Rahman, and the "Quad Squad", this dissertation was strengthened by your generous assistance and expertise. Thank you for the many insightful discussions and for patiently teaching me everything I know about staining and microscopy. It was a privilege to learn from this talented group.

I also acknowledge my long-time mentor and friend, Dr. Tyson Beach, for his continued support throughout this PhD journey. He is a scientist and teacher that I have looked up to since my first undergraduate biomechanics course and largely inspired my pursuit of graduate school. Thank you for taking a chance on me as an (under)graduate student and for the many invaluable discussions over the last 10 years.

I have been extremely fortunate to work alongside and develop friendships with many talented peers within and beyond the Callaghan lab. These fellow graduate students include: Jeff Barrett, Jessa Buchman-Pearle, Kayla Fewster, Donna Fok, Dan Martel, Annemarie Laudanski, Graham Mayberry, Mamiko Noguchi, Brendan Pinto, Lia Tennant, Dan Viggiani, and Taylor Winberg. I specifically acknowledge Kayla Fewster for taking me under her wing as a new PhD student and for being a senior student I looked up to along the way. I also return the shoutout to Jeff Barrett for his invaluable help with the robotic arm.

Beyond graduate school, I acknowledge the support from my best friends, Katie McCurdy and Mila Brankovan. Thank you for the many phone calls, check-ins, and visits that not only made me laugh but were a welcomed distraction from the intensity of graduate school. I further thank the McCurdy family for their encouragement, friendship, and hospitality over the years. It has meant the world to me.

I recognize and thank the Natural Sciences and Engineering Research Council Canada Graduate Scholarship Program, Ontario Graduate Scholarship Program, the Mitacs Accelerate Scholarship program, and the University of Waterloo President's Graduate Scholarship Program who collectively funded my doctoral studies.

To my parents (Sharon and Del), sister (Angela), and extended family, thank you for unconditionally supporting me through yet another graduate school endeavour. I promise this is the last degree. I am eternally grateful for this loving support system that kept me grounded during the highs, encouraged me through the lows, and believed in me every step of the way. I would not be the person or researcher I am today without them.

To my best friend and love, Andrew, thank you for your patience and endless support to pursue this research and my passion; he truly was and is my biggest fan. I am thankful for the joy, balance, and perspective he has brought into my life and his optimism was a constant source of inspiration.

Table of Contents

List of Figures

List of Tables

List of Equations

CHAPTER 1

General Introduction

Lifting, squatting, and bending incorporate the same general musculoskeletal movement pattern. This fundamental movement pattern is essential to the performance of occupational duties, daily living tasks, and sport manoeuvres. It is also used as a physical training modality intended to enhance performance, increase physical preparedness, and prevent musculoskeletal injury. In these contexts, however, the performance of lifting accounts for approximately 33-51% of reported incidental low back injuries (Jennings, Yoder, Heiner, Loan, & Bingham, 2008), which are strongly associated with absenteeism, disability, and a costly health care burden (Atlas & Deyo, 2001). Although medical and applied health fields continue to develop management strategies for debilitating low back injuries, efforts towards preventing their incidence will be hindered without understanding the time-course and causal mechanisms by which microdamage initiates and progresses. This knowledge gap yields an important opportunity to study the fundamental injury pathways within lumbar spine tissues. Insight into the microscopic initiation and progression of low back injury can be gained through a comprehensive understanding of how the structure, properties, and function are altered in response to prescribed loading (Figure 1.1). This inter-disciplinary framework will be central to the investigation of lifting-related low back injury mechanisms in this thesis.

A wide range of joint compression forces have been reported for manual lifting tasks. This range extends from a maximal effort deadlift (6.4 kN to 12.6 kN) (Cholewicki, McGill, & Norman, 1991) to submaximal but repetitive occupational lifting (i.e., 3.1 to 6 kN) (T. A. C. Beach et al., 2019; Gooyers, Beach, Frost, Howarth, & Callaghan, 2018; Marras, Knapik, & Ferguson, 2009;

Zehr, Carnegie, Welsh, & Beach, 2020; Zehr, Howarth, & Beach, 2018). When compared to existing estimates of ultimate compression tolerance (UCT) (6.9 kN to 13.8 kN) (Adams & Hutton, 1982; Biggemann, Hilweg, & Brinckmann, 1988; Brinckmann, Biggemann, & Hilweg, 1989; Gunning, Callaghan, & McGill, 2001; Hutton, Cyron, & Scott, 1979), the compression forces experienced by lumbar spine joints generally exceed 30% of the average UCT (i.e., 10.4 kN). Previous *in vitro* research conducted by Parkinson and Callaghan (2009) demonstrated that peak compressive forces exceeding 30% of the spinal unit's estimated compression tolerance will lead to fatigue-failure in the cartilaginous endplate (CEP) before the occurrence of intervertebral disc injury. Therefore, the study of lifting-related injury pathways within the CEP were examined in this dissertation.

CEP injuries are commonly diagnosed as an acute injury associated with an overexertion exposure. Indeed, the joint compression forces reported during maximal effort deadlifts performed by elite powerlifters may exceed some existing UCT estimates (Cholewicki et al., 1991); however, external loads of this magnitude (145.3 kg for women and 256.7 kg for men) are generally not lifted by the general population, non-powerlifting athletes, or as occupational duties. Since the joint compression associated with occupationally relevant lifting exertions does not typically exceed *in vitro* UCT estimates, an acute overexertion injury mechanism is generally not supported. Thus, lifting-related lumbar spine loading must facilitate, at the very least, an acute reduction in load-bearing capacity thereby elevating risk associated with abrupt high demand exposures or subsequent low demand repetitions. The acute and chronic implications of cyclic loading histories as a modulating factor of tissue structure, properties, and function are poorly understood despite recommendation (McGill, 1997) and evidence (Gooyers, Frost, McGill, & Callaghan, 2013) for

its consideration. This dissertation explored these knowledge gaps, specifically related to compression induced CEP injury mechanisms and microscopic pathways of damage.

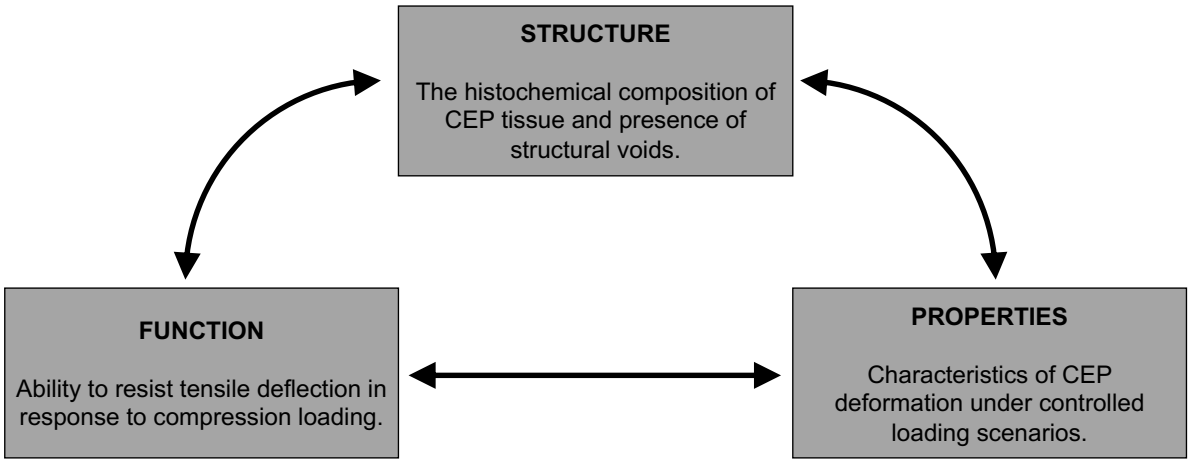

Figure 1.1. The adopted structure-properties-function framework for the analysis and characterization of CEP injury mechanisms in this dissertation.

1.1. Global Thesis Objectives

Mechanical overload is one of the most significant and preventable causes of low back injury (Marras, 2000). Therefore, this dissertation examined how cyclic compression paradigms influence the pattern and pace of microscopic and macroscopic injury in the cartilaginous endplate. Using *in vitro* mechanical testing together with immunofluorescence staining techniques, the global objectives were three-fold:

1) Quantify the effect of cyclic compression paradigms on the properties (i.e., ultimate compression tolerance, loading stiffness) and microstructure (i.e., microstructural damage and type I and type II collagen content) of the cartilaginous endplate.

2) Examine the effect of cyclic loading parameters on microscopic and macroscopic injury

patterns in the cartilaginous endplate.

3) Characterize the cycle-dependent ultimate compression trajectories in response to acute loading histories.

1.2. Thesis Layout

This thesis aimed to demonstrate how the CEP structure, properties, and function are altered at various points throughout the fatigue lifespan. In effect, the initiation and progression of microscopic injury within the CEP was examined. To achieve this, eight studies were completed (Figure 1.2.1). Three studies (summarized in Chapter 3) were completed to develop and/or justify the use of experimental procedures used in the five studies designed to collectively address the global objectives (Chapter 4-9). These methodological studies had the specific objectives to: 1) Quantify the compression and shear reaction forces and flexion-extension moments experienced by spinal units in constrained versus unconstrained *in vitro* testing systems; 2) Examine the interacting effects of loading rate and loading frequency on the cyclic loading lifespan of intact spinal units; and, 3) Develop and present a novel multi-colour immunofluorescence staining procedure for quantifying constitutive and microstructural damage resulting from repeated mechanical stimuli. The implementation of specific findings from each study are presented in Sections 3.1.5, 3.2.5, 3.3.4.

Studies one to four were basic science experimental research designs that focused on elucidating the pathways of overuse injury in the CEP. The fifth study proposes an approach with the intention to connect basic science findings and applied health research practices that aim to assess low back injury risk and improve injury prevention efforts in occupational contexts. The inclusion and transfer of spinal tissues used within and between studies is presented in Table 1.1.

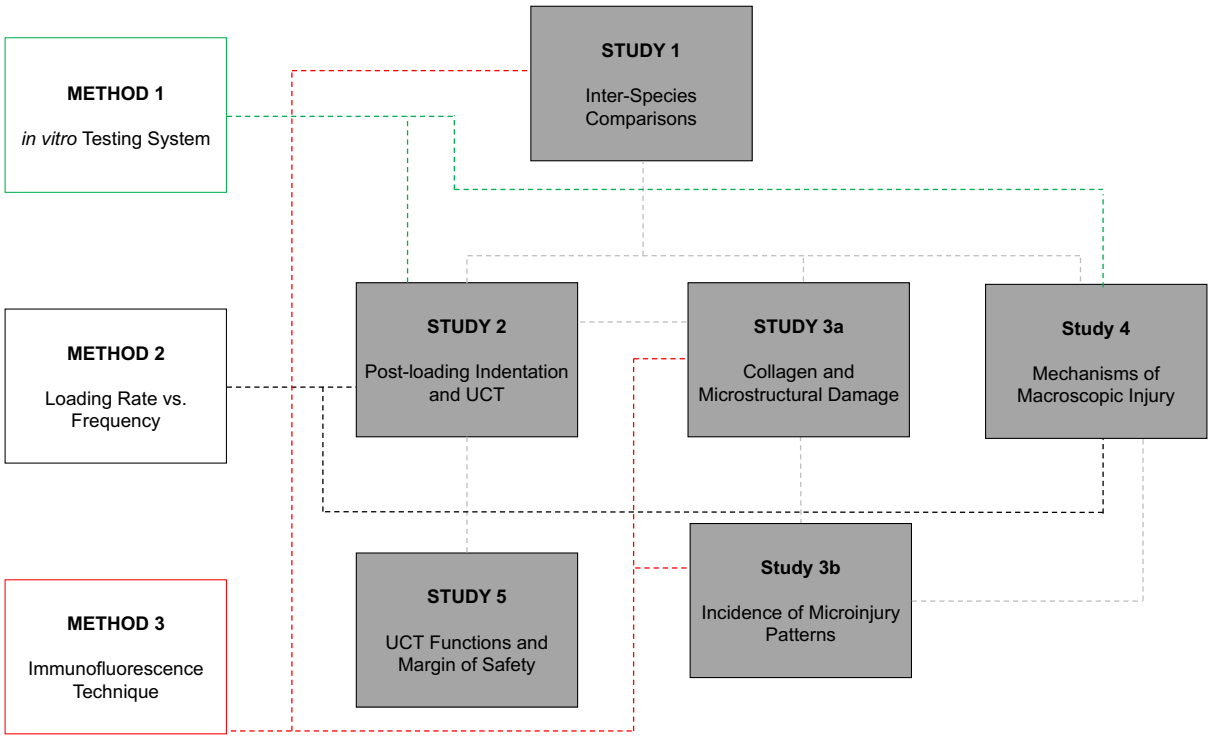

Figure 1.2.1. A flow chart of the eight studies comprising this thesis. White boxes indicate studies that were completed for the development and/or justification of experimental procedures used in the five studies designed to collectively address the global thesis objectives (grey squares).

Table 1.2. Inclusion and transfer of porcine spinal tissues and data between studies included in this thesis.

Study 1	6 porcine endplates from the control group of Study 2. 11 human cadaveric lumbar endplates (9 young, 2 aged).
Study 2	6 porcine spinal units assigned to the control group. 108 porcine spinal units assigned to 18 different experimental groups (N = 6 per group).
Study 3	6 porcine endplates from the experimental groups of Study 2. 107 porcine endplates from the experimental groups of Study 2.
Study 4	Separate sample of 30 porcine spinal units.
Study 5	Ultimate compression data from 6 porcine spinal units assigned to the control group in Study 2. Ultimate compression data from 107 porcine spinal units assigned to experimental groups in Study 2.

1.3. Specific Research Objectives and Hypotheses

Five studies were conducted to test specific hypotheses related to the global objectives. Evidence-based hypotheses were tested; however, some elements of this research were exploratory. Therefore, alternative hypotheses are stated where possible.

Study 1: Indentation Mechanics and Native Collagen Content in the Cartilaginous Endplate: A Comparison Between Porcine Cervical and Human Lumbar Spines

Study 1 aimed to characterize and compare the regional indentation mechanics and native collagen content in CEPs from the porcine cervical spine, young human cadaveric lumbar spine (19, 33 years), and aged human cadaveric lumbar spine (85 years). Microindentation and immunofluorescence staining were performed to evaluate the loading stiffness, creep displacement, fluorescence intensity (type I and II collagen), sub-surface void area, and cartilage thickness. This investigation provided insight on the suitability of porcine cervical and aged human lumbar CEPs for the study of overuse injury pathways.

H_1: The mechanical properties and biochemical composition of the intervertebral disc and CEP have been shown to change as a function of age (Antoniou et al., 1996; Martins et al., 2018). Therefore, the native collagen content and indentation properties were hypothesized to differ between CEPs extracted from young and aged human cadaveric lumbar spines.

H_2: Although CEPs from porcine and human species have a similar shape (Yingling, Callaghan, & McGill, 1999), morphological differences (i.e., thickness) have been observed (Li et al., 2022). As such, it is hypothesized that indentation properties will differ between CEPs from porcine cervical and human lumbar spines.

H_3: Biochemical differences between human and porcine CEPs have been further documented (Y. Zhang et al., 2014). Therefore, the fluorescence intensity for native collagen content was hypothesized to differ between porcine cervical and all human lumbar spine CEPs.

Study 2: Cyclic Loading History Alters the Joint Compression Tolerance and Regional Indentation Responses in The Cartilaginous Endplate

Study 2 used the porcine cervical spine model to examine the effects of posture (neutral, flexed), variation in peak compression force (10%, 20%, 40%), and loading duration (1000, 3000, 5000 cycles) on the joint compression tolerance and mechanical properties of isolated CEP tissue. After cyclic testing, one vertebra was assigned to destructive testing and the endplate of the other vertebra underwent non-destructive microindentation testing. A custom indenter was fabricated to the size and shape of porcine disc-vertebra unit and used to examine ultimate compression and yield forces. Regional indentation stiffness and creep displacement during microindentation testing were further examined. This study provided novel insight into how the joint strength and CEP properties change throughout the fatigue lifespan and in response to specific compression paradigms.

H_1: In previous studies, flexed postures have significantly reduced the joint lifespan during subthreshold cyclic loading tests (Callaghan & McGill, 2001a; Gooyers, McMillan, Noguchi, Quadrilatero, & Callaghan, 2015; Gooyers, McMillan, Howarth, & Callaghan, 2012). Therefore, ultimate compression tolerance and yield force were hypothesized to decrease when cyclically loaded in flexed postures compared to neutral at each loading duration.

H_2: Compared to 0% variation, a loading variation of at least 30% reduced the joint lifespan (Zehr, Tennant, & Callaghan, 2019a) and significantly increased the failure probability beyond 2600

cycles (Zehr et al., 2019a). Therefore, it was hypothesized that a high loading variation (i.e., 40%) would significantly reduce the ultimate compression tolerance and yield force beyond 3000 consecutive loading cycles.

H_3: In alignment with previous research on spinal joint fatigue (Gooyers et al., 2015), the ultimate compression tolerance and yield force were hypothesized to decrease as a function of loading duration.

H_4: Compared to peripheral regions, the central CEP experiences the greatest deflection in response to joint compression loading (Malandrino, Planell, & Lacroix, 2009). Therefore, the loading stiffness and creep displacement in the central region were expected to mimic the ultimate compression results; flexed postures were hypothesized to reduce loading stiffness and increase creep displacement at each loading duration and a high variation (i.e., 40%) was hypothesized to reduce indentation stiffness and increase creep displacement beyond 3000 cycles.

H_5: In consideration of evidence suggesting that compressive stress becomes more peripherally distributed as a function of loading duration (van Dieën, Kingma, Meijer, Hänsel, & Huiskes, 2001) and the prevalence of fatigue fractures in posterior and lateral CEP regions (Chapter 3.2), significant reductions in indentation stiffness and creep displacement were expected in the lateral and posterior regions following 5000 cycles.

Study 3a: Initiation and Accumulation of Loading Induced Changes to Native Collagen Content and Microstructural Damage in the Cartilage Endplate

Study 3a aimed to explain the altered joint and CEP properties observed in Study 2. The endplate tissue assigned to microindentation testing (Study 2) was used to examine the effects of posture (neutral, flexed), variation in peak compression force (10%, 20%, 40%), and loading

duration (1000, 3000, 5000 cycles) on the fluorescence area and intensity of type I and II collagen within central CEP. A secondary objective was to examine the initiation and accumulation of microstructural damage, which was quantified by pore area (transverse plane sections) and void area (sagittal plane sections) along the CEP-subchondral bone interface. Immunofluorescence staining was conducted on transverse and sagittal sections of the central endplate region and laser scanning confocal microscopy was used to visualize all sections. A total of 678 images were captured in this study and these data provided novel insight into the pathway of loading induced microscopic damage initiation and accumulation in the central CEP.

Transverse Plane

H_1: Previous research has demonstrated a strong relationship between collagen content and tensile modulus of isolated CEP tissue (Fields, Rodriguez, Gary, Liebenberg, & Lotz, 2013). On the basis of this relationship, it was hypothesized that joint posture, variation in peak compression force, and loading duration will interact to decrease the fluorescence intensity of type II collagen. This response would align with loading induced changes to indentation stiffness (Zehr, Barrett, & Callaghan, 2022).

H_2: The CEP is a porous structure and, in response to deflection, pore compaction occurs (Y. Wu et al., 2016). Furthermore, as the CEP surface is strained, the pores are a conceivable stress riser. As such, type II collagen around the pore perimeter is particularly susceptible to damage (i.e., negative staining). Furthermore, flexed postures facilitated greater central CEP deflection compared to a neutral alignment (Malandrino et al., 2009). Therefore, it was hypothesized that joint flexion will significantly decrease the fluorescence area of type II collagen compared to neutral postures.

H_3: In alignment with previous fatigue research (Gooyers et al., 2015), type II collagen fluorescence area was hypothesized to decrease as a function of loading duration.

H_4: A decrease in the fluorescence area of type II collagen can be expected to reveal the type I collagen content of the underlying subchondral trabecular bone. Therefore, it was hypothesized that flexed joint postures will increase the fluorescence area of type I collagen compared to neutral postures.

H_5: Type I collagen fluorescence area was hypothesized to increase as a function of loading duration.

Sagittal Plane

H_6: Previous research has demonstrated a strong relationship between collagen content and tensile modulus of isolated CEP tissue (Fields, Rodriguez, et al., 2013). On the basis of this relationship, it is hypothesized that joint posture, variation in peak compression force, and loading duration will interact to decrease the fluorescence intensity of type II collagen. This response would align with loading induced changes to indentation stiffness (Zehr, Barrett, et al., 2022).

H_7: Rodriguez et al. (2011) observed the formation of voids beneath the CEP surface and along the CEP-subchondral bone border in degenerated cadaveric spinal units. Although the presence of sub-surface voids has not been directly related to CEP properties, it was hypothesized that joint posture, variation in peak compression force, and loading duration will interact to increase the sub-surface microstructural void area. This response would suggest that changes to indentation stiffness observed by Zehr, Barrett, et al. (2022) would result from a reduction in native type II collagen content combined with microstructural void development.

H_8: In the presence of sub-surface voids along the CEP-subchondral bone border, the fluorescence area of type I and type II collagen will conceivably decrease. Therefore, it was hypothesized that

joint posture, variation in peak compression force, and loading duration will interact to decrease the fluorescence area of type I and type II collagen.

Study 3b: Incidence of Compression Induced Microinjuries in the Cartilage Endplate of the Spine

Study 3b used the sagittal and transverse plane images obtained in Study 3a to determine the incidence of microscopic injury patterns (circumferential pore damage, avulsion, node, and cartilage microfracture) in response to cyclic compression paradigms applied in Study 2. The distribution of microinjuries between vertebra (cranial, caudal), spinal level (C3C4, C5C6), and postures (flexed, neutral) were examined. The association of incidence and area of microinjuries with loading variation (10%, 20%, 40%) and loading duration (1000, 3000, 5000 cycles) were also determined. This study was first to associate specific microinjury patterns to acute cyclic loading histories.

H_1: The incidence of all microinjuries was hypothesized to be equal between spinal levels and vertebra.

H_2: Poromechanical finite element models of spinal units have demonstrated greater deflection of the central endplate surface when compressed in flexed joint postures (Malandrino et al., 2009). Therefore, microinjury patterns effecting the subchondral bone (node, avulsion) were hypothesized to be more prevalent in spinal units loaded in a flexed joint position.

H_3: In contrast, cartilage microfractures were hypothesized to be more prevalent in spinal joints that were cyclically loaded in a neutral position.

H_4: The area of all microinjury types was hypothesized to increase as a function of loading duration.

Study 4: Experimentally Dissociating the Overuse Mechanisms of Endplate Fracture Lesions and Schmorl's Node Injuries Using the Porcine Cervical Spine Model

Study 4 aimed to experimentally dissociate the overuse mechanisms of macroscopic CEP injuries; namely, fracture lesions and Schmorl's nodes. This work builds on Study 3b, where microinjuries were observed to the CEP and, in some cases, the trabecular bone (i.e., nodes), which is a hypothesized mechanism for Schmorl's node injuries (Mok et al., 2010; Peng et al., 2003; N. Zhang, Li, Huang, Teng, & Chen, 2010). However, Schmorl's nodes have not been reliability reproduced in a laboratory setting. In contrast, fracture lesions have been experimentally linked to cyclic compression loading and experimentally reproduced (Brinckmann, Biggemann, & Hilweg, 1988; Gallagher, Marras, Litsky, & Burr, 2006; Parkinson & Callaghan, 2007b; Zehr, Buchman-Pearle, & Callaghan, 2020). Therefore, this study examined the effects of localized trabecular bone integrity (control, sham, chemical fragility, structural void) and joint posture (flexed, neutral) on macroscopic CEP failure morphology and joint lifespan. A novel procedure was developed to induce a 49% reduction in strength to centrally positioned trabecular elements within intact vertebrae. This study was first to experimentally reproduce Schmorl's node injuries under subthreshold loading conditions and ultimately revealed the damage criteria required to produce common CEP injuries.

H_1: Considering existing hypotheses for the pathogenesis of Schmorl's nodes (Peng et al., 2003), the high prevalence of fracture lesions in response to cyclic loading applied to initially healthy spinal units (Brinckmann et al., 1988; Gallagher et al., 2006; Parkinson & Callaghan, 2007b; Zehr, Buchman-Pearle, et al., 2020), and the lack of compression-induced damage to the organic phase of trabecular bone (Zehr, Quadrilatero, & Callaghan, 2022b), it was hypothesized that Schmorl's

nodes would be exclusive to spinal joints that were pre-disposed with trabecular bone fragility and/or structural voids, irrespective of posture.

H_2: The presence of structurally compromised trabecular bone and flexed joint postures were hypothesized to independently result in significantly fewer tolerated loading cycles.

Study 5: Towards the Estimation of Ultimate Compression Tolerance as a Function of Cyclic Compression Loading History: Implications for Lifting-Related Low Back Injury Risk Assessment

Study 5 used joint tolerance data obtained in Study 2 to mathematically characterize the cycle-dependent joint tolerance associated with compression paradigms that differed by joint posture (neutral, flexed), variation in peak compression force (10%, 20%, 40%), and loading duration (1000, 3000, 5000 cycles). The relationship between joint tolerance, loading variation, and loading duration was first characterized with a three-dimensional surface. Secondly, the effect of posture was included, wherein curve-fitting was performed to characterize the joint tolerance–loading duration relationship for cyclic loading performed in flexed and neutrally positioned functional spinal units. The developed functions enable direct computation of the margin of safety for a given loading history and may form the basis for future low back injury risk evaluation approaches.

H_1: No specific hypotheses were tested in this study.

CHAPTER 2

Review of Literature

This chapter reviews the scientific foundation for the research completed herein. It contains five separate sub-sections: (i) Incidental Low-Back Injury Reporting; (ii) the Vertebral Endplate; (iii) Low Back Injury Framework; (iv) Demands vs. Capacity; and (v) Methodological Considerations.

2.1. Incidental Low Back Injury Reporting

Approximately 33-51% of incidental low back strains and sprains occur during the performance of lifting manoeuvres in occupational (e.g., public protection, health care, etc.) (Bento et al., 2020; Campbell, 2016; Dropkin, Moline, Power, & Kim, 2015; Friedenberg, Kalichman, Ezra, Wacht, & Alperovitch-Najenson, 2022; Frost, Beach, Crosby, & McGill, 2015; Hauret, Jones, Bullock, Canham-Chervak, & Canada, 2010; Katsavouni, Bebetsos, Malliou, & Beneka, 2014), exercise/sport (e.g., physical training, CrossFit, powerlifting, etc.) (Alekseyev et al., 2020; Ángel Rodríguez et al., 2022; Frost et al., 2015; Hauret et al., 2010; Klimek, Ashbeck, Brook, & Durall, 2018; Montalvo et al., 2017; Siewe et al., 2011; Weisenthal, Beck, Malony, DeHaven, & Giordano, 2014), and daily living (Waterman, Belmont, & Schoenfeld, 2012) contexts. Of these reported low back injuries, over half (51-71%) were sustained while performing lifting tasks that were qualitatively described to have been “heavy”, “high-intensity”, or “high demand” and generally coincided with what was classified by physicians as moderate-to-severe tissue damage (Jennings et al., 2008). Based on radiographic imaging, the most common medical diagnoses of injuries appended to high exertion lifting events include: intervertebral disc (IVD) disorders with and without neurological involvement, endplate fracture lesion, and vertebral body fracture

(Jennings et al., 2008). Further, the mechanism for what was documented as an acute incidental injury was attributed to overexertion in 30% (Campbell, 2016; Katsavouni et al., 2014) to 70% (Hauret et al., 2010; Nye, Pawlak, Webber, Tchandja, & Milner, 2016) of written medical documents.

Incidental low back injuries are personally and economically expensive. Individuals with radiographically confirmed IVD herniations, endplate fractures, or vertebral fractures are more likely to endure costs related to unemployment/work absenteeism, litigation/disability, and health care (e.g., advanced medical imaging, surgical intervention, frequent physician appointments, specialized physician consultation) compared to less severe low back disorders like muscular strains (Atlas & Deyo, 2001). The cost of medical treatment linked to these spinal pathologies ranges from 40 to 55 thousand dollars per patient over two years (Carreon et al., 2009; Dieleman et al., 2020; McInnis, Olchanski, Kemner, & Goss, 2010), with the number of individuals seeking treatment increasing by 54% since 1990 (Hartvigsen et al., 2018). The personal costs linked to incidental low back injuries include severe pain, physical disability, routine consumption of narcotic analgesics, and a spectrum of mental health disorders (Atlas & Deyo, 2001).

From the epidemiological data presented, the prevalence, nature, and severity of lifting-related low back injuries does not appear to be limited to a specific context. Rather, common to various contexts is the performance of lifting exertions. Given these financial and perhaps more importantly personal costs, there is considerable motivation to examine the underlying mechanisms and pathways of lifting-related low back injuries.

2.2. The Vertebral Endplate

During repetitive lifting, the cartilaginous endplate (CEP) is vulnerable to overuse injury. Generally, the joint compression forces associated with light and heavy exposures exceed 30% of

ultimate joint tolerance estimates. Research conducted by Parkinson and Callaghan (2009) identified that normalized compression loads exceeding 30% resulted in CEP fracture before intervertebral disc (IVD) herniations provided that the joint flexion-extension motion was within physiological limits. For this reason, lifting-related overuse injury pathways were examined in the CEP. Macroscopic injuries to the CEP profoundly influence the axial properties of spinal joints to a greater extent than IVD injuries, which significantly impacted the torsional joint properties (D. Wang et al., 2022). A perforating wound to the CEP surface caused a 25% increase in vertical displacement, 59% increase in axial hysteresis, and a 32% reduction in neutral zone stiffness (D. Wang et al., 2022). Furthermore, the CEP is a hypothesized origin of IVD degeneration (Lotz, Fields, & Liebenberg, 2013) and has been shown to accompany 60% of IVD herniations (Berg-Johansen, Fields, Liebenberg, Li, & Lotz, 2018; P. Lama et al., 2014) and most vertebral fractures (Brinckmann, Frobin, Hierholzer, & Horst, 1983; Holmes, Hukins, & Freemont, 1993). Taken together, the examination of injury pathways within the CEP may expose new avenues for explaining and preventing low back pain and injury development.

2.2.1. Endplate Structure

The CEP is histologically classified as hyaline cartilage. Like all supporting connective tissues, the CEP contains an extracellular matrix (ECM) comprised of ground substance and fibres (Lotz et al., 2013). The ground substance of hyaline cartilage has physical characteristics of a semi-solid gel and contains a mixture of glycoproteins and glycosaminoglycans (GAG). GAGs exist in the ECM as polysaccharide chains with profound water binding capacity, which provides volume, internal pressure, and compression resistance (Young, O'Dowd, & Woodford, 2014). Through covalent bonding, GAGs attach to various core proteins known as proteoglycans. Aggrecan is a prominent proteoglycan found in hyaline cartilage (Kiani, Chen, Wu, Yee, & Yang, 2002;

Tomaszewski, Saganiak, Gładysz, & Walocha, 2015). It specifically binds with hyaluronate (i.e., a type of GAG) and has an important role in mediating chondrocyte-ECM interactions for the purpose of re-modelling and growth (Kiani et al., 2002; Tomaszewski et al., 2015). With respect to the ECM fibers, collagen is the main structural protein of hyaline cartilage. In the CEP, type II collagen represents 100% of the total collagen content through much of the lifespan, with exception to the age ranges of 5-15 and 60-80 years (Antoniou et al., 1996). This collagen composition is similar to articular cartilage, where type II collagen represents 90-95% of the total collagen content (Sophia Fox, Bedi, & Rodeo, 2009). The presence of type II collagen enables the CEP to elastically deform and provides tensile strength to do so (Young et al., 2014). Unlike healthy articular cartilage where the orientation of collagen fibers is zone dependant, the collagen fibers in the CEP have a uniform horizontal orientation (Lotz et al., 2013; Roberts, Menage, & Urban, 1989), as illustrated in Figure 2.2.1.

The overall composition of fibres and ground substance constituents dictates the properties of CEP tissue. In CEPs from human cadaveric lumbar spines, collagen and GAGs made up 59.3% and 10.8% of the dry weight, respectively (Fields, Rodriguez, et al., 2013). As evidenced in Table 2.2.1, the dry weight composition reported by Fields, Rodriguez, et al. (2013) appears similar to reported dry weight compositions of articular cartilage (Sophia Fox et al., 2009) and annulus fibrosus (Skaggs, Weidenbaum, Iatridis, Ratcliffe, & Mow, 1994). However, the dry weight of collagen is conceivably underestimated by Fields, Rodriguez, et al. (2013) due to the specimen age (51-67 years). That is, an approximate 28.6% reduction in total collagen content was observed in human lumbar CEPs beyond 60 years (Antoniou et al., 1996), suggesting that the CEP may be more fibrous in a young and healthy state.

Table 2.2.1. Dry weight compositions of collagen and GAG in CEP, articular cartilage, and annulus fibrosus tissues.

Tissue	Reference	Collagen (% Dry Weight)	GAG (% Dry Weight)
CEP (Lumbar)	(Fields, Rodriguez, et al., 2013)	59.3	10.8
Articular Cartilage	(Sophia Fox et al., 2009)	60	10-15
Annulus Fibrosus	(Skaggs et al., 1994)	59.3-66.6	7.2-9.0

Within the spine, the CEP separates the IVD from the adjacent vertebral bodies (Figure 2.2.1). It is attached to the cranial and caudal endpoints of the vertebral body and is centrally supported by intricate networks of trabecular bone (Bogduk, 2012). Further, the CEP has a region-dependent thickness that varies from 0.1 mm to 1.6 mm (Moore, 2000; Roberts et al., 1989). The thickness of this cartilage layer is greatest around the structural perimeter and gradually tapers towards the central region (Berg-Johansen, Han, et al., 2018; Hou & Luo, 2009). Unique to the CEP, the porous properties of the surface (pore diameter ≈ 0.14 mm; pore density ≈ 6.24/mm) are less than articular cartilage, therefore reducing permeability for fluid flow and diffusivity for solute transfer (Rodriguez et al., 2011).

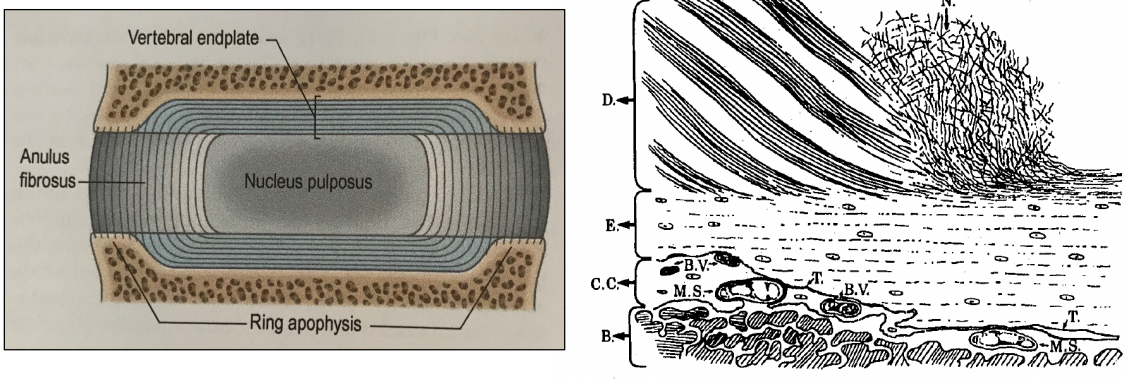

Figure 2.2.1. Left: A sagittal view of the vertebral endplates separating the IVD from the adjacent vertebrae. Image taken from page 14 of Bogduk, 2012. Right: A schematic representation of normal histology, where A = annulus fibrosus, N = nucleus pulposus, E = endplate, B = Bone. Image taken from page 167 of Roberts et al. 1989. Note the horizontal and homogenous orientation of the collagen fibers across the endplate.

Anchorage of the CEP with the annulus fibrosus is achieved by extension of annular and collagen fibers into the CEP surface (Paietta, Burger, & Ferguson, 2013; Wade, Robertson, & Boroom, 2011) (Figure 2.2.2). The strength of this connection is further reinforced by the annulus fibers joining the CEP at oblique angles, as visualized in Figure 2.2.2. (Berg-Johansen, Fields, et al., 2018). In contrast, the CEP is poorly integrated with underlying bone. Histological analyses conducted by Berg-Johansen, Fields, et al. (2018) demonstrated a clear demarcation between the bone and CEP without evident signs of structural integration (Figure 2.2.3). This lack of structural integration creates an anchoring mechanism that is highly susceptible to avulsion, which was visualized by Berg-Johansen, Fields, et al. (2018) using scanning electron microscopy (Figure 2.2.3). Specifically, a physical gap that ranged between 5-30 μm was measured (Berg-Johansen, Fields, et al., 2018)

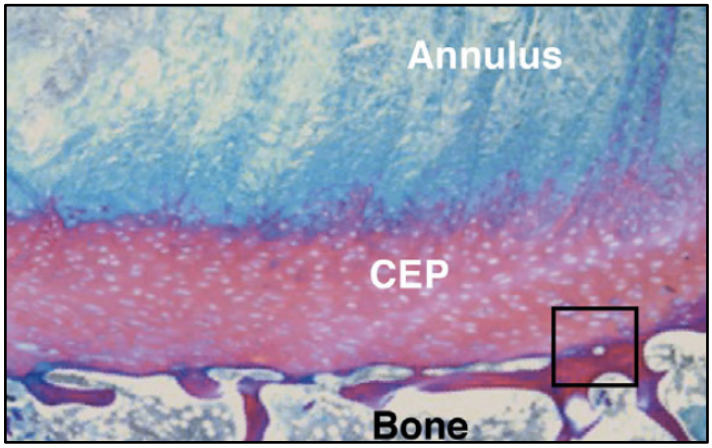

Figure 2.2.2. Structural integration of the annuls fibers with the cartilaginous endplate (CEP) at the IVD CEP junction. Image taken from page 196 of Berg-Johansen, Fields, et al. (2018).

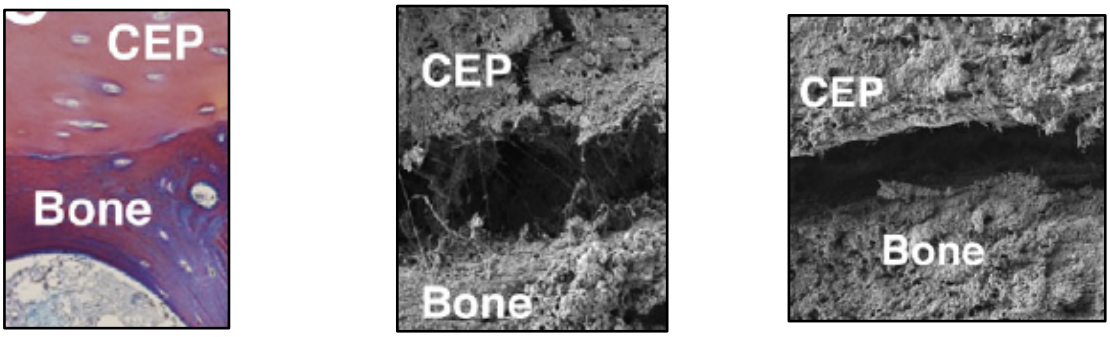

Figure 2.2.3. Histological confirmation of the demarcation between the CEP and bone (right); scanning electron microscopy (SEM) image of the weak structural integration between the CEP and bone (centre); SEM image of avulsion between the CEP and bone (right). Images taken from page 196 of Berg-Johansen, Fields, et al. (2018)

2.2.2. Endplate Properties

The mechanical properties across the CEP surface have been evaluated with uniaxial (Fields, Rodriguez, et al., 2013) and indentation (Grant, Oxland, & Dvorak, 2001; Hou & Luo, 2009; Patel et al., 2018) testing. Fields, Rodriguez, et al. (2013) dissected a mid-sagittal piece of CEP from human cadaveric lumbar spines and performed stress-relaxation tests in tension. A 2% CEP strain was applied over 8 seconds followed by 10-minute holding period. The average mechanical properties reported were: tensile modulus = 5.9 MPa, energy dissipation = 0.035 MPa, and long relaxation constant = 362 seconds (Fields, Rodriguez, et al., 2013). During an indentation test (3 mm hemisphere), Patel et al. (2018) loaded/unloaded endplate regions at a rate of 0.05 mm/s to a maximum load of 10 N, which was maintained for a 30 second duration. The results were collapsed across endplate regions, but an average loading stiffness of 61.8 N/mm was reported (Patel et al., 2018). A similar indentation setup was used by Grant et al. (2001), where CEP surface locations were indented at 0.2 mm/s to a depth of 3 mm. Centrally, the stiffness was approximately 120 N/mm, while the stiffness of peripheral regions ranged from 130-175 N/mm (Grant et al., 2001). It should be noted that similar stiffness responses were observed in endplates from the L3 to L5 spinal levels (Grant et al., 2001). Indentation tests have also been used to examine the mean

failure load in central and peripheral endplate regions (Grant et al., 2001; Hou & Luo, 2009). The mean failure load documented in peripheral and central regions ranged from 70-120 N and 50-60 N, respectively (Grant et al., 2001; Hou & Luo, 2009).

2.2.3. Endplate Function

The CEP has two primary functions in the lumbar spine:

The first function involves the transmission of compression loads through the spinal column. Under compression loading, the pressurization of the semi-solid nucleus pulposus (NP) facilitates vertical deflection of the CEP into the adjacent vertebral body (Bogduk, 2012; S. H. M. Brown, Gregory, & McGill, 2008). Vertical deflection imparts radial tensile stresses onto the CEP surface and offloads the magnitude of radial tension experienced by the inner concentric layers of the annulus fibrosis (AF) (Bogduk, 2012). In response to CEP deflection, vertically orientated columns of trabecular bone undergo bending (Fyhrie & Schaffler, 1994; McGill, 2002), which may initiate microcrack formation if large enough in magnitude (Wenzel, Schaffler, & Fyhrie, 1996). CEP deflection caused by repeated sub-threshold compression (Parkinson & Callaghan, 2007b, 2009) or acute trauma (Fahey, Opeskin, Silberstein, Anderson, & Briggs, 1998; Yingling, Callaghan, & McGill, 1997) may cause the CEP structure to fracture. Common endplate fractures include lesions of irregular and varying appearances (Brinckmann et al., 1988; Gallagher et al., 2006; Y. Wang, Videman, & Battié, 2012) and Schmorl's nodes which are defined by a circular fracture to the central endplate region and intrusion of the NP into the adjacent vertebral body (Schmorl & Junghanns, 1971; Seymour, Williams, Rees, Lyons, & Lloyd, 1998; Takahashi, Mitazaki, Ohnari, Takino, & Tomita, 1995). The loading and damage criteria have yet to be dissociated for these common CEP injuries.

Secondly, the CEP serves as the primary gateway for fluid flow and macromolecule transport into and out of the IVD (Y. C. Huang, Urban, & Luk, 2014). Since the IVD is avascular, CEP health is critical for maintaining physiological homeostasis (Y. C. Huang et al., 2014). Permeability for fluid flow and diffusivity for solute transport is largely governed by the porous structure and the radial strains imparted on the CEP (Jackson & Gu, 2009). Using magnetic resonance imaging, Martin et al. (2022), demonstrated that the volume of fluid transport was approximately 25% greater in cranial spinal levels compared to caudal spinal levels. Irrespective of spinal levels, fluid flow was greatest in the central region compared to peripheral regions that interface with the annulus fibrosis (Martin et al., 2022). A region-dependency was also demonstrated for diffusivity, which was strongly correlated with CEP thickness. That is, the central region had higher glucose (3.44×10^{-7} cm^2/s) and lactate (5.52×10^{-7} cm^2/s) diffusivities than the lateral (glucose = 2.46×10^{-7} cm^2/s; lactate = 4.11×10^{-7} cm^2/s) and posterior (glucose = 1.91×10^{-7} cm^2/s; lactate = 3.36×10^{-7} cm^2/s) regions (Y. Wu et al., 2016). In addition to thickness, these regional differences in diffusivity were attributed to a denser porosity observed in the central region compared to peripheral regions (Y. Wu et al., 2016). Changes in diffusivity were also apparent when CEPs were exposed to compression. The average diffusivity across the CEP systematically decreased under compressive strains of 0% (glucose = 2.68×10^{-7} cm^2/s; lactate = 4.52×10^{-7} cm^2/s) to 20% (glucose = 1.44×10^{-7} cm^2/s; lactate = 2.76×10^{-7} cm^2/s) (Y. Wu et al., 2016), which was likely driven by the compaction of pores as the CEP surface deflected. In addition to load, calcification of the CEP surface is strongly associated with aging and injury, which further reduces the surface permeability and diffusivity (Giers et al., 2017; Rodriguez et al., 2011).

2.3. Low Back Injury Framework

In this thesis, the various types of CEP lesions are considered injuries. Injury is defined herein as tissue disruption resulting from mechanical overload (Kumar, 2001; McGill, 1997) and manifests when the applied force exceeds the tissue tolerance. Within the low back, mechanical overload typically occurs through one of two scenarios: overexertion or overuse (McGill, 1997).

2.3.1. Theoretical Macroscopic Low Back Injury Mechanisms

The first injury mechanism is described as overexertion or synonymously referred to as acute (McGill, 1997). In these scenarios, a single loading exposure exceeds the ultimate tissue tolerance (Figure 2.3.1). The the ultimate tissue tolerance represents the maximum compression force that can be withstood prior to failure in one or more structures of the spine (Geniady, Waly, Khalil, & Hidalgo, 1993).

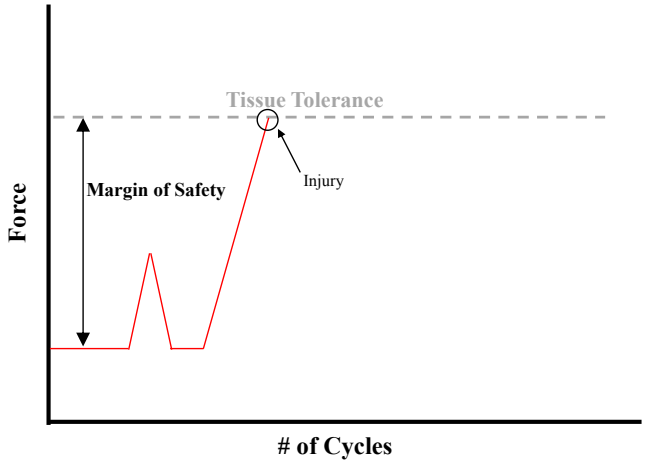

Figure 2.3.1. A schematic of an overexertion low back injury mechanism. Mechanical overload is depicted on the second loading cycle where the applied load (drawn in red) exceeds the tissue tolerance. This figure is adopted from McGill (1997).

The second injury mechanism is referred to as overuse or chronic (McGill, 1997). Overtime, tissues are mechanically overloaded due to repeated or prolonged loading exposures

that are *initially* sub-failure in magnitude, implying that a margin of safety exists (Figure 2.3.2). However, if the rate of tissue degradation exceeds the rate of tissue recovery and/or synthesis, there is a gradual reduction in tissue tolerance and margin of safety (Kumar, 2001).

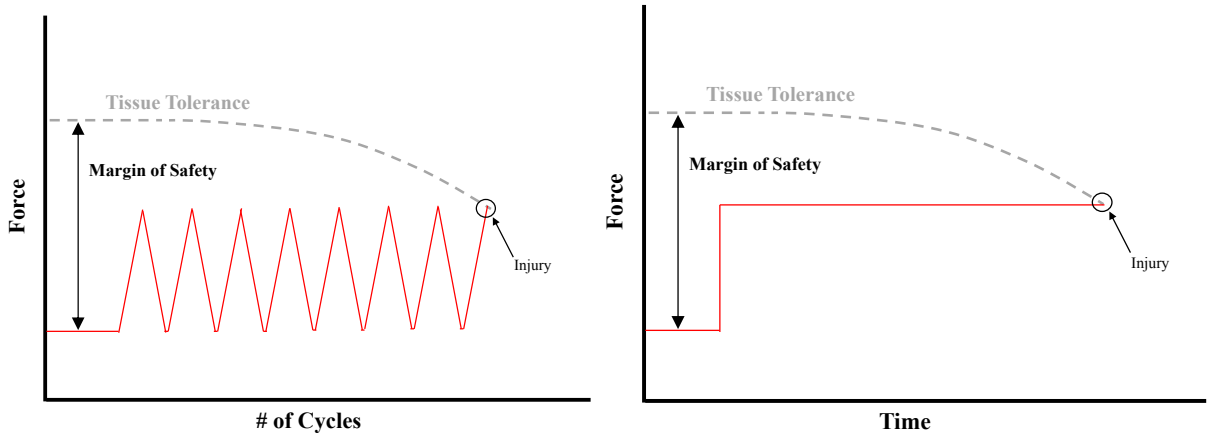

Figure 2.3.2. A schematic of repetitive (left) and sustained (right) overuse low back injury mechanisms. As depicted, there is a gradual reduction in tissue tolerance until it eventually becomes less than the applied load (drawn in red). These images are adopted from McGill (1997).

Overexertion injuries are theoretically and pictorially obvious for accidental traumas where the applied compression force far exceeds the tissue tolerance (Figure 2.3.1). However, existing knowledge on overuse low back injuries does not fully align with theoretical depictions (Figure 2.3.2). To date, *in vitro* experimental studies have demonstrated how different parameters (i.e., compression force, loading frequency, joint posture) influence the number of cycles that spinal joints can tolerate prior to failure, which is referred to as the joint lifespan (Callaghan & McGill, 2001a; Gooyers et al., 2018; Gooyers et al., 2012; Parkinson & Callaghan, 2007b, 2008). This aligns with traditional approaches for the study of mechanical fatigue (i.e., power law) and how lifting related low back injury risk is currently assessed in occupational settings (Gallagher, Sesek, Schall, & Huangfu, 2017). However, the understanding of injury pathways and risk will be ultimately hindered without evidence for how specific loading paradigms influence the strength

and properties of spine tissues overtime. Despite being depicted in Figure 2.3.2, time-varying changes in ultimate compression tolerance beyond the initial loading cycles are largely unknown in spinal tissues. Based on this missing information, the current theoretical understanding of overuse low back injury is depicted in Figure 2.3.3, where initial estimates of ultimate compression tolerance can be obtained from previous *in vitro* research where spinal joints were tested in a healthy and unloaded state (Adams & Hutton, 1982; Biggemann et al., 1988; Brinckmann et al., 1989; Gunning et al., 2001; Hutton et al., 1979). The acquisition of data demonstrating the cycle-dependent changes to the structure and properties of low back tissues has potential to advance knowledge on overuse injury mechanisms and improve low back injury risk assessment from a probability of failure for single load magnitude to margin that can be safety withstood for a given loading history.

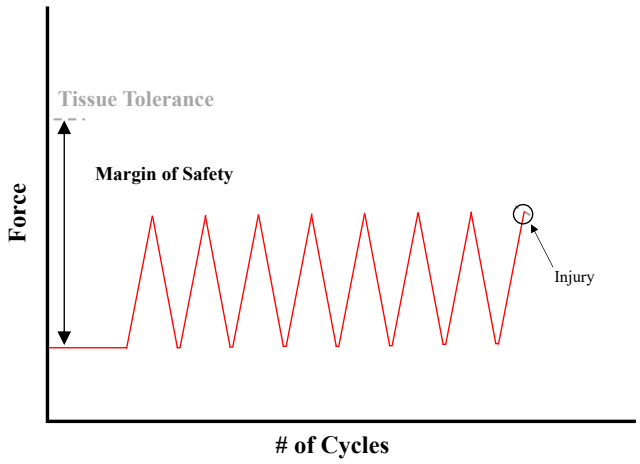

Figure 2.3.3. A schematic of an overuse injury mechanism based on known information. Ultimate compression tolerance is unknown beyond initial loading cycles leaving risk evaluations to the number of tolerated loading cycles.

2.3.2. Microscopic Damage Accumulation

The properties of connective tissues are dependent on the biochemical composition and molecular architecture. While mechanical loading is an important and essential stimulus to improve and preserve musculoskeletal tissue health, in high or prolonged doses, microscopic damage can accumulate. Within the CEP, microscopic damage has been compared between injured and uninjured human cadaveric CEPs. Rodriguez et al. (2011) used microcomputed tomography to demonstrate a greater porosity in the subchondral trabecular bone (9%) and vertebral cartilage (14%) adjacent to degenerated IVDs. These findings further demonstrate that microstructural damage initiates and accumulates below the CEP surface prior to macroscopic failure. Biochemical comparisons have been made between undamaged and damaged human cadaveric lumbar CEPs defined by erosion with exposure of subchondral bone at the junction of the nucleus pulposus (Fields, Rodriguez, et al., 2013). Damaged CEPs had 15.4% less water, 19.6% less GAG content, and 14.7% less collagen content compared to undamaged human cadaveric lumbar spine CEPs, but these differences did not reach statistical significance (Fields, Rodriguez, et al., 2013). In a later study by Fields, Han, Krug, and Lotz (2015), similarities in biochemical composition were also observed between damaged and undamaged human cadaveric lumbar CEPs. Despite these similarities in biochemical composition, subsequent logistical regressions demonstrated the strength of relationships between extracellular matrix constituents and tensile modulus (Fields, Rodriguez, et al., 2013). Compared to GAG content ($R = -0.34$) and water content ($R = 0.07$), collagen had the strongest relationship with tensile modulus ($R = 0.59$) (Fields, Rodriguez, et al., 2013).

As evidenced above, existing research on microstructural and biochemical damage has been exclusively conducted on human cadaveric lumbar spine CEPs. Although structural

differences between damaged and undamaged CEPs were identified, the pathways of microdamage (structural and biochemical) initiation and accumulation in response to specific loading paradigms remains unknown. Further, the link between microscopic damage within the CEP and its effect on tissue properties has not been well studied, with the current knowledge being limited to the linear regression results presented by Fields, Rodriguez, et al. (2013). To fail to acknowledge microstructural and biochemical changes in response to mechanical loading is to risk gaining an oversimplified understanding of CEP injury mechanisms, it being effectively hidden by macroscopic results that are ultimately generated by a premature accumulation of damage. In contrast, failure to relate measures of microstructural damage back to the tissue properties and function will ultimately stall efforts towards understanding how and why individuals injure their CEP during some loading cycles and not others; they must be studied in parallel.

2.4. Demands vs. Capacity

Against the described injury frameworks, biomechanical assessment of low back injury mechanisms must consider the applied forces together with what the tissues can withstand prior to failure occurring. The internal joint compression forces reported during manual lifting have ranged from 6.4 kN to 12.6 kN during maximal effort deadlifts (Cholewicki et al., 1991) to 3.1 to 6 kN during submaximal occupational lifting tasks (T. A. C. Beach et al., 2019; Gooyers et al., 2018; Marras et al., 2009; Zehr, Carnegie, et al., 2020; Zehr et al., 2018).

UCT has been quantified using *in vitro* mechanical testing on cadaveric spinal units from human lumbar and porcine cervical spines. Depending on the posture and loading rate, the ultimate compression tolerance ranged from 6.9 kN to 13.8 kN in healthy spinal units (Adams & Hutton, 1982; Adams, Hutton, & Stott, 1980; Biggemann et al., 1988; Brinckmann et al., 1989; Gunning et al., 2001; Hutton et al., 1979). The UCT is further dependent on many personal and experimental

factors, including biological sex, age, spinal level, body weight, physical activity, and the tested spinal component (Adams & Hutton, 1982; Brinckmann et al., 1989; Geniady et al., 1993; Hansson, Keller, & Spengler, 1987; Hutton & Adams, 1982; Porter & Adams, 1989). Based on a thorough review of personal factors and their effect on UCT, age was the most strongly correlated factor (R = -0.51 to -6.1) (Genaidy, Waly, Khalil, & Hidalgo, 1993). It was further stated that the UCT of spinal components (i.e., motion segments and lumbar vertebra) decreased by 10-22% per decade (Genaidy et al., 1993). Although accounting for less variance, biological sex and body weight were similarly correlated with UCT (R = 0.43 to 0.48) (Genaidy et al., 1993). On average, the UCT in females was 33% less than males (Adams & Hutton, 1982; Brinckmann et al., 1988, 1989; Hansson et al., 1987; Hutton & Adams, 1982; Hutton et al., 1979). Within the lumbar spine, the UCT of each vertebra increases systematically from the most cranial (L1) to the most caudal (L5), with the UCT of the L4 being approximately 85% of the L5 (Genaidy et al., 1993). Further, it has been documented that the UCT of lumbar motion segments (Adams & Hutton, 1982; Brinckmann et al., 1989; Hansson et al., 1987; Hutton & Adams, 1982) is greater than that of isolated lumbar vertebrae (Biggemann et al., 1988; Hutton et al., 1979), although it is unclear if this 10% difference was due to differing failure detection approaches.

In comparing the low back compression forces with existing estimates of ultimate compression tolerance, an overexertion injury mechanism is generally not supported for occupational lifting tasks. That is, a margin of safety ranging from 0.9 kN to 10.7 kN exists during the single time point that can be examined, that being when the joint is in a healthy and unloaded state. For maximal effort deadlifts, however, the internal compression forces, especially those experienced by male participants exceed some current UCT data. Although an overexertion injury mechanism appears possible during such scenarios, it could be argued that the professional

powerlifters examined by Cholewicki et al. (1991) have developed a greater compression capacity through prolonged training endeavours. It could be further argued that external loads of 145. 3 kg (women) and 256.7 kg are generally not lifted by the general population, non-powerlifting athletes, or as occupational duties. In collective consideration of the lifting demands and low back compression tolerance that is representative of a healthy and unloaded state, it is conceivable that incidental low back injuries related to lifting exertions are a cumulative loading issue.

With that said, appreciation is owed to cycle-dependent mechanical properties of the spinal tissues. In support of McGill's (1997) argument, the assignment of incidental CEP to a specific task without knowledge of the prior joint loading history should be done with extreme caution. The difficulty in discerning the precise mechanism of incidental injury was also encountered by Gooyers and colleagues (2013) who examined an unfortunate partial Achilles tendon rupture that occurred during the simulation of occupational tasks in an instrumented laboratory setting. The authors discussed that although the incidental injury would have likely been clinically attributed to an acute injury mechanism, their time-series data supported the likely modulation of tissue tolerance due to prior loading cycles in combination with cumulative loading exposures occurring before the experimental exposures (Gooyers et al., 2013). From this case study and the commentary of McGill (1997), it is evident that a comprehensive understanding of prior joint loading and its effect on CEP properties is needed to advance understanding of injury mechanisms and to mitigate potential for future incidental low back injuries.

2.4.1. Physical Loading History

Videman et al. (1990) examined the effects of life-time joint loading history on the type and severity of low back pathology post-mortem. Amongst many factors (e.g., history of disease, history of injury, etc.), physical loading histories were inferred from the occupational history of

149 male cadavers and subsequently related back to the observed spinal pathology. In collaboration with physicians, the research group classified the physical loading histories as either sedentary and cyclic, with cyclic exposures being further separated into “mixed” and “heavy”. Interestingly, the prevalence of spinal pathologies (i.e., IVD degeneration, annular ruptures, endplate defects, facet joint osteoarthrosis, osteophyosis of the vertebral body) was linked to loading history (Videman et al., 1990). Severe (Grade III) disc degeneration (Prevalence = 75%; OR = 2.8), endplate defects (Prevalence = ; 88%; OR = 5.0), and vertebral body osteophyosis (Prevalence = 57%; OR = 12.1) were strongly associated with heavy physical work, although the authors did not explicitly state if many/all of these pathologies co-existed (Videman et al., 1990). In contrast, a mixed loading history was associated with the smallest prevalence (32-55%) of all spinal pathologies (Videman et al., 1990). An important contribution of this work is the presentation of strong empirical evidence that highlights physical loading history as a risk factor for endplate injury.

Despite the strong associations between long-term physical loading history and low back pathology, the effect of an acute loading history on the potential for musculoskeletal injury development is unknown, particularly within the CEP. Several knowledge gaps pertaining to joint fatigue (i.e., the cycle-dependent tissue tolerance) must be addressed, precisely for what Videman et al. (1990) defined as “mixed” cyclic loading. Although “mixed” loading implicitly referred to mixed loading magnitudes, it may also refer to the variation of several loading characteristics (e.g., duration, magnitude, mode etc.).

2.4.2. Loading Variability

As discussed, variation in loading magnitude was associated with a significantly smaller occurrence of endplate pathology (55%) (Videman et al., 1990). In alignment with this finding,

variation in joint loading magnitude is also hypothesized to reduce the potential for musculoskeletal injury development (James, Dufek, & Bates, 2000; Mathiassen, 2006). However, in a recent study, a ±30% variation in peak compression exposures yielded a significant reduction in cumulative load tolerance compared to non-variable loading at average peak compression magnitudes of 30% (22.7 MN·s), 50% (12.1 MN·s), and 70% (0.6 MN·s) of the predicted ultimate compression tolerance (Zehr, Tennant, & Callaghan, 2019b). All macroscopic injuries were observed in the CEP (Zehr et al., 2019b). A subsequent analysis of Kaplan-Meier survival functions was performed to discern if these findings were consistent throughout the cyclic compression protocol or if there was a distinct point (i.e., number of continuous cycles) at which the probability of endplate fracture diverged between cyclic paradigms (Zehr et al., 2019a). The survival functions revealed that survivorship probability was greatest without compression variation but only beyond 2600, 575, and 15 cycles during 30%, 50%, and 70% loading, respectively (Zehr et al., 2019a). Taken together, this collection of studies demonstrates the need for examining the dynamic effect of compression variability on endplate tolerance during cyclic loading.

2.4.3. Lumbar Spine Postural Deviation

The effect of deviated joint postures within the lumbar spine on the tolerated cumulative compression load have been well documented (Callaghan & McGill, 2001a; Gooyers & Callaghan, 2015; Gooyers et al., 2012; Gunning et al., 2001). Compared to a neutral posture, there was a 32% (3.4 kN) decrease in ultimate compression strength when isolated spinal joints from the porcine cervical spine were statically positioned in flexion and loaded at a rate of 3000 N/s until macroscopic failure occurred (Gunning et al., 2001). Under prescribed cyclic sub-threshold loading paradigms, dynamic flexion-extension motion coupled with compression loading

accelerated fatigue damage in the annulus fibrosis (Callaghan & McGill, 2001a; Gooyers et al., 2015) and resulted in significantly greater IVD height loss (Gooyers & Callaghan, 2015; Gooyers et al., 2012). These changes in cumulative load tolerance and joint function were exacerbated under higher compression loading conditions.

These documented effects of posture on a reduced capacity for the CEP to withstand and transmit forces may be attributed to changes in load distribution within the joint (Adams & Hutton, 1980; McMillan, McNally, Garbutt, & Adams, 1996). A flexed spinal joint causes the pressure within the IVD (i.e., nucleus pulposus) to increase (Adams & Hutton, 1980; McMillan, McNally, et al., 1996), with the maximum IVD pressure occurring near the flexion limit, particularly beyond 2700 loading cycles (Noguchi, Gooyers, Karakolis, Noguchi, & Callaghan, 2016). Within the CEP, it has been shown that higher IVD pressures reduce the permeability for fluid expulsion from the IVD, which facilitates greater CEP deflection and increased tensile strains experienced by the central region (Malandrino et al., 2009; McMillan, McNally, et al., 1996). With fewer CEP regions sharing the load bearing burden and the central region undergoing larger stresses to do so, postural deviation is an important mechanical factor for understanding the effect of prior loading histories on CEP injury risk.

2.4.4. Cyclic Loading Duration

The cyclic loading duration was defined as the number of continuous loading cycles. It will not refer to the time of each loading cycle, as this parameter was fixed for all compression paradigms performed in this thesis. *In vitro* studies that exposed isolated spinal joints to cyclic compression loading demonstrated a physiological response related to osmotic-load equilibrium during sustained cyclic loading (Botsford, Esses, & Ogilvie-Harris, 1994; Krag, Cohen, Haugh, & Pope, 1990; Noguchi et al., 2016). This response was described as an expulsion of fluid from the

intervertebral disc by a diffusion mechanism through the superior and inferior CEPs when exposure to compression loading was continuous (i.e., no offloading/rest periods) and sustained (Botsford et al., 1994; Krag et al., 1990). The associated reduction in fluid content within the nucleus pulposus of the IVD resulted in a subsequent height loss, change in stress distribution across the spinal joint (Botsford et al., 1994; Krag et al., 1990; van Dieën, Kingma, et al., 2001) and IVD bulging (Gooyers & Callaghan, 2015; Gooyers et al., 2012). Fluid expulsion and the associated height loss explains a further decrease in disc pressure as the number of tolerated cycles increases, particularly beyond 2700 sub-threshold cycles (Noguchi et al., 2016). Collectively, these findings from *in vitro* experiments support the notion of cycle-dependent changes in load distribution and joint function. Quantifying the cycle-dependent changes in CEP properties and structure may provide new insight into overuse low back injury mechanisms.

2.5. Methodological Considerations

2.5.1. The Porcine Cervical Spine as a Surrogate for the Human Lumbar Spine

The porcine cervical spine was used as a surrogate for the human lumbar spine. Specifically, the osteoligamentous C3C4 and C5C6 functional spinal units (FSUs) excised from the porcine cervical spine – two adjacent vertebra and the intervening intervertebral disc (Oxland, Panjabi, Southern, & Duranceau, 1991; Yingling et al., 1999) – were included in experiments comprising this dissertation. The porcine animal model is a desirable alternative to the human lumbar spine based on the numerous functional, anatomical, and mechanical similarities. Functionally, the head of a domestic pig is cantilevered off of the thorax and supported against the force of gravity by an internally generated extensor moment similar to how the human lumbar spine is cantilevered off of the pelvis segment. Anatomically, FSUs from the porcine cervical spine are capable of rotating in three dimensions (i.e., flexion/extension, lateral bend, twist) and can

tolerate compression and shear loading (Oxland et al., 1991). Two notable differences, however, include the presence of anterior processes, which appear to have no documented mechanical function and endplates that have a smaller surface area (Yingling et al., 1999). Further, porcine cervical and human lumbar FSUs have a similar pedicle width (≈ 9 mm), sagittal facet angles (≈ 45°), transverse facet angles (≈ 81°), ultimate compressive load (6.7-8.9 kN), and anterior/posterior stiffness (150-200 N/mm/104-164 N/mm) (McLain, Yerby, & Moseley, 2002; Yingling et al., 1999). In addition, the architecture of the trabecular bone networks within the vertebral body are similar within the porcine cervical spine and human lumbar spine in the absence of disease (Busscher et al., 2010). In collective consideration of the anatomical, functional, and structural similarities a comparable mechanical response to compression loading is expected.

Although *in vitro* experimentation with healthy human cadaveric lumbar specimens is ideally preferred, this approach, however, does not feasibly afford the necessary number of test specimens or scientific control that is important to the study of CEP injury mechanisms. For example, tissues acquired from human donors are typically obtained from an elderly population with degenerative changes and/or injuries to the osteoligamentous tissues of interest. In contrast, the use of a porcine animal model permits experimental control over the potential confounding effects of age, activity, diet, and disease on joint function and fatigue. Since domestic pigs are explicitly raised as a food source in most developed countries in a relatively standardized time period (≈ 5 months) (Reiland, 1978), young and non-degenerated, tissues can reliably be obtained.

2.5.2. Freezing of Spinal Tissues

All porcine cervical spine specimens were thawed from a frozen state. In porcine FSUs, the ultimate compression failure load of a thawed specimen was approximately 24% greater compared to a fresh specimen (Callaghan & McGill, 1995). The energy stored at failure was also

33% greater in a thawed specimen compared to a fresh specimen (Callaghan & McGill, 1995). In human cadaveric tissues, a less than 1% difference in compressive stiffness and hysteresis was observed between thawed and fresh FSUs that were exposed to cyclic compression loading (500 N – 1000 N) (Smeathers & Joanes, 1988). Further, despite freezing causing an increase IVD height, this change is height was adequately recovered during the thawing process (Dhillon, Bass, & Lotz, 2001) and via a static compression (300 N) pre-loading procedure (Callaghan & McGill, 1995). The abovementioned limitations linked to the performance of mechanical testing on thawed FSUs are fully acknowledged. However, in spite of these limitations, it is not feasible to obtain and store fresh porcine cervical FSUs in the quantity that was necessary for the completion of this thesis.

2.5.3. Staining Techniques for the Analyses of Endplate Microstructure

Compared to articular cartilage surfaces, which primarily experience compression forces, the CEP primarily experiences tensile loading. Recall, pressurization of the nucleus pulposus in response to joint compression loading causes the CEP surface to deflect thereby imposing radial tension, especially in the central region. Since the compliance and tensile strength in cartilage are largely driven by type II collagen (Young et al., 2014), the study of loading-induced ECM damage within the CEP will focus on damage to collagen proteins. Therefore, a technique that simultaneously distinguishes native from damaged collagen proteins within the cartilage surface (type II) and subchondral bone (type I) is required. The ability to simultaneously assess microstructural damage would be an additional asset.

Numerous approaches have been implemented to study the microstructure and composition of isolated endplate tissues. These include: biochemistry (Fields et al., 2015; Fields, Rodriguez, et al., 2013), gene expression (Lakstins, Arnold, Gunsch, Flanigan, et al., 2020), and histological procedures like a standard hematoxylin-eosin (H&E) (Hou & Luo, 2009; Y. Wu et al., 2016),

enhanced resolution techniques like tri-chrome (Berg-Johansen, Fields, et al., 2018; Berg-Johansen, Han, et al., 2018; Fields, Rodriguez, et al., 2013), and Safranin-O-Fast Green (Alberton et al., 2019; B. Huang et al., 2021; Maerz, Newton, Marek, Planalp, & Baker, 2018; Morisako et al., 2022).

Biochemistry approaches have been used to quantify the content of proteins and carbohydrates that comprise the extracellular matrix of cadaveric CEPs (Fields et al., 2015; Fields, Rodriguez, et al., 2013). This technique typically involves normalizing the dry weight of each constituent to a percentage of total dry weight. A limitation of this technique is that native and damaged collagen proteins as well as collagen types are not dissociated. Therefore, damaged collagen proteins may still be detected as mass, but their function and therefore strength is conceivably altered. This limitation may explain the statistical similarities in water, collagen, and GAG content that were observed between visibly damaged and undamaged human cadaveric lumbar CEPs (Fields et al., 2015; Fields, Rodriguez, et al., 2013).

Various staining techniques have been used to visualize the CEP microstructure. Specifically, tri-chrome staining techniques are well-suited to visualize connective tissues, particularly collagen (Leonard et al., 2018). Tri-chrome indicates that the technique produces three colours. While variations exist, Mallory's procedure is commonly used to study cartilage, where three acidic dyes are used to identify nuclei (dark red), collagen fibers and/or cartilage matrix (blue) and erythrocytes (orange) (Mallory, 1900). This technique has been used to characterize morphological characteristics of the CEP such as thickness (Berg-Johansen, Fields, et al., 2018; Berg-Johansen, Han, et al., 2018; Hou & Luo, 2009) and porosity (Giers et al., 2017; Hou & Luo, 2009; Y. Wu et al., 2016). This technique also enables the organization of collagen networks to be visualized and quantified (Berg-Johansen, Fields, et al., 2018). One limitation, however, is this

technique is unable to dissociate the types of collagen fibers. It is known that collagen types have different functions (Young et al., 2014), and the ability to dissociate collagen types within and between tissues may provide more detailed insight into structure-function relationships within the CEP.

Safranin staining is useful for identifying and dissociating tissue types and cells (Jaffe, Hammond, Tolias, & Arinzeh, 2012). Safranin is a cationic dye that binds to proteoglycans in cartilage, giving cartilage surfaces an orange/red appearance when viewed under a brightfield microscope (Jaffe et al., 2012). Safranin staining, in particular, has been used to identify microinjuries in human cadaveric lumbar CEPs, such as avulsion from the subchondral bone (Berg-Johansen, Fields, et al., 2018). Often paired with Safranin staining is Fast Green, which stains the cytoplasm of osteocytes in underlying bone tissue green (Jaffe et al., 2012). Given the affinity of GAGs (attached to proteoglycan proteins) to bind with water and generate hydrostatic resistance to compression, this combination of Safranin O – Fast Green is a gold standard for histologically assessing the progression of osteoarthritis (Pauli et al., 2012). However, given the tensile loads experienced by CEPs, Safranin O – Fast Green may not fully capture the ECM damage, especially that to collagen proteins.

Immunohistochemistry techniques have been employed to quantify ECM and cellular responses to mechanical stimuli (Bian et al., 2016; Xu et al., 2014; Xu et al., 2016). An advantage of immunohistochemistry techniques over histology approaches is the ability to simultaneously stain multiple specific proteins. Thus, immunohistochemistry procedures may enable the simultaneous examination and dissociation between type I and type II collagen in the CEP and subchondral bone. All proteins, including collagen, have antigenic sites (i.e., epitopes) that are recognizable to antibodies. In collagen, the epitope is defined by the genetic sequence of three

polypeptide chains comprising the triple helix structure (Kim et al., 2000). Immunohistochemistry protocols use antibodies to visualize specific proteins such as collagen. Mammalian antibodies are structurally comprised of four polypeptide chains, two light chains and two heavy chains (Johnson & Spence, 2010). As demonstrated in Figure 2.5.1, the light chains consist of two domains; one variable (VL – variable light chain) and one constant (CL – constant light chain) domain (Johnson & Spence, 2010). In contrast, each heavy chain contains one variable (VH – heavy chain variable) and 3 or 4 constant (CH# – constant heavy chain) domains (Johnson & Spence, 2010). Characteristics of the heavy chain – the number of CH domains and the linkages between them – is what distinguishes the five antibody types (IgG, IgA, IgM, IgE, IgD) (Johnson & Spence, 2010). The structure of Immunoglobin G (IgG) is presented in Figure 2.5.1, and this antibody type is the most abundant in the human body, making up over 75% of the antibodies found in serum and synovial fluid (Johnson & Spence, 2010). Antibodies to native forms of type I and type II collagen naturally exist and are mainly IgG (Clague & Moore, 1984; Kim et al., 2000). Specifically, the incidence of IgG antibodies to native collagen II proteins have been measured in the serum and synovial fluid of healthy individuals and patients with rheumatoid arthritis (Clague & Moore, 1984).

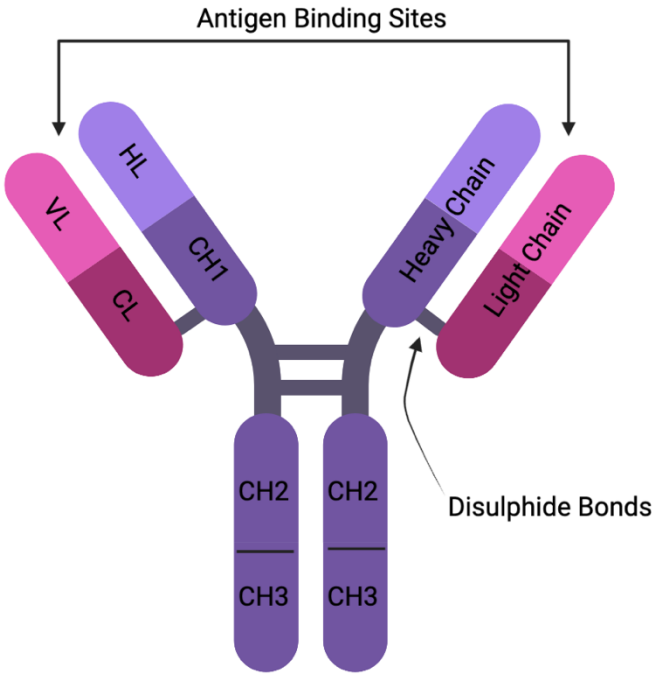

Figure 2.5.1. The structure of an Immunoglobin G (IgG) antibody. Domains of the light chains (pink) and heavy chains (purple) and depicted.

Antibodies that directly bind to the epitope of a target protein are defined as primary antibodies (Johnson & Spence, 2010). Generally, primary antibodies are unconjugated, meaning a detectable signal cannot not be visualized, despite successful antibody-epitope binding (Johnson & Spence, 2010). The use of conjugated secondary antibodies that bind with primary antibodies form the foundation for immunofluorescence protocols (Johnson & Spence, 2010). Conjugated secondary antibodies are attached to a fluorophore molecule (Figure 2.5.2), which is a fluorescent component that emits a detectable signal of a specified colour upon light excitation (Johnson & Spence, 2010).

A schematic of immunofluorescence staining conducted on a type II collagen protein in native (positive staining) and damaged (negative staining) form is depicted in Figure 2.5.2. As

demonstrated, the primary IgG antibody for native type II collagen binds to the epitope of an intact protein enabling secondary antibody attachment and labelling. However, damage to the native collage protein alters the epitope thereby inhibiting primary antibody binding and resulting in negative staining (Figure 2.5.2). This ability to dissociate between native and damaged collagen proteins may be informative for evaluating how mechanical loading affects damage initiation and progression in CEP tissues. Although staining for a single protein is depicted in Figure 2.5.2, multiple proteins (i.e., different collagen types) can be simultaneously stained for using a single antibody cocktail.

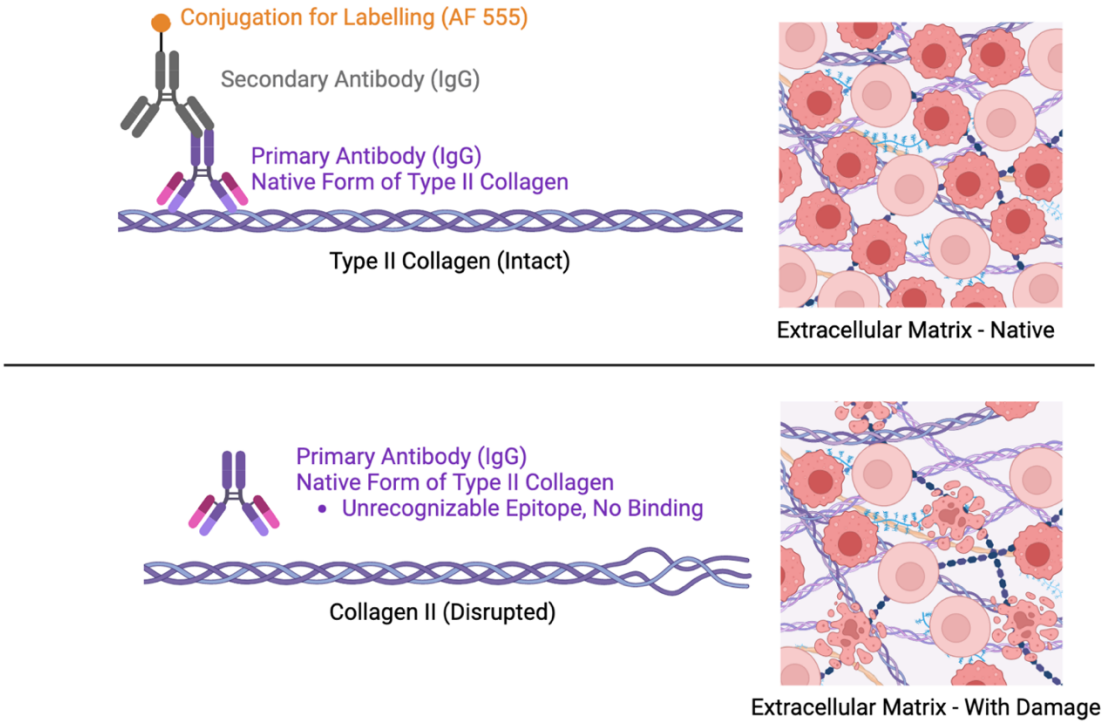

Figure 2.5.2. A schematic of immunofluorescence staining with a primary antibody for type II collagen and conjugated secondary antibody.

2.6. Summary

In summary, there is epidemiological evidence to suggest that incidental low back injuries, in particular CEP failure, occur in connection to lifting tasks that are qualitatively described as high demand. Despite the compression forces experienced by the spinal tissues being greater than habitual exposures, the cause and mechanistic pathway of these radiographically confirmed CEP injuries is unclear and lacks a theoretical justification. In the absence of fundamental knowledge describing the changes to CEP properties and structure, it is challenging to develop and evaluate the low back injury potential, improve safety, and/or and develop interventions intended to reduce the magnitude of internal compression loading.

CHAPTER 3

Methodology

This chapter describes three separate studies that were conducted for the development and/or justification of experimental approaches used in in Chapters 4-9. The implementation of findings from each study are further discussed.

3.1. Reaction forces and flexion-extension moments imposed on functional spinal units with constrained and unconstrained in vitro testing systems.

Jackie D. Zehr & Jack P. Callaghan

Journal of Biomechanical Engineering, 114(5), 054501, 2022

Overview

This study quantified how constrained and unconstrained *in vitro* testing systems altered the compression force, anterior-posterior shear force, and flexion-extension moment experienced by functional spinal units. The forces and moments applied to the superior aspect of the spinal joint were measured with a load cell and torque cell, respectively and these data were compared to force and moment measurements obtained using a six degree-of-freedom force and moment sensor that was positioned inferior to the spinal unit. In effect, this experimental setup permitted the analysis of load transfer through the functional spinal unit.

3.1.1. Introduction

In vitro experiments are frequently conducted on functional spinal units to investigate overuse injury mechanisms (Callaghan & McGill, 2001a; Tampier, Drake, Callaghan, & McGill, 2007; van Heeswijk, Thambyah, Robertson, & Broom, 2017) and the effectiveness of orthopaedic

interventions (Basra, Bucklen, Muzumdar, Khalil, & Gudipally, 2015; Minns & Walsh, 1997; Techens, Palanca, Éltes, Lazáry, & Cristofolini, 2020). To experimentally do so, physiological joint loading superimposed with intervertebral joint motions experienced by the *in vivo* spine must be simulated on cadaveric tissue. A specific combined loading scenario that is commonly simulated is subthreshold axial compression and sagittal plane joint rotation. This loading scenario, in particular, is used to study intervertebral disc mechanics (Adams, Green, & Dolan, 1994; Callaghan & McGill, 2001a; Tampier et al., 2007), endplate and/or bone fatigue (Parkinson & Callaghan, 2009; Zehr, Buchman-Pearle, et al., 2020; Zehr et al., 2019b), and fixation devices (Lund et al., 2003; McLachlin et al., 2008). Although numerous experimental methods and testing systems exist, a standardized goal for mechanical testing amongst the documented *in vitro* modalities is the application of concentric joint forces coupled with pure rotational moments. In effect, the goal being that the applied axial forces are equal to the joint reaction force(s) and do not induce an additional moment onto the tested joint.

From the vast body of literature, axial compression and flexion-extension moments are typically applied using constrained or unconstrained loading approaches. A previous study has demonstrated a clear experimental trade-off between constrained and unconstrained compression force vectors applied to deviated human cadaveric spinal joints (Cripton, Bruehlmann, Orr, Oxland, & Nolte, 2000). A compression force vector that was constrained to a perpendicular orientation with the cranial endplate, similar to the concept of a follower load (Patwardhan et al., 2003; Wilke, Claes, Schmitt, & Wolf, 1994), resulted in low flexion-extension reaction moments but imposed large anterior-posterior shear reaction forces (Cripton et al., 2000). To the contrary, less constrained compression force vectors reduced the shear reaction force, but at the cost of larger flexion-extension reaction moments (Cripton et al., 2000). These data collectively demonstrated

that varying methods of static (Cripton et al., 2000) and quasi-static (Patwardhan et al., 2003; Wilke et al., 1994) compression application can result in substantive differences in the tested loading scenario or a difference being the controlled loads applied and actual loads experienced by the spinal joints. However, to date there is little consensus on the most physiological loading approach.

The allowance of natural intervertebral movement when coupling axial compression with flexion-extension rotation has been previously emphasized (i.e., unconstrained pure moment approach) (Panjabi, 1988). Given the relative anterior-posterior displacement of adjacent vertebrae during physiological flexion and extension (Frobin, Brinckmann, Leivseth, Biggemann, & Reikerås, 1996; Ochia et al., 2006), implicitly, the centre-of-rotation (i.e., balance point) must also translate in a plane perpendicular to the applied load (i.e., anterior-posterior translation for axial compression). This notion has been demonstrated *in vivo* wherein the instantaneous center-of-rotation between two adjacent vertebrae oscillated in the anterior-posterior direction about an average point that was coincident with the approximate vertebral body center by up to 6 mm in each direction (Aiyangar, Zheng, Anderst, & Zhang, 2017; Bogduk, Amevo, & Pearcy, 1995; Gertzbein et al., 1986; M. J. Pearcy & Bogduk, 1988; Tencer & Ahmed, 1981). Center-of-rotation trajectories were further distinct for each motion segment during dynamic spine motion exhibited during a lifting task, for example (Aiyangar et al., 2017). These findings suggest that spinal levels of differing lordotic curvatures and geometries may have distinct loading responses when exposed to dynamic compression loading and flexion-extension moments. A joint-specific loading response induced by a testing system that permits anterior-posterior translation to accommodate an instantaneous center-of-rotation and while exposed to dynamic compression loads has yet to be

explicitly documented. This knowledge would contribute to the development of *in vitro* spine testing procedures that attempt to simulate physiological spine loading and motion characteristics.

The primary study objective was to quantify the joint reaction forces (compression and anterior-posterior shear) and flexion-extension moments during a dynamic compression loading protocol applied to porcine functional spinal units (FSU), which were used as a controlled surrogate of the human lumbar spine. Constrained and unconstrained systems were compared. The effects of sagittal plane joint posture, compression magnitude, and spinal level were further examined. Given the affordance for small anterior-posterior translations, the unconstrained system was hypothesized to significantly reduce reaction shear forces compared to the constrained system. Secondly, based on the evidence for an instantaneous center-of-rotation position (Aiyangar et al., 2017; Bogduk et al., 1995; Gertzbein et al., 1986; M. J. Pearcy & Bogduk, 1988; Tencer & Ahmed, 1981), the unconstrained system was hypothesized to induce similar reaction moments compared to the constrained system that inherently assumes a fixed center-of-rotation.

3.1.2. Methods

Specimens and Preparation

In this study, porcine cervical spine units were used as an anatomical and mechanical surrogate for the human lumbar spine (Busscher et al., 2010; McLain et al., 2002; Yingling et al., 1999). Thirty-two fresh-frozen porcine cervical FSUs (16 C3C4, 16 C5C6) were acquired. All specimens were stored frozen (-20°C) and thawed for 12 hours prior to testing. Muscle and adipose tissue were dissected away from the osteoligamentous structure and the C3C4 and C5C6 FSUs were excised. Each spinal unit contained the two vertebrae, the intervertebral disc, and the intact spinal ligaments. The quality of the exposed intervertebral discs were assessed for degeneration using the Galante (1967) scale. Only grade 1 specimens were included, which was defined by a

white gelatinous nucleus pulposus together with an annulus fibrosus without radial fissures (Galante, 1967). The visual assessment for microdamage and degeneration based on criteria established by Galante (1967) ensured that all tested FSUs were in a similar non-degenerated state.

The exposed endplates were centered on the base of custom machined aluminum cups and secured using a penetrating wood screw that perforated the endplate center. Particular attention was given to ensure a centered joint position. Additional reinforcement of the endplate to the cup base was provided by looping separate pieces of 19-guage steel wire around the cranial and caudal spinous processes. Each wire was threaded through pre-drilled holes in the cup base and tied off. Lastly, each cup was filled with dental plaster (Dentstone, Southbend, IN).

Instrumentation

The inferior aluminum cup was bolted to a high-density nylon base that was centered over a six degree-of-freedom force and torque sensor (MC3A, AMTI, Watertown, MA). The superior aluminum cup was attached to a flexion-extension rotation carriage, which was positioned in series with the compression actuator of a materials testing system (Model 8872, Instron, Toronto, ON) and was actuated by a separate torque motor (T120-106-1K, Sensor Data Technologies, Sterling Heights, MI). A linear potentiometer (TS 150, Novotechnik, Southborough, MA) was attached to the inferior base for the measurement of horizontal or joint anterior-posterior translation in the unconstrained system. The full experimental setup is depicted in Figure 3.1.1.

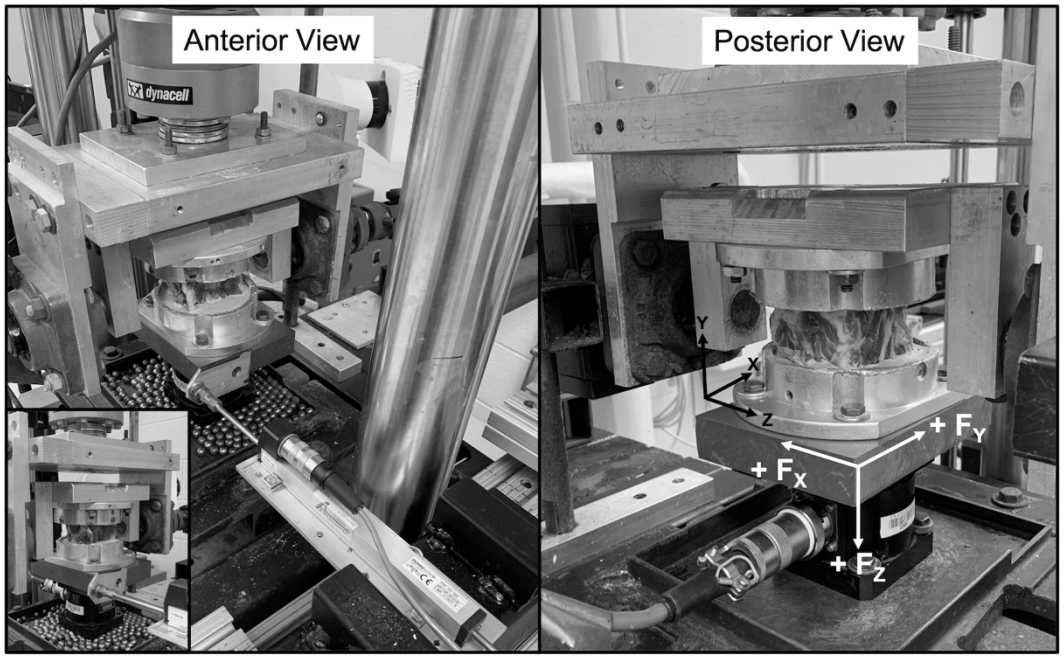

Figure 3.1.1. Anterior and posterior views of the experimental setup. The white coordinate system is that of the force and torque sensor, while the black is the joint coordinate system (X = anteroposterior axis; Y = longitudinal axis; Z = mediolateral axis). The image on the left depicts the unconstrained system and the image on the right depicts the constrained system.

Experimental Procedure

FSUs were preloaded with a static 0.3 kN compression load for 15-minutes while positioned in their natural resting posture (Callaghan & McGill, 1995). A flexion-extension range-of-motion test was then performed to identify the mechanical neutral zone based on the obtained moment-angle relationship (Panjabi, 1992). Effectively, the employed method for identifying the mechanical neutral zone is similar to how the neutral zone is defined in the human lumbar spine (Panjabi, 1992). The flexion-extension range-of-motion test was completed by flexing and extending each FSU until a nonlinear moment-angle response or a ±6 Nm was achieved for a total of five consecutive repetitions. A static 0.3 kN compression load was imposed in load control throughout the entire range-of-motion test. The moment and angular deviation from the preload posture (i.e., point of elastic equilibrium) were continuously sampled at a rate of 8 Hz using a 16-

bit analog-to-digital conversion system and custom control software (Galil Motion Control, Rocklin, CA). The obtained moment-angle time-series were used to identify the neutral zone limits, which were taken as the linear boundaries of a fourth-order polynomial curve fit of the final three repetitions (Thompson, Barker, & Pearcy, 2003). The neutral posture was identified as the average mid-point between the flexion and extension neutral zone limits (Figure 3.1.2). The neutral zone limits were labelled as 100% flexion and 100% extension. The reaction loading responses were also examined at postures of extreme physiological joint deviation, which corresponded to 300% of the neutral zone (Figure 3.1.2). These extreme physiological postures are labelled as 300% flexion and 300% extension and were calculated as three times the difference between the neutral posture and the respective 100% boundary (Gooyers & Callaghan, 2015; Gooyers et al., 2015). Collectively, the identified points of the neutral zone and physiological range-of-motion were used to mechanically normalize posture across specimens for dynamic compression testing.

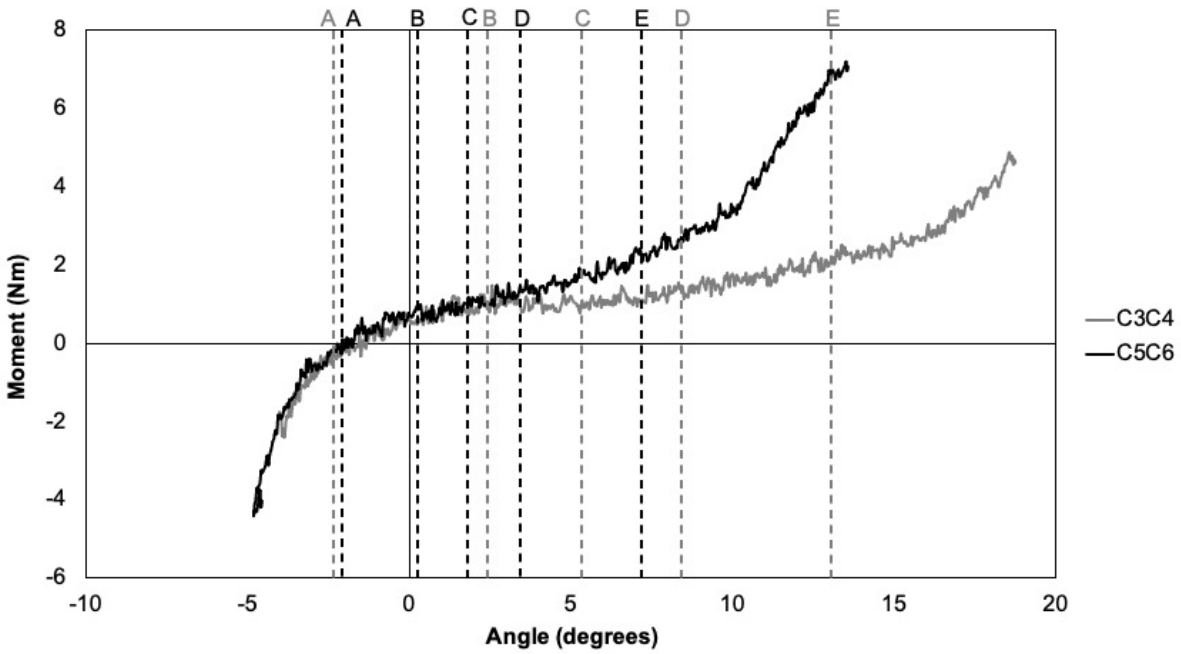

Figure 3.1.2. The moment-angle relationship obtained from C3C4 and C5C6 specimens. The labelled lines indicate: A) 300% Extension; B) 100% Extension; C) Neutral; D) 100% Flexion; E) 300% Flexion. Recall that the angular deviation presented in this figure is with respect to the natural resting joint posture and not with respect to the global vertical axis.

Each FSU was assigned to experimental groups that differed by the type of base constraint. The unconstrained system permitted anterior-posterior translation over an oiled bearing covered surface and the constrained system contained a fixed base. Group assignment was randomized while ensuring that eight C3C4 and eight C5C6 FSUs were assigned to each group. One cycle of a 1 Hz haversine compression waveform was applied in load control while FSUs were positioned in five postures (300% flexion, 100% flexion, neutral, 100% extension, 300% extension) and with two peak compression magnitudes (1 kN, 2 kN). A total of ten sub-threshold compression repetitions were performed on each specimen (5 postures × 2 loads). This loading scenario simulates the net joint compression force represented by a single force vector (Adams, 1995) and represents dynamic cyclic loading characteristics that are frequently used to study overuse injury mechanisms (Callaghan & McGill, 2001a; Tampier et al., 2007; van Heeswijk et al., 2017) and

material fatigue (Basra et al., 2015; Minns & Walsh, 1997; Techens et al., 2020). Appropriate tuning of the materials testing was conducted to ensure target loads were achieved with both constraint systems. The average applied compression forces are reported in Table 3.1.1.

Although all tested postures represent a percentage of the mechanical neutral zone, the angular deviation of each posture from a global vertical axis was also determined based on the difference from the FSU positioned with a horizontal rotation carriage (i.e., parallel endplates) and verified with a digital inclinometer. Effectively, this enabled further analysis to confirm that a similar relative (% neutral zone) and absolute (deviation from vertical) joint posture was induced in FSUs assigned to each constraint condition. The average angular deviations from a global vertical axis are presented in Table 3.1.2. The applied compression force (Instron actuator), applied moment (torque cell), reaction compression force (F_z of force sensor), reaction anterior-posterior shear (F_y of force sensor), and reaction flexion-extension moment (M_x of torque sensor) were sampled at a rate of 100 Hz.

Table 3.1.1. The average (standard deviation) applied compression force (kN) for each experimental condition. Columns labeled with the same letter indicate statistical similarity between constraint systems for a given load and spinal level ($p > 0.05$)

Posture	C3C4				C5C6			
	1 kN		2 kN		1 kN		2 kN	
	Constrained[A]	Unconstrained[A]	Constrained[B]	Unconstrained[B]	Constrained[A]	Unconstrained[A]	Constrained[B]	Unconstrained[B]
300% Flexion	-1.009 (0.014)	-1.015 (0.009)	-2.019 (0.020)	-2.017 (0.017)	-1.018 (0.019)	-1.021 (0.013)	-2.019 (0.025)	-2.028 (0.022)
100% Flexion	-1.021 (0.016)	-1.010 (0.023)	-2.014 (0.011)	-2.025 (0.018)	-1.018 (0.010)	-1.025 (0.012)	-2.027 (0.014)	-2.024 (0.022)
Neutral	-1.018 (0.014)	-1.020 (0.025)	-2.020 (0.021)	-2.026 (0.024)	-1.026 (0.023)	-1.020 (0.023)	-2.023 (0.022)	-2.023 (0.023)
100% Extension	-1.119 (0.021)	-1.013 (0.030)	-2.027 (0.019)	-2.030 (0.013)	-1.020 (0.010)	-1.014 (0.011)	-2.014 (0.015)	-2.013 (0.013)
300% Extension	-1.029 (0.022)	-1.021 (0.013)	-2.025 (0.019)	-2.022 (0.022)	-1.016 (0.012)	-1.021 (0.014)	-2.015 (0.019)	-2.022 (0.020)

Table 3.1.2. The average angular deviation (standard deviation) from a global vertical axis (degrees). Constraint groups labelled with a different letter but within a spinal level were statistically different ($p < 0.05$).

Posture	C3C4		C5C6	
	Constrained[A]	Unconstrained[A]	Constrained[B]	Unconstrained[B]
300% Flexion	8.9 (3.1)	8.8 (2.8)	-6.5 (3.9)	-5.3 (5.6)
100% Flexion	5.1 (2.9)	4.2 (2.1)	-11.5 (4.6)	-10.4 (5.7)
Neutral	3.1 (2.9)	1.9 (2.4)	-13.8 (5.1)	-12.9 (5.9)
100% Extension	-1.2 (2.9)	-0.5 (1.7)	-16.2 (5.6)	-15.5 (5.9)
300% Extension	-5.1 (2.8)	-5.1 (1.8)	-20.9 (6.9)	-20.5 (6.5)

Data Analyses

Raw force, moment, and horizontal position data were imported into a custom Matlab program (The MathWorks Inc., Natick, MA). The peak reaction shear force, peak reaction compression, peak reaction flexion-extension moment, anterior-posterior translation of the inferior cup (unconstrained only), and anterior-posterior translation of the center-of-pressure (CoP) were determined for all 10 trials. The CoP was calculated by dividing the instantaneous medio-lateral moment (M_x of the torque sensor) by the instantaneous axial force (F_z of the torque sensor) and averaged across the dynamic loading trial. Although the endplate was centered about the force and torque sensor, the exact anatomical position of the vertebral body center was not digitized with respect to the force and torque sensor. Therefore, all CoP translation was normalized with respect the defined neutral posture. For a positive angular deviation with respective to the global vertical axis, the negative shear component was extracted, and the positive shear component was extracted for a negative rotation with respect to vertical. The maximum compression and flexion-extension moment applied to each FSU from the position of elastic equilibrium were also extracted for each trial.

The average differences in reaction shear force, reaction compression force, reaction flexion-extension moment, horizontal base translation, CoP translation, and angular deviation

from the global vertical axis were assessed using separate analysis of variance (ANOVA) tests. Four statistical factors were included in each ANOVA test: spinal level (2 levels), constraint (2 levels), posture (5 levels), applied compression load (2 levels). Statistical significance was achieved as $p < 0.05$ and Tukey's *post hoc* test was used to examine pair-wise comparisons of significant main and interaction effects. Bonferroni corrections were used, where applicable. These statistical analyses were conducted using RStudio (Version 1.3.1093, RStudio Inc., Boston, MA).

3.1.3. Results

Postural Deviation

A significant constraint × spinal level interaction effect was observed for postural deviation with respect to the global vertical axis ($p = 0.039$). Within a given spinal level, the average deviation did not significantly differ ($p > 0.728$) (Table 3.1.2). The average differences between constraint conditions were 1.3 degrees and 0.5 degrees for C3C4 and C5C6, respectively. However, the average deviation from vertical was significantly different between spinal levels, regardless of the constraint condition ($p < 0.001$). These results confirm that similar relative and absolute postures were experimentally induced and that any differences in reaction shear force between constraint conditions and within a spinal level were not related to postural differences.

Reaction Anterior-Posterior Shear Force

A significant four-way interaction effect was detected for reaction shear force ($p < 0.001$). Given the distinct responses between spinal levels (Figure 3.1.3), their results are discussed separately.

In C3C4 FSUs, the reaction shear forces were significantly greater when constrained compared to unconstrained at each posture by an average of 25.5 N (1 kN of compression) and

27.8 N (2 kN of compression) ($p < 0.029$) (Figure 3.1.3a). Although the shear force significantly increased between target compression loads for constrained flexed postures ($p < 0.044$), significant differences were not observed between target compression loads for constrained neutral and extended postures ($p > 0.077$). When unconstrained, reaction shear forces proportionately increased when a 2 kN compression load was applied at all postures ($p < 0.034$). Lastly, the reaction shear force was significantly different between flexed and extended joint postures ($p < 0.043$), which was primarily driven by directional differences (Figure 3.1.3A).

In C5C6 FSUs, the reaction shear forces were significantly greater when constrained compared to unconstrained by an average of 46.9 N (1 kN) and 85.7 N (2 kN) ($p < 0.007$) (Figure 3.1.3B). Despite a systematic increase, reaction shear forces did not significantly increase when target compression loads were applied to the same posture with an unconstrained base ($p > 0.100$). To the contrary, a constrained base facilitated significantly higher reaction shear forces at all postures when compressed at 2 kN compared to 1 kN, except for at 300% flexion ($p = 0.073$). The reaction shear force was significantly less at 300% flexion compared to both extended postures ($p < 0.039$). The reaction shear force measured at 100% flexion did not statistically differ from extended postures ($p > 0.097$) (Figure 3.1.3B).

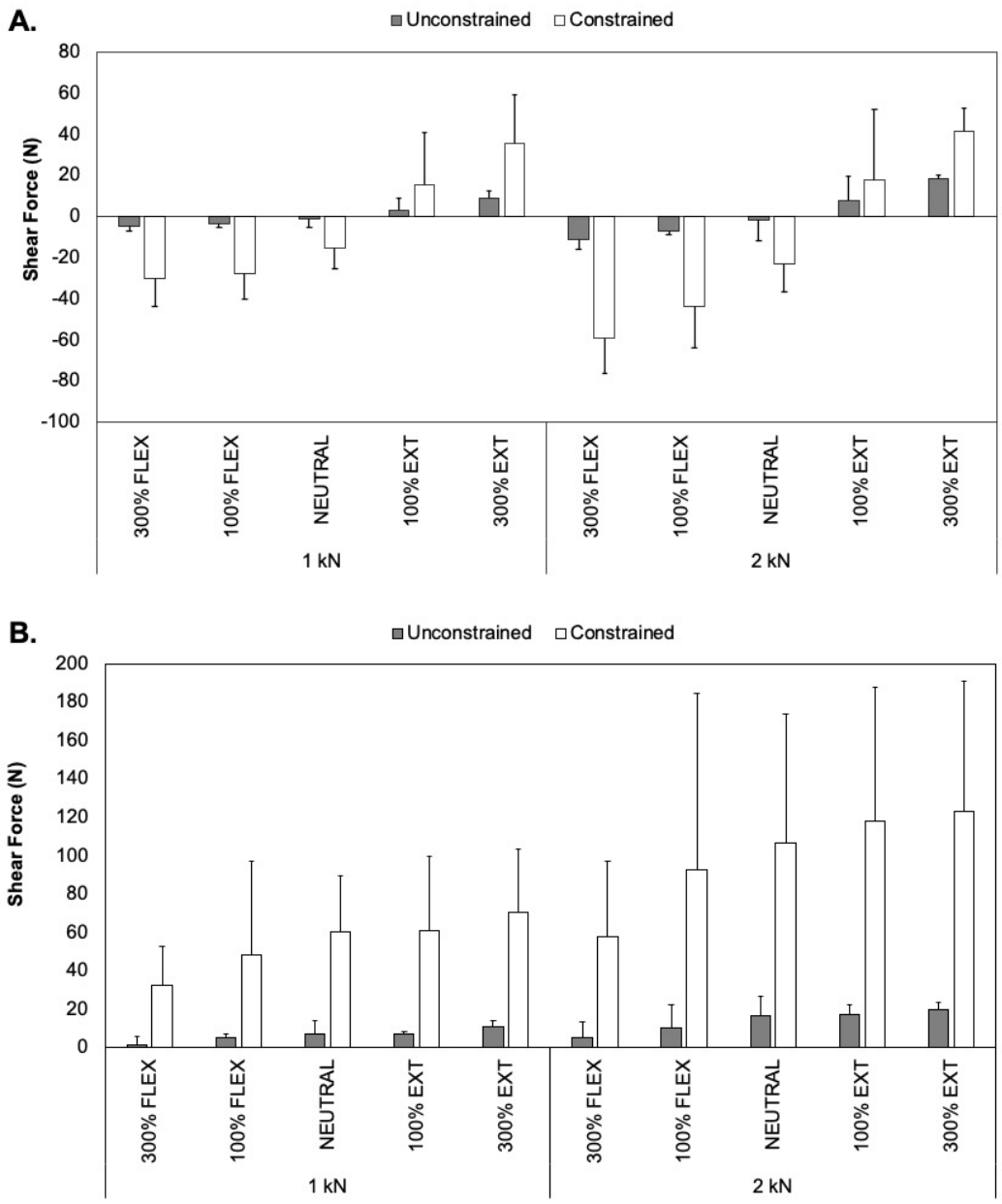

Figure 3.1.3. The resultant anterior-posterior shear force measured in C3C4 (A) and C5C6 (B) spinal units. Shear forces are presented for each posture, load, and constraint conditions. Error bars represent one standard deviation. Interaction effects are described in text.

Reaction Compression Force

There were no significant differences observed for reaction compression force between constraint systems, postures, or spinal levels ($p > 0.066$). Despite the statistical similarities between constraint systems at each posture, the constrained system facilitated a reaction compression force

that was less than the target force (Table 3.1.3). While there was a small reduction in compression in unconstrained systems, the reaction compression force became closer to the target force. That is, the overshoot associated with dynamic load control was partially reduced in unconstrained systems due to the small reaction anterior-posterior shear forces.

Reaction Flexion-Extension Moment

The reaction moment was significantly influenced by posture ($p = 0.037$) (Figure 3.1.4). While positioned in 300% extension, the reaction moment was significantly different from all other postures in constrained and unconstrained systems and in both spinal levels ($p < 0.001$). Like the postural differences in resultant shear force (C3C4), these directional differences in moments are due to the application of an extension moment *from* the natural resting joint posture (Figure 3.1.2). There were no additional significant differences observed between postures ($p > 0.098$). The differences between applied and reaction moments generated with constrained and unconstrained systems were comparable (Figure 3.1.4). For a given C3C4 posture, the average reaction moment differed from the applied moment by an average of 0.36 Nm and 0.37 Nm in constrained and unconstrained systems, respectively. In C5C6 FSUs, the reaction moments differed from the applied moments by an average 2.27 Nm when constrained and 2.78 Nm when unconstrained. These discrepancies between spinal levels are largely driven by the large reaction moment observed at 300% extension (C5C6).

Table 3.1.3. The average (standard deviation) resultant compression force (kN) for each experimental condition.

Posture	C3C4				C5C6			
	1 kN		2 kN		1 kN		2 kN	
	Constrained	Unconstrained	Constrained	Unconstrained	Constrained	Unconstrained	Constrained	Unconstrained
300% Flexion	-0.988 (0.016)	-1.009 (0.013)	-1.990 (0.026)	-2.012 (0.019)	-0.998 (0.024)	-1.004 (0.020)	-1.957 (0.019)	-2.001 (0.015)
100% Flexion	-0.922 (0.016)	-1.003 (0.021)	-1.988 (0.026)	-2.016 (0.013)	-0.988 (0.026)	-1.011 (0.015)	-1.961 (0.032)	-2.004 (0.008)
Neutral	-0.994 (0.003)	-1.010 (0.020)	-1.988 (0.022)	-2.014 (0.015)	-0.980 (0.022)	-1.010 (0.014)	-1.961 (0.029)	-2.007 (0.020)
100% Extension	-0.996 (0.019)	-1.013 (0.021)	-1.981 (0.019)	-2.015 (0.012)	-1.997 (0.027)	-1.012 (0.009)	-1.958 (0.033)	-2.000 (0.012)
300% Extension	-0.990 (0.022)	-1.016 (0.003)	-1.977 (0.027)	-2.011 (0.022)	-1.986 (0.026)	-1.013 (0.024)	-1.960 (0.024)	-2.002 (0.001)

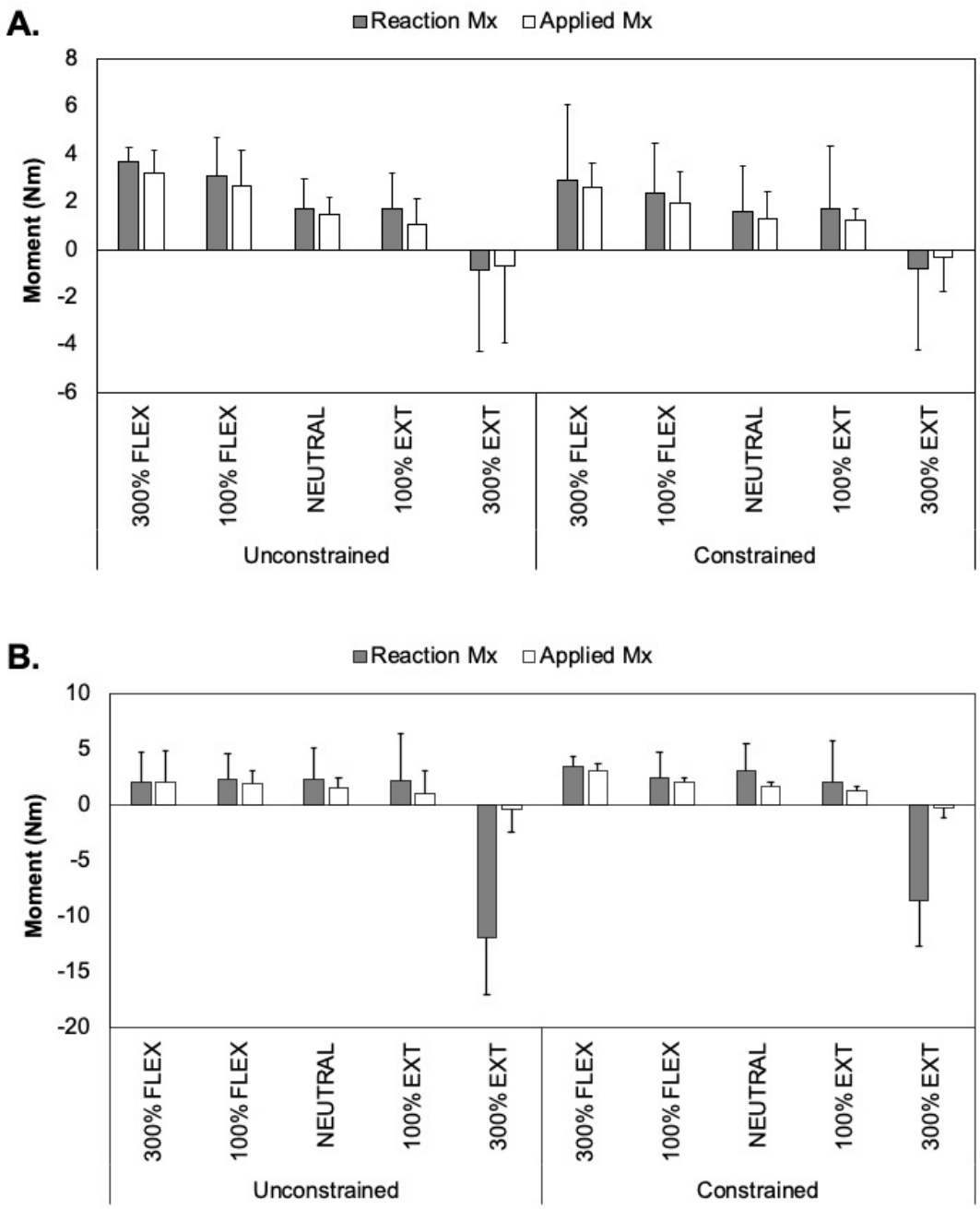

Figure 3.1.4. The resultant moment about the mediolateral joint axis in C3C4 (A) and C5C6 (B) spinal units. The moments are presented for each posture and constraint condition. Error bars represent one standard deviation. Interaction effects are described in text.

Anterior-Posterior CoP Displacement

There was a significant posture × level interaction effect detected for anterior-posterior CoP displacement (p = 0.021) (Figure 3.1.5). The 4.2 mm (constrained) and 3.9 mm

(unconstrained) posterior CoP translation at 300% extension was significantly greater than the CoP displacement observed all other postures in both C3C4 and C5C6 FSUs ($p < 0.018$). The anterior-posterior CoP displacement did not significantly differ between postures in C3C4 FSUs and postures between 300% flexion and 100% extension in C5C6 FSUs ($p > 0.776$).

Anterior-Posterior Base Translation

There were significant spinal level × constraint ($p = 0.032$) and spinal level × compression load ($p = 0.024$) interaction effects for horizontal displacement. At the C3C4 spinal level, the horizontal displacement (0.06 mm) with an unconstrained base did not significantly differ from a constrained base (i.e., zero translation) ($p = 0.706$). The horizontal displacement was, however, significantly greater in unconstrained C5C6 spinal units (0.91 mm) compared to constrained ($p < 0.01$). Although the horizontal translation did not significantly differ between target compression loads in C3C4 FSUs ($p > 0.229$), C5C6 FSUs translated significantly more (0.16 mm) when exposed to 2 kN compared to 1 kN ($p = 0.002$).

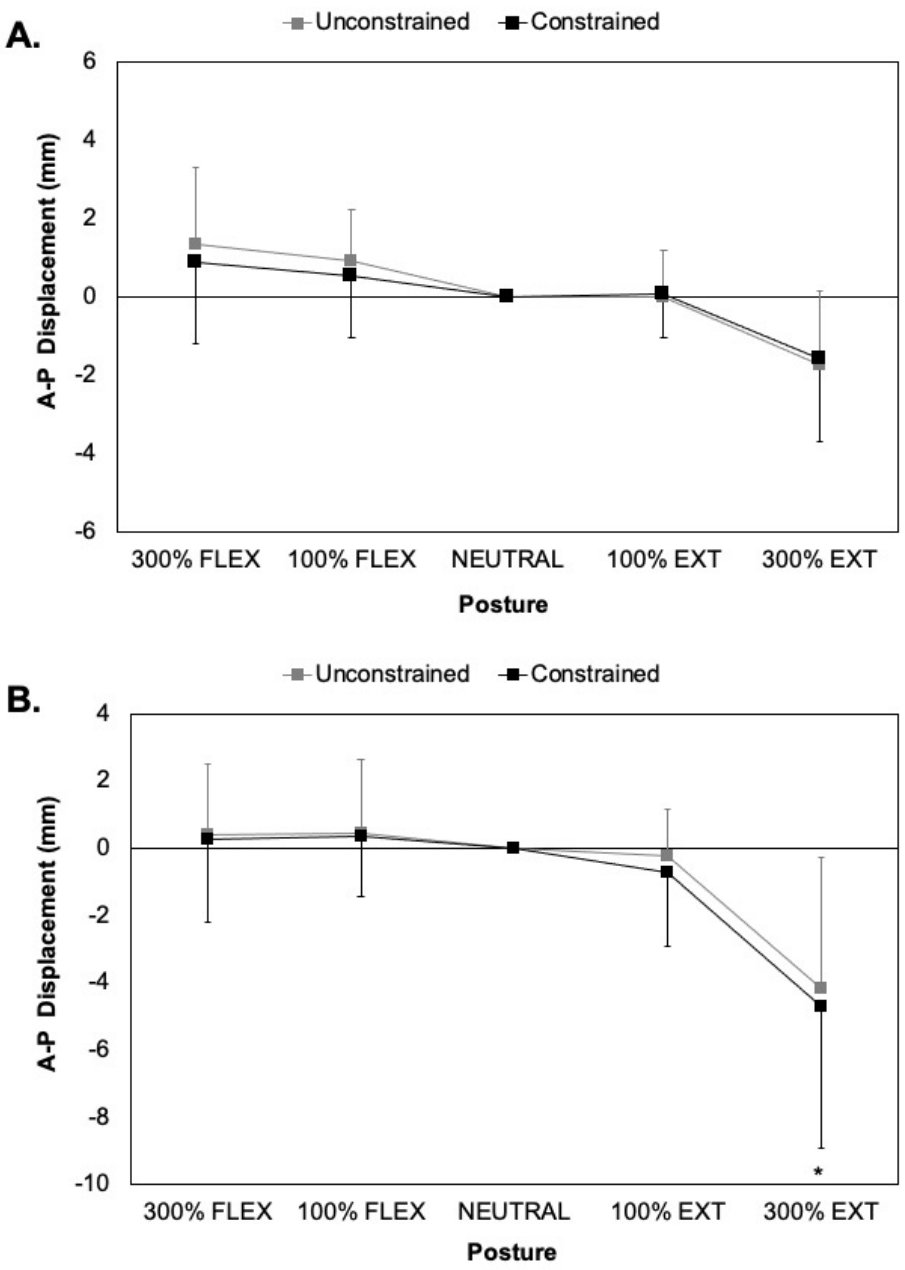

Figure 3.1.5. The average anterior-posterior (A-P) CoP translation with respect to the neutral posture in C3C4 (A) and C5C6 (B) spinal units. Error bars represent one standard deviation. The asterisk indicates a significant difference from all other postures ($p < 0.05$).

3.1.4. Discussion

This study demonstrated a difference in reaction shear forces, but similar reaction flexion-extension moments imposed on porcine FSUs loaded with constrained and unconstrained testing

systems. The reaction shear forces were significantly greater with a constrained loading system compared to unconstrained for C3C4 (25.5N – 27.8 N) and C5C6 (46.9 – 85.7 N) spinal levels (Figure 3.1.3). These findings support the first study hypothesis and are consistent with previous findings (Cripton et al., 2000). The higher shear reaction forces measured with a constrained system coincided with a reaction compression force that was less than the 1 kN and 2 kN target loads, while the target compression force was maintained with the unconstrained system (Table 3.1.3). The differences between constraint systems in compression reaction force, however, did not reach statistical significance. Furthermore, the difference between applied and reaction flexion-extension moments for a given a posture were similar between constraint systems, yielding an average difference of 0.01 Nm (C3C4) and 0.53 Nm (C5C6) between constraint types (Figure 3.1.4). The similarities in reaction flexion-extension moments between constraint systems support the second study hypothesis and the general goal of *in vitro* spine testing. Taken together, these findings demonstrate that an unconstrained testing approach can be implemented for *in vitro* testing of FSUs to offset shear reaction forces while minimizing the induction of moments of force due to eccentric force application.

With a constrained testing system, the observed differences between applied and reaction moments in C3C4 spinal units (0.36 Nm) were similar to previous studies (Cripton et al., 2000). Excluding the response observed in C5C6 FSUs at 300% extension (discussed below), the average difference between applied and reaction moments observed with a constrained testing system was 0.49 Nm, which aligns with previous reported errors observed for more neutrally positioned spinal joints (Cripton et al., 2000). These findings can be attributed to small (< 2 mm) physiological anterior-posterior CoP translations about the average balance point (Aiyangar et al., 2017; Bogduk et al., 1995; Gertzbein et al., 1986; M. J. Pearcy & Bogduk, 1988; Tencer & Ahmed, 1981). When

the inferior vertebra was unconstrained to afford anterior-posterior translation, a slightly higher, but statistically similar average reaction moment error was observed in C3C4 (0.37 Nm) and C5C6 (0.59 Nm, excluding 300% extension) spinal units. These reported errors were less than the measured flexion-extension moment error observed with an unconstrained force vector applied to a constrained testing system (Cripton et al., 2000). Furthermore, the similarity in reaction and applied moments observed between the examined testing approaches aligns with existing *in vivo* evidence for a center-of-rotation position that is dependent on joint flexion and extension (Aiyangar et al., 2017; Bogduk et al., 1995; Gertzbein et al., 1986; M. J. Pearcy & Bogduk, 1988; Tencer & Ahmed, 1981), particularly when motion and loading are dynamic (Aiyangar et al., 2017). Taken together, these findings demonstrate that constrained and unconstrained systems result in similar reaction moment errors, but these errors appear to be mechanically generated in differing ways. In a constrained system, the error appears to result from an anterior-posterior CoP translation about an assumed fixed center-of-rotation, while in an unconstrained system, the observed moment artifacts likely result from eccentric force application.

A second finding demonstrated in this study was the difference in loading response observed between spinal levels, irrespective of the testing system. Spinal units consisting of different combinations of lumbar vertebrae have been previously assessed; however, the loading responses specific to each joint level have not been fully described. The greater shear reaction forces and reaction moments observed in C5C6 FSUs, particularly in extension, may be related to the more lordotic resting position of C5C6 compared to C3C4. Lordosis is a geometric factor that has been identified to significantly influence lumbar spine loading (Putzer, Ehrlich, Rasmussen, Gebbeken, & Dendorfer, 2016), which is largely driven by the net muscle moment arm and line-of-action (McGill, Hughson, & Parks, 2000; McGill & Norman, 1986). Furthermore, the lordosis

of the C5C6 FSUs was associated with significantly greater deviation from the global vertical axis (up to -20 degrees) compared to C3C4 FSUs (Table 3.1.3). In fact, the C5C6 deviation at 300% flexion was similar to the C3C4 deviation at 300% extension and corresponded with similar reaction shear forces and moments (Figure 3.1.3 and Figure 3.1.4). In extended C5C6 FSUs, the greater shear reaction forces observed with both constraint systems are attributed to higher facet joint contact associated with joint extension (Dunlop, Adams, & Hutton, 1984), thereby reducing the magnitude of energy absorption associated with anterior-posterior joint translation prior to bony contact. High facet contact forces in C5C6 joints, particularly in 300% extension, combined with an abrupt increase in posterior CoP translation (Figure 3.1.5B) may have collectively driven the significant increase in reaction moments observed with both testing systems (Figure 3.1.4). Given the similarity in measured extension moments, however, it appears that constrained and unconstrained testing systems poorly accommodate large, yet physiological posterior center-of-pressure translations associated with highly deviated extended postures, particularly in lordotic FSUs.

Despite the differences observed in shear reaction forces, both of the examined *in vitro* testing approaches facilitated physiological loading environments. Although shear reaction forces observed in constrained testing systems significantly exceed the unconstrained system, the observed reaction forces were in no way injurious to the spinal joint (Gallagher & Marras, 2012; McGill, Norman, Yingling, Wells, & Neumann, 1998). For statistically similar applied compression forces, however, users of a constrained testing system are cautioned that the larger reaction shear forces imposed with this system may contribute to a joint compression force that is below the peak target force, as reported in Table 3.1.3. In addition to joint forces, the anterior-posterior CoP translation magnitudes observed with both testing approaches were within the 6 mm

limits documented during *in vitro* (Bogduk et al., 1995; Gertzbein et al., 1986; M. J. Pearcy & Bogduk, 1988; Tencer & Ahmed, 1981) and *in vivo* (Aiyangar et al., 2017) experiments. Furthermore, the measured horizontal translation of the inferior cup in the unconstrained system did not significantly differ from the constrained system in C3C4 joints (0.31 mm) and was biologically realistic in the lordotic C5C6 spinal units (0.91 mm). From these data, both testing approches can facilitate physiological loading scenarios for the analysis of injury mechanisms and orthopaedic interventions; however, the unconstrained system more wholefully met the stated goal of *in vitro* experimentation – the applied forces and moments are equal to the reaction forces and moments experienced by the joint

The current study included limitations that should be considered when interpreting the results. First, the applied axial compression loads were greater (Cripton et al., 2000; Wilke et al., 1994) and similar (Patwardhan et al., 2003) to previous studies; however, they were not representative of *in vivo* maximum joint contact forces documented while performing dynamic tasks such as sagittal plane lifting that could reach approximately 4.5 kN (Tyson A. C. Beach, Coke, & Callaghan, 2006; Dolan, Earley, & Adams, 1994; Gooyers et al., 2018). The *in vitro* joint loading response under higher physiological compression exposures is certainly of interest, but the peak applied compression forces were selected based on the capacity of the force sensor and remained below the accepted NIOSH compression action limit for lifting of 3.4 kN (NIOSH, 1981). Despite the reaction moments being largely unaffected by the applied compression force, the shear reaction forces may systematically increase, particularly at highly flexed and extended postures. Second, the results presented in this study are specific to isolated spinal joints and should not be used to infer the loading response of longer spine specimens consisting of more than one joint. Furthermore, given the observed differences in shear reaction force between spinal levels

and may not represent the same findings in other isolated joint combinations. Third, a porcine cervical spine model was used as a surrogate for the human lumbar spine. In addition to the scalable geometric similarities (Yingling et al., 1999), the porcine spinal joints were tested under similar mechanical parameters (i.e., normalized to the joint neutral zone) to how *in vitro* testing is conducted on human cadaveric spinal joints. As such, a similar joint loading response is expected to exist in human lumbar FSUs. Lastly, the current study examined the acute dynamic loading response on healthy spinal joints. Low back disorders or intervertebral disc degeneration can reduce the rotational stiffness of spinal joints (M. D. Brown, Holmes, & Heiner, 2002; Mimura et al., 1994) and stochastically influence the center-of-rotation trajectory (Bogduk et al., 1995; Gertzbein et al., 1985; Gertzbein et al., 1986). Future studies will attempt to understand the dynamic *in vitro* loading response in degenerated or fatigued spinal joints.

In conclusion, the unconstrained *in vitro* testing system resulted in significantly smaller shear reaction forces and similar flexion-extension moments compared to the constrained testing system. The greater shear reaction forces observed with a constrained system resulted in reaction compression forces that were less than the applied target loads (1 kN, 2 kN); however, they were not significantly different from the unconstrained system. Regardless of the testing system used, C3C4 and C5C6 spinal joints had distinct loading responses throughout the physiological range-of-motion that were largely driven by the differences in joint lordosis and anterior-posterior CoP translation.

3.1.5. Implementation of Findings

These findings collectively justify the use of an unconstrained *in vitro* testing system for the application of cyclic compression loading in Section 3.2, Section 3.3, Chapter 5, and Chapter

8. In these studies, only neutral and flexed postures were examined given their relevance to lifting-related load back injury risk (Marras et al., 1995; Marras et al., 1993).

3.2. Joint fatigue-failure: A demonstration of viscoelastic responses to rate and frequency loading parameters using the porcine cervical spine

Jackie D. Zehr, Jessa M. Buchman-Pearle, Jack P. Callaghan

Journal of Biomechanics, 113, 110081, 2020

Overview

Manipulating parameters of loading magnitude and loading frequency inherently alters the applied loading rate. Therefore, this study examined the effect of loading rate (4.2 kN/s, 8.3 kN/s) on the number of tolerated cycles at two different loading frequencies (0.5 Hz, 1 Hz). The cumulative loading dose was further normalized between experimental conditions. The results of this study identified a loading frequency where the differences between high and low loading rates had a marginal effect on the number of tolerated cycles following dose normalization. The effects of loading rate and loading frequency on energy storage and vertical displacement were further examined.

3.2.1. Introduction

Overtime, habitual compression loading can cause fatigue-failure in lumbar spine tissues (Gallagher & Heberger, 2013; Gallagher & Schall Jr., 2017). The fundamental concept of mechanical fatigue — accumulated cycle dependent damage — has traditionally been probed by analyzing the number of sustained loading cycles for an applied compression dose (Callaghan & McGill, 2001a; Gooyers et al., 2015; Parkinson & Callaghan, 2007b). Despite spinal motion segments having mechanical properties that depend on the temporal loading history (Gooyers et al., 2015; Gunning et al., 2001; Parkinson & Callaghan, 2007b; Zehr et al., 2019b), the sensitivity of the joint fatigue response to manifestations of viscoelasticity, particularly loading rate and

energy storage (i.e., hysteresis), remains largely unknown. This knowledge gap is a current barrier for the advancement of *in vitro* fatigue analyses and such information would yield a more comprehensive blueprint for how cyclic loading parameters (i.e., magnitude, frequency, rate) collectively drive fatigue-failure in lumbar spine segments.

Previous studies motivated by fatigue-failure in isolated spinal units (Gallagher, Marras, Litsky, & Burr, 2005; Gallagher et al., 2006; Parkinson & Callaghan, 2007b; Schmidt, Paskoff, Shender, & Bass, 2012; Zehr et al., 2019b) and independent musculoskeletal tissues (Fung et al., 2008; Lipps, Wojtys, & Ashton-Miller, 2013; Thornton, Schwab, & Oxland, 2007; Wren, Lindset, Beaupre, & Carter, 2003) have manipulated the applied dose per loading cycle — force–time integral — by altering the loading magnitude for a fixed loading frequency. Alternatively, the cyclic dose has been altered by manipulating the loading frequency for a given normalized force/stress magnitude (Caler & Carter, 1989; Gooyers et al., 2015; Schechtman & Bader, 2002; X. Wang, T., Ker, & Alexander, 1995; Yoganandan, Umale, Stemper, & Snyder, 2017; Zioupos, Curr, & Casinos, 2001). From this collection of studies, strong evidence to support a fatigue injury mechanism in spinal joints has emerged, with emphasis on the interaction between compression magnitude and loading frequency (Gallagher & Heberger, 2013; Gooyers et al., 2015). One persistent challenge associated with varying load magnitude and frequency is that it necessitates a change in the applied loading rate between cyclic loading conditions. It is therefore challenging to disentangle if force and repetition are indeed the primary modulators of low back fatigue-failure or if the demonstrated pattern of interaction is, at the very least, in part influenced by viscoelastic responses to altered loading rates.

Therefore, this study examined the effects of loading rate and loading frequency on the number of loading/unloading cycles tolerated by functional spinal units (FSU) with and without

cyclic compression dose-normalization (i.e., linear and nonlinear risk–exposure approximations). Based on previously conducted fatigue analyses (Caler & Carter, 1989; Gooyers et al., 2015; X. Wang, T. et al., 1995; Zioupos et al., 2001), it was hypothesized that higher loading rates and lower loading frequencies would separately accelerate fatigue-failure, evidenced by a significant reduction in the number of non-normalized tolerated compression cycles. Secondary to this hypothesis, linear and nonlinear dose-normalization were expected to reveal interacting effects of loading rate and frequency on the cyclic lifespan. To assist in explaining the observed joint fatigue responses, the second study objective was to assess the effects of loading rate and loading frequency on energy storage and vertical deformation throughout the cyclic lifespan. Consistent with the documented ultimate compression loading response in cadaveric FSUs (Hutton et al., 1979), it was hypothesized that higher loading rates would facilitate less vertical deformation and energy storage at all instances throughout the lifespan compared to lower loading rates.

3.2.2. Methods

Specimens and Preparation

Sixteen fresh-frozen porcine cervical spines were obtained from a local abattoir. All specimens remained frozen during storage (-20°C) and were gradually thawed at room-temperature. Once thawed, muscle and adipose tissue were dissected away from the osteoligamentous structure and two FSUs — two adjacent vertebrae with the intervening intervertebral disc (IVD) — were excised, totalling 32 FSUs (16 C3C4, 16 C5C6). The exposed IVDs were macroscopically assessed for degeneration using an accepted grading scale (Galante, 1967). Only Grade 1 specimens were tested. The medial-lateral width and anterior-posterior depth of the exposed endplates were measured with a digital caliper and used to calculate the ellipsoidal surface area (Callaghan & McGill, 1995). The calculated surface areas were averaged to

approximate the tested joint and to size-normalize the applied peak compression magnitudes (Parkinson, Durkin, & Callaghan, 2005).

Endplates of the superior and inferior vertebrae were mounted to separate aluminum cups using screws, wire, and dental plaster. Woodscrews penetrated the base and perforated the endplate center to an approximate depth of 5 mm. Separate pieces of 19-gauge galvanized wire were looped around the superior and inferior spinous processes and threaded through holes in the base prior to being tightened and tied off. Lastly, the base of each cup was filled with dental plaster (Dentstone, Southbend, IN).

Once potted, the superior aluminum cup was bolted to a flexion/extension carriage that was actuated by a torque motor (T120-106-1K, Sensor Data Technologies, Sterling Heights, MI). Attachment of the flexion/extension carriage in series to the compression actuator of a servohydraulic materials testing system (Model 8872, Instron Canada, Toronto, ON) permitted simultaneous control over sagittal plane joint posture and the magnitude of compression loading. The inferior aluminum cup was unconstrained and overlaid a bearing covered surface.

Cyclic Loading Procedure

The cyclic testing procedure was performed in a temperature-controlled laboratory at 21°C. A static 0.3 kN compression load was applied for 15-minutes to counter post-mortem tissue swelling (Callaghan & McGill, 1995). The mechanical neutral zone — linear region of the moment-angle curve (Panjabi, 1992) — unique to each FSU was assessed by performing five successive flexion/extension repetitions to a maximum ±6 Nm moment while simultaneously exposed to 0.3kN of compression. The specimen-specific neutral posture, which was statically maintained throughout the loading protocol, was identified as the average mid-point between the linear boundaries of the final three repetitions (Thompson et al., 2003).

Each FSU was randomly assigned to one of four experimental groups that differed by average compression loading rate (standard deviation) [4.2kN/s (0.25), 8.3kN/s (0.46)] and cyclic frequency [0.5Hz, 1Hz]. The average 4.2kN/s compression rate approximated the *in vivo* L4–L5 joint compression response during repetitive lifting (Tyson A. C. Beach et al., 2006). The loading frequencies included in this experimental paradigm were intended to simulate habitual (0.5Hz) and fast (1Hz) lifting cadences.

All time-varying waveforms were custom haversine functions (Figure 3.2.1), each containing a force ratio, $\boldsymbol{A}$, of 2, given by:

$$A = \Delta F / F_{mean} \qquad \textbf{Equation 3.2.1}$$

where $\boldsymbol{\Delta F}$ is equal to the difference between the maximum and minimum applied compression force for a single loading cycle and $\boldsymbol{F_{mean}}$ refers to the average compression force for a single loading cycle. This force ratio is conceptually similar to the stress ratio used to assess fatigue in cortical bone (Caler & Carter, 1989; Zioupos et al., 2001) given that peak compression magnitudes were scaled to the predicted endplate surface area (Parkinson et al., 2005). Force and/or stress ratios are further pervaded as a measure with more direct relation to cyclic loading history than the compression loading range alone (Caler & Carter, 1989). Effectively, this approach afforded the waveform profile to be maintained between experimental groups.

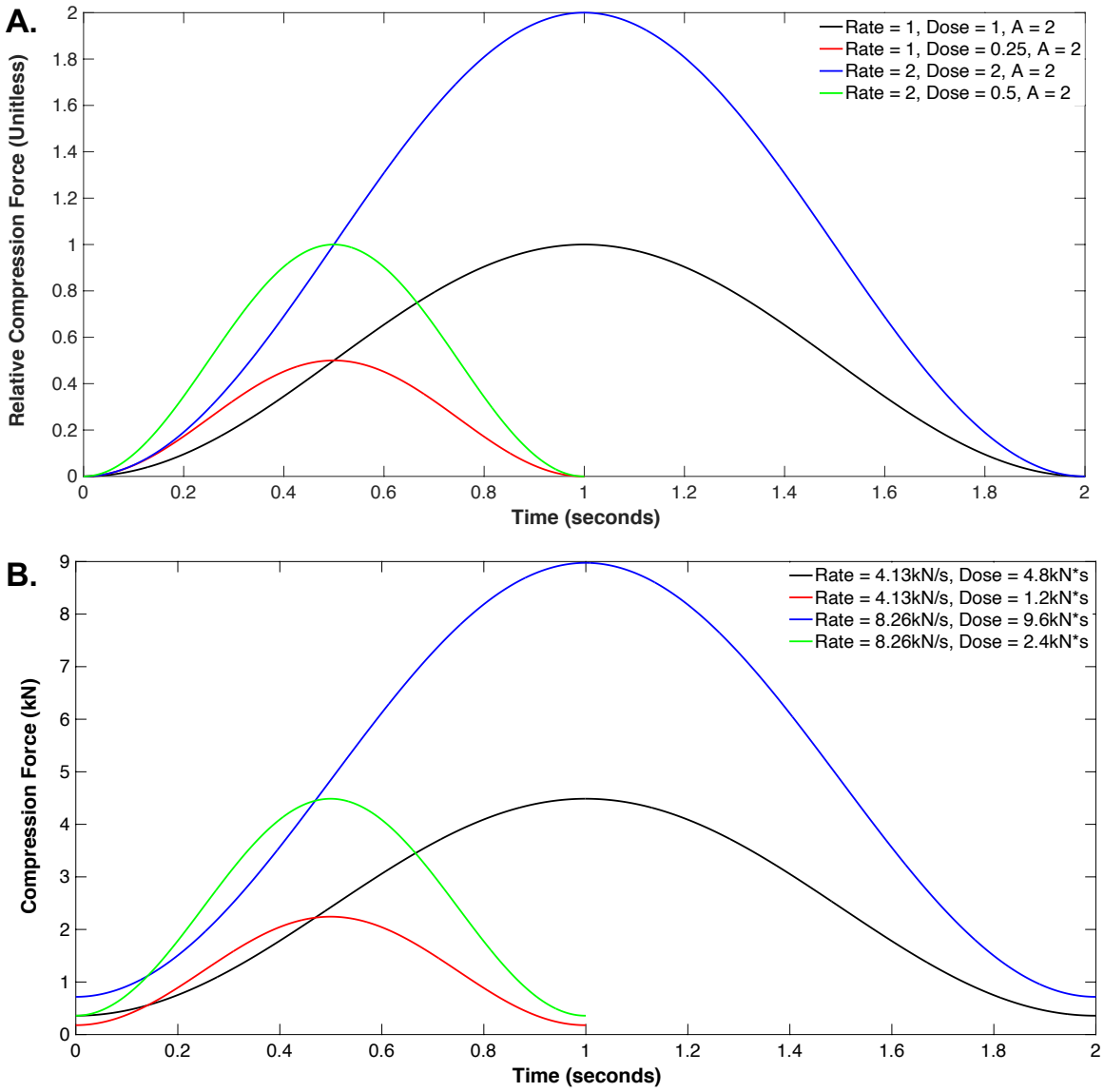

Figure 3.2.1. A) The relative compression haversine signals for each experimental condition. B) An example illustrating how the relative haversine signals were implemented for cyclic testing. The average predicted ultimate compression tolerance of 11.3 kN was derived using the average endplate area of all tested FSUs as input to a regression equation reported by Parkinson et al. (2005). The calculated UCT value was then used to scale the peak compression magnitude of each waveform. The loading rates and applied dose per cycle differ in equivalent multiples compared to the relative compression signals.

Table 3.2.1. Linear and nonlinear dose correction factors for each cyclic loading paradigm.

	Linear		**Nonlinear**	
	4.2 kN/s	8.3 kN/s	4.2 kN/s	8.3 kN/s
0.5 Hz	1.00	2.00	1.0027	5.5
1 Hz	0.25	0.50	0.25	0.5013

As evidenced in Figure 3.2.1 and Table 3.2.1, explicit control over loading frequencies and rates was only achieved by altering the maximum and minimum compression forces, which subsequently varied the applied dose per cycle between experimental conditions. Controlled differences in dose were accounted for *post hoc* by normalizing the number of tolerated cycles with dose correction factors calculated from linear and nonlinear risk–exposure relationships (Parkinson & Callaghan, 2007b), leaving one experimentally manipulated loading parameter for each experimental condition (either loading rate or frequency). This was achieved by normalizing the peak compression magnitudes to 20%, 40%, or 80% of the predicted ultimate compression tolerance (Parkinson et al., 2005) (Table 3.2.2). The minimum compression load was also normalized to 8% of the condition-specific peak compression magnitude, which enabled the loading/unloading rates between loading frequencies to be equalized (Table 3.2.2). Experimental errors quantified as the discrete difference between input and output waveforms for the maximum compression, minimum compression, and loading rates are reported in Table 3.2.3. The very small error (≈0.8%) observed confirms that differences in fatigue-failure are attributable to the differences in designed loading parameters and unlikely due to erroneous control of the testing system.

Table 3.2.2. The average (standard deviation) minimum and maximum compression loads for each experimental group.

	Minimum Compression (kN)		**Maximum Compression (kN)**	
	4.2 kN/s	8.3 kN/s	4.2 kN/s	8.3 kN/s
0.5 Hz	0.36 (0.02)	0.70 (0.03)	4.52 (0.24)	8.78 (0.43)
1 Hz	0.18 (0.02)	0.36 (0.02)	2.28 (0.18)	4.56 (0.21)

Table 3.2.3. Average error (standard deviation) between input and output signals during cyclic compression paradigms.

Condition	Min Load (N)	Max Load (N)	Loading Rate (N/s)
4.2 kN/s; 0.5 Hz	5.28 (2.87)	6.96 (2.45)	3.39 (3.64)
8.3 kN/s; 0.5 Hz	3.97 (2.81)	3.28 (3.99)	5.53 (3.38)
4.2 kN/s; 1 Hz	6.22 (2.29)	5.62 (0.18)	7.47 (5.22)
8.3 kN/s; 1 Hz	7.85 (1.18)	4.29 (2.11)	5.21 (2.57)

While operated in load control, the material testing system applied cyclic compression to the superior vertebra until fatigue-failure occurred or 10800 cycles were tolerated. Throughout each test, FSUs were wrapped in 0.9% saline-soaked plastic-backed gauze to maintain tissue hydration. The force and vertical position of the actuator were continuously sampled at 100 Hz.

Data Analyses

The employed fatigue-failure criteria were adopted from previous fatigue studies performed on porcine cervical and human lumbar spinal joints (Brinckmann et al., 1988; Gooyers & Callaghan, 2015; Parkinson & Callaghan, 2009). Cyclic loading was programmed to terminate when a cumulative height loss of 9mm (Gooyers & Callaghan, 2015; Parkinson & Callaghan, 2009) or a precipitous 0.35mm step in vertical displacement occurring within a ten cycle window (Brinckmann et al., 1988; Jackman, Hussein, Adams, Makhnejia, & Morgan, 2014) was achieved. Following the cyclic loading test, dissection was performed to assess macroscopic failure in the intervertebral disc, cartilaginous endplate, and facet joints. FSUs that tolerated 10800 continuous cycles were labeled as survivors. Endplate fractures were classified as an endplate crack, step, stellate, or crush (Gallagher et al., 2006).

Raw force and position data were processed (Matlab 2019a, The MathWorks Inc., Natrick, MA) to assess the dependent variables: number of tolerated cycles, energy storage, and vertical deformation.

First, the number of tolerated cycles between experimental groups were evaluated without dose-normalization. The following steps were performed for linear dose-normalization:

- The force-time curve of each relative compression signal was integrated to determine the linear dose correction factor (Table 3.2.1).
- The linear dose-normalized lifespan of each FSU was calculated by multiplying the number of tolerated cycles by the linear dose-correction factor corresponding to the respective experimental group.

From existing mathematical characterizations of fatigue-failure in musculoskeletal tissues, a nonlinear relationship between risk and exposure has been documented in the cartilaginous endplate (Parkinson and Callaghan, 2007). The following steps were performed for the computation of nonlinear dose correction factors.

- Using the developed relative compression signals (Figure 3.2.1A), a theoretical UCT (unitless) of 2.5 was selected to match the same normalized peak loading percentages used during experimental testing (i.e., 0.5/2.5 = 20% UCT; 1/2.5 = 40% UCT; 2/2.5 = 80% UCT).
- Weighting factors were calculated for each data point of all four relative compression signals using the fifth-order polynomial equation reported by Parkinson and Callaghan (2007).
- Each data point of the relative compression signals was then multiplied by the corresponding weighting factor, yielding a "weighted" relative compression signal that was adjusted for the potential effect of instantaneous compression magnitude on fatigue-failure in porcine spinal units (Parkinson and Callaghan, 2007).

- The weighted relative force-time curves were integrated to determine the nonlinear dose-correction factor for each experimental condition (Table 3.2.1).
- The nonlinear dose-normalized lifespan of each FSU was finally determined by multiplying the number of tolerated cycles by the nonlinear dose-correction factor corresponding to the respective experimental group.

Effectively, the determined dose correction factors indicate that experimental groups with a lower cyclic dose should theoretically exceed the cyclic lifespan of FSUs that experienced a higher cyclic compression dose if the altered loading rates and frequencies have no effect on the fatigue-failure response.

The energy storage (J) and vertical deformation (mm) were further assessed at a single cycle that corresponded to five different percentages of each FSU's lifetime: 1%, 10%, 50%, 90%, and 99%. The energy stored for a given cycle was calculated by determining the area under the compression–displacement curves via trapezoidal integration. The vertical deformation was calculated as the absolute difference in the actuator position at the instant of peak compression during cycle one and the actuator position at the instant of peak compression for a given loading cycle. This metric of deformation represents the cumulative peak height loss for a given loading cycle and should not be taken as the deformation within a single loading cycle. Further, this metric for vertical deformation represents the overall FSU height loss and does not partition deformation in the IVD from that caused by bone and/or endplate failure.

Statistics

Three separate statistical procedures were performed (Version 3.34, RStudio Inc., Boston, MA). First, randomization was evaluated using a three-way analysis of variance (ANOVA) to examine the effects of spinal level, loading frequency, and loading rate on endplate area and neutral

posture. Only FSUs with confirmed macroscopic fatigue-fracture were included in the statistical analyses of the normalized and non-normalized lifespan. Secondly, two-way ANOVAs were performed to evaluate the effect of loading rate and loading frequency on the number of tolerated cycles, for the non-normalized and both dose-normalized conditions. Lastly, a mixed three-way ANOVA was performed to evaluate the between-specimen effects of loading rate and loading frequency, and the within-specimen effect of lifespan on energy storage and vertical displacement. Statistical significance was achieved at $p < 0.05$, and where applicable, a Tukey's *post hoc* test was performed with Bonferroni corrections.

3.2.3. Results

Randomization

There were no significant effects detected for endplate area ($p \geq 0.058$) and neutral joint posture ($p \geq 0.186$). The summary statistics for each experimental group are presented in Table 3.2.4. These data confirm that specimen randomization was successful and enabled dependent measures to be collapsed across level.

Table 3.2.4. The average endplate area and neutral joint posture for each experimental group. Standard deviations are reported in parentheses. Groups marked with the same letter were statistically similar ($p > 0.05$).

Condition	**Endplate Area (mm^2)**	**Neutral Posture* (deg)**
4.2 kN/s, 0.5 Hz	803.16 (34.51) ^{A}	2.58 (5.86) ^{B}
8.3 kN/s, 0.5 Hz	761.08 (39.39) ^{A}	5.85 (1.08) ^{B}
4.2 kN/s, 1 Hz	789.16 (67.15) ^{A}	2.47 (3.37) ^{B}
8.3 kN/s, 1 Hz	763.26 (53.93) ^{A}	3.41 (2.84) ^{B}

* A neutral posture with a positive polarity represents the degrees of flexion from the resting joint posture.

Tolerated Loading Cycles

Without dose-normalization, there were significant main effects observed for loading rate ($p < 0.001$) and loading frequency ($p < 0.001$) on the number of tolerated cycles (Figure 3.2.2). When compressed at 8.3 kN/s, FSUs tolerated approximately 5977 (71%) fewer cycles compared to 4.3 kN/s. Similarly, FSUs, on average, tolerated 3541 (49%) fewer cycles when cyclic loading was performed at 0.5 Hz compared to 1 Hz. The average (standard deviation) non-normalized lifespan of each experimental group was: 4.2kN/s, 0.5Hz = 6399.6 (1647.8) cycles; 8.3kN/s, 0.5Hz = 42.5(38.6) cycles; 4.2kN/s, 1Hz = 9561.1 (1252.6) cycles; 8.3kN/s, 1Hz = 4964.1 (678.0) cycles.

Following linear normalization, a significant rate × frequency interaction was detected ($p < 0.001$) (Figure 3.2.3A). For a 1Hz loading frequency, the 92-cycle difference (4%) between loading rates was not significantly different ($p_{adj} = 0.988$). However, during a 0.5 Hz loading frequency, a significant effect of loading rate persisted ($p_{adj} < 0.001$), where FSUs compressed at 8.3 kN/s tolerated 7314 (99%) fewer cycles.

A significant rate × frequency interaction effect was also observed following nonlinear dose-normalization ($p < 0.001$). A similar trend pervaded wherein the number of tolerated cycles did not significantly differ (4%) between loading rates for a loading frequency of 1 Hz ($p_{adj} = 0.991$) (Figure 3.2.3B). Despite the mean difference between 4.2 kN/s and 8.3 kN/s being marginally reduced to 7185 cycles (97%) when cyclically loaded at 0.5 Hz, this difference remained statistically significant ($p_{adj} < 0.001$) (Figure 3.2.3B).

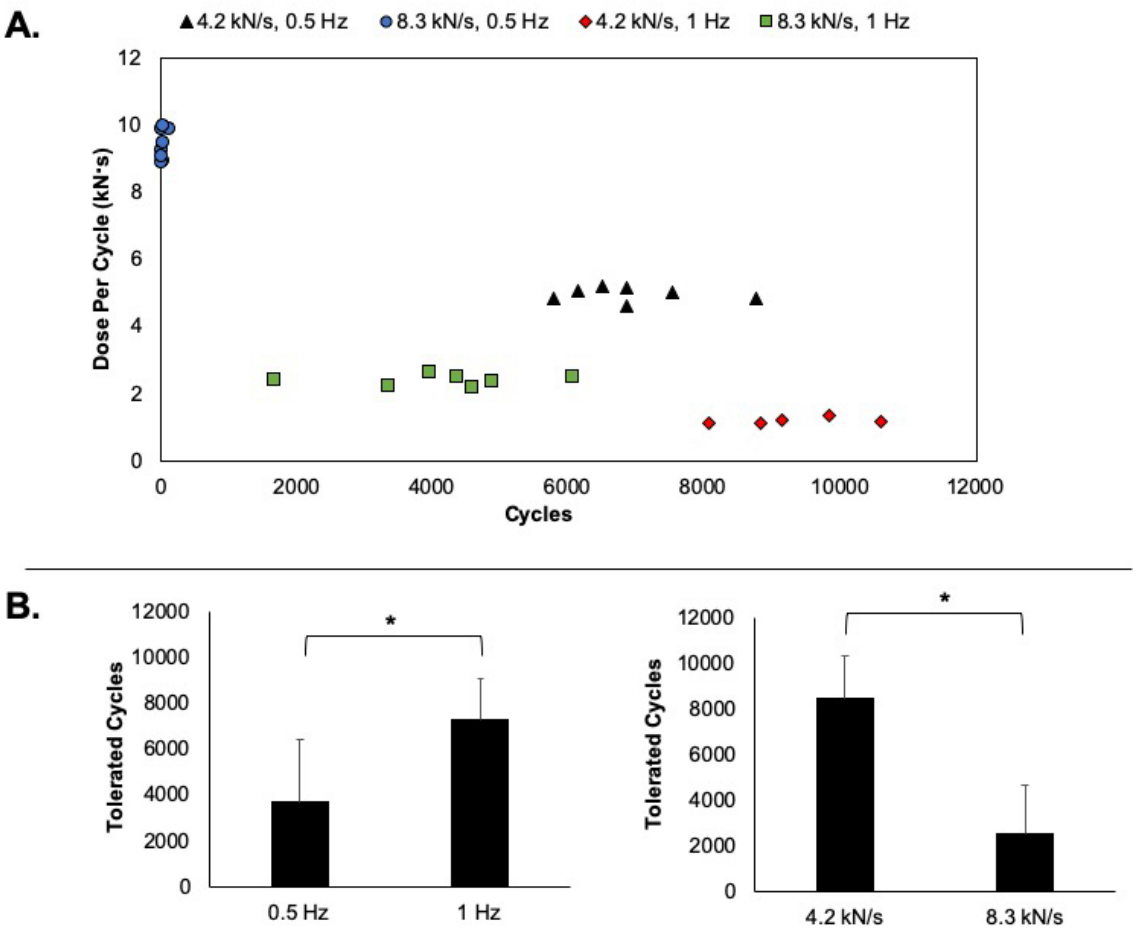

Figure 3.2.2. A scatter plot depicting the dose per cycle as a function of tolerated cycles for the 28 FSUs *with* macroscopic fracture (A). Bar graphs represent the mean cyclic lifetime for loading frequency and loading rate groups (B). Error bars represent one standard deviation and significant mean differences are indicated by an asterisk ($p < 0.05$).

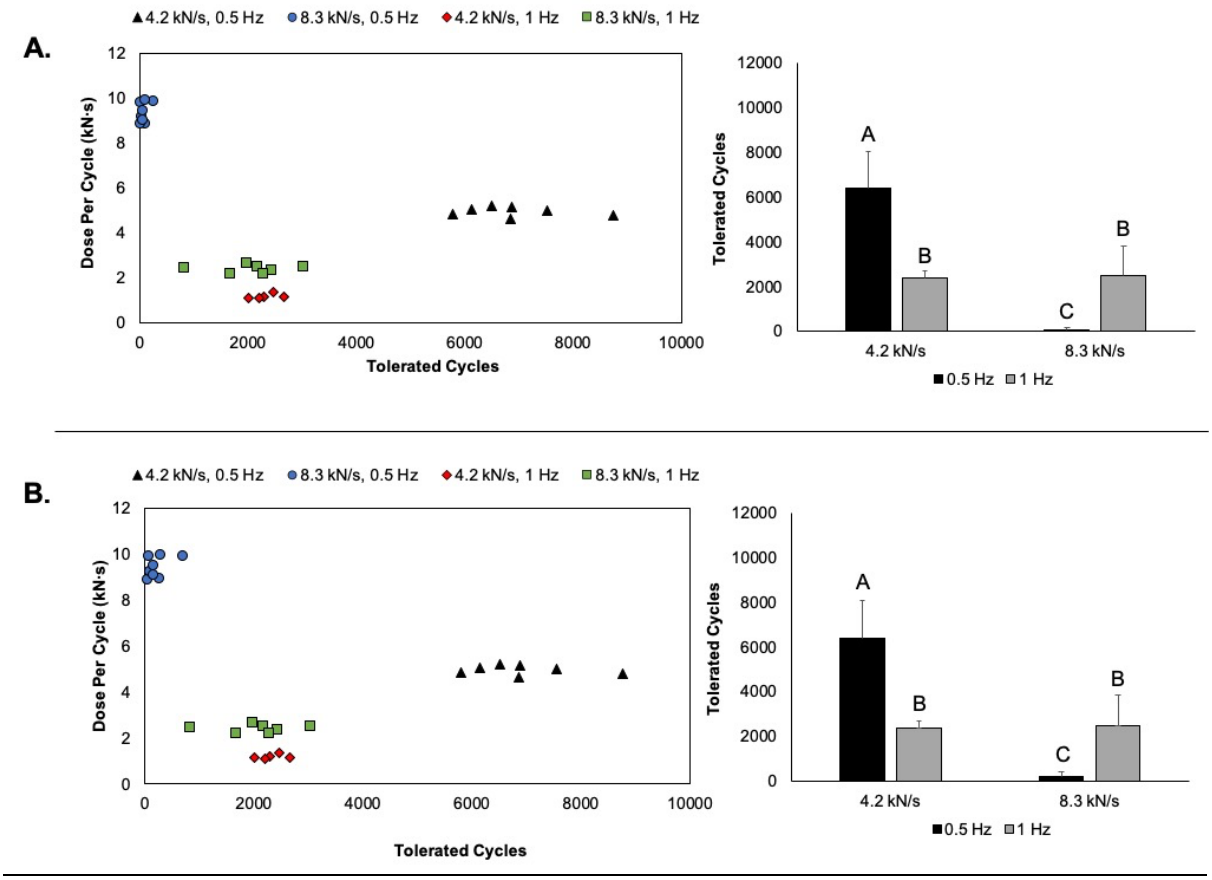

Figure 3.2.3. A scatter plot depicting the dose per cycle as a function of tolerated cycles for the 28 FSUs *with* macroscopic fracture following linear (A) and nonlinear (B) dose-normalization. The group mean for each experimental condition is depicted in the adjacent bar graph, where error bars represent one standard deviation (right). Bars marked with a different letter reached statistical significance ($p_{adj} < 0.05$).

Energy Storage & Deformation

A significant loading rate × time interaction effect was observed for energy storage (p = 0.005). Energy storage was, on average, 2.3 J (81%) greater when FSUs were compressed at 4.3 kN/s compared to 8.3kN/s. One exception to this trend was at 90% lifespan point, where the 1.2 J difference between loading rates did not achieve significance (p_{adj} = 0.056) (Figure 3.2.4).

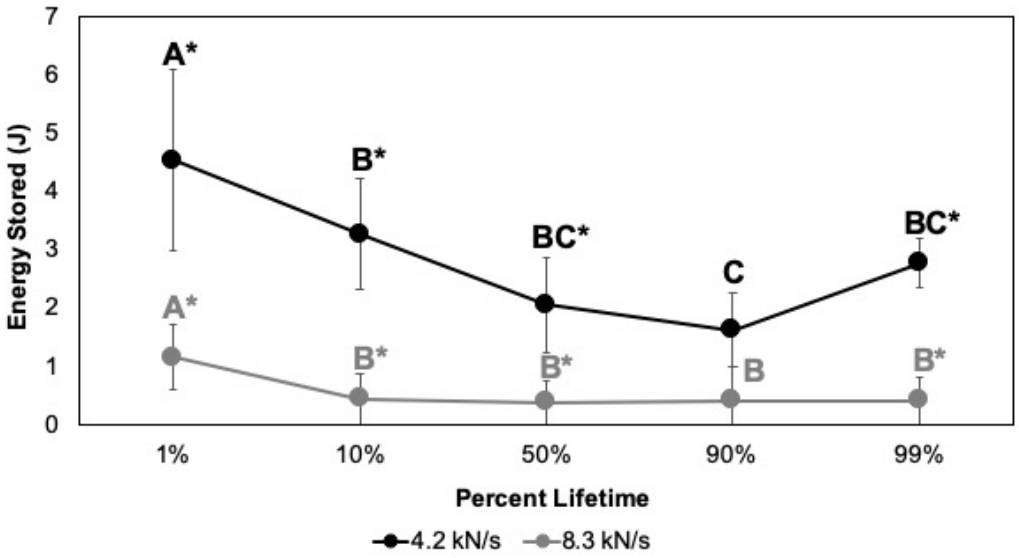

Figure 3.2.4. The magnitude of energy storage as a percentage of the specimen lifespan. Time points marked with a different letter reached statistical significance within a given loading rate ($p_{adj} < 0.05$). Time points marked with an asterisk reached statistical significance between loading rates ($p_{adj} < 0.05$).

Similarly, a significant loading rate × time interaction effect was observed for vertical deformation ($p < 0.001$). With exception to the 0.7mm (43%) difference at 1% of the lifespan ($p_{adj} = 0.108$), compression applied at 4.2 kN/s facilitated greater vertical deformation compared to 8.3 kN/s [10%: 1.5 mm (49%), 50%: 1.9 mm (45%), 90%: 1.9 mm (45%), 99%: 3.3 mm (76%)] ($p_{adj} \leq 0.0391$) (Figure 3.2.5).

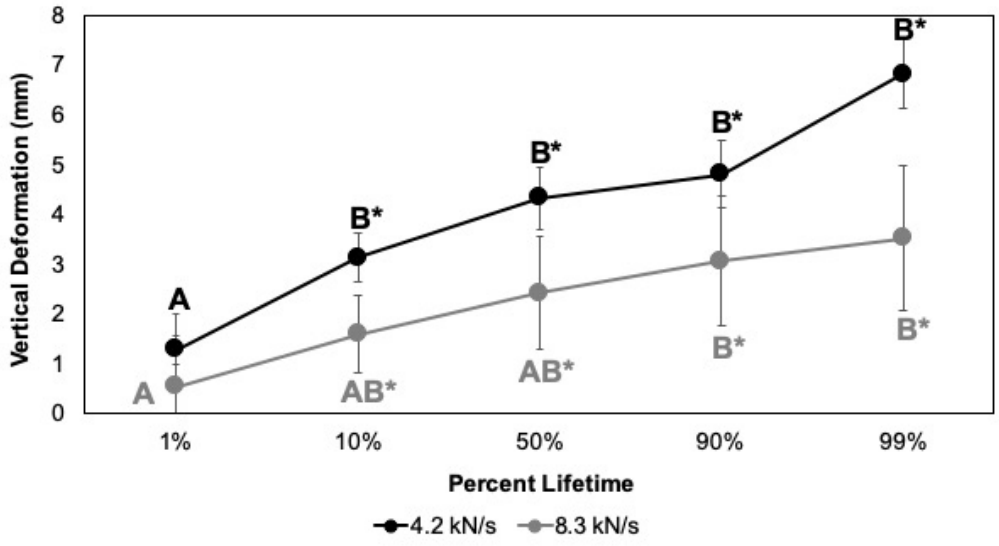

Figure 3.2.5. The magnitude of peak vertical deformation as a percentage of the specimen lifespan. Time points marked with a different letter reached statistical significance within a given loading rate (p_{adj}<0.05). Time points marked with an asterisk reached statistical significance between loading rates (p_{adj}<0.05).

Injury Incidence

Endplate fracture was observed in 27 of the 32 FSUs (84%) and no macroscopic damage was observed in the intervertebral disc or facet joints. Five FSUs tolerated 10800 continuous cycles without enduring macroscopic injury (i.e., survivors). The incidence of each fracture morphology and the endplate location are reported in Table 3.2.5 and Table 3.2.6, respectively. The regions with the highest incidence of fracture were the central region (12) and central/posterior regions (12). Damage to the central-posterior region was classified as a horizontal fracture along the approximate border of the posterior and central regions, or a crack that appeared to originate from the central region (i.e., stellate fracture), evidenced by greater damage to the central region.

Table 3.2.5. The incidence of each fracture type for each experimental condition

Condition	Fracture Morphology				
	Crack	**Step**	**Stellate**	**Crush**	**Survivor**
4.2 kN/s, 0.5 Hz	7	0	0	0	1
8.3 kN/s, 0.5 Hz	5	0	2	1	0
4.2 kN/s, 1 Hz	5	0	0	0	3
8.3 kN/s, 1 Hz	6	1	0	0	1

Table 3.2.6. The incidence of each fracture location within the endplate for each experimental condition.

Condition	Region of Macroscopic Endplate Damage				
	Cen	**Lat**	**Ant**	**Post**	**Cen/Post**
4.2 kN/s, 0.5 Hz	2	1	0	0	4
8.3 kN/s, 0.5 Hz	4	1	0	0	3
4.2 kN/s, 1 Hz	3	0	0	0	2
8.3 kN/s, 1 Hz	3	0	1	0	3

Cen = Central Region; Lat = Lateral Region (either right or left); Ant = Anterior Region; Post = Posterior Region; Cen/Post = Central and Posterior Regions

3.2.4. Discussion

The current study demonstrated that the effects of loading frequency and loading rate on endplate fatigue-failure depend on the consideration of differences in applied loading dose. Without accounting for dose discrepancies caused by altered loading parameters, a simplified fatigue response was revealed, such that lower loading frequencies (0.5 Hz) and higher loading rates (8.3kN/s) reduced the number of sustained loading cycles (Figure 3.2.2B). Although these data support the first study hypothesis and prior *in vitro* findings (Caler & Carter, 1989; Gooyers et al., 2015; X. Wang, T. et al., 1995; Zioupos et al., 2001), as hypothesized, the effect of loading rate became dependent on loading frequency following linear and nonlinear dose-normalization. Loading rate was further shown to influence the fatigue behavior – energy storage and vertical deformation – of FSUs at most instances throughout the lifespan. In partial alignment with the second study hypothesis, a 4.2 kN/s compression rate facilitated significantly greater energy storage and vertical deformation compared to 8.3 kN/s, except at 90% and 1% of FSU lifespan,

respectively. These data collectively demonstrate that the interpretation of viscoelastic responses to cyclic loading in spinal joints depend on dose-normalization. As such, future *in vitro* studies should account for dose discrepancies prior to evaluating the modulating effects of loading parameters on the mechanical fatigue response.

The interaction between loading frequency and loading rate on the dose-normalized fatigue responses reported herein may reflect the diversity of tissue types that structurally comprise spinal units (i.e., bone, cartilage, intervertebral disc, soft connective tissue). When compressed at 8.3kN/s, the dose-normalized fatigue response observed in the current study resembles patterns of uniaxial fatigue in cadaveric cortical bone (Caler & Carter, 1989; Zioupos et al., 2001); FSUs cyclically loaded at 0.5Hz sustained proportionately fewer cycles (97-99%) to failure compared to 1Hz. Using a strain-normalization approach, cortical bone cyclically loaded at 0.02 Hz and 0.5 Hz sustained proportionally fewer cycles compared to cyclic loading performed at 2 Hz and 5 Hz, respectively (Caler & Carter, 1989; Zioupos et al., 2001). In consideration of the differing normalization approaches (strain- vs dose-) together with the interaction effect observed in porcine FSUs, it is, however, possible that the accelerated fatigue-failure reported at 0.02 and 0.5Hz was due to bone specimens experiencing a greater dose per cycle, similar to our findings prior to dose-normalization (Figure 3.2.2). While the cited authors reported that frequency dependent bone fatigue persists independent of loading rate (Zioupos et al., 2001), the sensitivity of fatigue-failure in bone to dose correction remains unexplored.

In contrast, when FSUs were compressed at 4.2kN/s, the observed dose-normalized fatigue response was similar to recent mechanisms of fatigue damage observed in articular cartilage (Kaplan, Neu, Drissi, Emery, & Pierce, 2017) and modeled in tendon (Firminger et al., 2020); FSUs cyclically loaded at 1Hz tolerated 63% fewer compression cycles compared to 0.5Hz. Cyclic

indentation (28.3MPa) of articular cartilage performed at 2.88Hz lead to greater softening and more histologically verified damage (i.e., lesions and disorganization of the collagen network) compared to 1.44Hz (Kaplan et al., 2017). Moreover, a recent probabilistic cumulative damage model of the Achilles tendon during running demonstrated that, despite reduced cumulative dose at high loading frequencies (i.e., faster cadence), cycle dependent damage and probability of failure increased (Firminger et al., 2020). Taken together, there is evidence to suggest that the 63% reduction in lifespan at 4.2 kN/s for a loading frequency of 1Hz was conceivably related to greater endplate damage accumulation per cycle; however, microstructural damage in the cartilaginous endplate and supporting trabecular bone were not assessed in the current study.

While the number of sustained cycles were shown to depend on both loading rate and frequency following dose-normalization, the mechanism of endplate failure was most sensitive to loading rate (i.e., significant interaction between loading rate and time). For an 8.3kN/s loading rate, the energy storage was unaltered beyond 10% (Figure 3.2.4), wherein the FSUs possessed failure characteristics similar to brittle materials. This brittle endplate failure mechanism at high physiological loading rates was further supported by a linear increase in peak vertical deformation throughout the lifespan and a higher incidence of intrusion and more catastrophic endplate fractures. Similar to cortical bone (Choi & Goldstein, 1992; Fleck & Eifer, 2003; George & Vashishth, 2006), the linear increase in peak vertical deformation further suggests an endplate fatigue response that is dominated by the poroelastic response of fluids encapsulated within the spinal joint (i.e., nucleus pulposus).

Alternatively, compressive loading at 4.2 kN/s, demonstrated a systematic reduction in cycle energy storage (1–90%) followed by an abrupt 1 J increase (90–99%), which is characteristic of ductile material failure (Figure 3.2.4). This energy storage pattern was also supported by the

three-phase vertical deformation response observed in the current study and in the surface layer of articular cartilage (Kaplan et al., 2017; Sadeghi, Espino, & Shepherd, 2015): linear increase (0–50%), plateau (50–90%), and increase approaching failure (90–99%) (Figure 3.2.5). These findings, coupled with greater energy storage observed at most instances, would imply that endplate fatigue-failure was dominated by the elastic tissue elements at slower physiological loading rates.

The overarching evidence of an endplate fatigue response that is influenced by the inherent viscoelastic behavior of spinal tissues prompts the question of: how should future *in vitro* analyses attempt to control for and/or acknowledge the complex viscoelastic behaviour of isolated spinal joints? Two evidence-based recommendations have emerged from the study findings. First, given the 92-cycle difference at 1 Hz following dose-normalization, cyclic loading to different peak compression magnitudes can be performed without the associated changes in loading rate having a significant effect on fatigue-failure. Second, the effects of loading rate on endplate fatigue can be avoided by equalizing the loading rate when cyclic loading is performed at slower loading frequencies (i.e., 0.5 Hz). This approach, however, requires the loading frequency to change as a function of peak compression magnitude if the experimental design includes different magnitude conditions.

Four methodological limitations are acknowledged. First, a porcine cervical spine model was employed as an anatomical surrogate for the human lumbar spine (McLain et al., 2002; Yingling et al., 1999). Although precise transference of findings from a porcine model to human injury pathways remains largely unknown, our study design was strengthened by the use of healthy spinal joints obtained from mature adolescent pigs with a limited and similar prior loading history. Given the documented similarities in how porcine cervical and human lumbar spinal units fail

when exposed to compression loading (Yingling et al., 1999) combined with the appropriate scaling of compression loads, the current study findings are expected to elicit a comparable fatigue response in the human lumbar spine. Second, continuous cyclic compression loading was performed while spinal joints were statically positioned in neutral. Joint posture has the capacity to alter load distribution amongst spinal tissues (Adams & Hutton, 1980; McMillan, McNally, et al., 1996), and thus the location of fatigue-failure (Callaghan & McGill, 2001a). Greater joint flexion has been shown to increase intradiscal pressure, thereby increasing radial tension experienced by the annulus fibrosis (Adams & Hutton, 1980; McMillan, McNally, et al., 1996). Given the absence of dynamic joint flexion-extension (Callaghan & McGill, 2001a) and the application of moderate-to-high compression loads (Gooyers & Callaghan, 2015; Parkinson & Callaghan, 2007b, 2009), macroscopic IVD injury was not expected in the current study and microstructural damage in the annulus fibrosis was not histologically examined. Therefore, the implications of viscoelastic behavior on fatigue-failure observed in the current study may not reflect the manifestations of viscoelasticity in flexed FSUs, especially given the greater pressurization of fluid components. Third, the cyclic testing procedure was performed at room temperature. Although the effect of ambient temperature on the fatigue lifespan of spinal units has not been explicitly tested, a temperature dependency has been reported in cortical bone (Carter & Hayes, 1976); a type of tissue found in FSUs. Based on the findings of Carter and Hayes (1976), the number of tolerated cycles reported herein may be greater than if cyclic testing was performed at body temperature. Lastly, the number of tolerated cycles were determined based on very specific deformation criterion. Although the employed criteria were based on prior fatigue-failure studies performed on spinal joints (Brinckmann et al., 1988; Parkinson & Callaghan, 2009), the use of alternative displacement criteria and/or force criteria has potential to alter the reported number of

tolerated cycles. Therefore, the selected failure criteria are a conceivable source of inter-study lifespan differences.

In conclusion, our findings demonstrate the sensitivity of endplate fatigue-failure to viscoelastic tissue behaviour. The varying effects of loading frequency as a function of loading rate was reflective of isolated biological tissues that comprise spinal joints, specifically the mechanical behavior of articular cartilage and cortical bone. This interaction between loading rate and frequency was only revealed following the normalization of controlled dose discrepancies, thereby highlighting the importance of dose normalization for exposing modulators of the fatigue response and circumventing the potential for confounded relationships to emerge. The presented findings have further implications for assessing mechanical injuries related to loading rate and frequency and promote progression towards experimental consistency, which will conceive the ability to compare results from *in vitro* fatigue testing performed on FSUs.

3.2.5. Implementation of Findings

Data from this study informed three experimental decisions made in this thesis. First, the loading frequency was fixed to 1 Hz for cyclic compression testing performed in Study 2 (Chapter 5) and Study 4 (Chapter 8). This decision was based on the marginal 92-cycle dose-normalized difference between compression rates when loaded at 1 Hz. Second, microindentation was performed on central, posterior, anterior, and lateral regions (Chapter 5); however, given the prevalence of macroscopic injury to the central region (Table 3.2.6), immunofluorescence staining intended to identify the initiation of constitutive and structural damage was focused on the central endplate region (Chapter 6). This decision to focus staining analyses on the central region is further supported by research demonstrating that the central region was the thinnest and weakest element of the endplate and vertebra-disc unit (Ferguson & Steffen, 2003) thereby rendering it vulnerable

to injury. Third, the non-normalized joint lifespan of the 1 Hz, 8.3 kN/s group (4964.1 cycles) was used to predict the approximate lifespan for a normalized 30% compression force, which was applied in Chapter 5. The lifespan of this experimental group (i.e., 1 Hz, 8.3 kN/s) was specifically selected given the need for a 1 Hz loading frequency together with the normalized 30% compression force that was used in Chapter 5, thereby approximating an 8 kN/s loading rate. The average 4964.1 cycle lifespan observed at a 40% normalized compression force (i.e., used in the current study) was multiplied by a weighting factor of 1.07, which was calculated from an existing fifth order force weighting function (Parkinson & Callaghan, 2007b). This resulted in a predicted lifespan of 5311 continuous cycles for a 30% normalized compression force when applied at frequency of 1 Hz. This predicted lifespan of 5311 cycles informed the usage of the maximum 5000 cycle loading duration (i.e., 94% of the predicted lifespan) used in Chapter 5, which enabled overuse injury pathways to be examined near the joint lifespan but prior to a macroscopic injury event.

3.3. Mechanically induced histochemical and structural damage in the annulus fibrosus and cartilaginous endplate: A multi-colour immunofluorescence analysis

Jackie D. Zehr, Fasih A. Rahman, Jack P. Callaghan, Joe Quadrilatero

Cell and Tissue Research, 390(1), 1426-1438, 2022

Overview

This study described a novel multi-colour immunofluorescence staining procedure that quantifies mechanically induced changes to the fluorescence area and fluorescence intensity of native type I (subchondral bone) and type II (hyaline cartilage) collagen proteins as well as the area of pores and structural void development. In this proof of concept study, spinal units were loaded with the most extreme cyclic compression protocol employed in Chapter 5 (i.e., flexed posture, 40% variation in peak compression force, 5000 cycles) and the changes in native collagen content were quantified in the endplate and annulus fibrosis tissues. Hematoxylin & Eosin staining was also performed on all samples as a visual comparison.

3.3.1. Introduction

Lumbar spine tissues, including the hyaline cartilage endplate (CEP) and the fibrocartilage annulus fibrosis (AF), are commonly injured due to cumulative mechanical loading associated with work, recreation, and activities of daily living (Frost et al., 2015; Norman et al., 1998; Waterman et al., 2012). Significant work has been conducted on how mechanical factors – joint posture, joint contact forces, repetition – mediate the incidence of common low back injuries like CEP fracture (Gallagher et al., 2006; Parkinson & Callaghan, 2007b, 2009; Zehr, Buchman-Pearle, et al., 2020; Zehr et al., 2019b) and intervertebral disc herniations (Callaghan & McGill, 2001a; Gooyers & Callaghan, 2015). However, not all tissue injury is macroscopic, at least initially, and

knowledge of how and where mechanical damage accumulates in these spine tissues is not captured by mechanical and material testing alone. Thus, examination of microdamage in response to controlled mechanical exposures can provide important insights into structure-function relationships of lumbar spine tissues and injury initiation mechanisms.

Several techniques have been used to quantify damage in the lumbar spine tissues, including: 1) trichrome Mallory-Heidenhain (Berg-Johansen, Fields, et al., 2018) and hematoxylin and eosin (B. Huang et al., 2021) staining to evaluate gross morphological differences between pathological and healthy cadaveric tissue; 2) hematoxylin and eosin staining (Gooyers et al., 2015) and microcomputed tomography (Rodriguez et al., 2011) for quantifying the area occupied by structural voids and fissures; 3) Mallory's trichrome staining for the analysis of extracellular matrix organization in pathological and healthy tissue (B. Huang et al., 2021); 4) biochemical analyses for determining the dry weight of extracellular matrix molecules in cadaveric tissue (Fields, Rodriguez, et al., 2013; Lakstins, Arnold, Gunsch, Flanigan, et al., 2020; Lakstins, Arnold, Gunsch, Khan, et al., 2020); and, 5) extraction and assays of collagen in combination with immunohistochemistry for quantifying the amount of denatured collagen and localization of independent collagen types in AF tissue (Antoniou et al., 1996; Hollander et al., 1996).

Despite the utility of these existing techniques, there are limitations for assessing lumbar spine damage when used in isolation. That is, medical imaging approaches do not yield direct insight into the biochemical constituents that experience mechanical damage and biochemical approaches fail to dissociate between native and healthy forms extracellular matrix proteins, specifically collagen (Fields, Rodriguez, et al., 2013; Lakstins, Arnold, Gunsch, Flanigan, et al., 2020; Lakstins, Arnold, Gunsch, Khan, et al., 2020). Collagen extraction and assays can effectively quantify the amount of already damaged/denatured collagen in cadaveric tissue but a separate

immunohistochemistry approach is required to identify the location of such damage and collagen types are typically evaluated independently (i.e., without co-staining) (Antoniou et al., 1996; Hollander et al., 1996). Lastly, despite the capability of Mallory's trichrome to identify collagen, it does not dissociate specific types of collagen, which can provide important insight into the overall function of lumbar spine tissue in response to prolonged loading exposures. Furthermore, these techniques are almost exclusively conducted on human cadaveric tissue with a highly variable loading history and/or disease state and in the absence of controlled biomechanically relevant loading paradigms.

The purpose of this investigation was to describe a novel multi-colour immunofluorescence staining protocol that could address the aforementioned limitations. The intended purpose of this protocol was for examining mechanically induced microdamage in collagenous spine tissues, specifically the CEP and AF. Specifically, this study quantitatively assessed the change in native type I and type II collagen content and the colocalization of these constituents in control (i.e., exposed to no prior loading) and cyclically loaded (i.e., exposed to biofidelic repetitive joint compression loading) CEP and AF tissues. Structural metrics of damage included the normalized area of pores and/or void development and tortuosity of the CEP-subchondral bone interface and CEP surface.

3.3.2. Methods

Specimens

In this study, the porcine cervical spine was used as an anatomical, functional, and mechanical surrogate for the human lumbar spine. In addition to scaled morphological similarities (McLain et al., 2002; Yingling et al., 1999), the porcine animal model affords greater control over potentially confounding effects of age (Genaidy et al., 1993; Hansson et al., 1987) and prior

loading history (Gunning et al., 2001) on the ultimate strength of spinal joints, which is conceivably related to the amount of microdamage accumulation in the tissue.

Six fresh-frozen porcine cervical spine specimens were included in this study. All porcine specimens were acquired from a local abattoir and from mature adolescent market hogs. Mature adolescence of domestic pigs is defined as (i.e., 5-12 months and/or approximately 110 to 115 kg) (Reiland, 1978). All specimens were stored at -20ºC and gradually thawed at room-temperature. Once thawed, the C3C4 functional spinal units (FSU) – the adjacent vertebra and the intervening intervertebral disc – were excised and the surrounding musculature and adipose tissues were debrided. The exposed intervertebral discs were visually assessed for degeneration using the grading scale developed by (Galante, 1967). Only grade 1 specimens were included in this study (i.e., no signs of degeneration), indicating that all spinal joints were in a similar and healthy state prior to randomization. Measurements of the medial-lateral width and anterior-posterior depth of both exposed endplates were taken using a digital caliper for the derivation of average ellipsoidal surface area, which was then used to normalize the applied compression loading magnitudes (Parkinson et al., 2005).

Mechanical Loading Exposure

All mechanical testing procedures were performed in a temperature-controlled laboratory with an ambient temperature of 21°C. The exposed endplates were mounted to separate custom machined aluminum cups using a combination of screws, 19-gauge galvanized steel wire, and dental plaster (Dentstone, Sounthbend, IN). The aluminum cup secured to the superior vertebra was bolted to a flexion-extension rotation carriage that was actuated by a torque motor (T120-106-1K, Sensor Data Technologies, Sterling Heights, MI) to produce controlled joint rotation in the sagittal plane (i.e., flexion and extension). In series to the rotation carriage was the compression

actuator of a servohydraulic materials testing system (Model 8872, Instron Canada, Toronto, ON). Collectively, this experimental set up permitted the application of controlled compression loading in combination with controlled deviations in joint posture (Figure 3.3.1A).

All FSUs were first exposed to a 15-minute static 0.3 kN compression pre-load to counter post-mortem tissue swelling (Callaghan & McGill, 1995). Immediately following the preload, the mechanical neutral zone was defined (Panjabi, 1992). This test was performed by rotating the spinal joint into flexion followed by extension at a rate of 0.5 degrees/second while simultaneously exposed to a constant 0.3 kN compression force. A total of four consecutive repetitions were performed. Throughout this non-destructive range-of-motion test, moment and angular displacement data were sampled at a rate of 8 Hz using a 16-bit analog-to-digital conversion system (Galil Motion Control, Rocklin, CA) and a custom motor control program. The neutral zone was defined as the linear boundaries of a fourth-order polynomial function that was fit to the moment-angle data (Figure 3.3.1B). Effectively, the results from this test were used to normalize the postural deviation between specimens (described below).

FSUs were randomly assigned to one of two experimental groups, a control group or a mechanically loaded group, totalling three FSUs per group. FSUs assigned to the control group were not exposed to additional loading beyond the pre-load and range-of-motion test. The loaded group underwent a cyclic compression protocol that approximated the *in vivo* lumbar spine loading environment during moderate demand injury appended tasks such as lifting (T. A. C. Beach et al., 2019; Gooyers et al., 2018; Marras et al., 2009; Prairie, Plamondon, Hegg-Deloye, Larouche, & Corbeil, 2016). Specifically, the compression loading waveform was custom designed to have an average peak compression magnitude that was normalized to 30% of the predicted ultimate compression tolerance (3.53 kN ± 0.15) with a 40% variation in peak compression force about the

30% mean (maximum: 4.62 kN ± 0.21; minimum: 2.11 kN ± 0.09) (van Dieën, Dekkers, Groen, Toussiant, & Meijer, 2001; Zehr et al., 2019b), a loading frequency of 1 Hz (Zehr, Buchman-Pearle, et al., 2020), and a loading duration of 5000 consecutive cycles (Gooyers & Callaghan, 2015). This compression protocol was applied to spinal joints that were simultaneously positioned in a flexed posture that was normalized to 300% of the flexion neutral zone (absolute flexion from resting posture (i.e., 0): 10.89 degrees ± 1.29; total passive range-of-motion (i.e., 300% extension to 300% flexion): 8.67 degrees ± 0.77) (Figure 3.3.1B). Based on destructive mechanical testing, this mechanical loading exposure was estimated to be approximately 94% of the joint fatigue-failure lifespan (Zehr, Buchman-Pearle, et al., 2020). Throughout the mechanical exposure, specimens were wrapped in 0.9% saline-soaked plastic backed gauze to maintain tissue hydration (Adams, 1995).

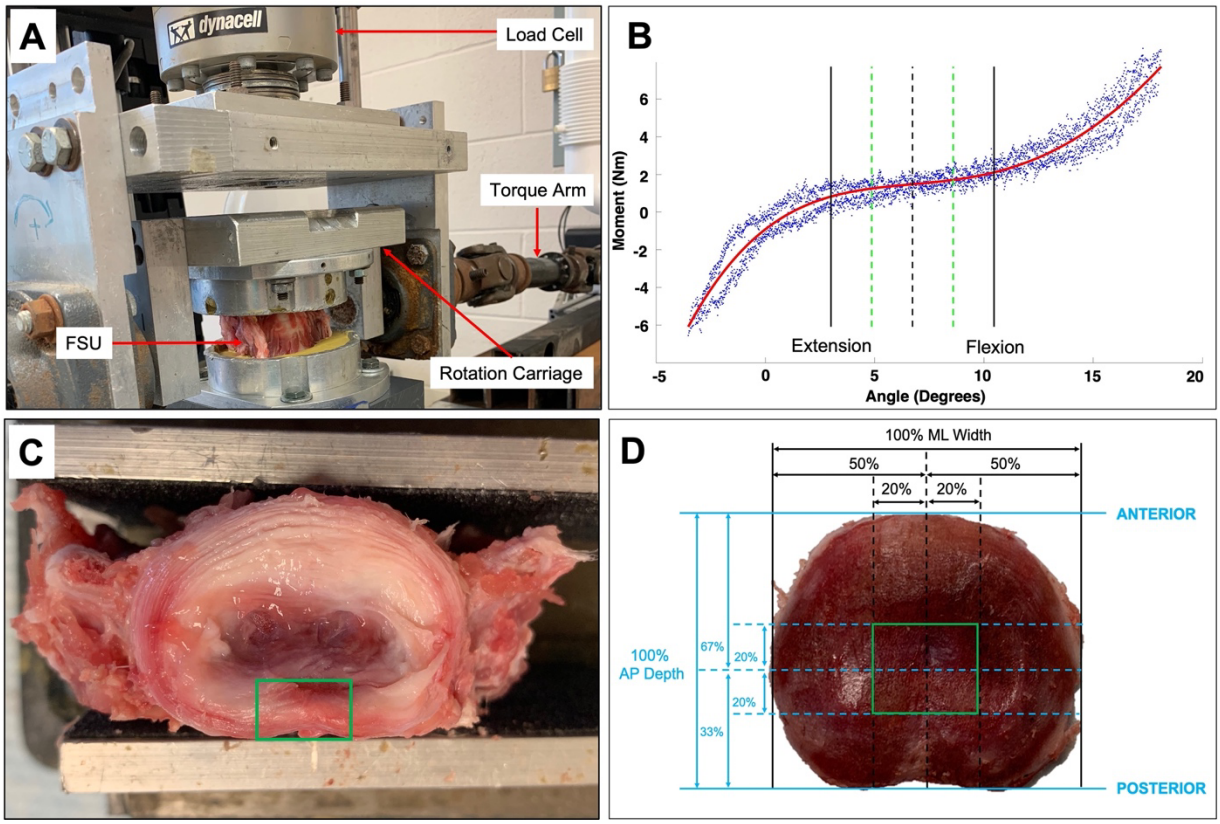

Figure 3.3.1. A) The potted functional spinal unit secured in the material testing system. B) The moment-angle relationship of the spinal joint rotated into flexion and extension. Line definitions: red = polynomial fit to the raw data (blue), green dashed = neutral zone limits, black dashed = neutral posture, black solid = 300% of the flexion and extension neutral zone. C) Transected spinal joint with posterior annulus fibrosis identified with the green box. D) Size normalization of the central endplate region based on measured anterior-posterior (AP) depth and medial-lateral (ML) width.

Post-Loading Tissue Preparation

A transverse incision was made through the mid-plane of the intervertebral disc and posterior spinal ligaments that span the superior and inferior spinous processes in all FSUs. Additionally, the bilateral facet capsules were cut at the approximate location of the facet joint space to free the superior vertebra from the inferior vertebra. Prior to tissue excision, a visual inspection for the presence of macroscopic injuries was performed. This included the examination for intervertebral disc herniations (i.e., annulus fissures), the presence of a gelatinous nucleus

pulposus, endplate fracture, and facet fracture. Beyond the viscoelastic creep response defined by progressive height loss (loaded group only) and related to the loss and/or redistribution of fluid within the intervertebral disc (Masuoka, Michalek, Maclean, Stokes, & Iatridis, 2007; McMillan, Garbutt, & Adams, 1996), there were no visual indications of macroscopic injury and/or degeneration.

First, AF tissue was excised from the posterior region for inclusion in staining analyses (Figure 1C), and the remining AF and nucleus pulposus were carefully debrided to expose the underlying CEP. The CEP of each C4 vertebra was removed along the plane of the epiphyseal plate using an oscillating saw. This landmark was repeatable and inherently controlled the total thickness across all specimens. The medial-lateral width and anterior-posterior depth dimensions were used to identify and size-normalize the central region (Noshchenko et al., 2013) (Figure 3.3.1D). Staining analyses were focused on the central CEP region because it is structurally the thinnest and weakest (Grant et al., 2001) yet functionally the most important in terms of its porosity for the diffusion of solutes to the adjacent intervertebral disc (Jackson & Gu, 2009; Y. Wu et al., 2016). Further, when exposed to compression loading, the centrally distributed stresses render this region most susceptible to microdamage that precedes macroscopic endplate fractures (van Dieën, Dekkers, et al., 2001). The posterior AF was selected for inclusion given the documented stress distributions associated with the simulated loading scenario combined with the imposed flexed joint posture (Adams, McMillan, Green, & Dolan, 1996) and the frequent incidence of intervertebral disc herniations in this region (Callaghan & McGill, 2001a).

Harvested CEP specimens were decalcified in 50 mM ethylenediamimetraactic acid (pH 8.0) in PBS at 4°C for a minimum of 14 days. AF and decalcified CEP samples were embedded in O.C.T. compound (Tissue-Plus™) and subsequently frozen in liquid nitrogen-cooled isopentane.

Serial cryosections (CEP: transverse and sagittal planes; AF: transverse plane) were cut to a thickness of 10 μm using a cryostat (Thermo Electronic) that was temperature-controlled to -20°C. All cryosections were placed on Gold Seal™ Rite-On glass microscope slides (Thermo Scientific). Within each AF (approximately 10 mm by 5 mm) and CEP (approximately 10 mm by 10 mm) region of interest, the location of transverse and sagittal sections was randomized.

Immunofluorescence Analysis

Immunofluorescence analysis for collagen expression was performed with primary antibodies against Type I (COL I) and Type II (COL II) collagen. The inclusion of COL I and COL II in the staining analysis is based on their documented significance to the structure-function relationships – collective contributions to mechanical function (Fields, Rodriguez, et al., 2013) and makeup of the fibrous framework in the AF (Roberts, Menage, Duance, Wotton, & Ayad, 1991) and CEP (Lakstins, Arnold, Gunsch, Flanigan, et al., 2020; Lakstins, Arnold, Gunsch, Khan, et al., 2020). Multi-channel staining further enabled the analysis and dissociation of damage occurring in hyaline cartilage (i.e., endplate) – primarily COL II (Antoniou et al., 1996) – from the subchondral bone – primarily COL I – along with how the interface responds to loading. All primary and secondary antibodies were purchased from Invitrogen (Table 3.3.1). The immunofluorescence staining procedure consists of six steps. Each step, including solution concentrations, incubation durations, and incubation temperatures are described in Table 3.3.2. Background staining controls were performed as outlined in Table 3.3.2 except that the primary antibody solution was replaced with 10% goat serum in PBS (i.e., the block solution) for the incubation period (Step 2). Visualization of prepared slides was performed with a confocal laser scanning microscope (Axio Observer Z1 LSM800, Zeiss, Oberkochen, Germany). Five representative images of each specimen were captured with a 20X Plan-Apochromt objective

(NA0.8) and ZEN 2.3 System software (Zeiss, Oberkochen, Germany). 488 nm and 561 nm lasers were used with a pinhole size set to 41µm. The master gain for AF 488 and AF 555 channels was 662 V and 650 V, respectively, with a corresponding digital offset of 0 and digital gain of 1.0 in both channels. All images were exported with 2092 x 2092 RGB resolution.

Table 3.3.1. Antibodies purchased and used for the co-staining of collagen in porcine CEP and AF tissues.

1° Host Species	Primary Antibody	Reactivity	Secondary Antibody
Mouse	Invitrogen™ Monocolonal Thermo Fisher Scientific, MA1-26771 Isotype: IgG1	Collagen I	Goat Anti-Mouse, Alexa Fluor 488, Thermo Fisher Scientific, A-11001 Isotype: IgG
Rabbit	Invitrogen™ Polycolonal Thermo Fisher Scientific, PA1-26206 Isotype: IgG	Collagen II	Goat Anti-Rabbit Alexa Fluor 555, Thermo Fisher Scientific, A-21422 Isotype: IgG

Table 3.3.2. Overview of the combined immunofluorescence staining protocol for COL I and COL II in porcine CEP and AF tissues.

1. Block	
Solution & Concentration	10% Goat Serum in PBS
Incubation Time	60 minutes
Incubation Temperature	Room Temperature
2. Primary Antibodies	
Solution & Concentration	COL I at 1:100 in 10% Goat Serum (Block Solution) COL II at 1:100 in 10% Goat Serum (Block Solution)
Incubation Time	Overnight = 20 Hours
Incubation Temperature	4°C
3. Wash (3 Cycles)	
Wash Solution	0.5% Triton X-100 in PBS
Wash Time	5 minutes
4. Secondary Antibodies	
Solution & Concentration	Alexa Fluor 488 at 1:500 in PBS (for COL I) Alexa Fluor 555 at 1:500 in PBS (for COL II)
Incubation Time	30 minutes
Incubation Temperature	Room Temperature
5. Wash (3 Cycles)	
Wash Solution	0.5% Triton X-100 in PBS
Wash Time	5 minutes
6. Mounting	
Mounting *Solution*	Invitrogen™ Fluoromount-G, Thermo Fisher Scientific (00-4958-02)

Quantification of fluorescence area and fluorescence intensity of COL I and COL II in AF, CEP sagittal, and CEP transverse sections was performed. Specifically, fluorescence area of each tissue was determined by subtracting the mean fluorescence area within a given colour channel of the respective tissue when unstained (i.e., background). For AF and CEP transverse sections, fluorescence area and fluorescence intensity were quantified for the entire image area. Given that CEP sagittal sections did not cover the entire image, set areas (461 pixels x 2038 pixels) of EP (COL II) and subchondral bone (COL I) were evaluated. Fluorescence area and florescence intensity are both expressed in arbitrary units (AU). A value of 1.0 was assigned to the control group, and the fluorescence area and fluorescence intensity obtained from the loaded group, was expressed relative to the control group. All fluorescence area and fluorescence intensity measurements were acquired using the ZEN 2.3 System software.

Colocalization of COL I and COL II was also evaluated in AF, CEP sagittal, and CEP transverse sections and was quantitatively expressed as Pearson's correlation coefficient (R). Weighted colocalization coefficients were further examined for independent colour channels. That is, the percentage of pixels that were green (AF 488) and also orange (AF 555), and vice versa, was quantified for control and loaded groups. All colocalization measurements were acquired using the ZEN 2.3 System software.

Tortuosity coefficients of the CEP surface and cartilage-subchondral bone interface were quantified in EP sagittal sections. Tortuosity is a measure used to examine the abnormality of a line and is used extensively for the study of curvature in blood vessels (Dougherty & Varro, 2000; Heneghan, 2002; Szabó & Merks, 2017) and paths of solid media in porous materials (Ghanbarian, Hunt, Ewing, & Sahimi, 2013; Nemati, Rahbar Shahrouzi, & Alizadeh, 2020). The modified numerical definition of tortuosity defined by Dougherty and Varro (2000) was employed in this

study given that simplistic measures, like the distance factor (Capowski, Kylstra, & Freedman, 1995), were insensitive to the gradient and frequency of surface deviations from the line connecting the surface endpoints, $\boldsymbol{S}$ (Capowski et al., 1995). In each image, 20 points with corresponding $\boldsymbol{X}$ and $\boldsymbol{Y}$ coordinates were manually digitized along the CEP surface and CEP-subchondral bone interface in an equal interval of 100 pixels (Figure 3.3.2A). These two-dimensional positions were defined in ImageJ and the coordinates of each point were concatenated and exported, such that:

$$L = \begin{bmatrix} X_1 & X_2 & \dots & X_{20} \\ Y_1 & Y_2 & \dots & Y_{20} \end{bmatrix} \quad \textbf{Equation 3.3.1}$$

This matrix of coordinate data, $\boldsymbol{L}$, were input into a custom Matlab program (2020b, The MathWorks Inc., Natrick, MA) that was developed to derive the tortuosity coefficients, $\boldsymbol{TC}$. Given that the line, $\boldsymbol{S}$**,** in each image was not aligned with the default image coordinate system, the obtained coordinates were first rotated by the angular deviation, $\boldsymbol{\theta}$, which was also measured in ImageJ (Figure 3.3.2B). The coordinates were rotated in two-dimensional space by post-multiplying each set of $\boldsymbol{X}$ and $\boldsymbol{Y}$ coordinates with a standard two-dimensional rotation matrix, $\boldsymbol{R}$, given by:

$$R[\theta] = \begin{bmatrix} cos\theta & sin\theta \\ -sin\theta & cos\theta \end{bmatrix} \quad \textbf{Equation 3.3.2}$$

$$R[-\theta] = \begin{bmatrix} \cos\theta & -sin\theta \\ sin\theta & cos\theta \end{bmatrix} \quad \textbf{Equation 3.3.3}$$

$$\begin{bmatrix} X' \\ Y' \end{bmatrix} = [R] \begin{bmatrix} X \\ Y \end{bmatrix} \quad \textbf{Equation 3.3.4}$$

Where $R[\theta]$ is used for a clockwise rotation defined as positive based on the image coordinate system and $R[-\theta]$ is used for a counterclockwise rotation defined as negative based on the image coordinate system. When expanded, $\boldsymbol{X'}$ and $\boldsymbol{Y'}$are derived for positive (Equation 3.3.5) and negative (Equation 3.3.6) rotations:

$$X' = X\cos\theta + Y\sin\theta \quad \text{and} \quad Y' = -X\sin\theta + Y\cos\theta \qquad \textbf{Equation 3.3.5}$$

$$X' = Xcos\theta - Ysin\theta \quad \text{and} \quad Y' = Xsin\theta + Ycos\theta \qquad \textbf{Equation 3.3.6}$$

This step is imperative to ensure the vectors to each digitized point are indeed orthogonal to line, $\boldsymbol{S}$, effectively $\boldsymbol{Y'}$. The iterative contribution of successive gradients formed between adjacent points to the tortuosity of the examined surface/interface was defined as, $\boldsymbol{\delta}$, given by:

$$\delta_j = \left(Y'_j - Y'_{j-1}\right) - \left(Y'_{j+1} - Y'_j\right) \qquad \textbf{Equation 3.3.7}$$

Finally, the sum of absolute delta values was divided by the sampling interval (100 pixels), $\boldsymbol{p}$, for the calculation of $\boldsymbol{TC}$. The absolute of each delta quantity indicates that positive and negative gradients equally contribute to the tortuosity.

$$TC = \frac{\left(\sum_{j=1}^{N}\left|\delta_j\right|\right)}{p} \qquad \textbf{Equation 3.3.8}$$

The TC for a straight line is equal to zero (Figure 3.3.2C), and when implementing this derivation for a half sine wave of 50 points, a TC of 0.1256 was achieved (Figure 3.3.2D), which precisely equals the simulated value reported by Dougherty and Varro (2000). Therefore, less damaged surfaces/interfaces would be expected to have a lower TC than more damaged surfaces/interfaces.

Lastly, the additive area of pores and/or voids observed in transverse CEP and sagittal CEP sections were examined. All area measurements were expressed as a percentage of the overall image area. In sagittal CEP sections, the area of pore development along the cartilage-subchondral bone border were examined. All area measurements were completed in ImageJ.

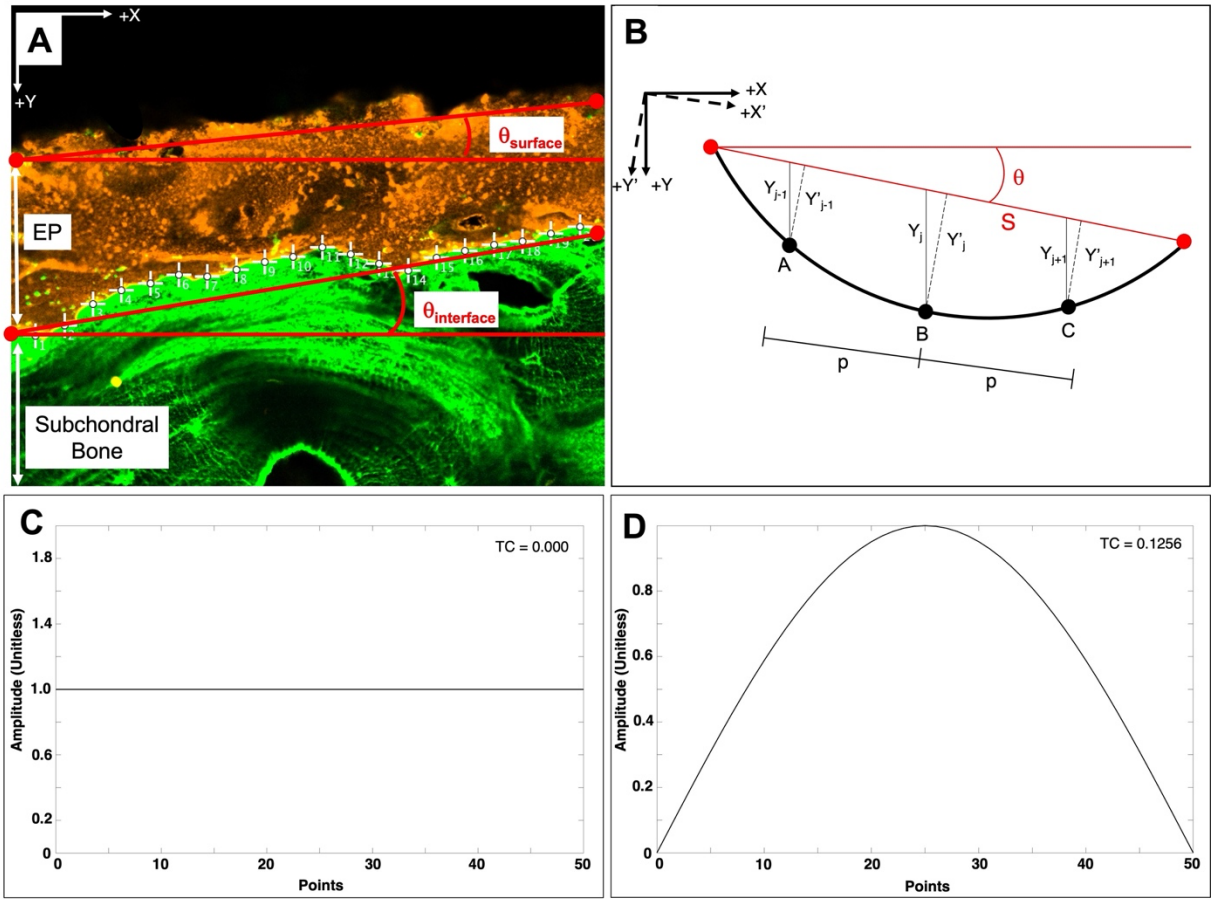

Figure 3.3.2. A) Digitization of 20 points (p = 100 pixels) along the EP-subchondral bone interface shown by COL I (green) and COL II (orange) staining and the determination of global angular rotation (θ) of each surface (S). The same digitization procedure was completed for the CEP surface. B) Rotation of the obtained X and Y coordinates by the measured theta to obtain perpendicular distance (Y') from surface, S, to each digitized point. C) The tortuosity coefficient for a simulated straight line of 50 points. D) the tortuosity coefficient for a simulated half sine wave of 50 points.

Hematoxylin & Eosin Staining

For visual comparison, hematoxylin and eosin (H&E) staining was performed on AF, CEP sagittal, and CEP transverse sections. Tissue sections were immersed in hematoxylin for 60 seconds, immediately rinsed with distilled water, and counterstained with eosin for 90 seconds. Ten consecutive one second submersions were performed in 75% ethanol, 90% ethanol, 100% ethanol, and Xylene. Tissue sections were air dried and mounted in Permount (Fischer Scientific Co., Fair Lawn, NJ) and a coverslip. Representative images were captured with a10X objective (2048 x 1536 RGB resolution) using Image Pro Plus software (Media Cybernetics, Silver Spring, USA) for each specimen.

Statistical Analyses

All statistical analyses were conducted using RStudio (Version 1.3.1093, RStudio Inc., Boston, MA). Student's t-tests were performed for each dependant variable to compare metrics of histochemical and structural damage between the control and mechanically loaded groups. Alpha was set *apriori* to 0.05.

3.3.3. Results and Discussion

Strong fluorescent staining was observed for AF and CEP tissues incubated with the COL I/COL II antibody cocktail with negligible staining on slides that were incubated with secondary antibody cocktail only (Figure 3.3.3). Therefore, all experiments were performed with the antibody cocktail described herein. Furthermore, the mean background fluorescence area quantified in loaded AF (0.99) and CEP (1.0) tissue was similar to respective slides from the control group ($p \geq 0.760$).

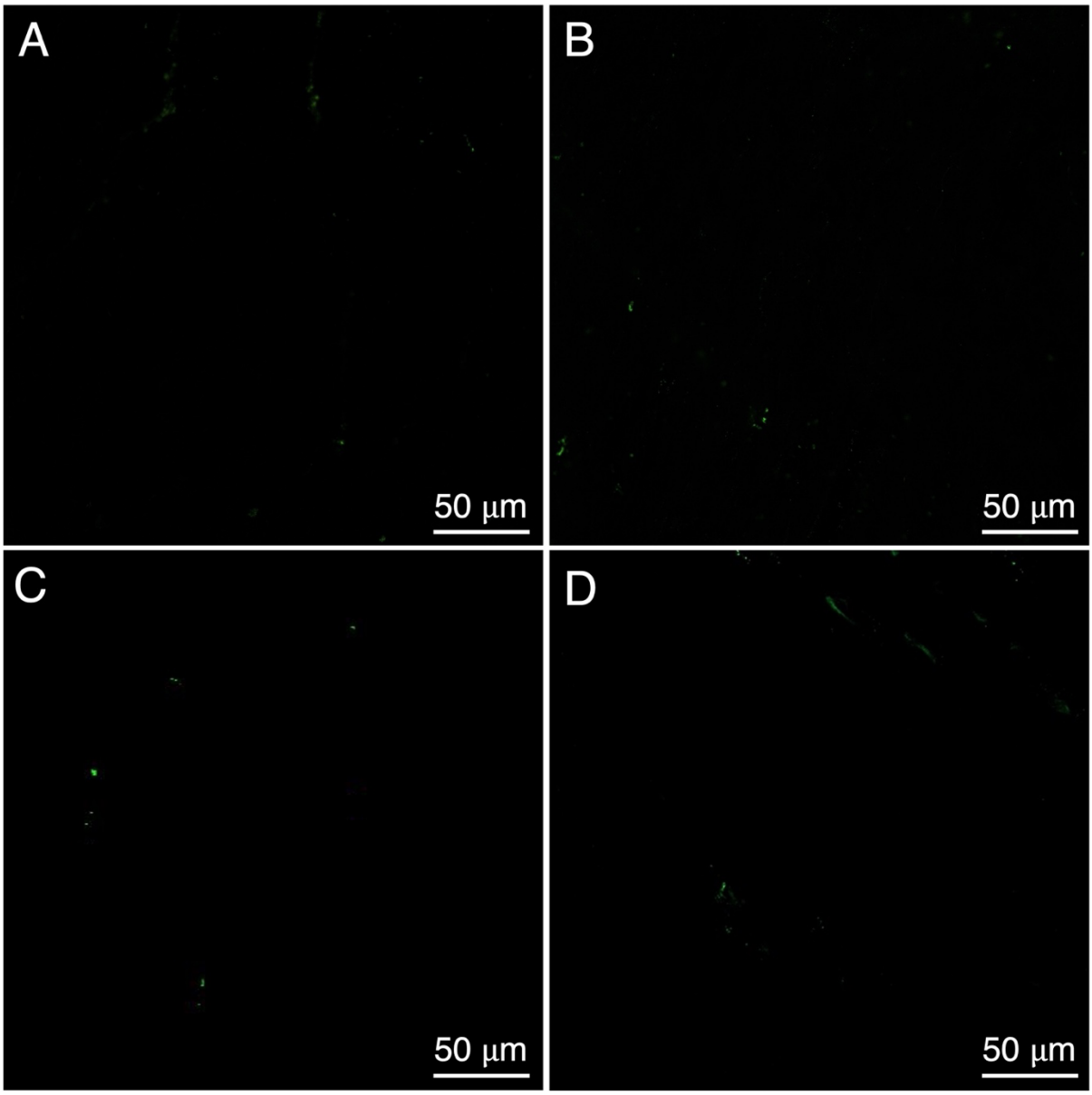

Figure 3.3.3. Background staining controls for: A) AF tissue assigned to the control group, B) AF tissue assigned to the loaded group, C) CEP tissue assigned to the control group, D) CEP tissue assigned to the loaded group.

Native Collagen Content in the Annulus Fibrosus

The mean fluorescence area of COL I and COL II decreased in the loaded group by -3.6% and -54.9%, respectively (Table 3.3.3). Similarly, mean fluorescence intensity observed in loaded AF tissue significantly decreased for COL II (-44.8%), but not COL I (-1.1%). These findings

collectively demonstrate that, for the given loading scenario, COL II is most susceptible to compression induced damage in the posterior AF region (Figure 3.3.4 A-C vs. E-G). The presence of microdamage was further confirmed through the visual comparison of representative H&E stained AF sections (Figure 3.3.4 D, H). Compared to other types of cartilage (i.e., articular cartilage) and within the same cadaver, an immunohistochemistry approach involving the extraction and assay of COL II demonstrated that AF is particularly sensitive to the denaturing of COL II, even in clinically healthy intervertebral discs defined as the absence of radiographic evidence for injury (Hollander et al., 1996). The observed reduction of COL II content in the initially healthy and non-degenerated intervertebral discs included in this study is therefore conceivable and supported by the significant age-related denaturation of COL II observed in cadaveric tissue (Hollander et al., 1996). It is, however, unclear how the mechanisms of COL II damage in specimens exposed to *in vitro* mechanical paradigms compare to the aged spine exposed to a complex mechanical and biochemical environment. Although denaturation was reported throughout the intervertebral disc (Hollander et al., 1996), future work is required to understand the potential localization of COL II damage due maldistributed stress concentrations associated with deviated lumbar spine postures (Adams et al., 1996).

As evidenced by the colocalization coefficients (Table 3.3.3), COL I and COL II are mutually exclusive in healthy and loaded posterior AF tissue. The independence of the examined collagen types may imply that COL I and COL II are arranged in parallel with a lower occurrence of perpendicular cross-linkages.

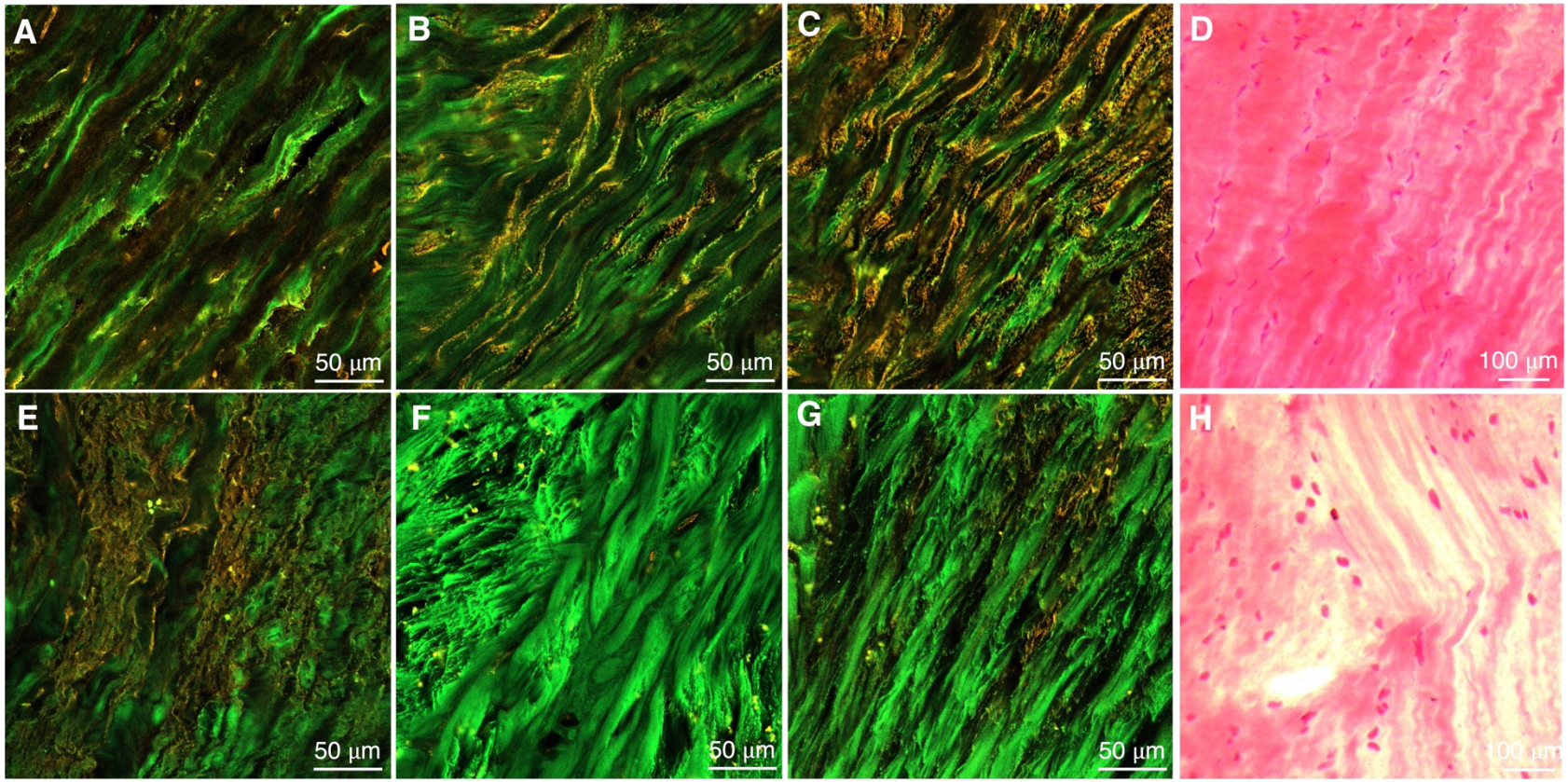

Figure 3.3.4. A-C) Characteristic immunofluorescence images of the AF sectioned in the transverse plane for each control specimen showing COL I (green) and COL II (orange) staining (N = 3). D) Representative H&E image of the AF in the transverse plane from the control group. E-G) Characteristic immunofluorescence images of transverse AF sections for each loaded specimen showing COL I (green) and COL II (orange) staining (N = 3). H) Representative H&E image of the AF from the loaded group.

Table 3.3.3. Mean ± standard deviation of fluorescence area, fluorescence intensity, and colocalization coefficients. All fluorescence area and fluorescence intensity values are expressed relative to the control group value of 1.0. Significance was achieved at $p < 0.05$.

	Fluorescence Area (AU)		Fluorescence Intensity (AU)		Colocalization (R)			W. Coefficient (AF 488)			W. Coefficient (AF 555)		
	Loaded	*p*	Loaded	*p*	Control	Loaded	*p*	Control	Loaded	*p*	Control	Loaded	*p*
Annulus Fibrosus													
COL I	0.96 ± 0.13	0.199	0.99 ± 0.62	0.471	0.21 ± 0.05	0.34 ± 0.11	0.090	0.12 ± 0.07	0.05 ± 0.01	0.140	0.18 ± 0.12	0.04 ± 0.03	0.076
COL II	0.45 ± 0.27	**0.002**	0.56 ± 0.30	**< 0.001**									
Endplate (Sagittal)													
COL I	0.64 ± 0.31	**0.003**	1.00 ± 0.45	0.973	0.03 ± 0.02	0.13 ± 0.09	0.078	0.06 ± 0.05	0.03 ± 0.03	0.231	0.04 ± 0.02	0.05 ± 0.03	0.695
COL II	0.62 ± 0.37	**0.027**	0.69 ± 0.36	**0.043**									
Endplate (Transverse)													
COL I	1.17 ± 0.71	0.648	0.93 ± 0.42	0.202	0.04 ± 0.01	0.07 ± 0.04	0.279	0.05 ± 0.02	0.06 ± 0.05	0.578	0.09 ± 0.06	0.07 ± 0.03	0.771
COL II	0.64 ± 0.38	**0.031**	0.65 ± 0.38	**0.038**									

Native Collagen Content of the Endplate – Transverse Plane

In the transverse plane, the mean fluorescence area and mean fluorescence intensity of COL II significantly decreased in the loaded group by -36.1% and -34.8%, respectively (Table 3.3.3). No significant changes in mean fluorescence area and mean fluorescence intensity were observed for COL I, which was localized to the pore perimeter (Figure 3.3.5 A-C vs. E-G). Although a progressive increase in COL I content was found to coincide with a decrease in COL II content in older age demographics (> 40 years) experiencing severe degeneration of the corresponding intervertebral disc (Antoniou et al., 1996), the 17% increase in mean fluorescence area observed for COL I in the current *in vitro* study is attributed to greater circumferential damage of COL II surrounding the pores thereby exposing the illuminated subchondral bone (i.e., COL I).

Despite visually apparent reduction in COL II around the pores, the normalized surface area occupied by pores did not significantly change between the control (12.7%) and loaded (15.9%) groups ($p = 0.338$) (Figure 3.3.5 A-C vs. E-G). Therefore, extended exposures to moderate mechanical loads does not appear to interrupt the potential for nutrient diffusion in non-calcified CEP tissue, which suggests that diffusion barriers (i.e., i.e., calcification) may be driven by changes in chondrocyte function (Oda et al., 2004). From a structural standpoint, the small increase in pore area is not an apparent source of structural impairment in the examined CEP tissue, despite its relevance in highly aged tissue with co-existing intervertebral disc degeneration (Rodriguez et al., 2011).

Quantification of colocalization revealed that COL I and COL II are highly distinct in transverse CEP sections ($R \leq 0.07$). As evidenced in Figure 3.3.5, the localization of COL I to the perimeter of surface pores may add mechanical reinforcement to resist excessive deformation

around potential stress risers when exposed to radial tensile strains associated with compression induced deflection.

Native Collagen Content of the Endplate – Sagittal Plane

When visualized in the sagittal plane, the mean fluorescence area in EP tissue significantly decreased for COL I (35.6%) and COL II (37.7%) (Table 3.3.3). Similar to the transverse plane, a significant reduction (-31.1%) in mean fluorescence intensity was only observed in COL II (Figure 3.3.6 A-C vs. E-G). Mechanically induced microstructural damage to the network of subchondral bone has been well studied (Lambers, Bouman, Tkachenko, Keaveny, & Hernandez, 2014; Massarwa, Aboudi, Galbusera, Wilke, & Haj-Ali, 2017; Mattei, 2018; Mirzaali et al., 2018; O'Callaghan, Szarko, Wang, & Luo, 2018; Purcell, Tiernan, McEvoy, & Morris, 2015) and is supported by the observed reduction in mean fluorescence area for COL I. A novel finding observed with the immunofluorescence method was that the hyaline cartilage CEP (COL II) and subchondral bone (COL I) experience approximately the same magnitude of histochemical damage when approaching the estimated tissue lifespan. Future research will investigate the timeline of histochemical damage in both structures throughout a multitude of loading durations to determine if damage is equivalent throughout the tissue lifespan or if one experiences damage before the other. This knowledge has further potential to guide the understanding of injury initiation mechanisms for common endplate protrusion injuries, such as Schmorl's nodes.

The extent of colocalization was minimal ($R \leq 0.13$) with a distinct demarcation between the hyaline cartilage endplate (COL II) and subchondral bone (COL I). This demarcation was also visually apparent in EP sections that were H&E stained (Figure 3.3.6 D, H). This finding, in control and loaded specimens, aligns with histochemistry analyses and scanning electron microscopy of CEP anchorage to adjacent intervertebral disc and subchondral bone (Berg-Johansen, Fields, et al.,

2018; Paietta et al., 2013; Wade et al., 2011) and microcomputed tomography imaging of damage accumulation below the CEP surface (Rodriguez et al., 2011). The development of structural voids along the CEP-subchondral bone interface of loaded CEP tissue supports the notion of a structurally vulnerable anchoring mechanism to the accumulation of microtrauma and avulsion injuries (Berg-Johansen, Fields, et al., 2018). The normalized area of structural voids along the EP-subchondral bone interface in loaded EP tissue (7.0%) significantly exceeded the control group (0.2%) ($p < 0.001$) in this study. Voids were also visualized in H&E stained sections presented in Figure 3.3.6.

Derivation of tortuosity coefficients revealed that the mechanically induced deviations of CEP-subchondral bone interface (control = 7.0, loaded = 19.3, $p = 0.002$) were greater than the CEP surface (control = 6.8, loaded = 10.5, $p = 0.154$), despite being similar in the control group. The greater tortuosity coefficients quantified in loaded CEP tissue indicate a more irregular CEP-subchondral bone interface which was characterized by the presence of voids or penetration of the cartilage structure into the subchondral bone (Figure 3.3.6E). The combined analyses of tortuosity outcomes with the development of structural voids suggests that most histochemical and structural damage originates at the CEP-subchondral bone border.

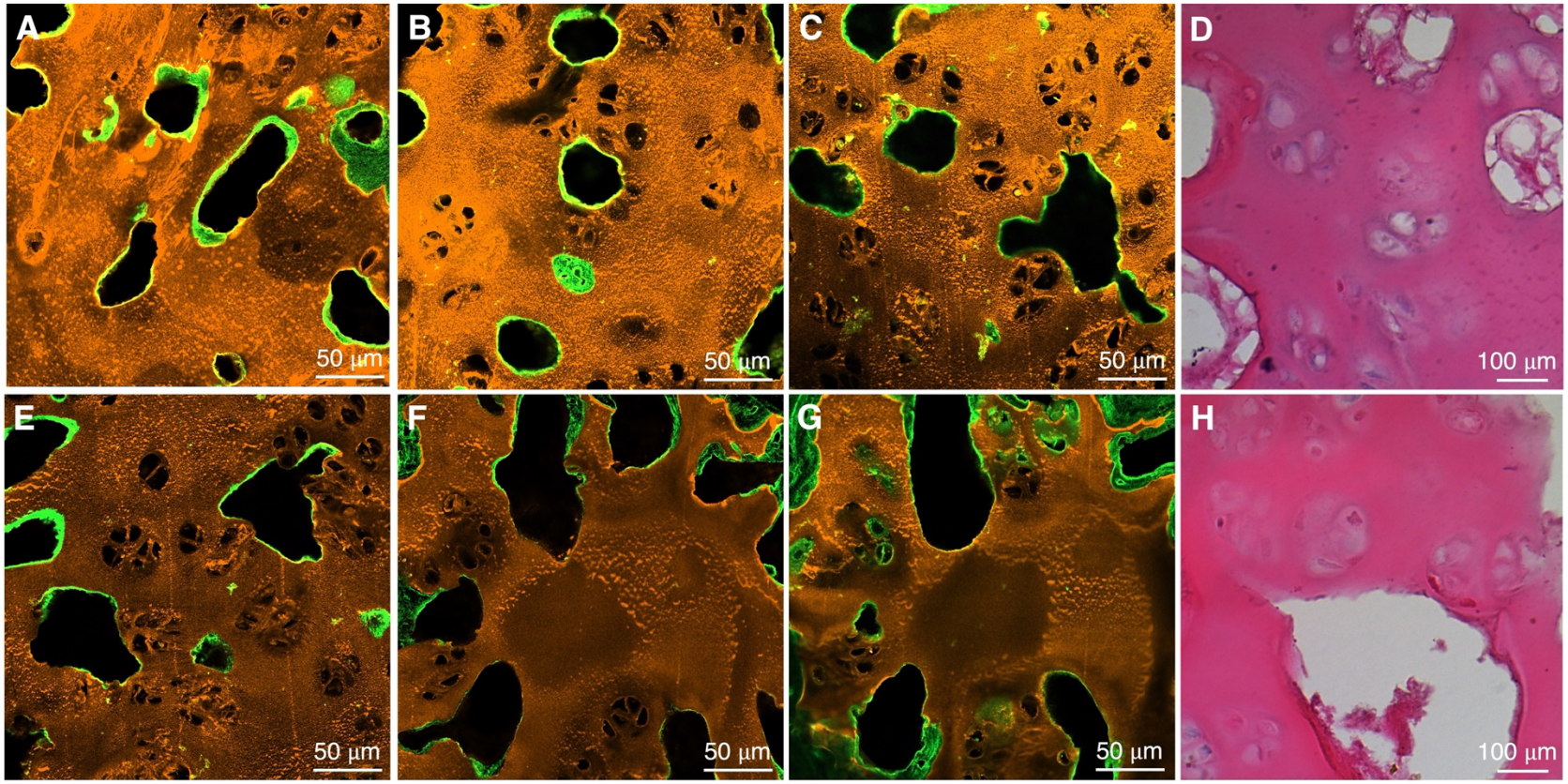

Figure 3.3.5. A-C) Characteristic immunofluorescence images of the CEP sectioned in the transverse plane for each control specimen showing COL I (green) and COL II (orange) staining (N =3). D) Representative H&E image of the CEP in the transverse plane from the control group. E-G) Characteristic immunofluorescence images of the transverse CEP sections for each loaded specimen showing COL I (green) and COL II (orange) staining (N = 3). H) Representative H&E image of the CEP in the transverse plane from the loaded group.

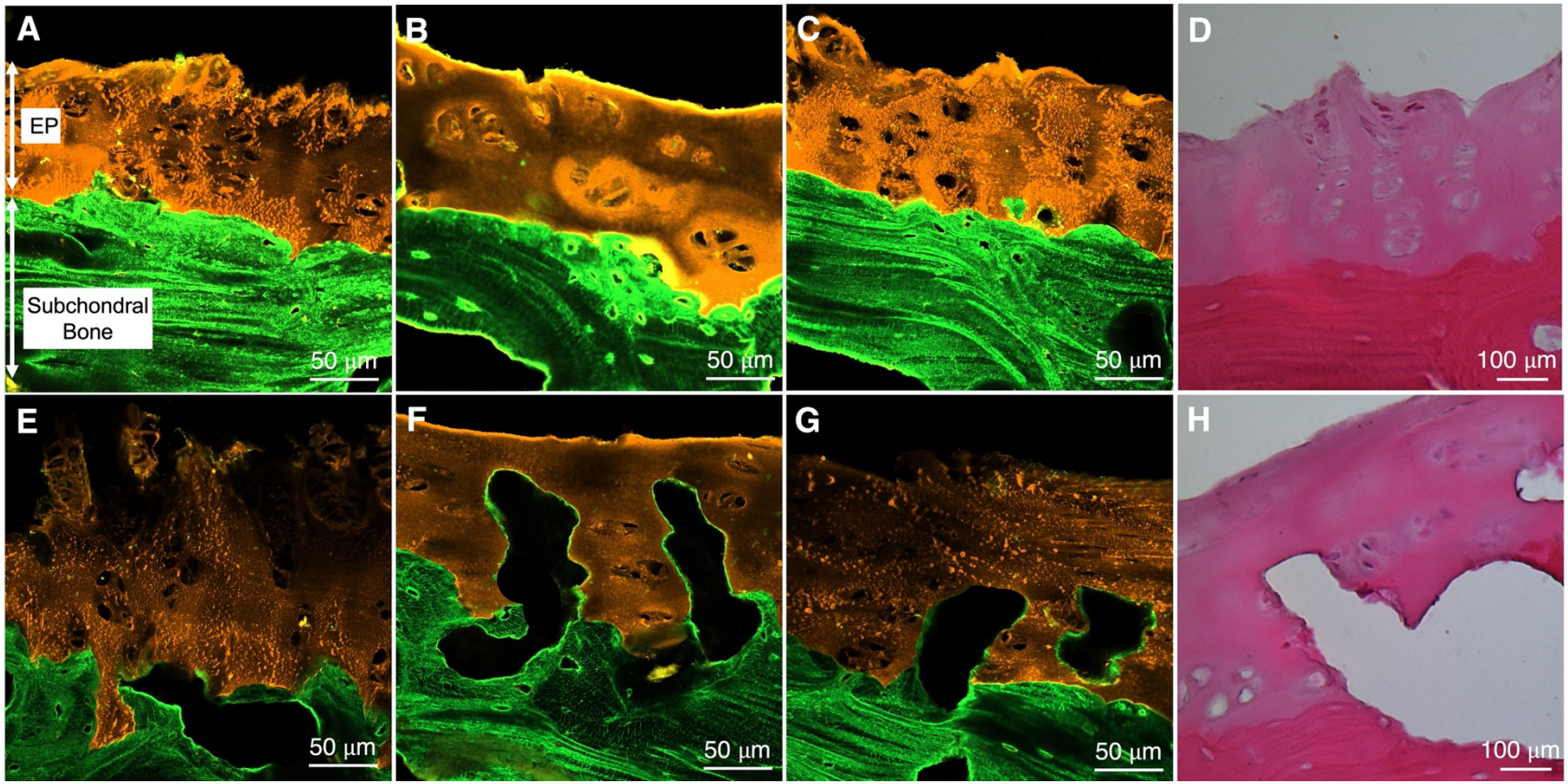

Figure 3.3.6. A-C) Characteristic immunofluorescence images of the CEP sectioned in the sagittal plane for each control specimen showing COL I (green) and COL II (orange) staining (N =3). D) Representative H&E image of the CEP in the sagittal plane from the control group. E-G) Characteristic immunofluorescence images of the sagittal CEP sections for each loaded specimen showing COL I (green) and COL II (orange) staining (N = 3). H) Representative H&E image of the CEP in the sagittal plane from the loaded group.

The following limitations should be considered when interpreting the study findings. First, all mechanical testing was performed with an ambient temperature of 21°C and hydrated with saline solution acclimated to the same temperature. Although the temperature of irrigation fluids can influence chondrocyte metabolism and death in culturing experiments (Kocaoglu, Martin, Wolf, Karahan, & Amendola, 2011), there were no significant differences in morphological characteristics when cartilage explants were viewed with a scanning electron microscope following 2-hours of irrigation in saline solution with a temperature of 25°C and 37°C (Cheng, Jou, Chern, Wang, & Chen, 2004). Despite these studies being specific to articular cartilage, a similar response is conceivable in the hyaline cartilage endplate. From a mechanical standpoint, research on cortical bones samples have demonstrated a longer lifespan when cyclically loaded at room-temperature (Carter & Hayes, 1976). Cortical bone is but one type of tissue comprising the spinal unit, and it remains unknown if spinal joints mimic the same temperature-dependency. It is emphasized that mechanical parameters were estimated from fatigue studies conducted in similar thermal environments (Gooyers & Callaghan, 2015; van Dieën, Dekkers, et al., 2001; Zehr, Buchman-Pearle, et al., 2020). Second, the presented immunofluorescence staining protocol was only tested on frozen cryosections. It is therefore unknown if this protocol is effective for examining histochemical damage in formalin-fixed paraffin embedded tissues. Third, the tissues were excised from control group specimens immediately following the pre-condition protocols and prepared for staining. Based on similar cartilage morphology reported between control and experimental irrigation groups (of 25°C and 37°C) (Cheng et al., 2004), it is unlikely that appreciable degeneration or damage occurred due to time differences between groups. This decision further prevented the potential for water retention in an unloaded spinal unit.

In conclusion, a novel multi-colour immunofluorescence method for quantifying collagen and microstructural damage in collagenous spine tissues was described. The presence of microdamage was visually confirmed by H&E staining of the AF and CEP. The presented method was deemed effective for the objective quantification of microdamage pathways prior to the occurrence of a macroscopic low back injuries such as intervertebral disc herniations and endplate fractures. Although development was based on an *in vitro* experimental design and in a porcine animal model, unpublished data from our laboratory demonstrate that the presented antibody cocktail is effective for the staining of collagenous spine tissues extracted from human cadavers and a live rat animal model.

3.3.4. Implementation of Findings

Although developed and tested on the annulus fibrosus, this immunofluorescence staining technique was used to quantify loading induced microdamage in the CEP only (Chapter 4, 6, 7). Furthermore, colocalization was not evaluated in Chapter 4, 6, and 7 given the minimal colocalization observed between collagen proteins observed in this study. Tortuosity was also not used in future studies of this dissertation given the strong correlation with sub-surface void area. Therefore, any changes to tortuosity of the CEP-subchondral bone border were driven by the development of sub-surface voids.

CHAPTER 4

Indentation Mechanics and Native Collagen Content in the Cartilaginous Endplate: A Comparison Between Porcine Cervical and Human Lumbar Spines

Abstract

Objectives: This study characterized the regional indentation mechanics (loading stiffness, creep displacement) and a native collagen content (type I and II) in cartilaginous endplates (CEPs) from the porcine cervical spine, young human lumbar spine (19, 33 years), and aged human lumbar spine (85 years). Inter-species measurements of sub-surface void area and cartilage thickness were further examined.

Methods: Seventeen endplates were included in this exploratory study: six porcine cervical, nine young human lumbar, and two aged human lumbar. Width and depth measurements were obtained using a digital caliper and used to size-normalize and identify the central, anterior, posterior, and lateral regions. Regional microindentation tests were performed using a serial robot, where surface locations were loaded/unloaded at 0.1 mm/s and held at a constant 10 N force for 30 seconds. Loading stiffness and creep displacement were obtained from force-displacement data. Immunofluorescence staining for type I and type II collagen was subsequently performed on sagittal sections of all endplate regions. 255 images were obtained from which fluorescence intensity, sub-surface void area, and cartilage thickness were measured.

Results: CEPs from the young human lumbar spine were, on average, 27% more compliant, 0.891 mm thicker, had a lower fluorescence intensity for native collagen proteins within the cartilage (-

58%) and subchondral bone (-24%), and had a sub-surface void area that was 19.7 times greater than porcine cervical CEPs. Compared to aged human lumbar CEPs, young human lumbar CEPs were 57% stiffer, 0.568 mm thicker, had a higher fluorescence intensity for native collagen proteins within the cartilage (+30%) and subchondral bone (+46%), and had a sub-surface void area that was 10.6 times smaller.

Conclusions: Although not a perfect mechanical and structural surrogate, porcine cervical CEPs provided initial conditions that may be more representative of the young and healthy human lumbar spine compared to aged human cadaveric specimens. Therefore, this study provided initial data to support the use of porcine CEPs in favour of aged human lumbar CEPs for the study of injury initiation and pathways.

4.1. Introduction

The cartilaginous endplate (CEP) separates the intervertebral disc from adjacent vertebral bodies (Bogduk, 2012). Its structural and functional characteristics influence load transmission through spinal tissues and intervertebral disc health (Berg-Johansen, Fields, et al., 2018; P. Lama et al., 2014). Specifically, sufficient structural integrity is essential for regulating the transport of nutrients and metabolites into and out of the intervertebral disc (Y. C. Huang et al., 2014; Y. Wu et al., 2016), preventing intervertebral disc degeneration (Giers et al., 2017; Rodriguez et al., 2011), and preserving vertebral bone health (M. F. Brown et al., 1997; Fields, Liebenberg, & Lotz, 2013). The CEP mechanical properties, however, are largely dependent on the composition of extracellular matrix constituents (Fields, Rodriguez, et al., 2013). Thus, characterization of the extracellular matrix constituents is essential for understanding how the CEP resists deformation and how the properties of this heterogenous structure may change in response to mechanical overload.

The extracellular matrix of human cadaveric CEPs contains a high density of horizontally orientated collagen (type II), glycosaminoglycans, proteoglycans, and water within its extracellular matrix (Fields, Rodriguez, et al., 2013; Lotz et al., 2013). Biochemistry approaches have been employed to quantify the dry weight of extracellular matrix proteins (Fields, Rodriguez, et al., 2013). Compared to glycosaminoglycan and water content, collagen was strongly related to the tensile properties of isolated CEP tissue (Fields, Rodriguez, et al., 2013). While effective, a limitation to biochemistry techniques is that healthy and damaged collagen proteins are not dissociated. Therefore, collagen proteins may still be present in form (i.e., mass), but may have been damaged such that their function is altered. The ability to assess the amount and density of collagen in its native and healthy form may provide new avenues to assess CEP health in addition

to how mechanical loading may influence the structure-function relationship. Given the specificity of protein markers, immunofluorescence approaches have demonstrated promise to dissociate native from damaged collagen proteins through positive and negative staining, respectively (Zehr, Rahman, Callaghan, & Quadrilatero, 2022).

A current barrier for the assessment of loading induced damage is the absence of constitutive and microstructural data in non-degenerated and minimally loaded CEP tissue. A feasible way to bypass the limitation of age constraints frequently associated with human cadaveric tissue is to use an animal model. For example, the porcine cervical spine model is an accessible surrogate for the human lumbar spine. It specifically affords greater control over the potential confounding effects of age, diet, and loading history on spine health and degeneration. Further, the porcine cervical spine has been used extensively for *in vitro* studies to gain insight into overuse injury pathways (Callaghan & McGill, 2001a; Gooyers & Callaghan, 2015; Gooyers et al., 2012; Parkinson & Callaghan, 2007a, 2007b, 2008; Zehr et al., 2019b). Despite the documented structural and functional similarities between spinal units of the porcine cervical and human lumbar spines (Busscher et al., 2010; Oxland et al., 1991; Yingling et al., 1999), the similarity in mechanical properties and native collagen content has yet to be characterized within the CEP. Acquisition of these data could determine the suitability of porcine cervical spine models for examining overuse injury pathways in the CEP.

This exploratory study aimed to characterize and compare regional indentation mechanics and native collagen content in CEPs from the porcine cervical spine, young human lumbar spine (19, 33 years), and aged human lumbar spine (85 years). Indeed, within specimen comparisons between endplate regions are relevant and have been explored in prior studies (Berg-Johansen, Han, et al., 2018; Hou & Luo, 2009). However, this study sought to compare regional responses

between species. Specifically, loading stiffness and creep displacement were quantified from microindentation tests. An immunofluorescence staining procedure was used to quantify the fluorescence intensity of type I and type II collagen proteins (i.e., fluorescence intensity) within the hyaline cartilage endplate and subchondral bone. The cartilage thickness and void area along the CEP-subchondral bone border were further quantified from sagittal plane images.

Three specific hypotheses were tested. First, the mechanical properties and biochemical composition of the intervertebral disc and CEP have been shown to change as a function of age (Antoniou et al., 1996; Martins et al., 2018). Therefore, the native collagen content and indentation properties were hypothesized to differ between endplates extracted from young and aged human cadaveric lumbar spines. Second, although CEPs from porcine and human species have a similar shape (Yingling et al., 1999), morphological differences (i.e., thickness) have been observed (Li et al., 2022). As such, it is hypothesized that indentation properties will differ between CEPs from porcine cervical and human lumbar spines. Third, biochemical differences between human and porcine CEPs have been further documented (Y. Zhang et al., 2014). Therefore, the fluorescence intensity for native collagen content was hypothesized to differ between porcine cervical and all human lumbar spine CEPs.

4.2. Methods

Overview

Non-destructive microindentation testing was performed to quantify the stiffness and creep displacement in CEPs extracted from cadaveric human lumbar and porcine cervical spines. This study subsequently used immunofluorescence staining to quantitatively compare fluorescence intensity (type I and type II collagen), cartilage thickness, and void area along the CEP-

subchondral bone border. A flow chart of the indentation, tissue handling, and staining procedures is depicted in Figure 4.2.1.

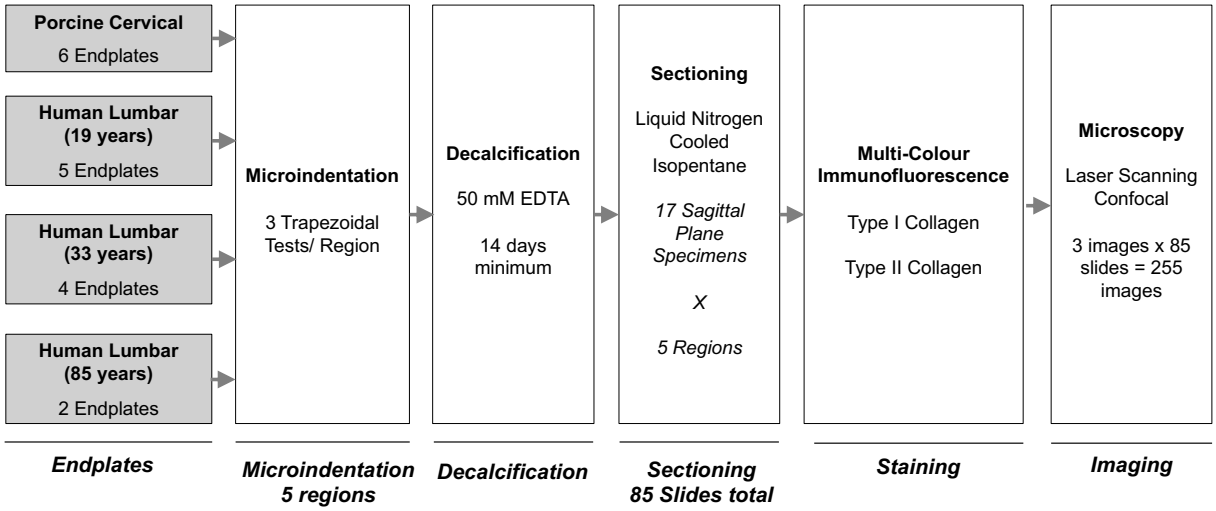

Figure 4.2.1. A schematic of the experimental procedures.

Specimen Inclusion and Dissection

Three fresh-frozen porcine cervical spine specimens were acquired for this study. These porcine specimens were obtained from mature adolescent market hogs, which is defined as 6-12 months and/or 110 to 115 kg at the time of slaughter (Reiland, 1978). All surrounding musculature was removed and the C3C4 and C5C6 functional spinal units (FSU) were excised. These six FSUs were part of the control group included in Chapter 5, 6, and 7. Therefore, these FSUs underwent a 15-minute static preload (0.3 kN) and a non-destructive flexion-extension range-of-motion test prior to the indentation and staining procedures (Chapter 5.2). Following these tests, one endplate was extracted from each spinal unit at the approximate epiphyseal plate. Width and depth dimensions were measured with a digital caliper and are reported in Table 4.2.1.

Three cadaveric human lumbar spines were included in this study (Figure 4.2.2). Two donors were admitted through the University of Waterloo School of Anatomy and the third was acquired from a tissue bank in the United States. All donors were male and had an age of 19, 33,

and 85 years at the time of death. Similar to the porcine cervical spine, all intact spine specimens were first sectioned into FSUs and underwent a 15-minute static preload (0.3 kN) followed by non-destructive flexion-extension and anterior-posterior shear range-of-motion tests. Data obtained from these tests were part of a separate study. The following tissue was extracted from each lumbar spine:

- 19 years: Intervertebral discs of the T12L1, L2L3, and L4L5 joints were removed, and the facets were deranged to separate each joint. Cranial and caudal endplates within each joint were successfully extracted at the approximate epiphyseal plate and included in this study. The width and depth dimensions were measured with a digital caliper and are reported in Table 4.2.1.
- 33 years: Intervertebral discs of the L1L2, L3L4, and L5S1 joints were removed, and the facets were deranged to separate each joint. Cranial and caudal endplates within the L1L2 and L3L4 joints were successfully extracted at the approximate epiphyseal plate. The measured width and depth dimensions are reported in Table 4.2.1. A significant depression was observed in the endplates of the L5S1 joint. Therefore, they were excluded from this study.
- 85 years: Intervertebral discs of the L1L2, L3L4, and L5S1 joints were removed, and the facets were deranged to separate each joint. Significant degeneration was observed in all endplates, except for the L3L4 joint. Therefore, only two endplates were successfully extracted for testing. The width and depth dimensions were measured and reported in Table 4.2.1. Severe degeneration, characterized by erosion such that trabecular bone appeared through the cartilage endplate. This form and severity of degeneration was common in aged donors. In fact, the lumbar spines of six additional donors (aged 83-100) were examined,

but the endplates were either macroscopically injured or unsalvageable due to advanced degeneration.

Representative images of endplates dissected from porcine and human lumbar spines are depicted in Figure 4.2.3. Prior to endplate excision, all intervertebral discs were examined for degeneration using the criteria developed by Galente (1967) and visually assessed for indications of pre-existing macroscopic injury (i.e., herniations, radial annulus tears, endplate fracture). All intervertebral discs examined from porcine cervical and young human lumbar (i.e., 19 and 33 years) specimens satisfied grade 1 criteria (non-degenerated and healthy). However, the intervertebral discs from the aged human lumbar spine (i.e., 85 years) were classified as grade 3 – the nucleus was dry and occasionally disordered with the boundary between the nucleus and annulus no longer existing (Galante, 1967). All procedures included in this study received approval from the University of Waterloo Office of Research Ethics (ORE#41394).

Table 4.2.1. Summary of endplate inclusion. Spinal levels and dimensions of each endplate are included.

		Width (mm)	Depth (mm)	Average Thickness (mm)
Porcine Cervical				
C3	caudal	37.6	24.8	2.2 ± 0.9
C5	caudal	29.9	25.6	2.3 ± 1.1
C4	cranial	36.4	27.5	2.0 ± 0.8
C6	cranial	39.3	30.0	2.1 ± 1.1
C3	caudal	36.9	27.4	2.0 ± 0.9
C6	cranial	36.3	26.1	2.3 ± 1.3
Human Lumbar (19 years) – cause of death: overdose				
L1	cranial	43.6	29.5	3.0 ± 0.9
L2	caudal	45.5	31.1	3.1 ± 0.9
L3	cranial	47.2	35.2	3.1 ± 0.4
L4	caudal	48.5	35.8	3.0 ± 1.1
L5	cranial	48.6	37.8	3.1 ± 0.8
Human Lumbar (33 Years) – cause of death: complications from head trauma				
L1	caudal	46.7	31.2	3.1 ± 0.9
L2	cranial	47.8	31.9	3.0 ± 1.0
L3	caudal	49.7	33.0	3.0 ± 0.1
L4	cranial	51.8	35.7	3.2 ± 0.6
Human Lumbar (85 Years) – cause of death: natural causes				
L3	caudal	46.3	27.4	3.1 ± 1.0
L4	cranial	47.1	28.1	3.0 ± 0.8

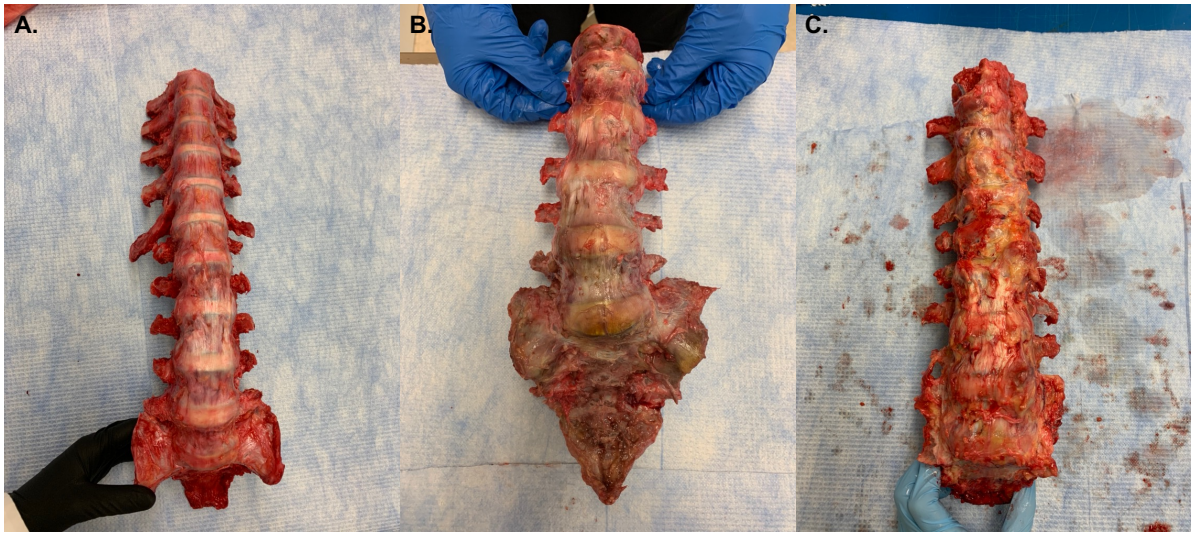

Figure 4.2.2. Intact specimens from a 19-year old (A) 33-year old (B) and 85 year old (C) human lumbar spine.

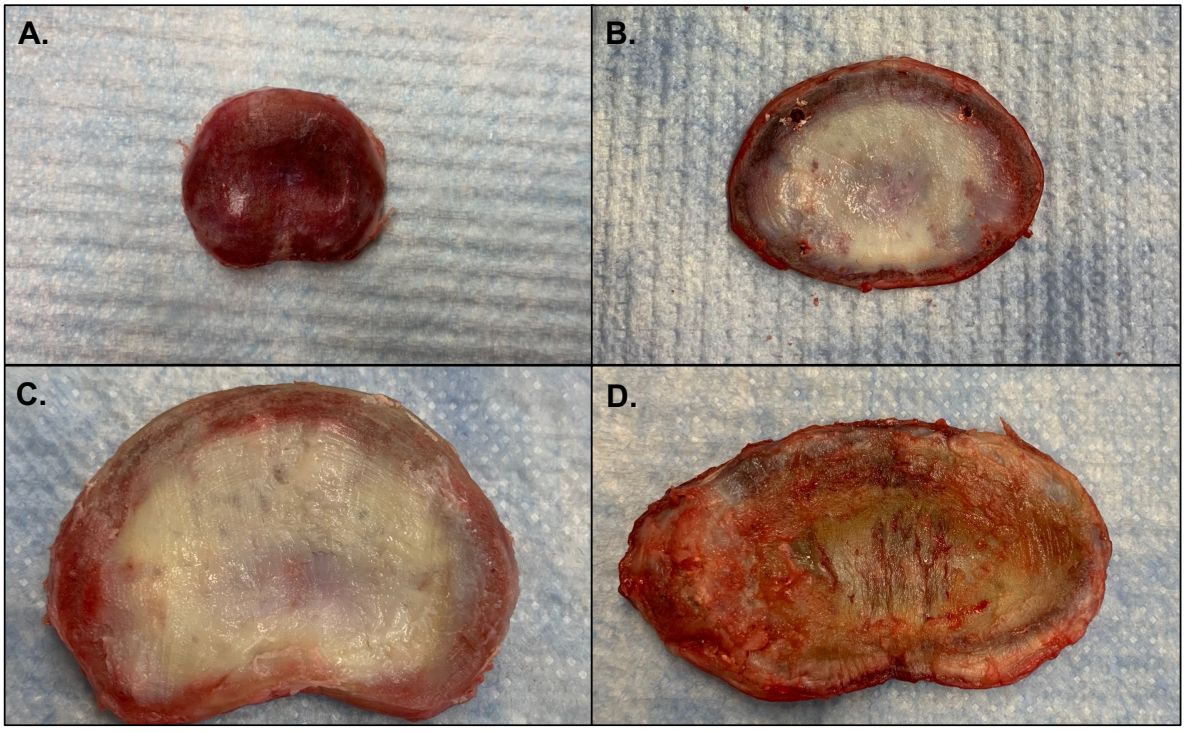

Figure 4.2.3. Representative endplates excised from the porcine cervical spine (A) and the human lumbar spine of 19 year old (B), 33 year old (C) and 85 year old (D) donors.

Microindentation

Indentation testing was performed and loaded the collagen fibers in a similar manor to the pressurized nucleus pulposus, that being a vertical and perpendicular load application. The width

and depth measurements of each CEP were used to determine the relative dimensions of five endplate regions: central, anterior, posterior, and lateral (Figure 4.2.4) (Noshchenko et al., 2013). The boundaries of each region were marked on the endplate surface using permeant marker (Figure 4.2.5). The Cartesian location of the indented surface sites included midpoint of the size-normalized regions.

EP Dimensions		20%	33%	50%	67%
AP Depth	25.7	5.14	8.481	12.85	17.219
ML Width	37.4	7.48	12.342	18.7	25.058

INFERIOR ENDPLATE		
**Measurements relative to the left and top		
Points	**Width (mm)**	**Height (mm)**
Anterior	18.7	12.079
Left Lateral	11.22	17.219
Posterior	18.7	22.359
Right Lateral	26.18	17.219

SUPERIOR ENDPLATE		
**Measurements relative to the left and top		
Points	**Width (mm)**	**Height (mm)**
Anterior	18.7	12.079
Left Lateral	26.18	17.219
Posterior	18.7	22.359
Right Lateral	11.22	17.219

Section Dimensions	Width (mm)	Height (mm)	Area (mm^2)
Anterior	14.96	12.079	180.70184
Central	14.96	10.28	153.7888
Left Lateral	11.22	10.28	115.3416
Right Lateral	11.22	10.28	115.3416
Posterior	14.96	3.341	49.98136

Figure 4.2.4. An example calculation of regional endplate dimensions determined with anterior-posterior (AP) depth and medial-lateral width (ML) of 25.7 mm and 37.4 mm, respectively. The measurements of AP depth and ML width are used as input to subsequently populate all other cells in the spreadsheet.

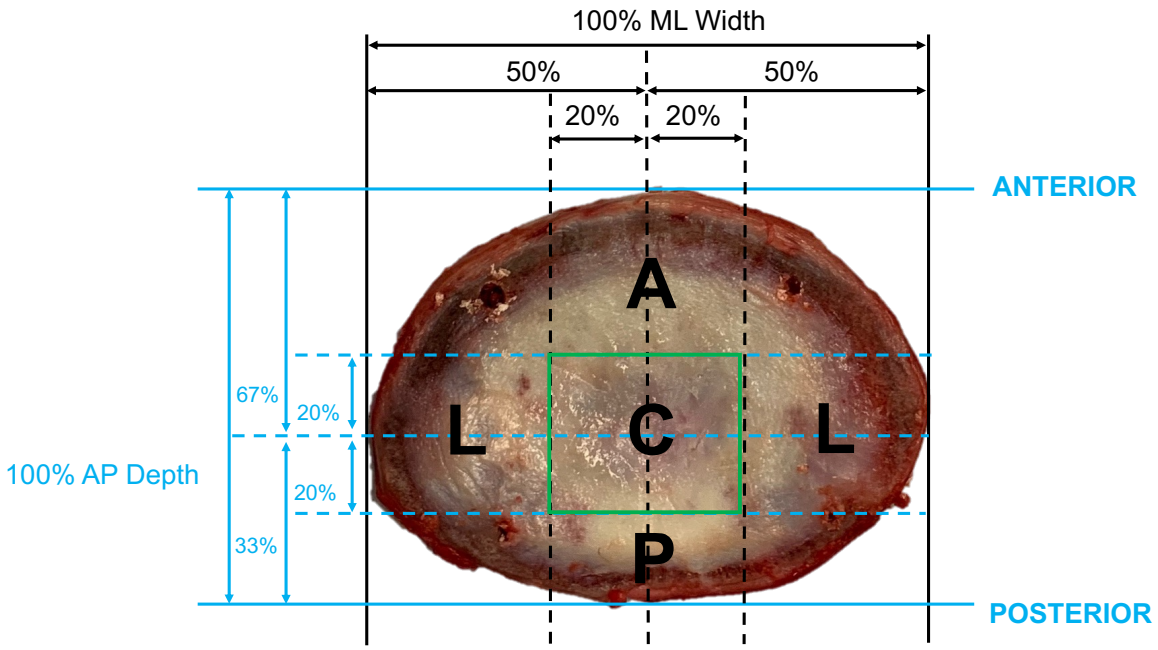

Figure 4.2.5. Size-normalization of the endplate surface regions. C = central, A = anterior, P = posterior, L = lateral

A custom-built testing apparatus was constructed where CEPs were rigidly secured to custom machined aluminum stanchions (tissue interfacing diameter of 2mm) using perforating screws at each corner of the size-normalized surface. Magnets (20 lbs total pull force) were custom machined and attached to the base of each stanchion to prevent tipping and/or translation on the height-adjustable carbon steel base (Figure 4.2.6). This mounting strategy was selected in favour of the intact endplate-vertebra unit to eliminate structural contributions from the intact trabecular bone. In effect, the mechanical properties of the CEP were isolated in this study. Indeed, it could be argued that some regions (i.e., central) are at a greater distance from the stanchions compared to others (i.e., anterior, posterior, lateral); however, global deflection was not induced by the 10 N force. Therefore, the employed approach examined the local microindentation responses of the CEP surface.

Indentation testing was performed with a serial robot (Displacement Resolution = 0.001

mm, Yaskawa Motoman, Miamisburg, OH, USA) that was equipped with a load cell secured to the end-effector (Force resolution (Z axis) = 0.01 N, 110516-2, ATI Industrial Automation, Apex, NC, USA) and a custom machined aluminum indenter (3 mm hemisphere) attached in series (Figure 4.2.6). The employed indentation protocol was adopted from Patel et al. (2018) and was applied at each surface location using custom multi-mode control. These steps included: i) the endplate surface was indented at a rate of 0.1 mm/s until a 10 N load was achieved; ii) the 10 N load was maintained for 30 seconds; iii) the endplate surface was unloaded at a rate of 0.1 mm/s. A schematic of the indentation with respect to the cartilage tissue is illustrated in Figure 4.2.7. In block randomized order, this protocol was performed three times at each regional site with a 30-second unloading phase between each trial. Throughout each test, the force and vertical position of the end-effector were sampled at a rate of 10 Hz.

The loading stiffness (N/mm) and creep displacement (mm) were determined from the resulting force-displacement curves. Loading stiffness was derived from the linear region of the loading phase and creep displacement was determined as the change in vertical position during the 30-second holding phase. The regional tissue thickness was measured after indentation testing using a digital caliper. These data are presented in Table 4.2.1.

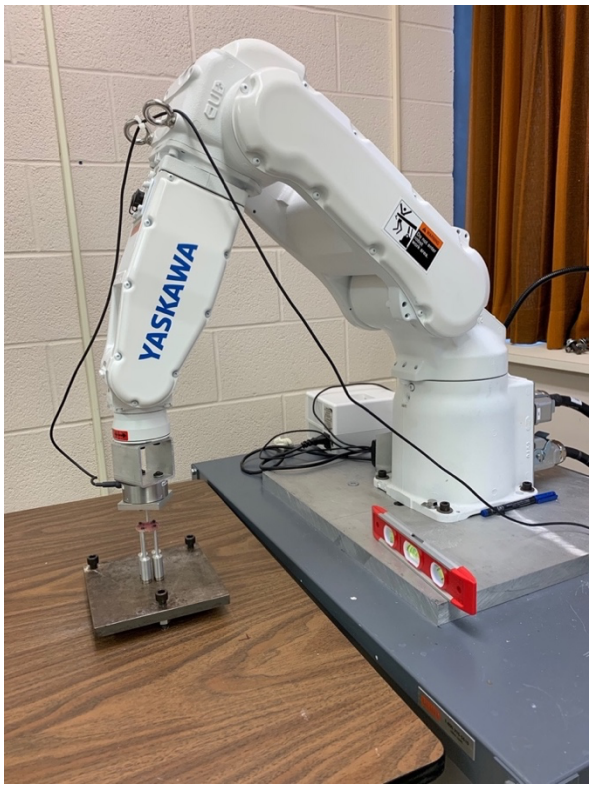

Figure 4.2.6. The microindentation setup, including the serial robot, load cell, aluminum stanchions, and carbon steel base.

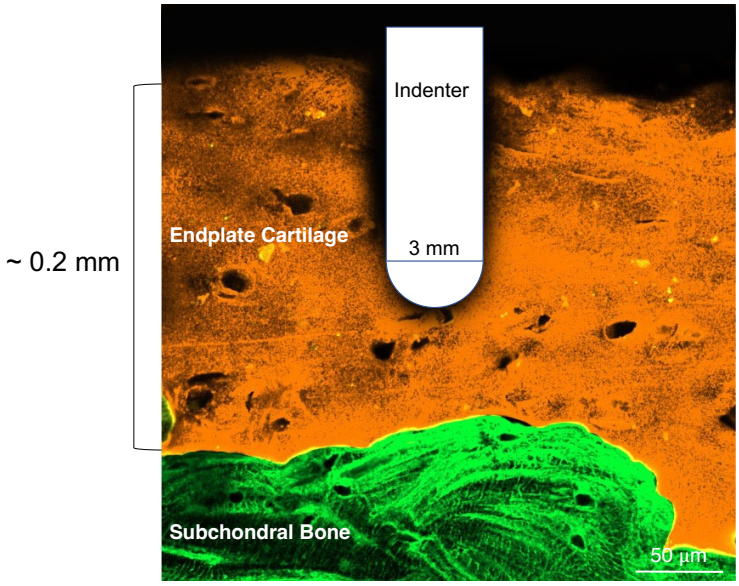

Figure 4.2.7. A schematic of the excised endplate tissue (hyaline cartilage in orange and subchondral bone in green) undergoing the indentation test and inducing an approximate strain of 0.50.

Immunofluorescence Staining

Immediately following microindentation, CEPs were cut into independent regions and placed in 50 mM ethylenediamimetraactic acid (pH 8.0) for a minimum of 14 days. Submersion in ethylenediamimetraactic acid was performed to decalcify the tissue such that it could be easily sectioned. Specimens were stored at 4°C throughout the decalcification period. Decalcified samples were washed in PBS, embedded in O.C.T. compound (Tissue-Plus™), and subsequently frozen in liquid nitrogen-cooled isopentane. Serial cryosections were cut in the sagittal plane to a thickness of 10 μm using a cryostat that was temperature-controlled to -20°C. This study focused on the analysis of sagittal plane sections since measures of collagen fluorescence (type I and type II collagen) could be obtained together with morphological measures like cartilage thickness. All cryosections were placed on charged Superfrost™ Plus Gold glass microscope slides. Each slide contained sagittal sections of a single endplate region; therefore, 85 slides were prepared for immunohistochemistry staining (17 endplates × 5 regions).

All sections were stained with primary antibodies against type I and type II collagen (Zehr, Rahman, et al., 2022). The immunofluorescence procedure, including all antibody cocktails, was conducted as described in Section 3.3.2. The collection of 85 slides were stained in four separate batches. Concentrations of commercially purchased antibodies and the volumes mixed into each cocktail are provided in Appendix A.

Visualization of prepared slides was performed with a laser scanning confocal microscope (Axio Observer Z1 LSM800, Zeiss, Oberkochen, Germany). Three representative images were taken of each region, totalling 15 images per endplate. A 20X Plan-Apochromt objective (NA0.8) and ZEN 2.3 System software (Zeiss, Oberkochen, Germany) was used for visualization and obtaining images. 488 nm (Alexa Fluor 488, type I) and 561 nm (Alexa Fluor 555, type II) lasers

were used with a pinhole size set to 41µm. The master gain for AF 488 and AF 555 channels was 662 V and 650 V, respectively.

A total of 255 images were acquired. The fluorescence intensity of type I and type II collagen was determined using ZEN 2.3 System software. Fluorescence intensity represents the density of native collagen proteins for a given channel. Therefore, higher intensity (brighter staining) would represent a greater density of collagen proteins. Fluorescence intensity was evaluated for pre-determined areas (461 pixels x 2038 pixels) that were initially selected to capture protein density across areas of positive staining in sagittal images of porcine cervical CEPs (Zehr, Rahman, et al., 2022). The width (2092 pixel) of images captured of human lumbar spine endplates was the same as images of porcine cervical spine endplates (Figure 4.2.8). However, the length dimensions required to capture the thickness of the human endplate cartilage was six times that of the porcine (12552 pixels). The fluorescence intensity of human lumbar specimens was therefore averaged across multiple areas that could be placed within the region of positive staining (Figure 4.2.8). Fluorescence intensities are expressed as arbitrary units (AU). A value of 1.0 was assigned to the average fluorescence intensity obtained for each region of the porcine cervical CEPs. Therefore, the regional fluorescence intensities of the human endplates were expressed relative to the same region in the porcine species.

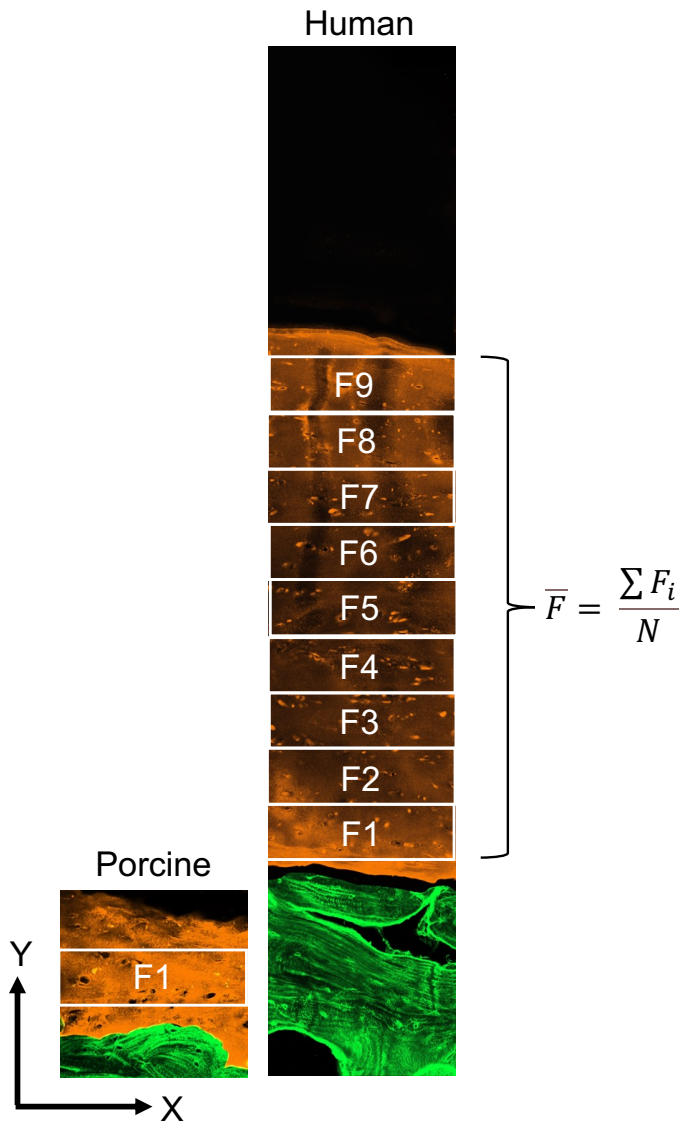

Figure 4.2.8. Pre-defined areas used to assess fluorescence intensity in porcine and human species. *F* represents the fluorescence intensity for the pre-defined area, and *N* equals the number of separate areas examined.

The total area occupied by voids along the CEP-subchondral bone border was computed using ZEN 2.3 System software. All area measurements were expressed as microns squared (μm^2). Lastly, the cartilage thickness, defined as the perpendicular distance from the CEP-subchondral bone border to the cartilage surface was determined using ZEN 2.3 System software. Given the

irregularity of cartilage surfaces, three measurements were taken for each image and averaged across the endplate region.

Statistics

While the use of 17 endplate specimens prohibits the use of statistical analyses, there were some trends which pervaded the results. Descriptive statistics for regional indentation stiffness and creep displacement are presented for the porcine cervical and human lumbar CEPs. Similarly, descriptive data are presented for fluorescence intensity (type I and type II collagen), cartilage thickness, and sub-surface void area measured in each CEP region. In line with the objective, comparisons were made within a region but between species (i.e., porcine cervical, young human lumbar, aged human lumbar).

4.3 Results

Data presented in this chapter are collapsed across spinal levels. While data are presented separately for CEPs examined from the 19 and 33 year old lumbar spines, they were collapsed and referred to as the young human species in the results. Within each species, data was further collapsed across the right and left lateral endplate regions and is termed lateral heron after. Descriptive data and images for independent spinal levels are presented in Appendix B.

Indentation Stiffness

Average indentation stiffness data for central, anterior, posterior, and lateral regions are reported in Table 4.3.1. In all regions, the loading stiffness differed between species with the order of stratification from most stiff to least stiff being porcine cervical spine, young human lumbar spine, and aged human lumbar spine. The stiffness of porcine cervical CEPs was greater than the stiffness of young and aged human lumbar CEPs by an average of 14.33 N/mm and 36.40 N/mm,

respectively. The loading stiffness of young and aged human lumbar CEPs differed by 22.06 N/mm.

Creep Displacement

Average creep displacements measured during the 30 second hold period are reported in Table 4.3.2. In all regions, the creep displacement differed between species with the order of stratification from greatest to least being aged human lumbar, young human lumbar, and porcine cervical. The creep displacement of aged human lumbar CEPs was, on average, greater than young human lumbar and porcine cervical CEPs by 0.033 mm and 0.077 m, respectively. The creep displacement of young human lumbar CEPs was 0.043 mm greater than porcine cervical CEPs, on average.

Table 4.3.1. The indentation stiffness for each endplate region within the porcine cervical and human lumbar endplates (average ± standard deviation)

Region	Porcine Cervical (N/mm)	Human Lumbar (19 years) (N/mm)	Human Lumbar (33 years) (N/mm)	Human Lumbar (85 years) (N/mm)
Central	43.32 ± 4.67	26.69 ± 1.19	37.45 ± 2.34	12.41 ± 1.47
Anterior	64.22 ± 11.64	36.99 ± 6.12	55.83 ± 6.35	21.45 ± 0.84
Posterior	58.99 ± 14.65	32.76 ± 9.16	48.69 ± 4.43	17.70 ± 1.04
Lateral	45.40 ± 8.05	29.84 ± 2.25	40.90 ± 2.49	14.76 ± 0.21

Table 4.3.2. The creep displacement for each region within the porcine cervical and human lumbar endplates (average ± standard deviation).

Region	Porcine Cervical (mm)	Human Lumbar (19 years) (mm)	Human Lumbar (33 years) (mm)	Human Lumbar (85 years) (mm)
Central	0.031 ± 0.006	0.088 ± 0.023	0.064 ± 0.011	0.111 ± 0.033
Anterior	0.012 ± 0.005	0.068 ± 0.044	0.053± 0.020	0.094 ± 0.018
Posterior	0.014± 0.005	0.069 ± 0.006	0.058 ± 0.012	0.087 ± 0.013
Lateral	0.025 ± 0.003	0.055± 0.012	0.059 ± 0.010	0.097 ± 0.027

Fluorescence Intensity

The regional fluorescence intensities are reported with respect to the porcine cervical CEP (Table 4.3.3, Table 4.3.4). Representative sagittal plane images are depicted in Figure 4.3.1 to Figure 4.3.4. The average fluorescence intensity of type I collagen was 0.75 (-25%) in young human lumbar CEPs and 0.30 (-70%) in aged human lumbar CEPs. With respect to type II collagen, the average fluorescence intensity was 0.42 (-58%) in young human lumbar CEPs and 0.12 (-88%) in aged human lumbar CEPs.

Table 4.3.3. The fluorescence intensity of type I collagen for each endplate region within the human lumbar endplates (average ± standard deviation). All values are expressed relative to the same region within the porcine cervical spine (1.0).

Region	**Human Lumbar (19 years) (AU)**	**Human Lumbar (33 years) (AU)**	**Human Lumbar (85 years) (AU)**
Central	0.68 ± 0.11	0.86 ± 0.08	0.33 ± 0.08
Anterior	0.67 ± 0.15	0.86 ± 0.12	0.32 ± 0.08
Posterior	0.68 ± 0.11	0.79 ± 0.12	0.24 ± 0.09
Lateral	0.68 ± 0.09	0.85 ± 0.13	0.31 ± 0.09

Table 4.3.4. The fluorescence intensity of type II collagen for each endplate region within the human lumbar endplates (average ± standard deviation). All values are expressed relative to the same region within the porcine cervical spine (1.0).

Region	**Human Lumbar (19 years) (AU)**	**Human Lumbar (33 years) (AU)**	**Human Lumbar (85 years) (AU)**
Central	0.31 ± 0.12	0.54 ± 0.15	0.12 ± 0.09
Anterior	0.32 ± 0.17	0.51 ± 0.16	0.12 ± 0.03
Posterior	0.29 ± 0.14	0.53 ± 0.12	0.11 ± 0.05
Lateral	0.30 ± 0.14	0.55 ± 0.13	0.12 ± 0.06

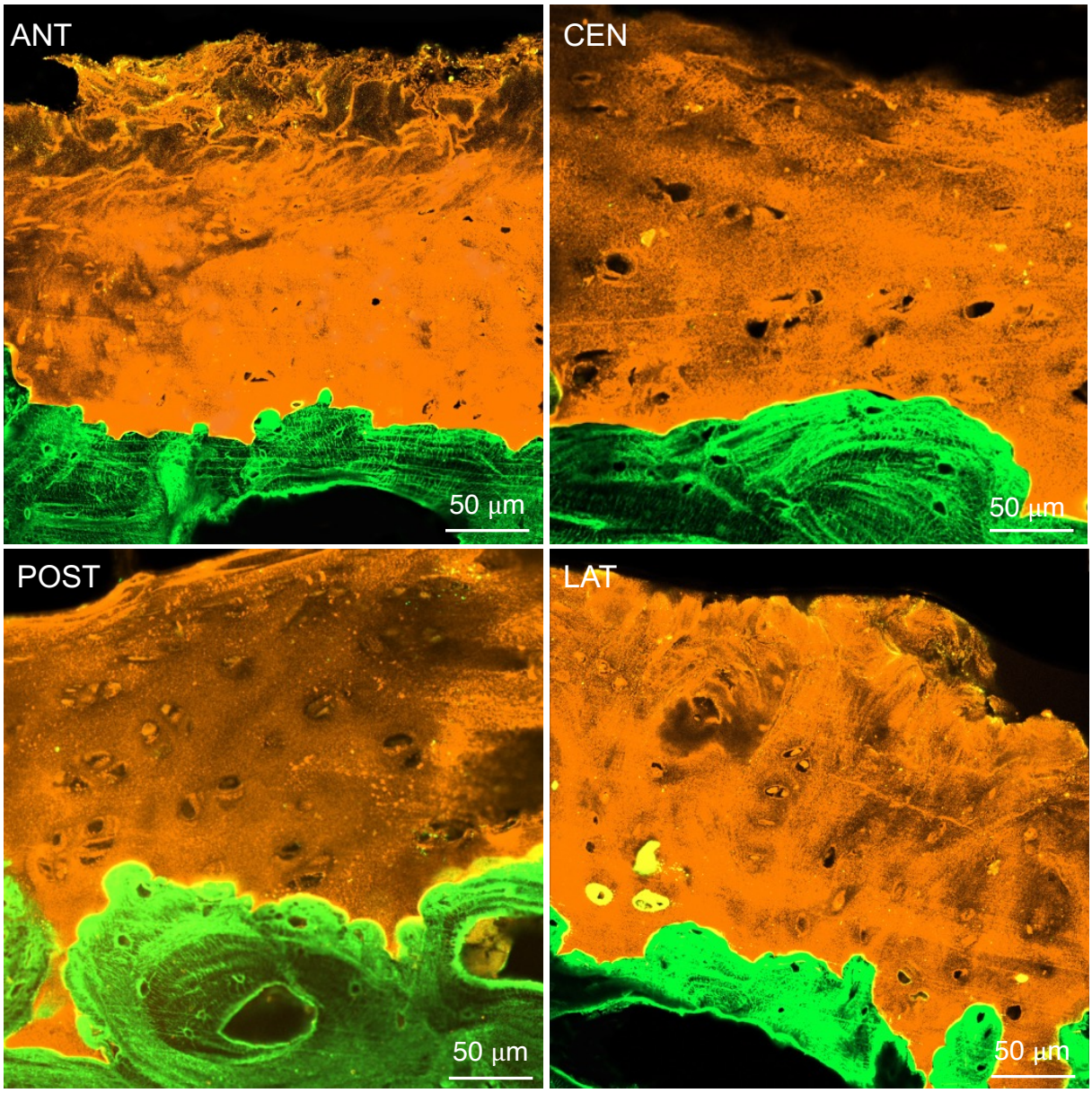

Figure 4.3.1. Representative images of the anterior (ANT), central (CEN), posterior (POST), and lateral (LAT) regions of the porcine cervical spine endplate. All images were taken in the sagittal plane. Positive staining is observed for type I (green) and type II (orange) collagen.

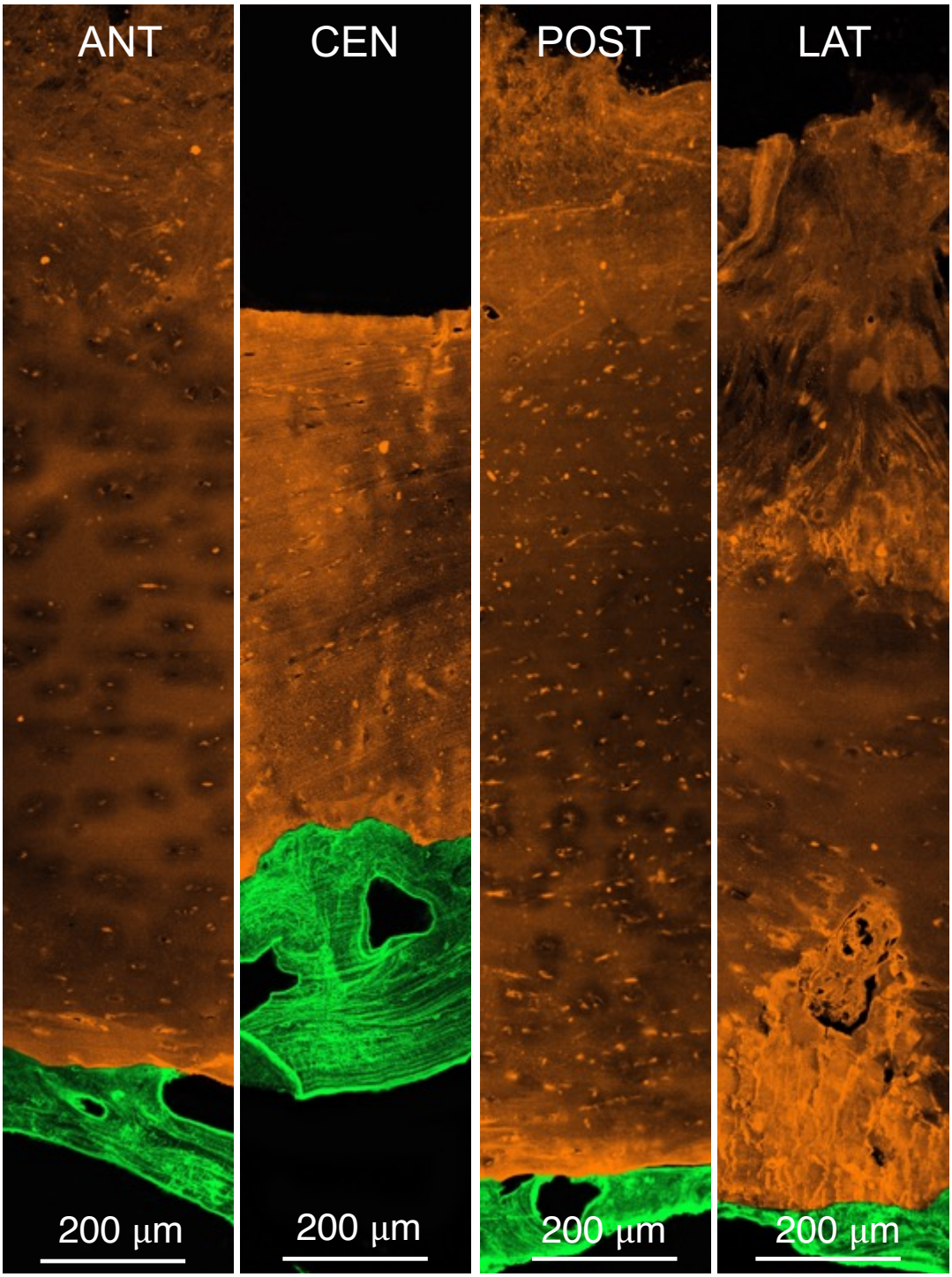

Figure 4.3.2. Representative images of the anterior (ANT), central (CEN), posterior (POST), and lateral (LAT) regions of the L4 lumbar spine vertebra (33 years). All images were taken in the sagittal plane. Positive staining is observed for type I (green) and type II (orange) collagen.

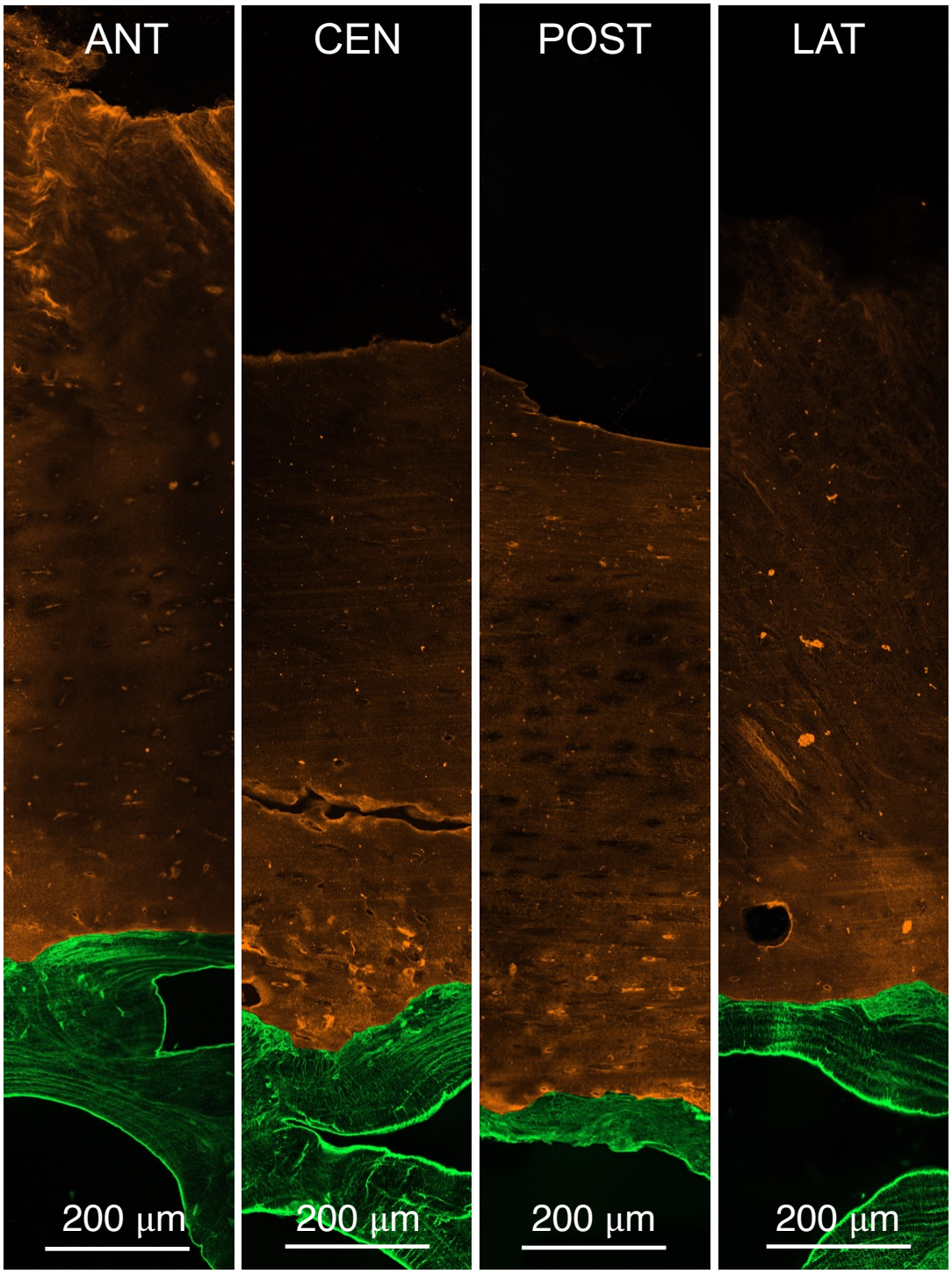

Figure 4.3.3. Representative images of the anterior (ANT), central (CEN), posterior (POST), and lateral (LAT) regions of the L4 lumbar spine vertebra (19 years). All images were taken in the sagittal plane. Positive staining is observed for type I (green) and type II (orange) collagen.

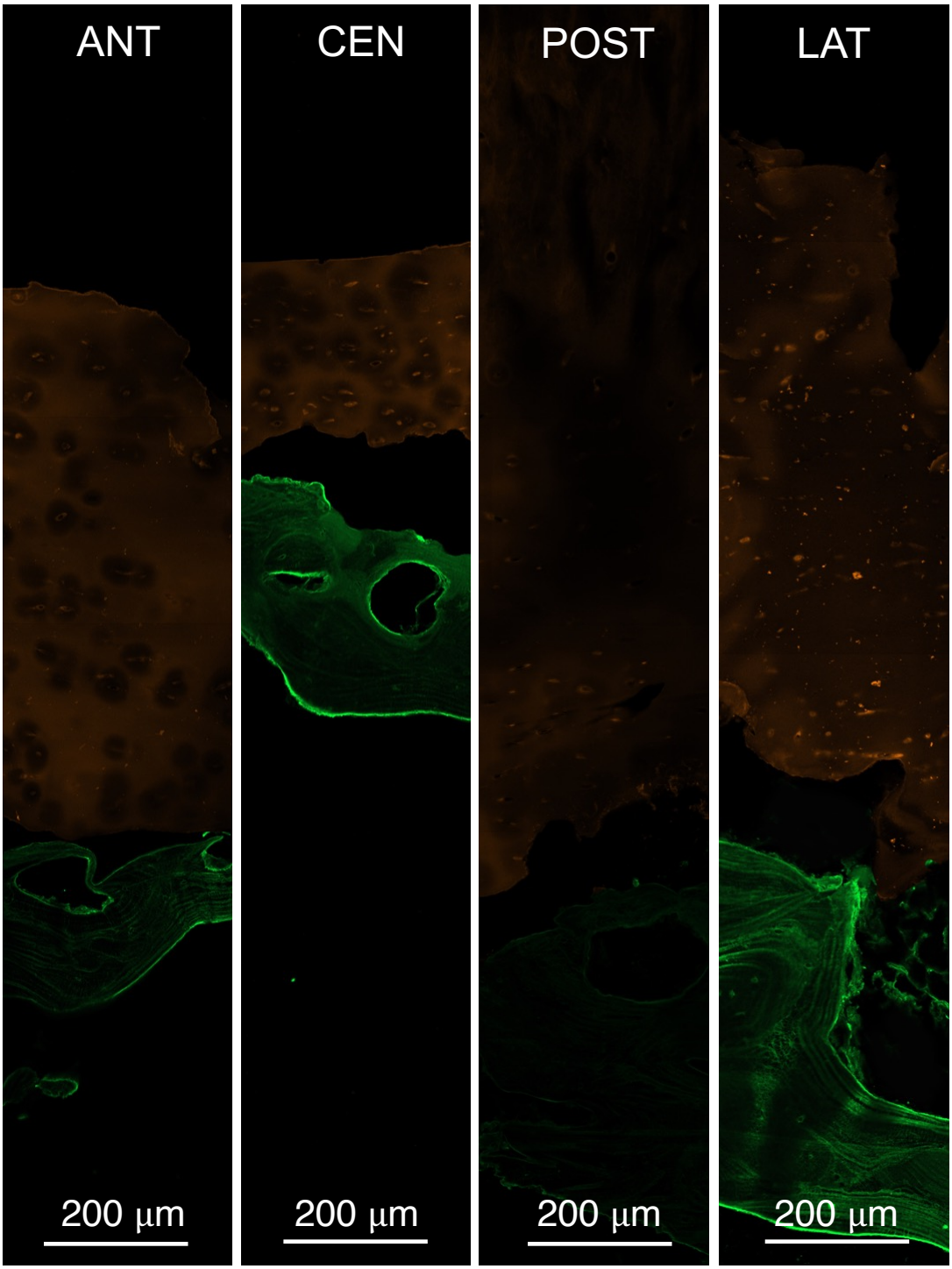

Figure 4.3.4. Representative images of the anterior (ANT), central (CEN), posterior (POST), and lateral (LAT) regions of the L4 lumbar spine vertebra (85 years). All images were taken in the sagittal plane. Positive staining is observed for type I (green) and type II (orange) collagen.

Cartilage Thickness

Average regional cartilage endplate thickness data are reported in Table 4.3.5. On average, young human lumbar CEPs had a thickness that was 0.891 mm and 0.568 mm greater than porcine cervical and aged human lumbar CEPs, respectively. The cartilage thickness of aged human lumbar CEPs was 0.430 mm greater than porcine cervical CEPs.

Void Area

Average regional void areas measured between the CEP and subchondral bone border are reported in Table 4.3.6. On average, the void area in aged human lumbar CEPs was 12861.4 μm^2 and 11700.8 μm^2 greater than porcine cervical and young human lumbar CEPs, respectively.

Table 4.3.5. The cartilage thickness for each endplate region within the human lumbar endplates (average ± standard deviation).

Region	Porcine Cervical (mm)	Human Lumbar (19 years) (mm)	Human Lumbar (33 years) (mm)	Human Lumbar (85 years) (mm)
Central	0.195 ± 0.035	0.616 ± 0.129	0.938 ± 0.414	0.298 ± 0.061
Anterior	0.250 ± 0.025	1.234 ± 0.374	1.525 ± 0.513	0.740 ± 0.096
Posterior	0.243 ± 0.041	1.131 ± 0.381	1.245 ± 0.514	0.896 ± 0.114
Lateral	0.206 ± 0.026	1.050 ± 0.355	1.181 ± 0.457	0.680 ± 0.184

Table 4.3.6. The void area for each endplate region within the human lumbar endplates (average ± standard deviation).

Region	Porcine Cervical (μm^2)	Human Lumbar (19 years) (μm^2)	Human Lumbar (33 years) (μm^2)	Human Lumbar (85 years) (μm^2)
Central	71.2 ± 36.7	167.8 ± 76.0	1263.1 ± 465.0	13543.1 ± 538.0
Anterior	23.0 ± 18.1	143.3 ± 74.6	2523.4 ± 420.6	3853.1 ± 311.6
Posterior	104.8 ± 59.1	697.4 ± 197.3	3361.0 ± 633.0	20254.9 ± 518.6
Lateral	49.1 ± 30.1	721.8 ± 150.6	902.6 ± 395.8	14042.6 ± 585.9

4.4. Discussion

This study compared the mechanical properties (loading stiffness, creep displacement), native collagen content (type I and II), existing microstructural damage (void area), and morphological characteristics (cartilage thickness) of CEPs extracted from the porcine cervical spine, young human lumbar spine, and aged human lumbar spine. On average, young human lumbar CEPs were 27% more compliant than porcine cervical CEPs, but 57% stiffer than aged human lumbar CEPs (Table 4.3.1). The observed differences in loading stiffness corresponded with inter-species differences in creep displacement. That is, endplates with a stiffer loading response exhibited less creep displacement when exposed to a 10 N indentation force (Table 4.3.2). The mechanical properties observed between species may, in part, be attributed to constitutive and structural differences. Compared to the porcine cervical spine, human lumbar CEPs had a weaker fluorescence intensity for type I (young: -24%, aged: -70%) and type II (young: -58%, aged: -88%) collagen and had a greater area of pre-existing sub-surface voids (young: +1160.5 μm^2, aged: +12861.4 μm^2). Collectively, these data support the study hypotheses and demonstrate mechanical, structural, and constitutive differences between CEPs of the porcine cervical and human lumbar spines as well as between young and aged human lumbar spines.

The differences in mechanical properties observed between species is attributed to the combined effects of native collagen content and the presence of sub-surface voids measured in this study. As demonstrated using human cadaveric articular cartilage explants (Hosseini, Veldink, Ito, & Van Donkelaar, 2013), early and advanced changes to cartilage stiffness have been attributed to sub-surface void development and altered native collagen content, although the interaction between structural and constitutive damage has not been explicitly examined. In all human species evaluated herein, substantially higher void areas (Table 4.3.6) and lower fluorescence intensities

(type I and II collagen) were measured and visually observed compared to the porcine cervical spine (Figure 4.3.1 to Figure 4.3.4). Differences in fluorescence intensity observed between young and aged human lumbar CEPs may, in part, be attributed to the age-related changes in native type II collagen content (Antoniou et al., 1996). Compared to the 15-69 year age range, total collagen content decreased by approximately 28.6% beyond 60 years (Antoniou et al., 1996), which may contribute to the greater compliance observed in aged human lumbar CEPs. A surface with a higher collagen density, like seen in porcine cervical CEPs, is arguably better suited to resist tensile forces associated with deflection compared to a surface with a lower density of collagen proteins (i.e., young human), despite being many times thicker. The effect of reduced fluorescence intensities on indentation mechanics may be further exacerbated by the presence of structural voids beneath the surface and avulsion between the cartilage and subchondral bone, as observed in aged human lumbar CEPs. Therefore, mechanical differences observed between porcine and young human species may, at the very least, in part be attributed to existing evidence of sub-surface microstructural damage and different collagen densities.

The loading stiffness of human cadaveric CEPs included in this study was less than previous *in vitro* indentation tests (Grant et al., 2001). Within the central region, Grant et al. (2001), reported a loading stiffness of approximately 98 N/mm, with marginal differences observed between L3-L5 spinal levels of aged lumbar spine specimens (mean age = 74.5). Patel et al. (2018) recorded an average loading stiffness of 61.8 N/mm, which is close to the stiffness observed in porcine cervical CEPs but substantially greater than the stiffness in young and aged human lumbar CEPs examined in this study. The differences in loading stiffness are attributed to the experimental setup for indentation testing. Grant et al. (2001) conducted indentation testing on endplate-vertebra units, where the endplate was supported by intact trabecular elements. Since similar displacements

were achieved during the loading phase of both studies (~ 0.346 mm in this study and a controlled depth of 0.3 mm in Grant et al. (2001)), the force required to reach the controlled displacement (~29.4 N in Grant et al. (2001)) would have been approximately three times the non-destructive force used in the current study. This suggests that stiffness measurements reported by Grant et al. (2001) may have resulted from the bone and cartilage interaction, whereas the focus in the current study and more broadly this thesis, was on the isolated CEP. Despite the explainable differences in loading stiffness, similar trends were observed between regions within a given CEP. Similar to the current study (Table 4.3.1), Grant et al. (2001) observed significant differences in stiffness between the central and anterior/posterior regions, but marginal differences between the central and lateral regions.

The study of overuse injury pathways necessitates tissue that is structurally and biochemically healthy in its initial state. Given the control of age, diet, and intervertebral disc health, the porcine cervical spine model is commonly used to study intervertebral disc injury and joint mechanics (Briar & Gregory, 2023; Callaghan & McGill, 2001a; Gooyers & Callaghan, 2015; Gooyers et al., 2012; Kawchuk, Decker, Dolan, & Carey, 2009; Parkinson & Callaghan, 2007a, 2007b, 2008; Yang, Xiang, Wang, & Liu, 2022; Zehr et al., 2019b). Although a perfect mechanical and structural surrogate for young and healthy human lumbar CEPs was not identified from the examined specimens, the porcine cervical model was deemed more appropriate for the study of CEP fatigue and overuse injury pathways compared to the aged human lumbar spine. This statement is largely informed by the evidence for advanced damage observed within aged human lumbar CEPs; namely, larger sub-surface void areas together with less native collagen content. The presence of pre-existing damage observed in aged human lumbar CEPs ultimately prevents the examination of injury initiation and the progression of overuse injury pathways, which was a

central component to this thesis. In contrast, the negligible sub-surface void areas observed in porcine cervical CEPs together with the similar localization of type I and type II collagen compared to young human lumbar CEPs, is suggestive of a healthy model from which injury pathways can be examined. Of course, further work is necessary to determine if the presented findings hold true across a larger sample size of young and aged human cadaveric endplates.

The application of findings presented in this study are, of course, limited by the small sample size of human cadaveric endplates. This sample size did not permit statistical comparisons between species. Second, the loading histories of all human cadaveric donors are unknown. Information about the nature of lifelong physical loading may provide additional insight into why inter-species differences were observed. Third, although collagen comprises most of the extracellular matrix, other extracellular matrix constituents (i.e., water, proteoglycans, glycosaminoglycans) were not quantified in this study. Compared to other proteins and water, collagen content was most strongly correlated with the tensile modulus of CEP tissue (Fields, Rodriguez, et al., 2013). Insight into proteoglycan content, however, may have provided additional insight into the resistance for fluid dispersion when exposed to a localized indentation stress, which may, in effect influence the loading stiffness.

4.5. Conclusions

This study demonstrated mechanical and structural differences between CEPs of the porcine cervical and human lumbar spine. Porcine cervical spine CEPs were stiffer, exhibited less creep displacement, processed a higher density of type I and type II collagen proteins, and were thinner compared to human lumbar CEPs. Young human lumbar spine CEPs, however, were mechanically and structurally different from aged human lumbar CEPs. While acknowledging the

limitations of the sample size, the consistent and healthy initial conditions of porcine cervical CEPs have advantages over aged human lumbar CEPs for the study of overuse injury pathways.

CHAPTER 5

Cyclic Loading History Alters the Joint Compression Tolerance and Regional Indentation Responses in the Cartilaginous Endplate

Jackie D. Zehr, Jeff M. Barrett, Jack P. Callaghan

Journal of the Mechanical Behavior of Biomedical Materials, 136; 105542, 2022

Abstract

Objectives: This study quantified the effect of subthreshold loading histories that differed by joint posture (neutral, flexed), peak loading variation (10%, 20%, 40%), and loading duration (1000, 3000, 5000 cycles) on the post-loading ultimate compressive tolerance (UCT), yield force, and regional indentation responses (loading stiffness and creep displacement) in the cartilaginous endplate.

Methods: One hundred and fourteen porcine spinal units were included. Following conditioning and cyclic compression exposures, spinal units were transected and one endplate from each vertebra underwent subsequent UCT or microindentation testing. UCT testing was conducted by compressing a single vertebra at a rate of 3 kN/s using an indenter fabricated to a representative intervertebral disc size and shape. Force and actuator position were sampled at 100 Hz. Non-destructive uniaxial CEP indentation was performed at five surface locations (central, anterior, posterior, right, left) using a serial robot and aluminum indenter (3 mm hemisphere). Force and end-effector position were sampled at 10 Hz.

Results: A significant three-way interaction was observed for UCT ($p = 0.038$). Compared to neutral, the UCT was, on average, 1.9 kN less following each flexed loading duration. No effect

of variation was observed in flexion; however, 40% variation caused the UCT to decrease by an average of 2.13 kN and 2.06 kN following 3000 and 5000 cycles, respectively. The indentation stiffness in the central CEP mimicked the UCT response.

Conclusions: These results demonstrate a profound effect of posture on post-loading UCT and CEP behaviour. Control of peak compression exposures became particularly relevant only when a neutral posture was maintained and beyond the midpoint of the predicated lifespan.

5.1. Introduction

Approximately 50% of low back injuries are attributed to lifting in occupational (Dropkin et al., 2015; Frost et al., 2015; Hauret et al., 2010) and sport/exercise (Frost et al., 2015; Klimek et al., 2018; Weisenthal et al., 2014) contexts. Of these confirmed cases, the alleged cause of injury was the performance of lifting tasks described to have been "heavy" and/or "high demand" (Hauret et al., 2010; Jennings et al., 2008; Nye et al., 2016). Indeed, the average peak joint compression forces measured during high demand lifting tasks (4.5-6 kN) (T. A. C. Beach et al., 2019; Gooyers et al., 2018; Marras et al., 2009; Prairie et al., 2016) are substantially greater than habitual (Zehr, Carnegie, et al., 2020; Zehr et al., 2018) and recommended (NIOSH, 1981) exposures (< 3.4 kN). However, they do not exceed existing estimates of ultimate compression tolerance (UCT) that, on average, range between 10 kN and 10.5 kN (Gunning et al., 2001; Jager & Luttmann, 1989; Porter & Adams, 1989). The comparison of modelled joint compression estimates with existing UCT data highlights a knowledge gap in the understanding of overuse injury mechanisms and risk evaluation. That is, how factors of the loading history interact to instantaneously alter tissue properties and ultimately reduce joint tolerance over time remains unknown.

Fundamentally, overuse injuries to low back tissues are caused by physiological changes to the structural properties that occur in response to applied loads. Existing estimates of UCT were obtained from destructive testing performed on human lumbar cadaveric (Adams & Hutton, 1982; Biggemann et al., 1988; Brinckmann et al., 1989; Hutton & Adams, 1982) or porcine cervical (Gunning et al., 2001) spinal joints. While factors like sex, posture, bone mineral density, and hydration have been collectively considered, the estimates obtained from these studies are limited to a single time point, typically when the joint is in a healthy and/or unloaded state. Alternatively, UCT estimates have been derived with predictive equations based on geometric (Parkinson et al.,

2005) and personal factors (Genaidy et al., 1993). A similar limitation exists with predictive estimates wherein factors related to the loading history are omitted.

A lifetime physical loading history described as moderate or heavy was further highlighted as a prominent risk factor for injury to specific spine tissues; namely the cartilaginous endplate (CEP) (Videman et al., 1990). The mechanical and poroelastic response of the CEP to compression load is particularly relevant to joint health. When spinal joints are exposed to compression force, the vertical deflection aids in the transmission of force between vertebra and offloads inner concentric layers of the annulus fibrosis (Bogduk, 2012; S. H. M. Brown et al., 2008). Secondly, loading parameters and cumulative damage to the CEP has significant implications on the surface permeability and thus the transport of nutrients and waste by-products in and out of the intervertebral disc (Giers et al., 2017; Rodriguez et al., 2011). The effect of loading exposures on the ability for fluid to flow through the CEP has implications for the onset and progression of degenerative processes in the intervertebral disc (Lotz et al., 2013). Despite these data demonstrating the functional importance of the CEP, the effect of cyclic loading on its mechanical behaviour throughout the joint lifespan remains less clear. The documented effects of posture (Callaghan & McGill, 2001a; Gooyers & Callaghan, 2015; Gooyers et al., 2012), peak loading variation (Zehr et al., 2019b), and loading duration (Gooyers & Callaghan, 2015) on the CEP lifespan and vertebral joint mechanics particularly motivated the investigation of these factors as modulators of tissue and joint behaviour.

This study examined the effect of posture, loading variability, and loading duration on the ultimate and yield forces obtained from post-loading destructive testing. Regional differences in the post-loading properties (i.e., loading stiffness, creep displacement) of the isolated CEP were also examined using a microindentation test.

Five specific hypotheses were made. First, in previous studies, flexed postures have significantly reduced the joint lifespan during subthreshold cyclic loading tests (Callaghan & McGill, 2001a; Gooyers & Callaghan, 2015; Gooyers et al., 2012). Therefore, ultimate compression tolerance and yield force were hypothesized to decrease when cyclically loaded in flexed postures compared to neutral at each loading duration. Second, compared to 0% variation, a loading variation of at least 30% reduced the joint lifespan (Zehr et al., 2019b) and significantly increased the failure probability beyond 2600 cycles (Zehr et al., 2019a). Therefore, it was hypothesized that a high loading variation (i.e., 40%) would significantly reduce the ultimate compression tolerance and yield force beyond 3000 consecutive loading cycles. Third, in alignment with previous research on spinal joint fatigue (Gooyers et al., 2015), the ultimate compression tolerance and yield force were hypothesized to decrease as a function of loading duration. Fourth, the central CEP region experiences the greatest deflection in response to joint compression loading (Malandrino et al., 2009). Therefore, the loading stiffness and creep displacement in the central region were expected to mimic the ultimate compression results; flexed postures were hypothesized to reduce loading stiffness and increase creep displacement at each loading duration and a high variation (i.e., 40%) was hypothesized to reduce indentation stiffness and increase creep displacement beyond 3000 cycles. Fifth, in consideration of evidence suggesting that compressive stress becomes more peripherally distributed as a function of loading duration (van Dieën, Kingma, et al., 2001) and the prevalence of fatigue fractures in posterior and lateral CEP regions (Chapter 3.2), significant reductions in indentation stiffness and creep displacement were expected in the lateral and posterior regions following 5000 cycles.

5.2. Methods

Overview

This study exposed porcine cervical spine FSUs to sub-threshold cyclic compression loading paradigms that differed by sagittal plane posture, variation in peak compression magnitudes, and loading duration. Following the conditioning loads, each FSU was transected. One CEP was assigned to microindentation testing and the other CEP was assigned to ultimate compression testing. Ultimate compression and yield forces were quantified and the regional differences in stiffness and creep displacement were examined. Collectively, these data demonstrated the initiation and time-course of mechanical changes to the spinal joint and the isolated CEP. The general procedural steps are outlined in Figure 5.2.1.

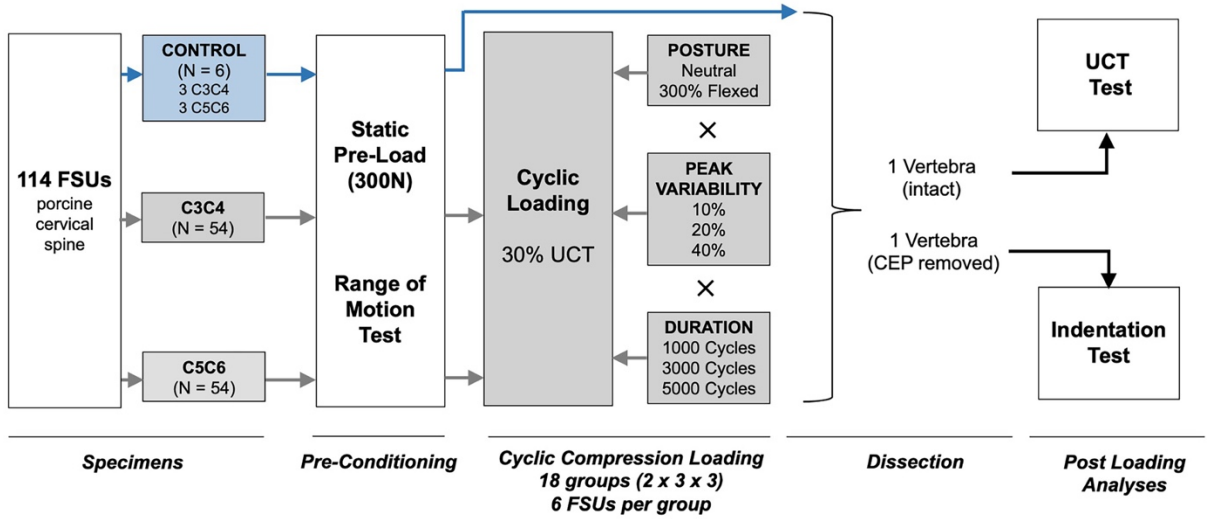

Figure 5.2.1. A flow chart of the experimental procedure. All FSUs (i.e., control and experimental) underwent the procedural steps identified with a white background. Boxes and arrows identified with a grey and blue background represented specific procedural steps completed by the experimental and control groups, respectively.

Specimen Preparation

This study used porcine cervical spine FSUs as a surrogate for the human cadaveric lumbar spine. Similarities in morphology (Yingling et al., 1999), as well as trabecular architecture and strength have been documented (Busscher et al., 2010). The porcine animal model further enabled control of age (Genaidy et al., 1993), loading history (Gunning et al., 2001), and intervertebral disc health (Hansson et al., 1987) on compression strength and fatigue lifespan.

One hundred and fourteen fresh-frozen porcine cervical FSUs were included in this study. All acquired specimens were stored at a temperature of -20°C and thawed for a minimum of 12 hours prior to preparation and testing. Following the removal of surrounding muscle and adipose tissue, the C3C4 and C5C6 FSUs were excised with each spinal unit containing two vertebrae, the intervertebral disc, and all joint spanning spinal ligaments. The quality of all exposed intervertebral discs was assessed for visual signs of degeneration and only grade 1 specimens were included for testing (Galante, 1967). Grade 1 was defined as having an annulus without visual evidence for radial fissures and a white gelatinous nucleus pulposus (Galante, 1967). This evaluation for degeneration and tissue damage ensured that all FSUs were in an initially healthy and non-degenerated state prior to applying the conditioning loading exposures.

A digital caliper was used to obtain width (W) and depth (D) measures of the exposed cranial and caudal endplates of each joint. These measurements were used to determine the endplate surface areas ($\pi/4 \times W \times D$), which were then averaged to approximate the endplate area of the joint. The average endplate area was used to estimate the FSUs ultimate compression tolerance using a validated regression equation (Parkinson et al., 2005) from which the normalized peak compression forces could be determined for cyclic loading tests. The exposed endplates of the cranial and caudal vertebrae were secured to the centre of machined aluminum cups using 19-

guage steel wire and each cup was filled with dental plaster (Dentstone, Southbend, IN) and allowed to harden.

The aluminum cup fastened to the cranial vertebra was bolted to the flexion-extension rotation carriage. This rotation carriage was positioned in series with the compression actuator (20 kN load cell capacity) of a materials testing frame (Model 8872, Instron, Toronto, ON) and was actuated by a torque motor (T120-106-1K, Sensor Data Technologies, Sterling Heights, MI). This setup enabled the simultaneous application of compression force together with rotation of the FSU about its flexion-extension axis. The aluminum cup of the caudal vertebra was secured to an unconstrained aluminum base that overlaid an oiled bearing covered surface (Zehr & Callaghan, 2022). A schematic of the *in vitro* testing setup is depicted in Figure 5.2.2.

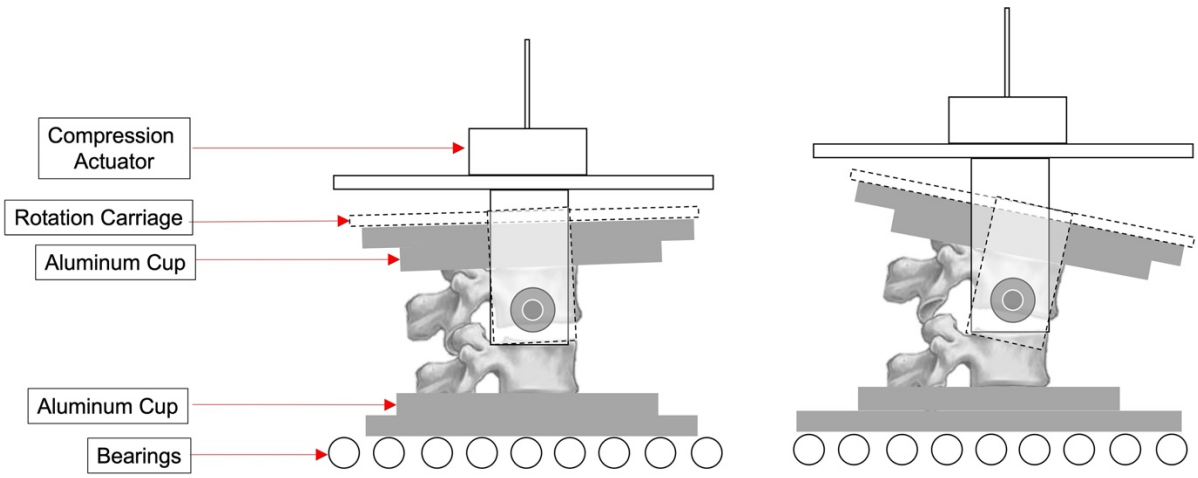

Figure 5.2.2. A schematic of the in vitro testing system for the application of compression force to neutral (left) and flexed (right) spinal joints.

Pre-Conditioning

To prevent dehydration, specimens were wrapped with saline soaked plastic-backed gauze and received additional superficial moistening every 20 minutes throughout the duration of pre-

conditioning and cyclic loading exposures. First, a static 0.3 kN compression load was applied for 15-minutes to normalize the intervertebral disc water distribution. Following this preload, a flexion-extension range-of-motion test was performed to identify the mechanical neutral zone from the obtained moment-angle relationship. The range-of-motion test was performed by rotating the FSU into flexion and then into extension at a rate of 0.5 degrees/second until a ±6 Nm moment was achieved for a total of four consecutive repetitions. Throughout this test, the FSU was simultaneously exposed to a static 0.3 kN compression force. The moment and angular deviation from the point of elastic equilibrium were continuously sampled at a rate of 8 Hz using a 16-bit analog-to-digital conversion system and custom control software (Galil Motion Control, Rocklin, CA). From the moment-angle time-series data, the neutral zone limits were determined as the linear boundaries of a fourth-order polynomial curve fit of the final two repetitions (Thompson et al., 2003). The identified neutral zone boundaries were used to mechanically normalize the postures across specimens. Effectively, the employed method for identifying the mechanical neutral zone is similar to how the neutral zone is defined in the human lumbar spine (Panjabi, 1992).

Cyclic Compression Loading

A 3 x 3 x 2 experimental design was used for the application of cyclic compression loading. FSUs were randomly assigned to one of eighteen experimental groups that differed by posture (neutral, flexed), loading duration (1000, 3000, 5000 continuous cycles), and variation of peak compression force about a normalized mean of 30% UCT (10%, 20%, 40%), with a total of six FSUs per group. This sample size was deemed sufficient based on the results of a post hoc power analyses (power ≥ 0.795). A control group (N = 6; 3C3C4, 3C5C6) was exposed to the pre-conditioning tests (i.e., static preload and range-of-motion tests) which were immediately followed

by dissection, microindentation, and UCT testing. No cyclic loading was applied to the control group (Figure 5.2.1). The rationale for each experimental factor and the associated levels are described below:

- Posture: Neutral was defined as the average mid-point between the flexion and extension limits of the neutral zone. Flexed was calculated as three times the difference between the neutral posture and the linear flexion limit (Gooyers & Callaghan, 2015; Gooyers et al., 2015). This posture corresponds to 300% of the flexion neutral zone and although considered extreme, it is within the physiological range and is not destructive to ligamentous tissue. The range of joint deviation from neutral to 300% of the flexion neutral zone ranged was 7.74 to 11.97 degrees in this study.
- Loading Duration: A maximum cyclic loading duration of 5000 cycles was selected based on destructive fatigue testing (Zehr, Buchman-Pearle, et al., 2020). As discussed in Section 3.2.5, 5000 cycles approximated 94% of the joint fatigue lifespan for the normalized 30% compression force. That is, 4964.1 cycles was multiplied by a weighting factor of 1.07 to yield a predicted lifespan of 5311 cycles. Therefore, a loading duration of 5000 cycles permitted the analysis of how mechanical joint and tissue properties changed at an exposure that was close the predicted failure point without exceeding it. A loading duration of 1000 cycles has been previously used to approximate the exposure of a single, one-hour repeated exertion (Hansson et al., 1987), and a duration of 3000 cycles was the mid-point of these durations.
- Loading Variation: The magnitude of peak compression variation was selected to cover the range of peak compression variation documented during the performance of a moderately constrained *in vivo* repetitive lifting task (10-40%) (van Dieën, Dekkers, et al., 2001) and prior

experimentation on the incorporation of loading variation into *in vitro* injury analyses (0% and 30%) (Zehr et al., 2019b).

Time-varying biofidelic signals from laboratory-simulated repetitive lifting tasks were appropriately scaled and used for cyclic testing. Compression force-time signals were previously quantified using an electromyographic-assisted musculoskeletal model of the lumbar spine (Granata & Marras, 1995) and represent the joint contact forces experienced by the L4-L5 spinal joint. A total of three cyclic compression waveforms were constructed (Figure 5.2.3). All compression cycles had a loading frequency of 1 Hz (Zehr, Buchman-Pearle, et al., 2020) and an average peak compression that was normalized to 30% of the initial predicted ultimate compression tolerance (i.e., determined from endplate area). This normalized magnitude approximates the average internal joint loading during repeated lifting associated with habitual physical demand (Alessa & Ning, 2018; Callaghan & McGill, 2001b; Callaghan, Patla, & McGill, 1999; Gooyers et al., 2018) and is considered to be a safe occupational loading exposure by virtue of the NIOSH action limit (3.4 kN) (NIOSH, 1981). Furthermore, highly variable loading cycles (i.e., +40% variation = 4.37 kN) only nudge the internal loading range associated with high demand, injury appended tasks (i.e., high load, high speed) (T. A. C. Beach et al., 2019; Gooyers et al., 2018; Marras et al., 2009; Prairie et al., 2016).

As demonstrated in Figure 5.2.3 and Table 5.2.1, the cumulative load between all conditioning waveforms was similar and, in fact, equalized after each five-cycle loading block. The equalization of cumulative dose following each five cycle block compared to a single equalization (i.e., after 30 cycles only) (Zehr et al., 2019b) resulted in less additive differences between signals on a cycle-by-cycle basis (Figure 5.2.3). Each 40-cycle loading block was repeated until the examined loading durations (1000, 3000, 5000 cycles) were reached. That is,

each waveform was repeated 25, 75, and 125 times for the 1000, 3000, and 5000-cycle loading durations, respectively. Lastly, a bias compression load of 0.3 kN was incorporated into all conditioning loads to represent the equivalent baseline compression associated with maintaining the mass of the human trunk in an upright posture.

Compression waveforms were applied to intact FSUs using the materials testing system that was operated in load control (Software: Instron SAX, Version 7.1). Appropriate tuning of the materials testing was conducted on a representative specimen to ensure target loads were achieved. The average and peak compression forces for all experimental groups are reported in Table 5.2.2. Throughout the assigned cyclic loading protocol, the applied compression force and vertical position of the actuator were sampled at a rate of 100 Hz.

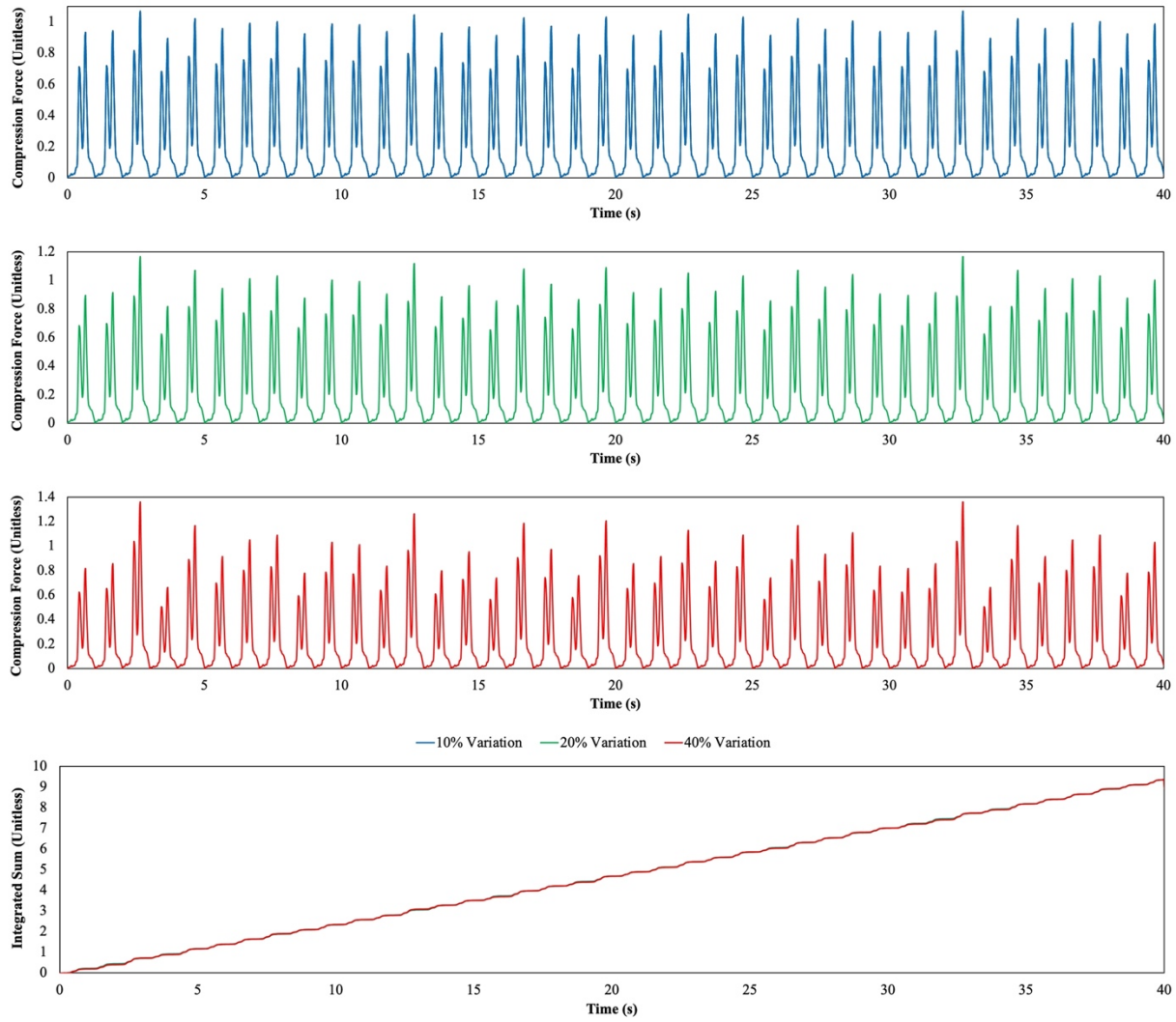

Figure 5.2.3. Relative cyclic compression waveforms for a 10% (blue), 20% (green), and 40% (red) variation in peak compression force. The similarity in inter-cycle cumulative load (force – time integral) is demonstrated by the integrated sum of all three waveforms plotted as a function of time (bottom). A bias load of 300 N was incorporated when waveforms were scaled to 30% of the predicted UCT.

Table 5.2.1. Equalization of the integrated sum of all biofidelic waveforms at eight instances in time. All values are unitless.

Cycles	10%	20%	40%
5	1.17	1.17	1.17
10	2.34	2.34	2.34
15	3.51	3.51	3.51
20	4.68	4.68	4.68
25	5.85	5.85	5.85
30	7.01	7.01	7.01
35	8.18	8.18	8.18
40	8.94	8.94	8.94

Table 5.2.2. Summary statistics for parameters of the cyclic compression tests. No significant differences were observed between groups for mean compression ($p > 0.05$). Within variation groups, no significant differences were observed for maximum compression ($p > 0.05$).

Conditioning Load (kN)	Flexed									Neutral								
	1000			3000			5000			1000			3000			5000		
	10%	20%	40%	10%	20%	40%	10%	20%	40%	10%	20%	40%	10%	20%	40%	10%	20%	40%
Mean Compression	3.225	3.126	3.267	3.265	3.448	3.167	3.043	3.223	3.293	3.122	3.365	3.348	3.245	3.358	3.395	3.175	3.215	3.468
Mean Compression SD	0.234	0.183	0.328	0.337	0.361	0.234	0.195	0.172	0.200	0.432	0.183	0.334	0.304	0.224	0.195	0.321	0.191	0.109
Maximum Compression	3.248	3.453	4.277	3.290	3.837	4.135	3.048	3.565	4.140	3.135	3.736	4.385	3.268	3.731	4.450	3.187	3.562	4.555
Maximum Compression SD	0.256	0.217	0.457	0.373	0.437	0.327	0.217	0.207	0.456	0.476	0.219	0.469	0.334	0.269	0.272	0.353	0.228	0.154

Dissection

Following the cyclic compression testing, endplates that interface with the intervening IVD were randomly assigned to undergo microindentation testing or destructive ultimate strength testing (Figure 5.2.4). The randomization process was controlled such that an equal number of cranial and caudal endplates were appointed to all experimental groups. Post-loading dissection was performed while the FSU was potted and included a transverse incision through the intervertebral disc and posterior spinal ligaments together with bilateral derangement of the facet joints to separate the cranial and caudal vertebra. Once transected, visual inspections for macroscopic injury were performed, which included inspection for intervertebral disc fissures, the presence of a gelatinous nucleus pulpous, endplate fracture, and facet fracture. A single endplate fracture was observed, and this specimen was omitted from the UCT, microindentation, and statistical analyses. The vertebra assigned to ultimate testing remained secured to its aluminum cup and nucleus pulposus was carefully removed while ensuring that the annulus fibrosis remained intact. The vertebra assigned to microindentation testing was removed from its potting fixation and ruminants of the annulus fibrosis and nucleus pulposus were debrided from the endplate. The cartilage endplate was then removed from the vertebral body at the epiphyseal plate.

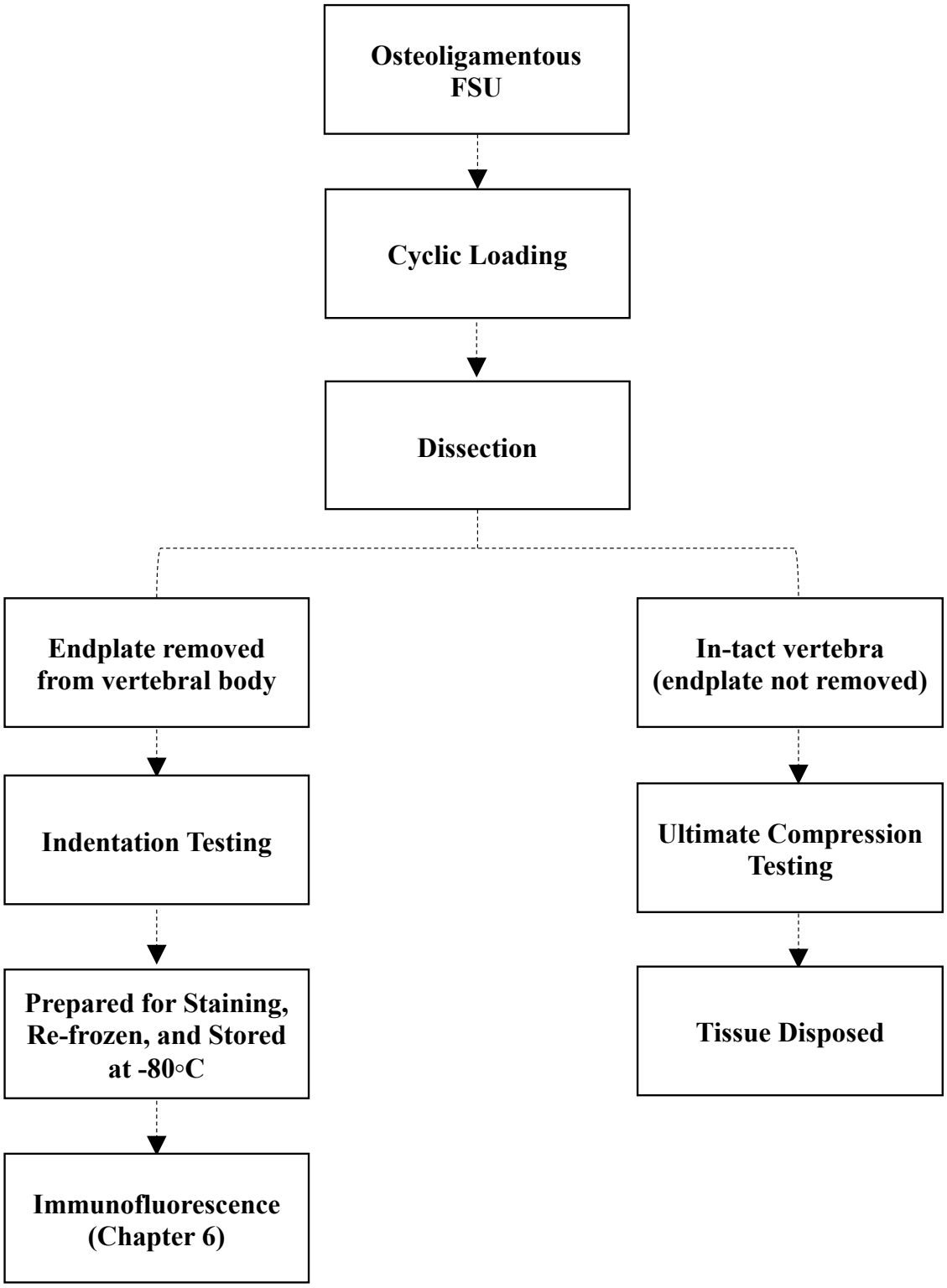

Figure 5.2.4. A flow chart depicting the testing protocols performed on each endplate following cyclic compression testing.

Microindentation Testing

A total of five endplate surface sites were marked and tested under uniaxial indentation. The Cartesian location of the tested surface sites included the midpoint of the size-normalized central, anterior, left lateral, posterior, and right lateral regions (Figure 5.2.5). The dimensions of the employed mapping approach closely followed methods developed by Grant et al. (2001) and implemented by Patel et al. (2018) and Noshchenko et al. (2013). A custom-built testing apparatus was constructed wherein the CEP was rigidly secured to machined aluminum stanchions (tissue interfacing diameter of 2mm) using perforating screws at each corner of the size-normalized surface (Figure 5.2.6). Magnets (20 lbs total pull force) were custom machined and attached to the base of each stanchion to prevent tipping and/or translation on the height-adjustable carbon steel base.

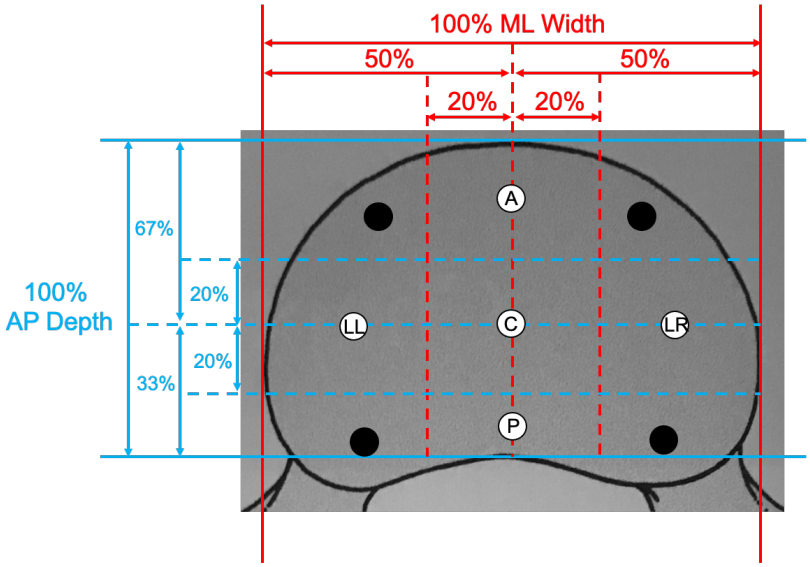

Figure 5.2.5. A map of the indentation sites across the endplate surface area. Indentation sites were defined based on relative percentages of vertebral endplate dimensions. A = anterior; C = central; LR = right lateral; P = posterior; LL = left lateral. Black circles indicate the location of perforating M2 screws.

Indentation testing was performed with a serial robot (Displacement Resolution = 0.001 mm, Yaskawa Motoman, Miamisburg, OH, USA) that was equipped with a load cell secured to the end-effector (Force Resolution (Z-axis) = 0.01 N, 110516-2, ATI Industrial Automation, Apex, NC, USA) and a custom machined aluminum indenter (3 mm hemisphere) attached in series (Figure 5.2.6). A trapezoidal waveform was applied at each surface location using custom multi-mode control (Patel et al., 2018): i) the endplate surface was indented at a rate of 0.1 mm/s until a 10 N load was achieved; ii) the 10 N load was maintained for 30 seconds; iii) the endplate surface was unloaded at a rate of 0.1 mm/s (Figure 5.2.7). In block randomized order, this protocol was performed three times at each regional site with a 30-second unloading phase between each trial. Throughout each test, the force and vertical position of the end-effector were sampled at a rate of 10 Hz (Figure 5.2.7).

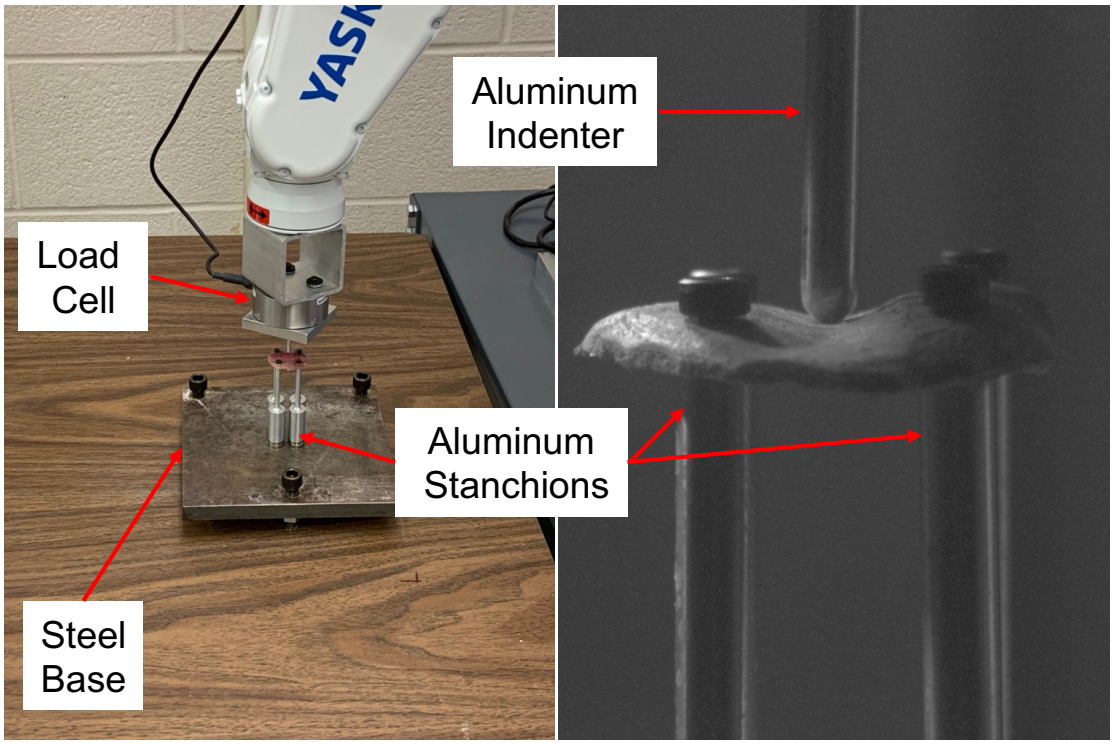

Figure 5.2.6. Experimental setup for the post-loading microindentation test.

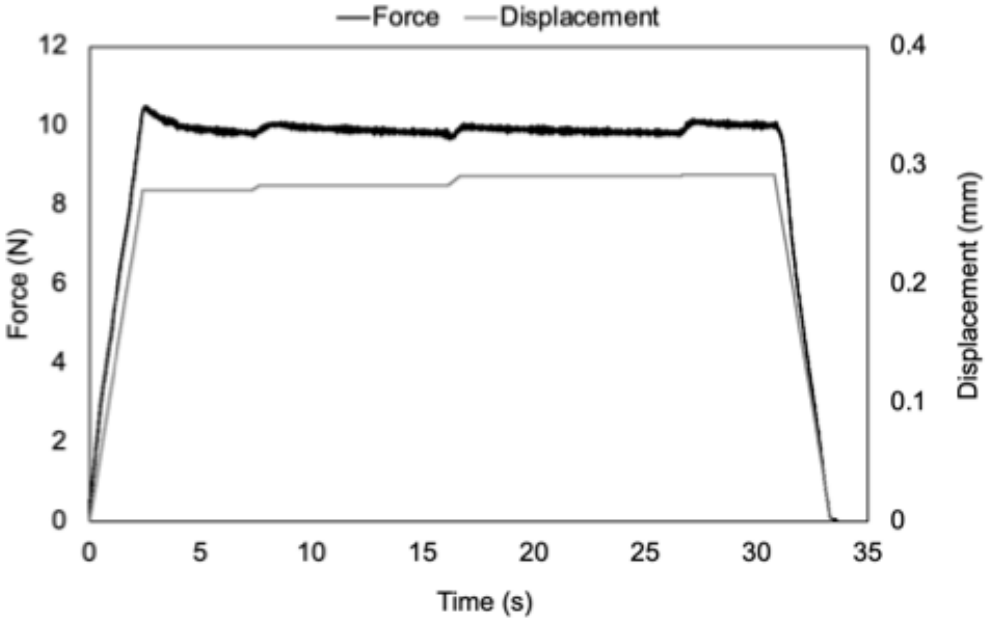

Figure 5.2.7. Representative force- and displacement-time data collected during each indentation trial. Loading and unloading phases were performed in position control (0.1 mm/s) and the 10 N force was maintained.

The loading stiffness and creep displacement were determined from the resulting force-displacement curves. Loading stiffness was derived from the linear region of the loading phase and creep displacement was determined as the change in position during the 30-second holding phase. Following the indentation procedure, the CEP was cut into independent regions and the thickness was measured using a digital caliper. The regional thickness was similar between groups (Table 5.2.3) and the observed tapering in thickness from the structural perimeter to the central region aligns with previous morphological analyses (Berg-Johansen, Han, et al., 2018; Hou & Luo, 2009).

Table 5.2.3. Regional endplate thickness for control and experimental specimens. No significant main effect or interactions were observed ($p > 0.05$).

Endplate Region	Control		Experimental	
	Mean (mm)	SD (mm)	Mean (mm)	SD (mm)
Central	1.54	0.54	1.54	0.25
Anterior	2.81	0.49	2.86	0.42
Posterior	2.77	0.41	2.76	0.50
Right	2.44	0.22	2.44	0.38
Left	2.43	0.24	2.44	0.39

Ultimate Compression Strength Testing

Since the vertebrae comprising the FSU were separated, a carbon steel indenter was fabricated to represent the size and shape of the annulus fibrosis and nucleus pulposus (Figure 5.2.8). The indenter had a 40 mm width and 30 mm depth. The inner spherical eclipse had a width of 17 mm and a depth of 10 mm. These dimensions were selected based on the average anterior-posterior (10.05 mm ± 1.45) and medial-lateral (17.08 mm ± 1.97) measurements of the inner annulus borders taken from a subset of eight FSUs that were included in a separate study sample (Zehr & Callaghan, 2022).

Testing was conducted to compare the mechanical response observed during UCT performed on three intact C3C4 FSUs and on three isolated C4 vertebrae in conjunction with the fabricated indenter (Figure 5.2.9). Mechanical parameters of each specimen are reported in Table 5.2.4. The average yield forces of 4.97 kN (FSU) and 5.62 kN (IND) were within the 4.27 kN to 5.92 kN yield point range reported by Gunning et al. (2001) for similarly hydrated FSU specimens. The average compression forces (FSU = 9.86 kN; IND = 9.33 kN) observed at ultimate failure were also within the previously reported ultimate strength ranges for hydrated FSUs (9.23 kN – 10.62 kN) (Gunning et al., 2001). From this analysis, the fabricated indenter was deemed to simulate an acceptable and physiological mechanical response to UCT testing compared to an intact porcine cervical FSU.

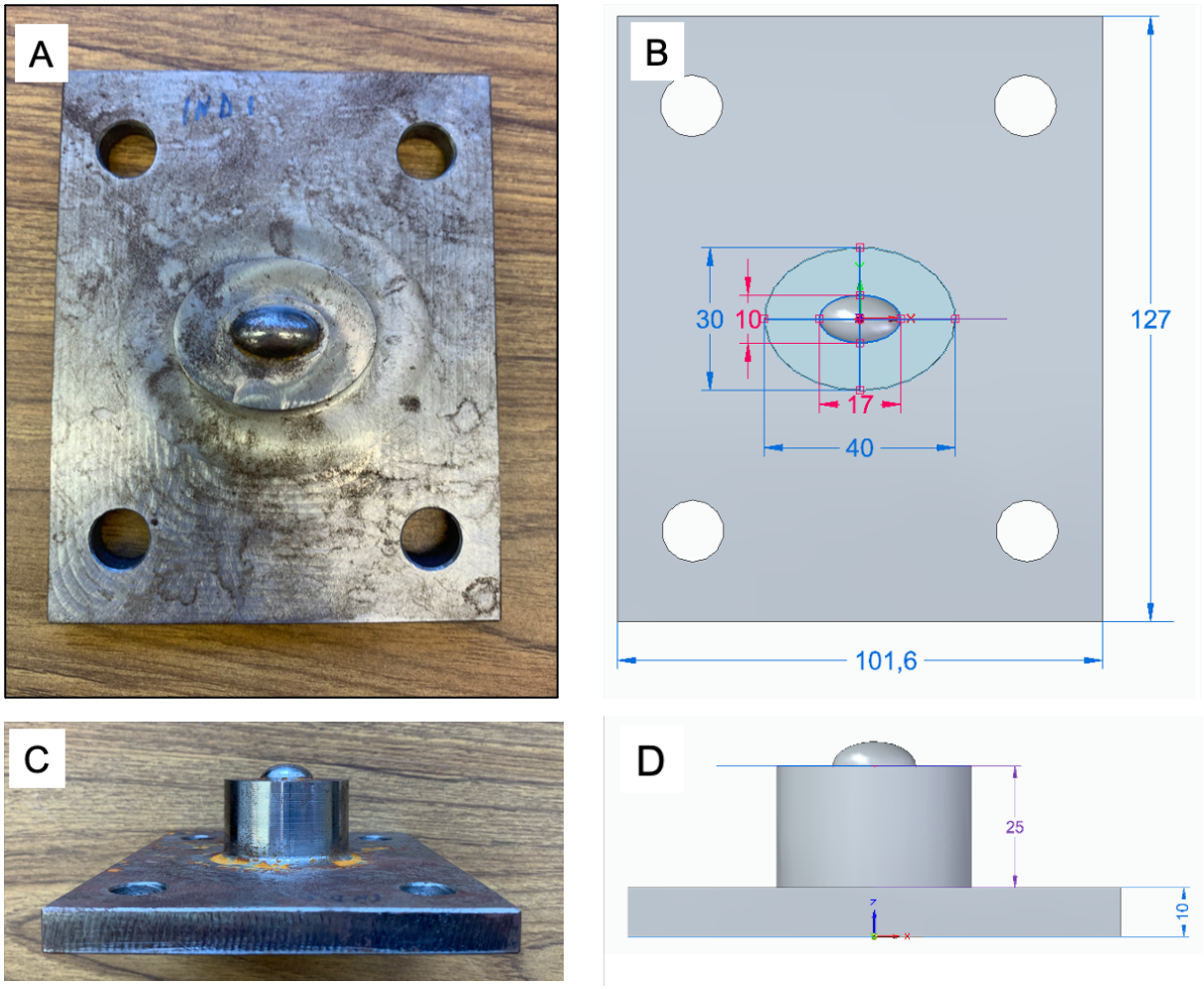

Figure 5.2.8. The fabricated indenter used for UCT testing. A) Superior view; B) Superior view dimensions (mm); C) Side view; D) Side view dimensions (mm).

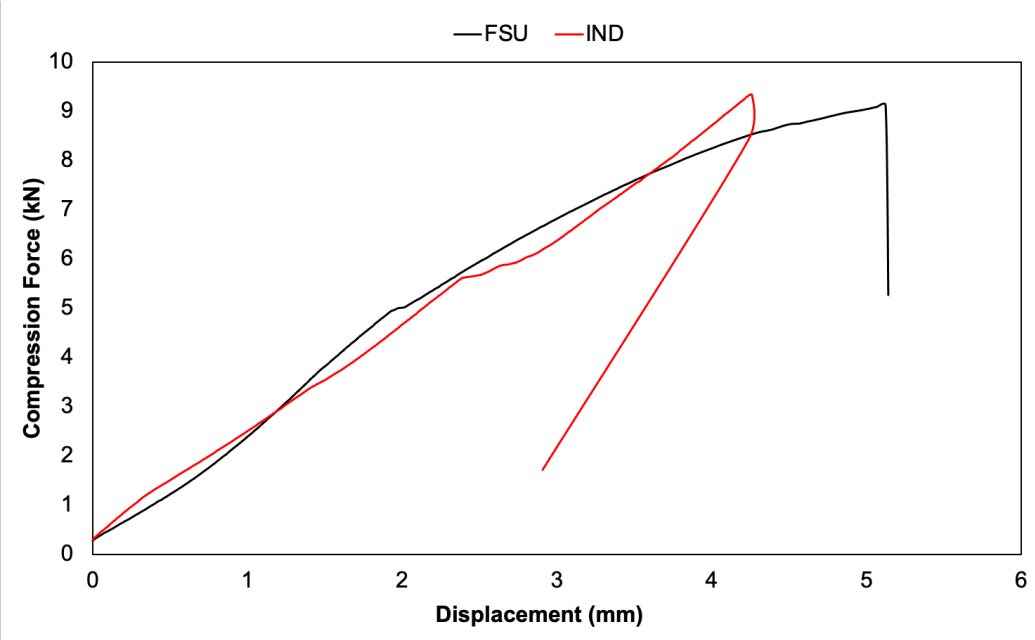

Figure 5.2.9. Representative force-displacement curves for ultimate compression strength testing performed on intact FSUs and on an isolated vertebrae interfaced with an indenter (IND).

Table 5.2.4. The average (standard deviation) mechanical loading parameters for UCT testing performed on intact FSUs and on an isolated vertebrae interfaced with an indenter (IND).

Loading Parameter	FSU	IND
Stiffness (kN/mm)	2.41 (1.33)	2.23 (0.99)
Yield Force (kN)	4.97 (0.83)	5.62 (0.41)
Ultimate Failure Force (kN)	9.86 (1.03)	9.33 (1.11)

The indenter was bolted to the flexion-extension rotation carriage, which was rotated until a zero-degree angle with respect to a global vertical axis was achieved. This alignment of the rotation carriage created a perpendicular interface between the endplate surface and the indenter (Figure 5.2.10). The vertebra was loaded in compression at a rate of 3000 N/s until ultimate failure was observed (Gunning et al., 2001). The vertical position and axial force were sampled at 100 Hz. For all UCT testing, the point of yield was determined by a 5% reduction in compression stiffness (Brinckmann et al., 1989; Gunning et al., 2001) and ultimate failure was objectively

determined by a 3.25% drop in the force signal within a 50 ms window and/or a visually apparent step in the force-displacement curve (Gunning et al., 2001).

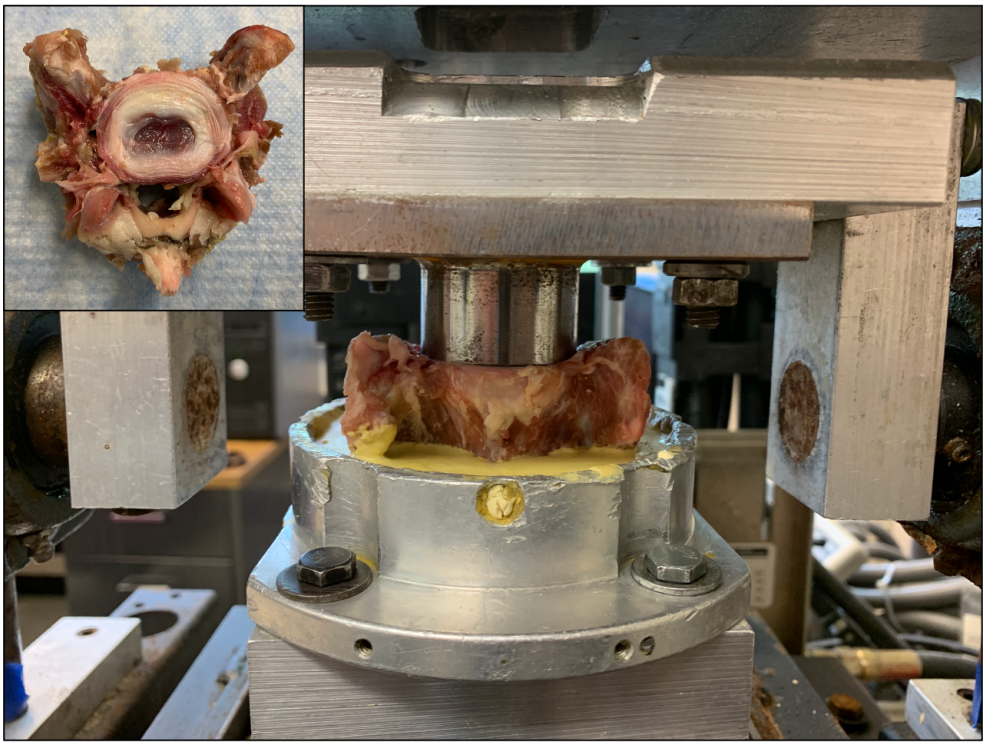

Figure 5.2.10. An anterior view of the indenter-vertebra interface. The inner spherical eclipse of the indenter was aligned with the space previously occupied by the nucleus pulposus.

Statistics

Assumptions of parametric tests (i.e., normality and homogeneity of variance) were evaluated and confirmed. First, randomization of specimens was assessed via endplate area using an analysis of variance test (ANOVA) with between-group factors for level, posture, loading duration, and loading variation. Separate three-way ANOVA tests were performed with between-group factors for posture, loading duration, and loading variation for the evaluation of UCT, yield force, regional indentation stiffness, and creep displacement. Regional comparisons within a specimen were not compared in this study. Where applicable, Tukey's *post hoc* test was performed

with Bonferroni corrections. These statistical procedures were conducted using R statistical programming language (RStudio Version 3.34, Rstudio Inc, Boston, MA).

5.3. Results

Randomization

Effective randomization of specimens was evidenced by the observation of no significant differences for endplate area ($p \geq 0.086$). Since endplate area was used to predict the initial UCT and normalized applied compression forces, this finding confirms that any differences in post loading UCT are unlikely to result from between group differences in initial UCT. No significant main effects or interactions were found for spinal level ($p \geq 0.127$). Therefore, all dependent measures were collapsed across spinal levels.

Ultimate Compression Tolerance

A significant duration × variation × posture interaction effect was observed for UCT ($p = 0.038$). The average UCT of each experimental group exposed to cyclic loading in a flexed posture was significantly less than the control group (10.81 kN ± 0.69). The average UCT significantly changed as a function of duration, with the average decreasing to 9.06 kN ± 0.89, 6.61 kN ± 0.61, and 5.16 kN ± 0.63 after 1000, 3000, and 5000 cycles, respectively. Within each loading duration, the UCT did not significantly differ between variation groups.

When cyclic loading was applied to neutrally positioned joints, the following loading conditions resulted in a mean UCT that was significantly less than the control group: 20% 3000 cycles, 40% 3000 cycles, 10% 5000 cycles, 20% 5000 cycles, and 40% 5000 cycles (Figure 5.3.1). Compared to 1000 cycles (10.49 kN ± 0.37), the average UCT significantly decreased to 8.87 kN ± 0.81 and 7.26 kN ± 0.77 after 3000 and 5000 cycles, respectively. Within each duration,

significant differences between variation groups were observed after 3000 and 5000 cycles (Figure 5.3.1). After 3000 cycles, the 40% variation group had a UCT that was 2.37 kN and 1.88 kN less than the 10% and 20% variation groups, respectively. Variation groups exhibited even larger differences after 5000 cycles. A mean difference of 1.3 kN was observed between 10% and 20% variation and a 1.41 kN difference was observed between the 20% and 40% variation groups.

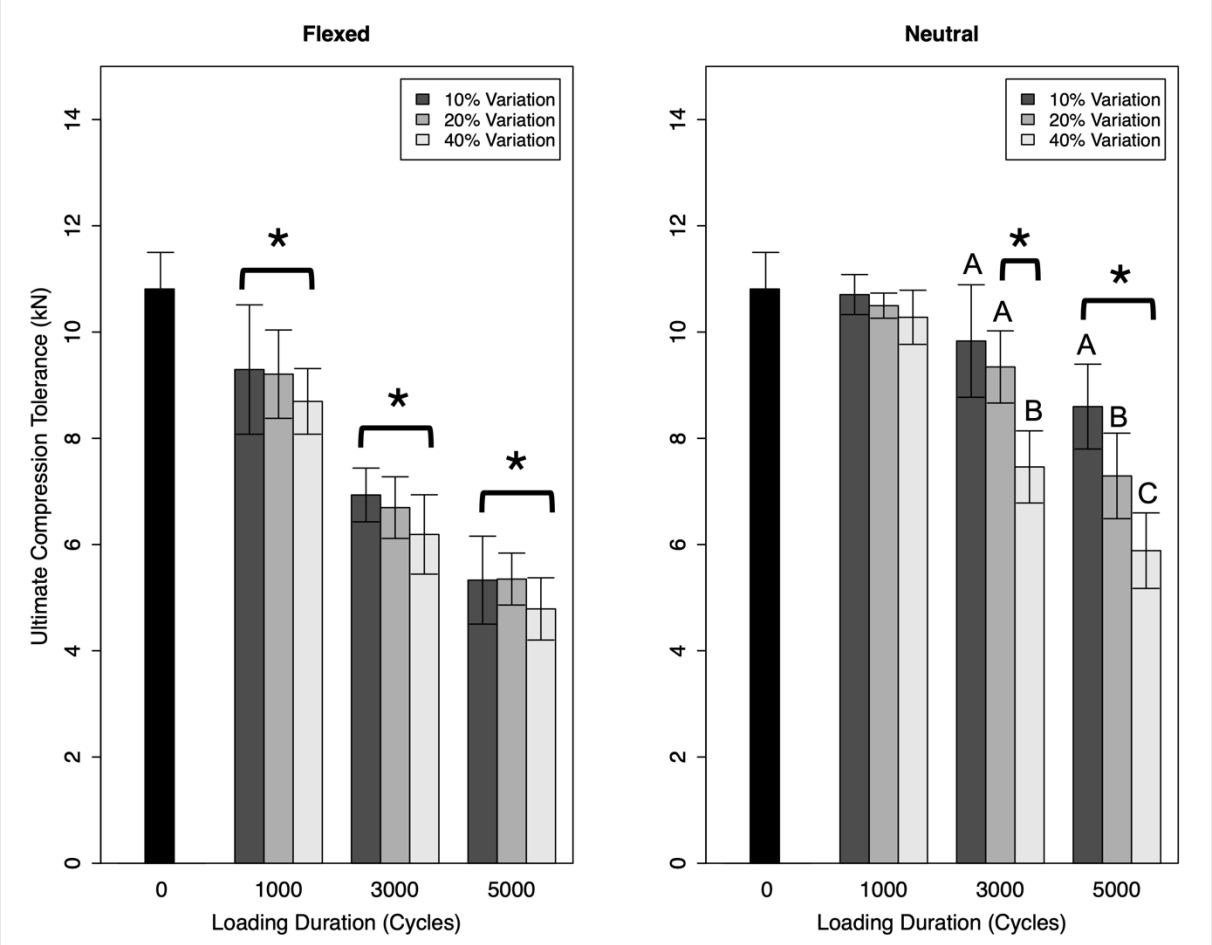

Figure 5.3.1. Mean UCT data in flexed (left) and neutral (right) postures. Statistical significance from the control group (black) is indicated by an asterisk (*). Within a given loading duration, loading variation groups marked with a different letter were significantly different ($p < 0.05$). Error bars represent one standard deviation.

Yield Force

Significant main effects of posture ($p = 0.02$) and duration ($p < 0.01$) were observed for yield force. The yield force of FSUs cyclically loaded in a neutral posture was, on average, 0.93 kN greater than cyclically loaded flexed postures (Figure 5.3.2). Systematic reductions in yield force were observed between 1000 and 3000 cycles (1.45 kN) and 3000 and 5000 cycles (1.42 kN). The yield force after 1000 cycles did not significantly differ from the control group (6.98 kN ± 1.72).

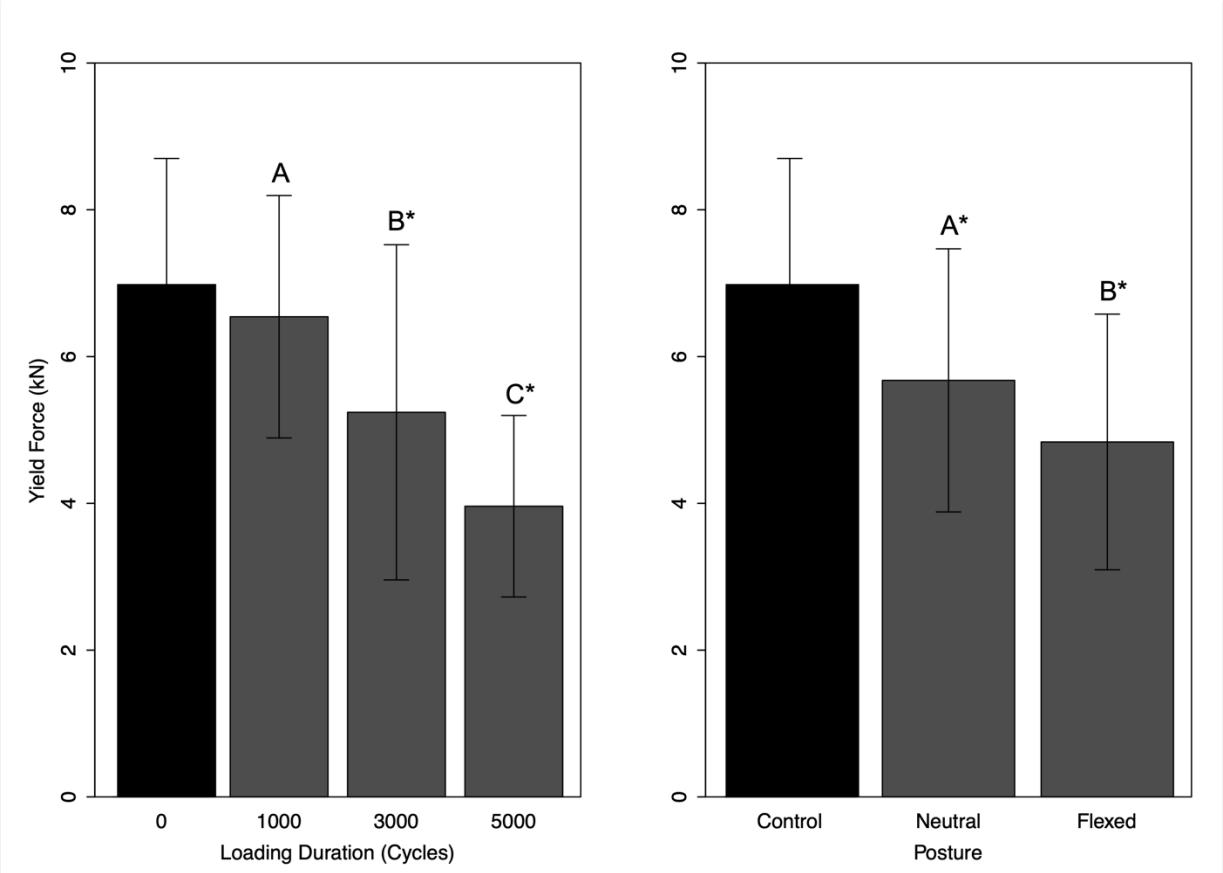

Figure 5.3.2. Mean yield force data as a function of loading duration (left) and posture (right). Statistical significance from the control group (black) is indicated by a superscripted asterisk (*). Duration and posture levels marked with a different letter were significantly different ($p < 0.05$). Error bars represent one standard deviation.

Indentation Stiffness

The results for indentation loading stiffness are separately presented for each CEP region. Given the similarity in response, the right and left lateral regions were combined and are presented as lateral hereon after. There were no significant findings in the anterior region (control: 63.46 N/mm ± 9.09; experimental: 60.39 N/mm ± 11.28).

A significant duration × variation × posture interaction effect was observed in the central region ($p = 0.019$). For the flexed group, the average stiffness significantly decreased as a function of duration; the loading stiffness was reduced to an average of 37.65 N/mm ± 3.88, 30.85 N/mm ± 5.94, and 20.26 N/mm ± 4.20 following 1000, 3000, and 5000 cycles, respectively (Figure 5.3.3). No effects of variation were observed within duration groups. In neutral, the average stiffness after 1000 cycles (42.69 N/mm ± 3.72) was similar to the control group (43.32 N/mm ± 4.97), but significantly decreased to 36.55 N/mm ± 4.12 and 24.57 N/mm ± 2.67 after 3000 and 5000 cycles, respectively. Within the 3000 and 5000 cycles durations, a 40% variation resulted in a reduction of 4.3 N/mm and 5.4 N/mm, respectively compared to the 10% and 20% variation groups.

A significant duration × posture interaction effect was found in the posterior region ($p = 0.007$). Cyclic loading applied to a flexed joint resulted in a significant 5.74 N/mm reduction after 5000 cycles (Figure 5.3.4). No other differences between postures were observed.

Significant duration × posture ($p \leq 0.011$) and duration × variation ($p \leq 0.044$) interactions were observed in the lateral regions. Compared to neutral, compression applied to a flexed joint facilitated an average significant reduction in stiffness by 6.09 N/mm after 5000 cycles (Figure 5.3.5). No other significant effects of posture were observed. A significant effect of variation was also observed after 5000 loading cycles (Figure 5.3.5). Within this duration, a significant 4.13 N/mm decrease in stiffness was observed for a 40% variation compared to 10% and 20% groups.

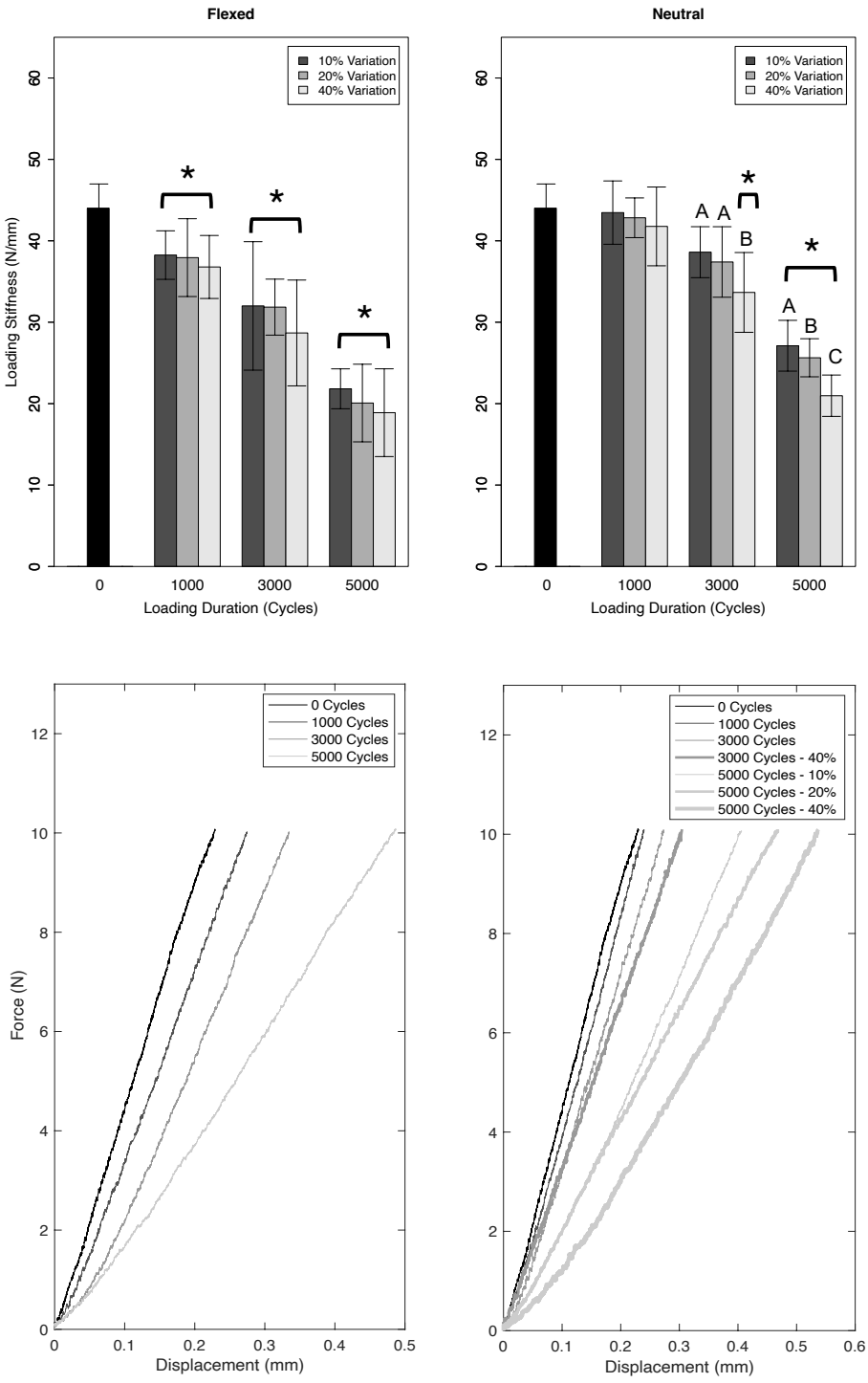

Figure 5.3.3. Mean indentation stiffness data for the central CEP region. Statistical significance from the control group (black) is indicated by an asterisk (*). Variation, duration, or posture levels marked with a different letter were significantly different ($p < 0.05$). Error bars represent one standard deviation. Force-displacement data from representative indentation trials are presented immediately below each bar graph.

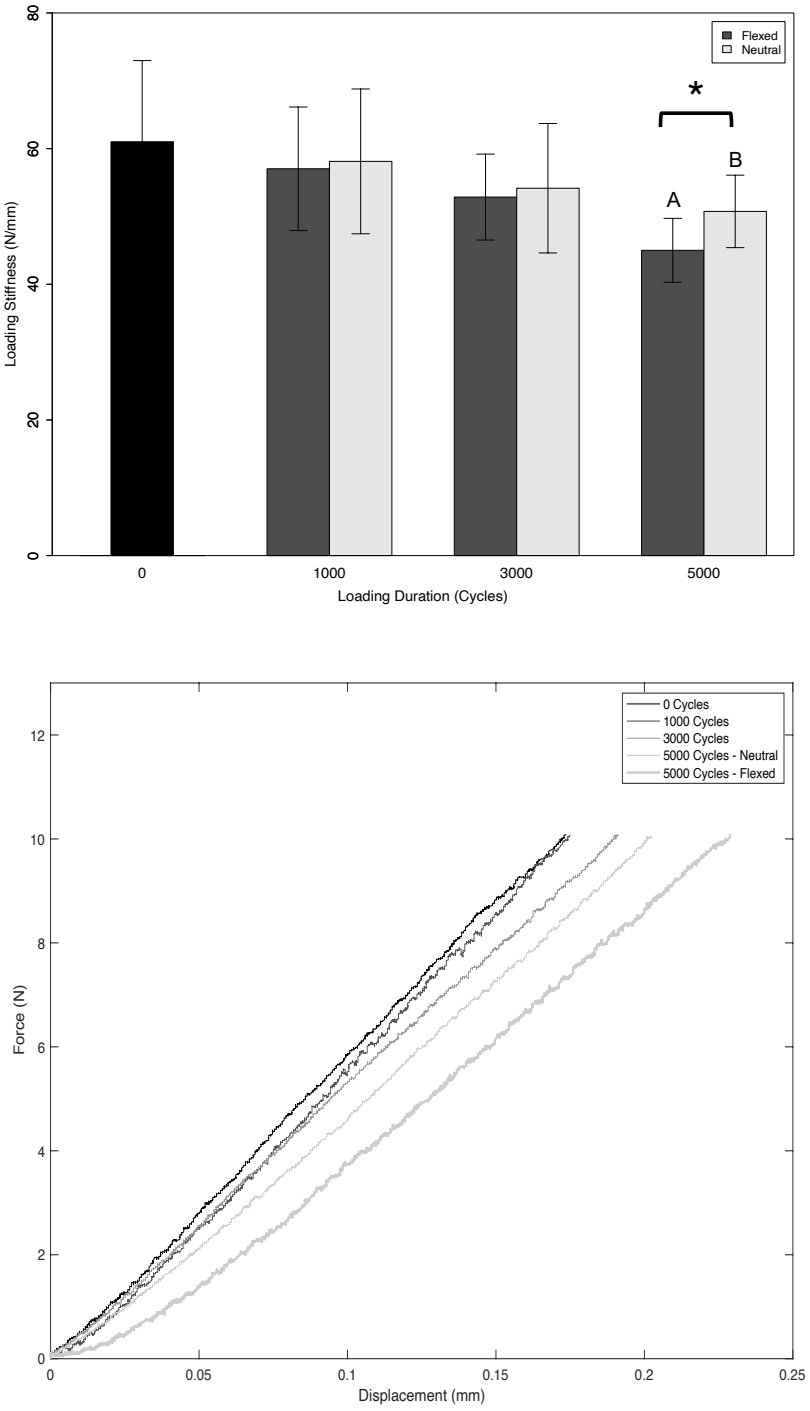

Figure 5.3.4. Mean indentation stiffness data for the posterior CEP region. Statistical significance from the control group (black) is indicated by an asterisk (*). Posture levels marked with a different letter were significantly different ($p < 0.05$). Error bars represent one standard deviation. Force-displacement data from representative indentation trials are presented immediately below each bar graph.

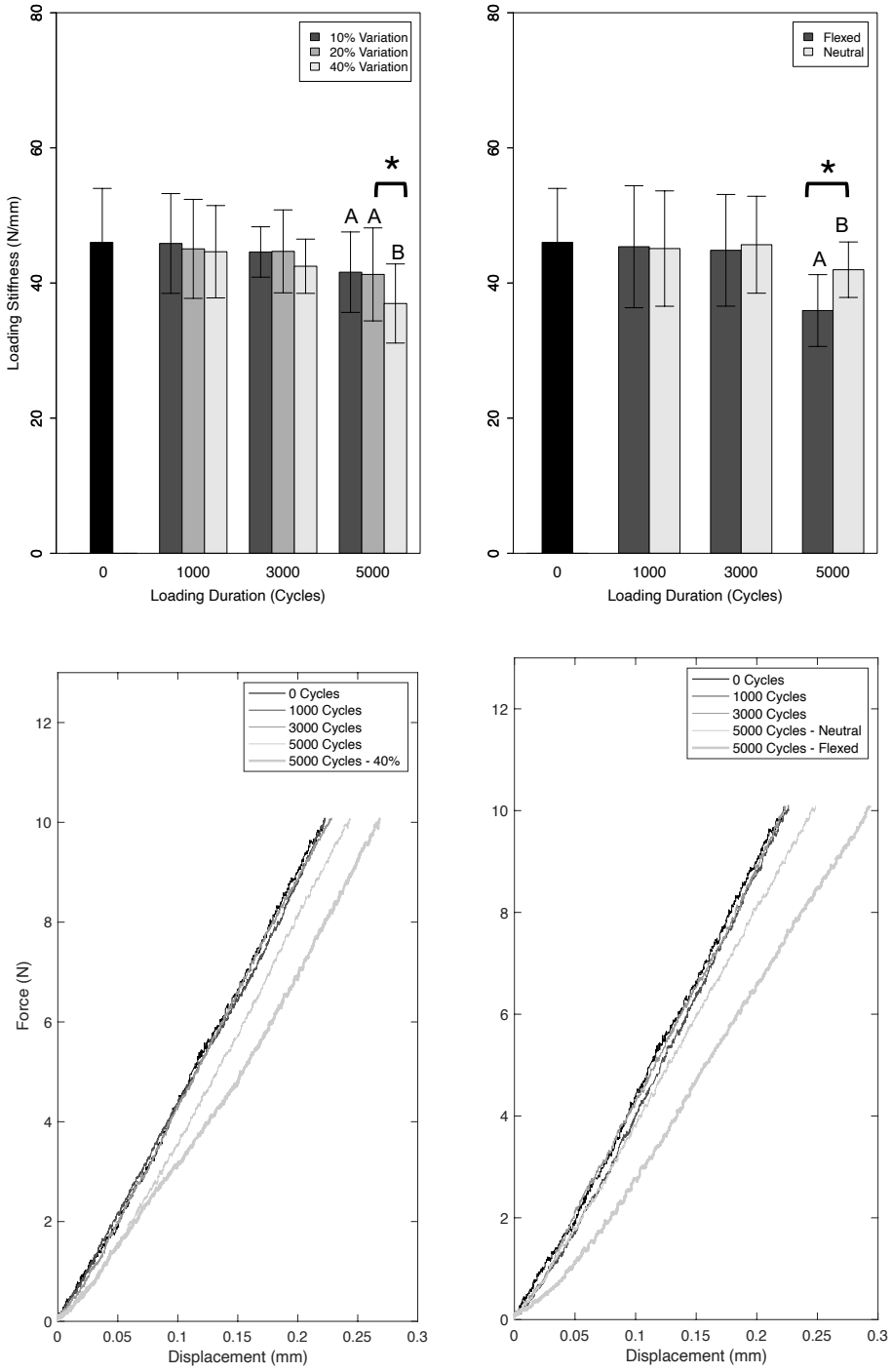

Figure 5.3.5. Mean indentation stiffness data for the lateral CEP region. Statistical significance from the control group (black) is indicated by an asterisk (*). Posture and variation levels marked with a different letter were significantly different ($p < 0.05$). Error bars represent one standard deviation. Force-displacement data from representative indentation trials are presented immediately below each bar graph.

Creep Displacement

No significant findings were observed for creep displacement in all CEP regions ($p \geq 0.054$), suggesting that any change in total displacement was driven by the indentation loading response and is therefore reflected by the analysis of loading stiffness. Summary statistics for creep displacement are presented in Table 5.3.1.

Table 5.3.1. Regional endplate creep displacement for control and experimental specimens. No significant main effect or interactions were observed with each region ($p > 0.05$).

Endplate	Control		Experimental	
Region	Mean (mm)	SD (mm)	Mean (mm)	SD (mm)
Central	0.03	0.01	0.03	0.07
Anterior	0.01	0.01	0.01	0.05
Posterior	0.01	0.05	0.01	0.05
Right	0.03	0.03	0.02	0.03
Left	0.03	0.03	0.02	0.03

5.4. Discussion

The effect of posture, loading variability, and loading duration on the post-loading UCT and regional indentation responses in the CEP were examined. Cyclic loading applied to a flexed joint was associated with a reduced UCT at each duration, which supported the first study hypothesis. An effect of loading variation was observed beyond 3000 cycles in a neutral posture only. Therefore, the second study hypothesis was partially supported (Figure 5.3.1). Furthermore, a systematic reduction in UCT with respect to the control group was observed in flexed postures, but this decline, on average, did not occur until the approximate mid-point of the predicted joint lifespan in neutral (i.e., 3000 cycles). This finding partially supported the third study hypothesis. With respect to yield force, the main effects for posture support the first and third study hypotheses, respectively. No significant main effects or interactions involving loading variation were observed for yield force (Figure 5.3.2). This result did not support the second study hypothesis. The

indentation stiffness measured in the central region mimicked the three-way interaction observed for UCT. As such, the hypothesis related to posture was supported but hypotheses for the effects of loading variation and loading duration were only partially supported (Figure 5.3.3). In the peripheral CEP regions, posture (posterior and lateral) and variation (lateral) interacted with loading duration, and these effects were only observed after 5000 cycles. Despite these interactions the loading stiffness in the posterior and lateral regions was significantly less than the control groups, which supports the fifth study hypotheses. The creep displacement measured in this study was unaffected by the loading history in all CEP regions. Collectively, these data demonstrate the sensitivity of UCT and loading stiffness in four of five CEP regions (central, posterior, lateral) to parameters of the joint loading history.

The average UCT of the control group (10.81 kN ± 0.69) was within one standard deviation of previously reported values for unloaded and hydrated porcine cervical spine units (Gunning et al., 2001) and cadaveric lumbar spine joints extracted from male donors aged 20-29 years (Hutton & Adams, 1982). These data confirm that the control group and initial conditions were representative of spinal units in a healthy and unloaded state.

This study was the first to demonstrate a cycle-dependent UCT response throughout the predicted joint lifespan. The effects of posture and peak compression magnitude (neutral only) on the UCT findings are attributed to the associated fatigue responses that are seemingly driven by poroelastic behaviour during the subthreshold cyclic tests. *In vitro* (Schultz, Warwick, Berkson, & Nachemson, 1979) and *in vivo* (Wilke, Neef, Caimi, Hoogland, & Claes, 1999) studies have collectively shown that joint flexion significantly increases intradiscal pressure for a given compression magnitude. A bone – disc – bone poromechanical finite element analysis further demonstrated that as nucleus pulposus pressure increased due to flexion, a linear reduction was

observed in CEP permeability thereby limiting fluid flow to the adjacent vertebral bodies (Malandrino et al., 2009). Despite the presence of more fluid reducing the vertical intradiscal displacement of the nucleus pulposus, the coincident increase in total joint displacement was driven by greater CEP deflection, particularly in the central region (Malandrino et al., 2009). In effect, this poroelastic response would suggest that higher cyclic radial tensile strains due to greater CEP deflection may have accelerated fatigue-related damage and therefore reduced the UCT at each time point evaluated in this study.

Although a similar mechanism underlying the UCT response in neutral postures is probable, the poroelastic and fatigue responses to cyclic testing are conceivably governed by the interactions between compression magnitude and rate. In caprine bone-disc-bone segments, high normalized cyclic compression (130 N) resulted in a 24% increase in intradiscal pressure compared to low normalized cyclic compression (50 N) over a 4-hour exposure (Vergroesen, Van Der Veen, Van Royen, Kingma, & Smit, 2014). Despite the association of intradiscal pressure and CEP permeability (Malandrino et al., 2009), this response is complicated by loading rate (Gullbrand et al., 2015). For a moderate compression magnitude and fixed 0.5 Hz loading frequency, a high compression rate resulted in a 15% reduction in permeability mediated solute transport through the CEP in a live rabbit study (Gullbrand et al., 2015). In contrast, a lower compression rate facilitated a 5% increase in permeability and the associated solute transport compared to their control group (Gullbrand et al., 2015). This effect of loading rate at a 0.5 Hz frequency was further supported by a significant reduction in the *in vitro* joint lifespan of porcine cervical spine units (Zehr, Buchman-Pearle, et al., 2020). However, the effect of high and low loading rates on fatigue lifespan were equalized with a 1 Hz frequency when normalized for differences in cyclic compression dose (Zehr, Buchman-Pearle, et al., 2020). While the fatigue mechanism was altered

from ductile (0.5 Hz) to brittle (1 Hz) (Zehr, Buchman-Pearle, et al., 2020), these data informed the use of a 1 Hz loading frequency for cyclic testing to offset the potentially confounding effect of inter-cycle differences in compression rate on joint fatigue and thus UCT in this study. From this modelling and experimental data together with the cyclic loading parameters, it is likely that the fatigue-related changes in UCT were driven by differences in peak compression magnitude in a neutral posture. Higher compression magnitudes embedded within the 20% and 40% variation paradigms conceivably caused greater central CEP deflection together with a central distribution that facilitated the separation in UCT between variation groups following 3000 and 5000 cycles (Figure 5.3.1). Taken together, the UCT data presented herein align with posture and magnitude dependent poroelastic material responses, which have significant implications for mechanisms of load and fluid transfer within the spinal joint.

Yield force measured in the current study ranged from 3.81 kN to 7.21 kN, which is similar to that of Gunning et al. (2001) for a neutral failure test. The 15% decrease in yield force observed in flexed postures was similar to the trend observed by Gunning et al. (2001); however, the yield force was 2.2 to 3.4 times greater in the current study. This stark difference may have been a result of the posture in which the ultimate tests were performed. Given the necessary use of a fabricated indenter, a perpendicular tissue interface was required to prevent slippage and excessive anterior-posterior translation of an unmounted vertebra-cup unit. This approach differed from Gunning et al. (2001) who performed ultimate testing with the FSU positioned in a flexed posture. Both studies, however, captured the effect of flexed joint conditioning loading on yield force.

The indentation loading response observed in the central compared to peripheral CEP regions reinforces the notion of a centrally distributed compression load and poroelastic behaviour mechanism in both postures. In previous studies, CEP loading stiffness was strongly correlated

with biochemical measurements of collagen content (Fields, Rodriguez, et al., 2013). Furthermore, Rodriguez et al. (2011) showed that aged and degenerated spinal tissue was distinguished from healthy joints by the presence of microstructural voids beneath the endplate surface. These data collectively suggest a feasible explanation for the central CEP stiffness response observed herein.

Given the likelihood of greater CEP deflection caused by flexed postures and higher compression magnitudes (Malandrino et al., 2009; Vergroesen et al., 2014), these collective poroelastic responses may have resulted in earlier initiation and more rapid accumulation of microstructural constitutive damage and void development below the endplate surface. This notion of accelerated damage and the corresponding decrease in loading stiffness is further reinforced by the reduction in fatigue lifespan when spinal units were cyclic loaded in flexed postures (Gooyers et al., 2015; Parkinson & Callaghan, 2009) or when higher compression magnitudes were randomly imposed through variation (Zehr et al., 2019b). Based on the similarity in central CEP loading stiffness and UCT for flexed cyclic loading postures (Figure 5.3.1 and 5.3.2), the fatigue-related damage processes appear to be dominated by posture. The intation and progression of constitutive and structural damage in the central CEP region throughout the tissue lifespan was explored in Chapter 6 to further elucidate mechanisms underlying the mechanical responses observed.

The loading stiffness quantified in the lateral and peripheral regions gleans insight into mechanisms of common CEP fatigue-fracture patterns (Figure 5.3.3). Horizontal crack and step fractures make up approximately 60-85% of compression-induced CEP fractures (Parkinson & Callaghan, 2007b; Zehr, Buchman-Pearle, et al., 2020; Zehr et al., 2019b). These fracture patterns, in particular, are characterized by a crack that extends through the central or posterior-central and both lateral CEP regions (Brinckmann et al., 1988; Gallagher et al., 2006). Although the reduction

in stiffness is clearly observed much earlier in the central region, stiffness significantly decreased in the posterior and lateral regions after 5000 cycles (Figure 5.3.4 and 5.3.5). If fatigue damage is related to loading stiffness, this would suggest that microstructural damage preceding many macroscopic fractures originates centrally and propagates laterally and/or posteriorly as the CEP approaches its fatigue lifespan. In alignment with stiffness results from the central CEP, the decrease in posterior and lateral stiffness after 5000 cycles was also exacerbated by flexed postures and 40% compression variation.

Although the changes in loading stiffness and ultimate tolerance can be explained by existing data and theoretical models, there are no clear explanations for the similarities in creep displacement. The adopted indentation profile has been previously implemented for the analysis of loading and unloading CEP behaviour (Noshchenko et al., 2013; Patel et al., 2018) and does not exceed the elastic loading region based on destructive ultimate testing (Grant et al., 2001). While effective for examining the changes in cycle-dependent CEP loading behaviour, future studies with a particular interest in viscoelastic properties (i.e., creep, stress-relaxation) may require a longer hold duration to potentially capture loading induced differences in creep displacement.

This study was subject to the following limitations. First, the *in vitro* study design permitted the analysis of progressive tissue fatigue, but the analysis of mechanically induced tissue repair and synthesis resulting from periods of unloading was not afforded. Spinal joints, and specifically the CEP, have the potential to benefit from low loading rate and low to moderate magnitude loading through adaptive cellular processes that increase tissue strength via chondrocyte hypertrophy and biosynthesis of the extracellular matrix content (Englemark, 1961; Jin, Frank, Quinn, Hunziker, & Grodzinsky, 2001). Future studies will use techniques like tissue culturing or live animal models to explore how the time-course of tissue regeneration can influence joint and

CEP behaviour. Second, a porcine animal model was used as a surrogate for the human lumbar spine. Although the exact transference of the findings between species is unknown, our study design was strengthened by using healthy spinal joints extracted from mature pigs with a similar age and loading history. The documented similarities in morphology (Yingling et al., 1999) together with appropriate scaling of compression forces are expected to yield comparable fatigue-related changes in UCT and CEP responses between species. Third, ultimate compression testing was performed with an indenter that was designed to represent a hydrated intervertebral disc, which may not fully represent the altered hydration state in response to cyclic loading. The ultimate compression tolerance has been shown to increase in dehydrated FSUs compared to hydrated (Gunning et al., 2001), and this response can be attributed to a more peripheral stress distribution across the endplate (van Dieën, Kingma, et al., 2001). As a result of this hydration response, the ultimate compression tolerance of FSUs after 5000 cycles may have been underestimated given the use of a single indenter across all specimens.

5.5. Conclusions

The UCT and central CEP indentation stiffness were significantly influenced by the joint posture imposed during the cyclic loading tests. Specifically, posture appears to influence the joint and CEP behaviour within 1000 cycles, which is within a daily cyclic loading range for occupations that require repeated lifting exertions. To a lesser extent, high variation in peak compression magnitude significantly reduced the UCT and central CEP stiffness beyond the mid-point of the predicted joint lifespan (i.e., 3000 cycles). The effect of 20% variation only became significant after 5000 cycles. Therefore, control of peak compression exposures (i.e., abrupt high demand tasks), is particularly relevant between the mid-point and end of the joint lifespan. These responses are attributed to the poroelastic joint behaviour related to posture and compression

magnitude. Lastly, the delayed effect of posture and loading variation on the indentation stiffness of lateral and posterior regions further supports common fracture patterns like crack and step morphology.

CHAPTER 6

Initiation and Accumulation of Loading Induced Changes to Native Collagen Content and Microstructural Damage in the Central Endplate

Jackie D. Zehr, Joe Quadrilaterio, Jack P. Callaghan

The Spine Journal, Submitted February 2023

Abstract

Objective: This *in vitro* study examined the effect of cyclic loading on the initiation and accumulation of changes to native collagen content (type I, type II) and microstructural damage in the central endplate region of cadaveric porcine endplates.

Methods: 114 porcine cervical spinal units were included (N = 6 per group). The study contained a control group (no cyclic loading) and 18 experimental groups that differed by loading duration (1000, 3000, 5000 cycles), joint posture (flexed, neutral), and cyclic peak compression variation (10%, 20%, 40%). Multi-colour immunofluorescence staining was used to quantify loading induced changes to native type I (i.e., subchondral bone) and type II (i.e., endplate) collagen content (fluorescence area, fluorescence intensity) and microstructural damage (pore area (transverse plane), void area along the endplate-bone border (sagittal plane)).

Results: Significant main effects of loading duration and posture were observed for fluorescence area and fluorescence intensity of type I and II collagen. In the transverse plane, type II fluorescence area significantly decreased following 1000 cycles (-12%), but a significant change in fluorescence intensity was not observed until 3000 cycles (-17%). Type II fluorescence area (-14%) and intensity (-10%) were both significantly less in flexed postures compared to neutral.

Similar trends were observed for type I collagen in the sagittal plane sections. Generally, significant changes to fluorescence area were accompanied by the development of microstructural voids along the endplate-subchondral bone border.

Conclusions: These findings demonstrate that microstructural damage beneath the central endplate surface occurs before significant changes to the density of type I and II collagen fibers. Although flexed postures were associated with greater and accelerated changes to collagen content, the injury initiation mechanism was similar to neutral postures.

6.1. Introduction

The cartilaginous endplate (CEP) separates the intervertebral disc from adjacent vertebral bodies. This hyaline cartilage structure exhibits unique mechanical properties that enable the transmission of compression force through lumbar spine joints (Bogduk, 2012; S. H. M. Brown et al., 2008). Furthermore, permeability for fluid flow and the diffusivity of macromolecules into the avascular intervertebral disc is largely governed by the pores and their response to radial stretch of the endplate surface in response to pressurization of the nucleus pulposus (Giers et al., 2017; Y. C. Huang et al., 2014; Jackson & Gu, 2009). The CEP is therefore critical to regulating the physiological and hydrostatic homeostasis of the intervertebral disc (Y. C. Huang et al., 2014), and alterations to the biochemical and microstructural properties are linked to disc degeneration (Adams, Freeman, Morrison, Nelson, & Dolan, 2000; Urban, Smith, & Fairbank, 2004) and low back pain (M. F. Brown et al., 1997; Ohtori et al., 2006). Despite the connection of the CEP to clinically relevant low back disorders (Adams et al., 2000; M. F. Brown et al., 1997; Ohtori et al., 2006; Urban et al., 2004), the effects of mechanical loading on the initiation and pace of microstructural changes are poorly understood.

The CEP contains interspaced chondrocytes within an extracellular matrix that is primarily comprised of type II collagen along with proteoglycans, and water (Antoniou et al., 1996; Fields, Rodriguez, et al., 2013; Lakstins, Arnold, Gunsch, Flanigan, et al., 2020; Lotz et al., 2013; Yongren Wu et al., 2015). Biochemistry analyses performed on human cadaveric CEP tissue established a relationship between collagen content and material properties (Fields, Rodriguez, et al., 2013). Specifically, a reduction in collagen content was moderately correlated with a reduction in tensile modulus (Fields, Rodriguez, et al., 2013). The use of microcomputed tomography has further revealed a greater porosity and depth-dependant changes in subchondral bone morphology in aged

lumbar spine joints with severe intervertebral disc degeneration (Rodriguez et al., 2011). Although the loading histories of the studied cadaveric tissue are conceivably variable and unknown, these data suggest that loading induced CEP injury is likely a product of biochemical and microstructural adaptations, but the time course of these changes remain unexplored. An understanding of the early changes in native collagen content and microstructure would provide novel insights into how mechanical loading can mediate CEP injury initiation and pathways.

This *in vitro* study quantified the cycle dependant change in native collagen content within the CEP (type II) and subchondral bone (type I) resulting from repeated compression exposures applied to porcine functional spinal units (FSU). A secondary objective was to examine the initiation and accumulation of microstructural damage, which was quantified by pore area (transverse plane sections) and void area (sagittal plane sections) at the CEP-subchondral bone interface. The effects of joint posture, loading duration, and variation in peak compression force on native collagen content and microstructural damage were specifically examined using a multi-colour immunofluorescence technique (Zehr, Rahman, et al., 2022).

A total of five specific hypotheses were made for transverse plane images. First, previous research has demonstrated a relationship between collagen content and tensile modulus of isolated CEP tissue (Fields, Rodriguez, et al., 2013). On the basis of this relationship, it is hypothesized that joint posture, variation in peak compression force, and loading duration will interact to decrease the fluorescence intensity of type II collagen. This response would align with loading induced changes to indentation stiffness (Zehr, Barrett, et al., 2022). Second, the CEP is a porous structure and, in response to deflection, pore compaction occurs (Y. Wu et al., 2016). Furthermore, as the CEP surface is strained, the pores are a conceivable stress riser. As such, type II collagen around the pore perimeter is particularly susceptible to damage (i.e., negative staining).

Furthermore, flexed postures facilitated greater central CEP deflection compared to a neutral alignment (Malandrino et al., 2009). Therefore, it was hypothesized that joint flexion will significantly decrease the fluorescence area of type II collagen compared to neutral postures. Third, in alignment with previous fatigue research (Gooyers et al., 2015), type II collagen fluorescence area was hypothesized to decrease as a function of loading duration. Fourth, a decrease in the fluorescence area of type II collagen can be expected to reveal the type I collagen content of the subchondral trabecular bone. Therefore, it was hypothesized that flexed joint postures will increase the fluorescence area of type I collagen compared to neutral postures. Fifth, type I collagen fluorescence area was hypothesized to increase as a function of loading duration.

In the sagittal plane, three hypotheses were made. First, previous research has demonstrated a relationship between collagen content and tensile modulus of isolated CEP tissue (Fields, Rodriguez, et al., 2013). On the basis of this relationship, it is hypothesized that joint posture, variation in peak compression force, and loading duration will interact to decrease the fluorescence intensity of type II collagen. This response would align with loading induced changes to indentation stiffness (Zehr, Barrett, et al., 2022). Second, Rodriguez et al. (2011) observed the formation of voids beneath the CEP surface and along the CEP-subchondral bone border in degenerated cadaveric spinal units. Although the presence of sub-surface voids has not been related to CEP properties, it was hypothesized that joint posture, variation in peak compression force, and loading duration will interact to increase the sub-surface microstructural void area. This response would suggest that changes to indentation stiffness observed by Zehr, Barrett, et al. (2022) would result from a reduction in native type II collagen content combined with microstructural void development. Third, in the presence of sub-surface voids along the CEP-subchondral bone border, the fluorescence area of type I and type II collagen will conceivably

decrease. Therefore, it was hypothesized that joint posture, variation in peak compression force, and loading duration will interact to decrease the fluorescence area of type I and type II collagen.

6.2. Methods

Overview

This study used a novel multi-colour immunofluorescence procedure to quantify compression induced changes to native collagen content and microstructural damage. The loading parameters have been presented in Chapter 5 and included joint posture, variation in peak compression force, and loading duration. Endplate tissue from 113 specimens was included in this study and was sectioned in the transverse and sagittal planes. A total of 678 images were captured using laser scanning confocal microscopy, from which quantitative measurements of native collagen content and void/pore area could be made.

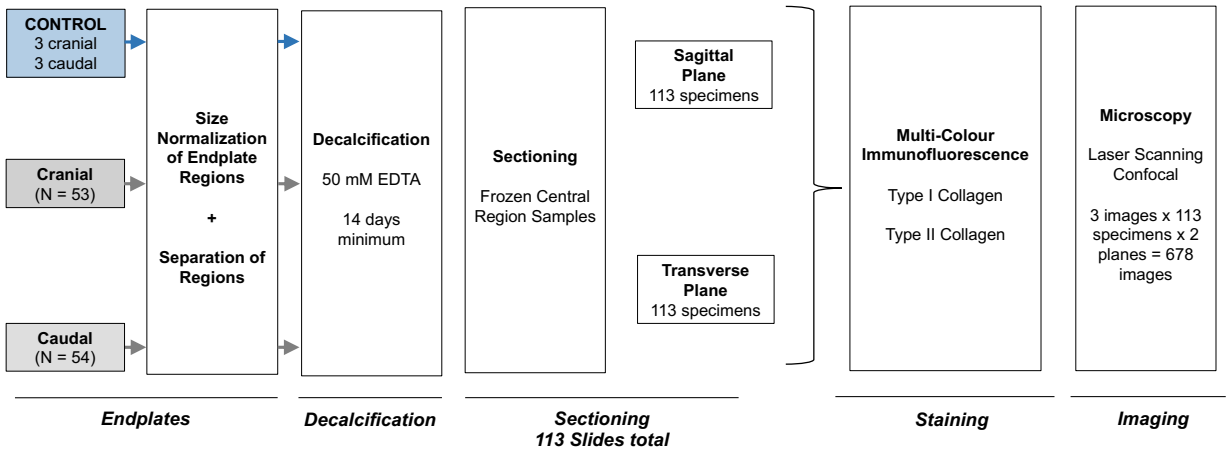

Figure 6.2.1. Schematic of the experimental procedure performed on cyclically loaded central endplate tissue.

Tissue Inclusion & Preparation

The central region of 113 endplates were included in this study. This study was focused on the central endplate region given its structural vulnerability to fatigue fracture (Grant et al., 2001;

van Dieën, Kingma, et al., 2001) and the prevalence of macroscopic endplate fracture effecting the central region (Zehr, Buchman-Pearle, et al., 2020). Prior to inclusion, all 113 endplate specimens underwent cyclic compression paradigms and post-loading microindentation procedures outlined in Chapter 5. This sample was deemed sufficient based on the results of a *post hoc* power analysis (power > 0.784). Immediately following the non-destructive microindentation test, the size-normalized and marked central region was extracted and immediately placed in 50 mM ethylenediamimetraactic acid (pH 8.0) for a minimum of 14 days. Samples were stored at 4°C for the decalcification period.

Decalcified tissue was rinsed using phosphate buffered saline, embedded in O.C.T compound, and frozen in liquid nitrogen cooled isopentane. These prepared endplate samples were stored at -80°C for approximately 3 months prior to sectioning. Frozen OCT embedded samples were transferred directly from the -80°C freezer to a temperature-controlled cryostat (-20°C) for sectioning. Serial cryosections in the transverse (approximate depth of 80 μm) and sagittal planes were cut to a thickness of 10 μm and placed on Superfrost™ Plus Gold glass microscope slides. Within a specimen, transverse and sagittal plane sections were placed on a single microscope slide (Figure 6.2.2); therefore, a total of 113 slides were prepared for staining.

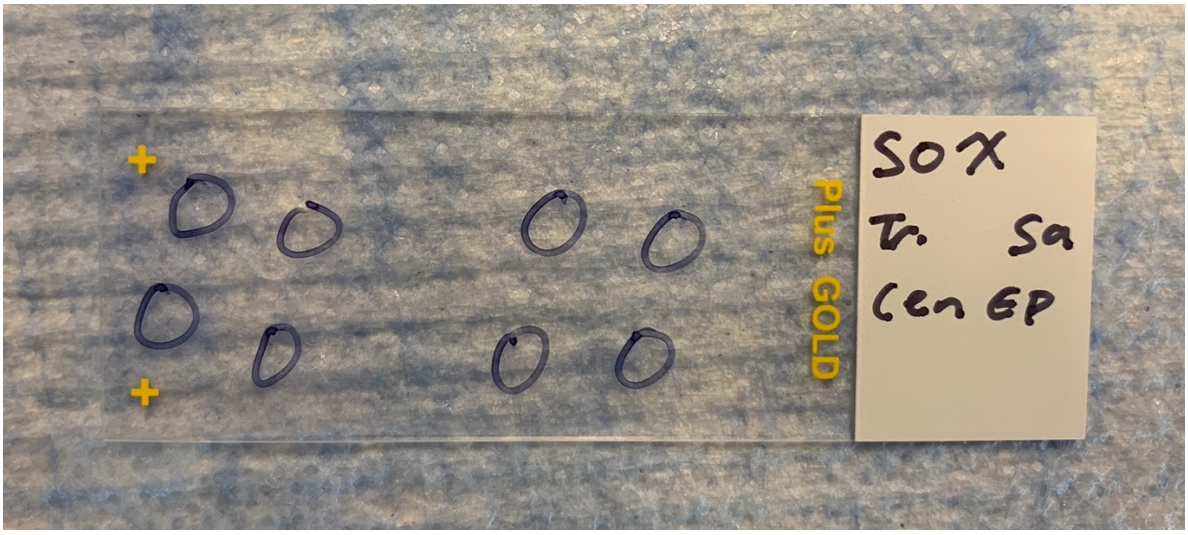

Figure 6.2.2. Layout of transverse (left) and sagittal (right) plane cryosections

Immunofluorescence Staining

Immunofluorescence staining was performed with primary antibodies against type I and type II collagen (Zehr, Rahman, et al., 2022). Sections were first incubated in a 10% goat serum (in PBS) solution for 60 minutes at room temperature. Primary antibodies for type I (mouse, Invitrogen MA1-26771) and type II (rabbit, Invitrogen PA1-26206) collagen were mixed with a concentration of 1:100 in 10% goat serum solution and allowed to incubate for 20 hours at 4°C. Secondary antibodies were conjugated with Alexa Fluor 488 (type I, goat anti-mouse, Invitrogen A-11001) and Alexa Fluor 555 (type II, goat anti-rabbit, Invitrogen A-21422). Both were mixed to a concentration of 1:500 in PBS and incubated for 30 minutes at room temperature. The immunofluorescence staining procedure was performed in five separate batches; where batches 1-4 contained 25 specimens and the fifth batch contained 13 specimens. The concentrations of commercially purchased antibodies and the associated volumes mixed into each batch to achieve the desired cocktail concentrations are presented in Appendix A.

Visualization of prepared slides was performed with a laser scanning confocal microscope (Axio Observer Z1 LSM800, Zeiss, Oberkochen, Germany). Three representative images were

taken of each specimen and in each plane, totalling six images per specimen. A 20X Plan-Apochromt objective (NA0.8) and ZEN 2.3 System software (Zeiss, Oberkochen, Germany) were used for visualization and obtaining images. 488 nm (Alexa Fluor 488, collagen I) and 561 nm (Alexa Fluor 555, collagen II) lasers were used with a pinhole size set to 41µm. The master gain for AF 488 and AF 555 channels was 662 V and 650 V, respectively.

Data Processing

A total of 678 images were acquired. For all dependent measures, the transverse and sagittal plane images were separately examined. Therefore, fluorescence and void metrics obtained from the three images per plane were included in the statistical procedures. Fluorescence area and fluorescence intensity of type I and type II collagen were determined for sagittal and transverse plane images using ZEN 2.3 System software. Fluorescence area represents the relative area of positive staining of a given collagen protein, and fluorescence intensity represents the density of collagen proteins for a given channel. Therefore, higher intensity (brighter staining) would represent a higher density of native collagen. For transverse plane sections, mean fluorescence area and fluorescence intensity were determined for the entire image. For sagittal plane images, pre-determined areas (461 pixels x 2038 pixels) of cartilage (type II) and subchondral bone (type I) were evaluated (Zehr, Rahman, et al., 2022). Both fluorescence area and fluorescence intensity are expressed as arbitrary units (AU). A value of 1.0 was assigned to the mean of the control group and fluorescence metrics of the eighteen experimental groups were expressed relative to the control group. Lastly, the additive area occupied by pores and voids along the CEP-subchondral bone border was computed using ImageJ. A pore was only measured in the transverse plane and functions as a gateway for fluid to flow through the endplate (Figure 6.2.3). The boundaries of a pore were areas of negative staining for type I and type II collagen. Void area was only quantified

in sagittal plane images and represents a physical space that forms at the interface of the hyaline cartilage and subchondral bone (Figure 6.2.3). All area measurements are expressed as a percentage of the total image area.

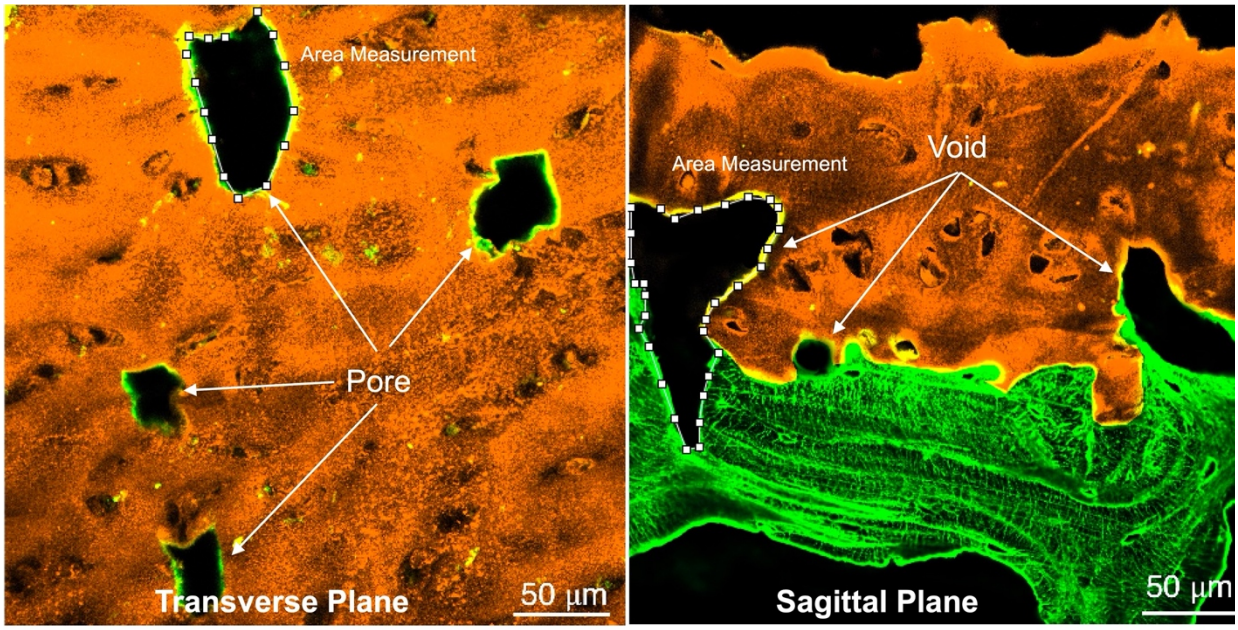

Figure 6.2.3. Quantification of pore (transverse plane) and void (sagittal plane) area. The total area was the additive sum of all pores or voids present.

Statistics

RStudio (RStudio Version 3.34, RStudio Inc, Boston, MA) was used to conduct all statistical analyses. First, analysis of variance tests (ANOVA) with factors for spinal level, posture, loading variation, and loading duration was used to evaluate sample randomization based on endplate surface area. Separate ANOVA tests were conducted to examine the effects of spinal level, posture, loading variation, and loading duration on each dependent measure (alpha = 0.05). Where applicable, a Tukey's *post hoc* test was performed with Bonferroni corrections.

6.3. Results

Randomization

There were no significant effects observed for endplate area ($p \geq 0.086$), which demonstrates that randomization was effective. No significant effects of spinal level ($p \geq 0.095$) or vertebra ($p \geq 0.113$) were observed for dependant measures examined in the transverse and sagittal planes. Therefore, all dependant measures were collapsed across spinal level and vertebra within a given plane. Representative images from the control group are depicted in Figure 6.3.1.

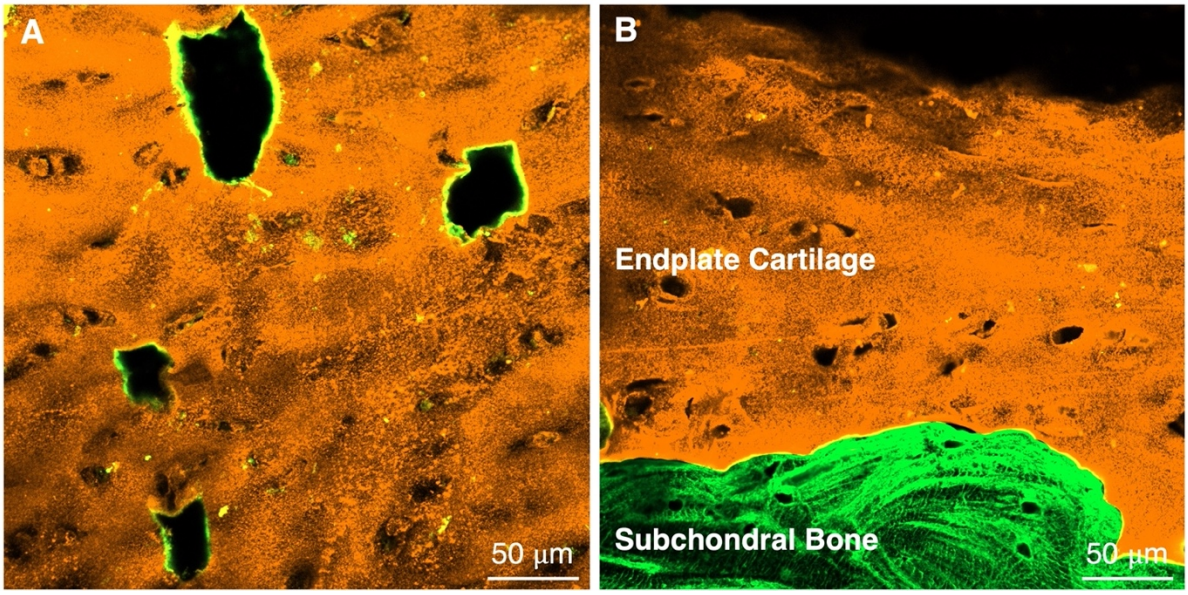

Figure 6.3.1. Representative CEP images from the control group in the transverse (A) and sagittal (B) plane. Green represents positive staining for type I collagen (i.e., subchondral bone) and orange represents positive staining for type II collagen (i.e., hyaline cartilage).

Transverse Plane

Statistically significant main effects of loading duration and posture were observed for the fluorescence area and fluorescence intensity of type II collagen (Table 6.3.1). The mean type II fluorescence area was significantly less than the control group after 1000 (-18%), 3000 (-25%),

and 5000 (-36%) cycles (Table 6.3.1). Furthermore, the type II fluorescence area after 5000 cycles was significantly less than 1000 (-18%) and 3000 (-11%) cycles (Figure 6.3.2, Table 6.3.1). The fluorescence intensity of type II collagen significantly decreased as loading progressed from 1000 to 3000 cycles (-12%) and from 3000 to 5000 cycles (-10%); however, only the 3000 (-19%) and 5000 (-29%) cycle durations were significantly less than the control group (Table 6.3.1, Figure 6.3.2). The mean fluorescence area and fluorescence intensity of type II collagen were significantly less when cyclic loading was applied to flexed joint postures compared to neutral by a magnitude of -15% and -13%, respectively (Table 6.3.1, Figure 6.3.3).

Despite a visually apparent increase in type I fluorescence area around the perimeter of the CEP pores (Figure 6.3.2, Figure 6.3.3), there were no significant main effects or interactions detected for the fluorescence area and fluorescence intensity of type I collagen (Table 6.3.1). There were also no significant changes in pore area (Figure 6.3.4).

Table 6.3.1. Mean ± standard deviation of fluorescence area and fluorescence intensity of transverse and sagittal plane images. For significant main effects, differences between durations and postures are indicated by bolded font ($p < 0.05$). Values superscripted with an asterisk (*) were significantly different from the control group. Values superscripted with different capital letters were significantly different between durations or postures.

	Loading Duration				Posture		
	1000 cycles	3000 cycles	5000 cycles	*p*	Flexed	Neutral	*p*
TRANSVERSE PLANE							
Type I Collagen Fluorescence Area (AU)	1.02 ± 0.77	1.16 ± 0.84	1.29 ± 0.92	0.076	1.21 ± 0.86*	1.10 ± 0.84	0.228
Type II Collagen Fluorescence Area (AU)	0.82 ± 0.43^{A*}	0.75 ± 0.34^{AB*}	0.64 ± 0.27^{C*}	**0.002**	0.67 ± 0.32^{A*}	0.81 ± 0.39^{B*}	**< 0.001**
Type I Collagen Fluorescence Intensity (AU)	1.00 ± 0.55	0.98 ± 0.86	0.92 ± 0.58	0.697	0.97 ± 0.67	0.97 ± 0. 69	0.991
Type II Collagen Fluorescence Intensity (AU)	0.93 ± 0.27^{A}	0.81 ± 0.22^{B*}	0.71 ± 0.27^{C*}	**< 0.001**	0.76 ± 0.21^{A*}	0.91 ± 0.28^{B}	**< 0.001**
SAGITAL PLANE							
Type I Collagen Fluorescence Area (AU)	0.96 ± 0.36^{A}	0.89 ± 0.40^{AB*}	0.79 ± 0.39^{B*}	**0.007**	0.79 ± 0.32^{A*}	0.96 ± 0.43^{B}	**< 0.001**
Type II Collagen Fluorescence Area (AU)	0.88 ± 0.50^{A*}	0.82 ± 0.47^{AB*}	0.70 ± 0.32^{B*}	**0.003**	0.73 ± 0.38^{A*}	0.87 ± 0.44^{B*}	**0.005**
Type I Collagen Fluorescence Intensity (AU)	1.00 ± 0.39	0.99 ± 0.43	0.90 ± 0.34	0.123	0.96 ± 0.36	0.97 ±.0.45	0.730
Type II Collagen Fluorescence Intensity (AU)	0.94 ± 0.41^{A}	0.83 ± 0.37^{B*}	0.71 ± 0.33^{C*}	**< 0.001**	0.80 ± 0.37^{A*}	0.90 ± 0.40^{B}	**0.009**

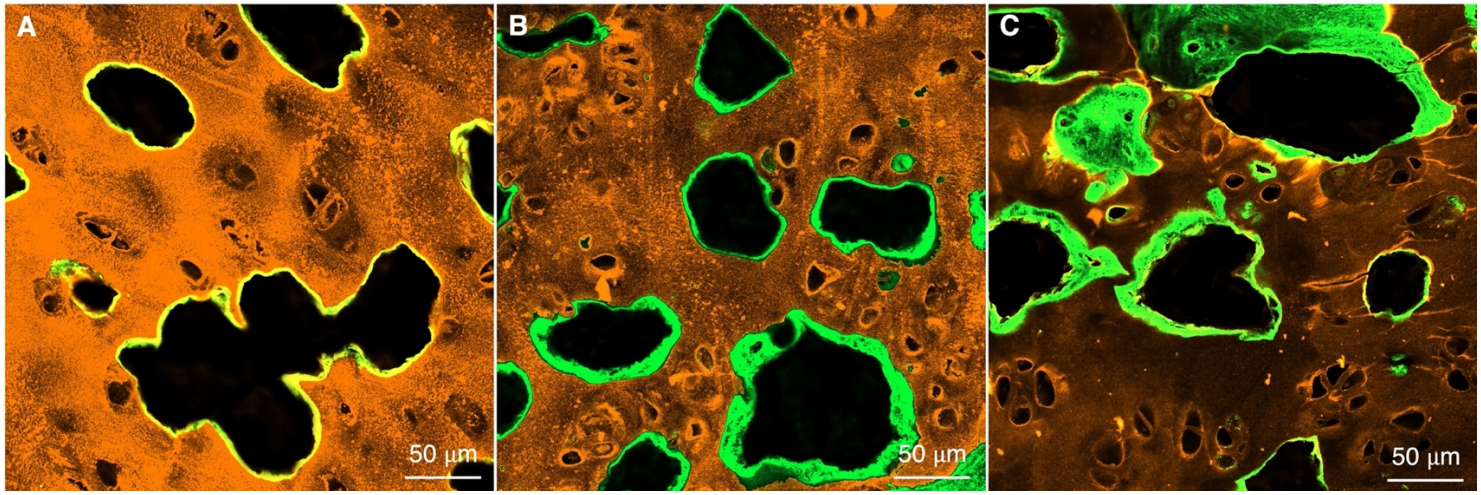

Figure 6.3.2. Representative CEP images in the transverse plane following 1000 (A) 3000 (B) and 5000 (C) cycles.

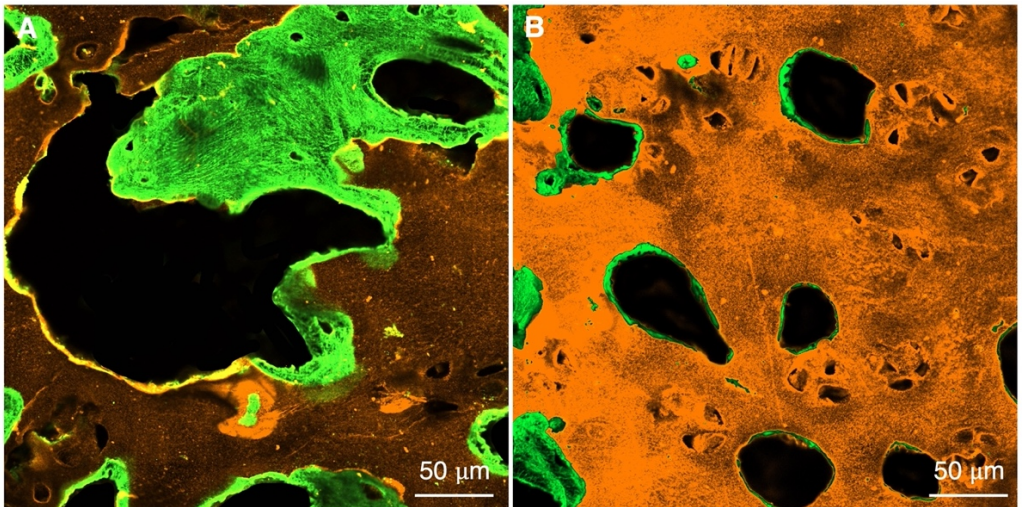

Figure 6.3.3. Representative CEP images in the transverse plane corresponding to cyclic loading applied in flexed (A) and neutral (B) joint postures.

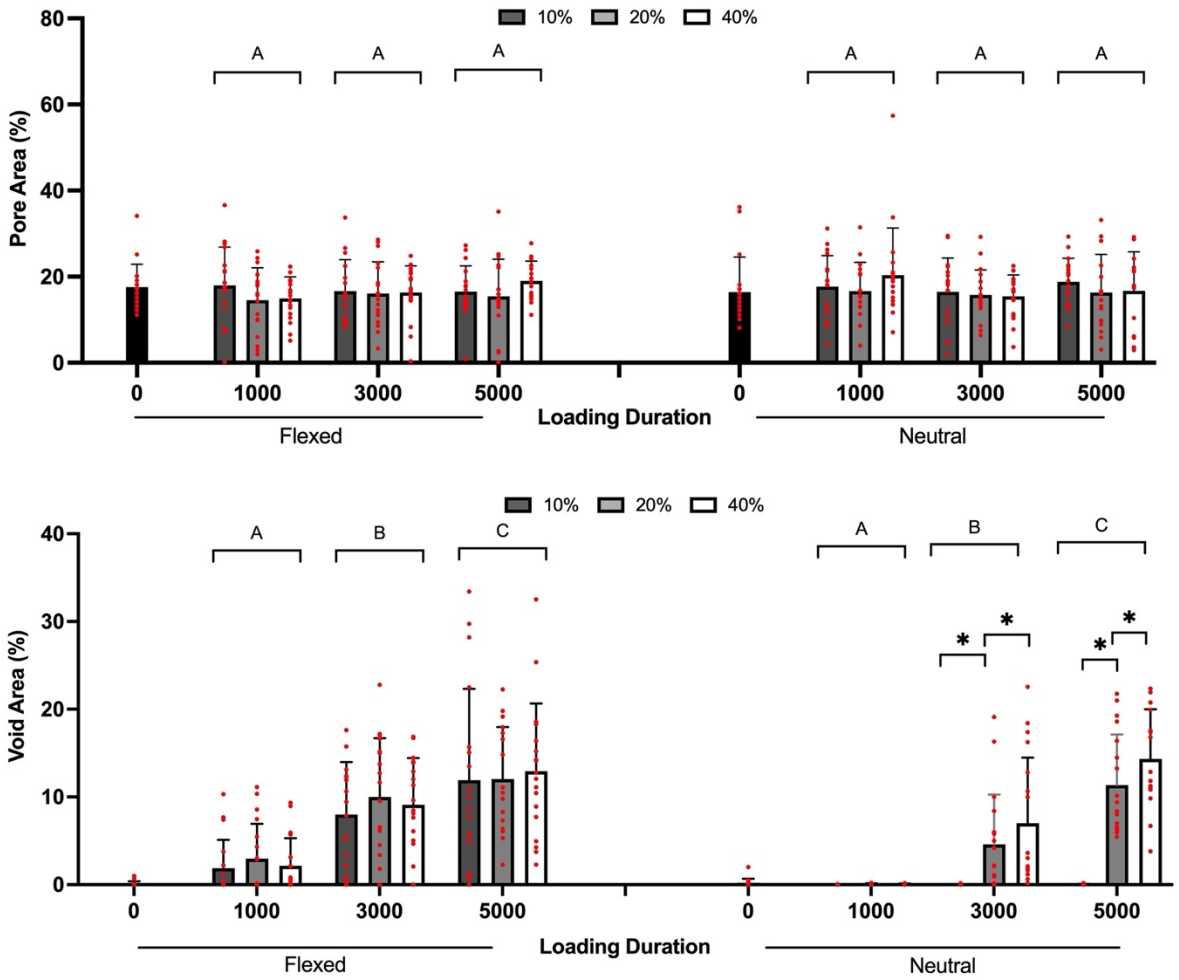

Figure 6.3.4. Pore area observed in transverse plane images (top) and void area along the CEP-subchondral bone interface observed in sagittal plane images (bottom) for each experimental group. Data presented for a loading duration of zero represents the control group. Significant differences between durations for a given posture are indicated by different capital letters. Within each duration, significant differences between variation groups are indicated by an asterisk (*). Red circles represent individual data, bars represent the mean, and error bars represent one standard deviation.

Sagittal Plane

Statistically significant main effects of loading duration and posture were detected for type II fluorescence area and fluorescence intensity (Table 6.3.1). Compared to the control group, type II fluorescence area significantly decreased following 1000 (-12%), 3000 (18%), and 5000 (-30%) cycles (Figure 6.3.5, Table 6.3.1). The mean type II fluorescence area also differed between 1000 and 5000 cycles (-18%). Type II fluorescence intensity was significantly less than the control group following 3000 (-17%) and 5000 (-29%) cycles (Table 6.3.1), but significant differences were observed been 1000-3000 (-11%) cycles and 3000-5000 (-12%) cycles, respectively (Figure 6.3.5, Table 6.3.1). Similar to the transverse plane, cyclic loading with a flexed posture significantly reduced type II fluorescence area (-14%) and fluorescence intensity (-10%) compared to neutral (Figure 6.3.6).

Main effects of loading duration and posture were observed for type I fluorescence area (Table 6.3.1). No significant effects or interactions were observed for type I fluorescence intensity (Table 6.3.1). After 3000 (-11%) and 5000 (-21%) cycles, type I fluorescence area was significantly less than the control group. The -17% reduction in type I fluorescence area between 1000 and 5000 cycles was also significant (Table 6.3.1, Figure 6.3.5). Cyclic loading applied to flexed postures reduced the type I fluorescence area by a magnitude of -17% compared to neutral (Figure 6.3.6, Table 6.3.1).

A three-way interaction effect between loading duration, loading variation, and posture was detected for the void area between the along the CEP-subchondral bone border (Figure 6.3.4). As evidenced in Figure 6.3.1, a clear demarcation without the presence of microstructural voids at the CEP-bone interface was observed in the control group. Void area corresponding to flexed postures was significantly altered as a function of loading duration. The average surface area

increased to 3.07% ± 5.44, 9.03% ± 5.98, and 12.34% ± 8.05 following 1000, 3000, and 5000 cycles, respectively (Figure 6.3.4). These changes in void area were significantly greater than the control group. Within each loading duration, however, the average void area did not significantly differ between peak variation groups when loaded in a flexed posture. Significant differences were also observed between loading durations when cyclic loading was applied to neutrally positioned joints. The average void area increased to 0.05% ± 0.06, 3.17% ± 5.92, and 8.68% ± 7.78 after 1000, 3000, and 5000 cycles, respectively. The void area after 3000 and 5000 cycles was significantly greater than the control group. Within the 3000 and 5000 cycle durations, significant differences were observed between all variation groups (Figure 6.3.4).

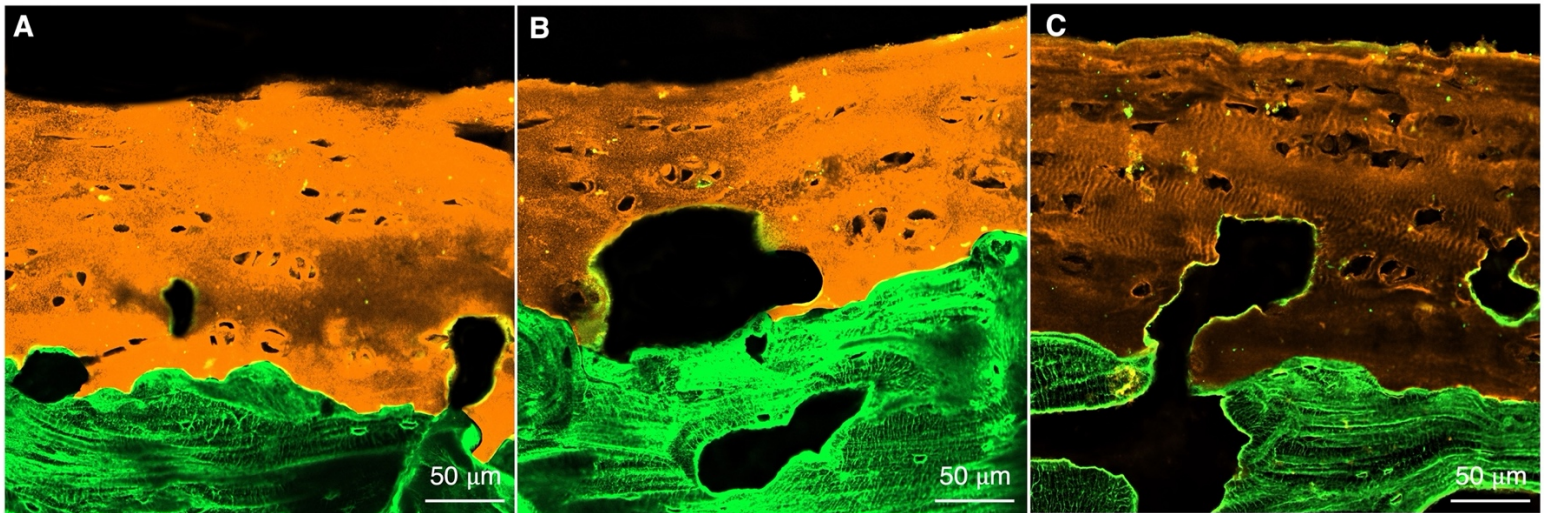

Figure 6.3.5. Representative CEP images in the sagittal plane following 1000 (A) 3000 (B) and 5000 (C) cycles.

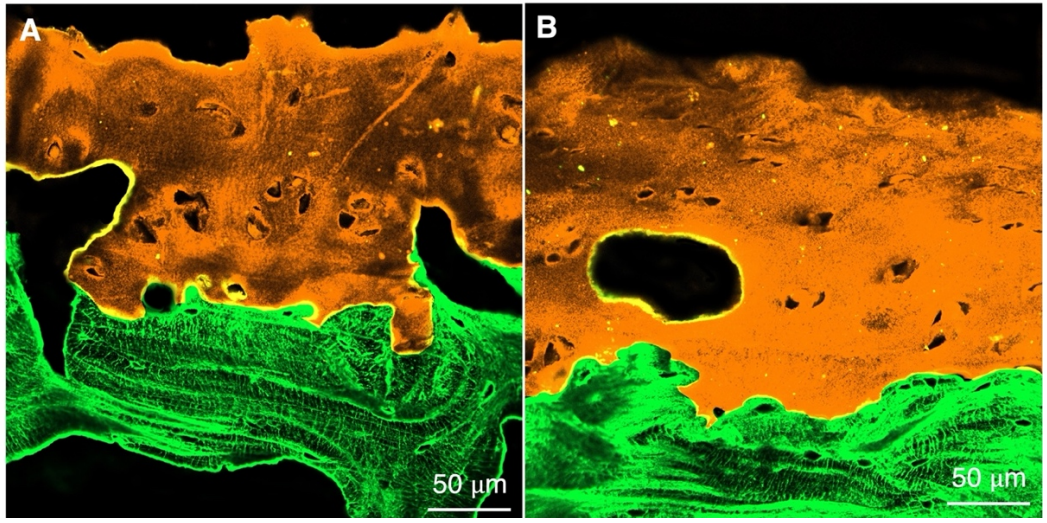

Figure 6.3.6. Representative CEP images in the sagittal plane corresponding to cyclic loading applied in flexed (A) and neutral (B) joint postures.

6.4. Discussion

Cyclic compression loading and joint posture notably influenced native type II collagen content and microstructural void development. In the transverse plane, significant changes were observed between loading durations and postures for the fluorescence intensity of type II collagen, which does not support the hypothesized interaction effect. As hypothesized, the fluorescence area of type II collagen was significantly less in flexed postures compared to neutral. However, an effect of loading duration on the fluorescence area of type II collagen was only observed after 3000 cycles, which partially supported the third study hypothesis. There were no significant changes to the fluorescence area and fluorescence intensity of type I collagen. Therefore, the fourth and fifth study hypotheses were not supported. Furthermore, the pore area was unaltered due to cyclic loading (Figure 6.3.4).

In the sagittal plane, main effects were observed for loading duration and posture on the fluorescence intensity of type II collagen, which did not support the hypothesized interaction. There was a three-way interaction between posture, loading variation, and loading duration on sub-surface void area. Generally, the void area increased with loading duration, but the time-course and magnitude of void development for a given loading duration was accelerated by cyclic loading applied to flexed spinal joints. When joints were neutrally positioned, significant effects of peak compression variation were observed beyond 3000 cycles, with greater variation yielding larger void areas (Figure 6.3.4). Despite the interaction observed for sub-surface void area, the fluorescence area of type I and type II collagen was independently affected by a loading duration greater than 3000 cycles and flexed joint postures. This finding does not support the eighth study hypothesis. Although an interaction between sub-surface void development and native collagen

content can be generally concluded, it appears that overuse injury in the CEP is initiated by sub-surface void development followed by changes to the native collagen content beyond 3000 cycles.

Although the magnitude of changes to collagen fluorescence and void area differed between flexed and neutral postures, a common pathway for injury initiation was observed, specifically when studied in the sagittal plane. That being, microstructural damage appears to precede meaningful changes to native collagen content. Given the marginal -4% change in type I fluorescence intensity resulting from flexed postures (Table 6.3.1), the significant -11% (3000 cycles) to -21% (5000 cycles) reduction in type I fluorescence area is likely driven by void development along the CEP-subchondral bone border, which, on average, increased to +9.03% and +12.34% after 3000 and 5000 cycles, respectively. This finding suggests that the extracellular matrix of the subchondral bone may have been reorganized due to microstructural voids, but the statistical similarity in type I fluorescence intensity between durations confirms that the density of collagen I fibers was similar.

With respect to type II collagen, the average fluorescence intensity of 0.94 following 1000 cycles (i.e., statistically similar to the control group), together with the significant reduction in type II fluorescence area (-12%) and increase in void area (+ 3.07%) after the same duration, suggests that microstructural damage to the CEP precedes detectable changes to the density of type II collagen fibrils when cyclic loading was applied to flexed spinal joints. A similar process is likely true in neutrally positioned joints, where a significant reduction in type II fluorescence area was observed (-13%) in the absence of a significant change to fluorescence intensity (-10%) (Table 6.3.1). As such, cycle-dependant reductions in type II fluorescence area are conceivably driven by microstructural voids, which occurred for the 20% and 40% variation groups after 3000 and 5000 cycles, respectively (Figure 6.3.4). These findings are generally supported by observations made

in articular cartilage where cyclic indentation induced early softening (i.e., shorter relaxation time) but without positive immunostaining for mechanically damaged (Col2-3/4M) and enzymatically cleaved collagen (Col2-3/4C) (Hosseini et al., 2013).

When a localized stress is applied to hyaline cartilage via indentation, water is displaced, and loads are gradually transferred to the solid matrix. The viscoelastic nature of the collagen-proteoglycan matrix is important for explaining the greater reduction in native type II collagen content (fluorescence area and intensity) for flexed joint postures and after longer loading durations in the sagittal plane. Joint flexion has been shown to increase stress concentrations experienced by the central CEP region, which subsequently increased the magnitude of vertical deflection for a given joint compression force compared to neutral postures (Malandrino et al., 2009; Wilke et al., 1999). Although moderate stresses stimulated proteoglycan synthesis in cultured articular cartilage explants following recovery (Guilak, Meyer, Ratcliffe, & Mow, 1994), higher physiological stresses (1 MPa) resulted in a > 50% reduction in proteoglycan content compared to controls (Guilak et al., 1994; Saadat, Lan, Majumdar, Rempel, & King, 2006). Proteoglycan content was not measured in the current study, but these previous findings support the notion that higher stress concentrations associated with flexed postures may have caused a more rapid loss of proteoglycan content and earlier load transfer to type II collagen fibrils compared to neutral postures. Furthermore, prolonged cyclic loading was shown to inhibit proteoglycan biosynthesis and resulted in a net loss of proteoglycan and water content (Steinmeyer & Knue, 1997). Therefore, the fibular network was conceivably exposed to more load at the 3000 and 5000 cycles durations which may have facilitated damage to the native type II collagen network (Table 6.3.1, Figure 6.3.2, Figure 6.3.5). This notion is evidenced in the current study by

a reduction in collagen II fluorescence intensity following these durations where the altered collagen structure would have decreased the affinity for primary antibody binding.

The changes in collagen fluorescence area observed in the transverse plane are unlikely to have an immediate effect on fluid and macromolecule transport through the CEP. The circumferential reduction in type II fluorescence area around the surface pores is attributed to pore compaction and deformation as the surface deflects to accommodate pressurization within the nucleus pulposus. Extracellular matrix degradation, like observed in the current study, is indeed an important element related to the calcification of CEP tissue (Guiot & Fessler, 2000). However, a necessary component includes the altered pathways of cell differentiation within the CEP (Guiot & Fessler, 2000), which was beyond the scope of the current study. CEP calcification is an important adaptation that impedes nutrient transport into the intervertebral disc and is strongly linked to intervertebral disc degeneration (Urban et al., 2004). CEP calcification is complex and involves several contributing factors and the effect of cyclic loading on the initiation of cell signalling pathways and the processes of CEP calcification are largely unknown, but this information would generate important knowledge on how CEP injury may directly contribute to the physiological homeostasis of the intervertebral disc.

The primary antibodies incorporated into the immunofluorescence stain are reactive to the native helical form of type I and type II collagen. Overtime, mechanical loading alters the helical structure of collagen within the cartilage endplate (Hosseini et al., 2013), which consequently changes the protein epitope (i.e., the piece of the antigen to which the antibody binds). Damage to the collagen epitope resulting from repeated compression render the protein unrecognizable to the primary antibody and therefore binding cannot occur. Despite the changes to the fluorescence properties (type I and type II collagen) observed in this study, it is unknown why primary antibody

binding is reduced. The first and likely reason is that the collagen proteins are damaged via cleaving and/or tearing. Therefore, the protein is likely still present in some kind of form (i.e., mass) but its functional contribution is altered. The second is that the collagen proteins have physically disappeared; however, given the *in vitro* design, enzymatic activity leading to collagen turnover is likely negligible.

The immunofluorescence stain was used to examine microstructural void development in this study despite the specificity to type I and type II collagen. The endplate extracellular matrix has a collagen composition of approximately 60% of the dry weight (Fields, Rodriguez, et al., 2013). Therefore, defined voids within the native collagen content, as observed in this study, are attributed to the presence of a structural void. The alignment of physical tissue voids with areas of negative collagen staining was confirmed via hematoxylin and eosin staining that was conducted in parallel to the multi-colour immunofluorescence approach (Zehr, Rahman, et al., 2022). Future research is required to relate structural analyses conducted via specific and general staining techniques to medical imaging modalities such a microcomputed tomography.

Some image analyses included in Chapter 3.3 were not included in the current study. The tortuosity of the CEP-subchondral bone border was quantified in all images. The relationship between tortuosity of the CEP-subchondral bone border and sub-surface void area was examined and a strong relationship was observed ($R^2 = 0.989$). Therefore, any changes to tortuosity were attributed to void development and presenting these tortuosity findings would have been redundant. Second, the tortuosity of the endplate surface (sagittal plane images) was not examined given that significant changes between control and loaded specimens (flexed, 40% compression variation, 5000 cycles) were not observed by Zehr, Rahman, et al. (2022). These findings collectively suggest that future research involving the multi-colour immunofluorescence approach

for the study of damage initiation and progression in the CEP does not require the determination of CEP-subchondral bone border tortuosity as this metric is effectively captured by subsurface void area.

Some limitations of this study are acknowledged. First, cyclic testing was performed in an ambient temperature of 21°C and specimens were hydrated with saline that was acclimated to the same temperature. Indeed, the temperature of irrigation fluid has a profound effect on cell metabolism and death in culturing experiments (Kocaoglu et al., 2011). However, when collagen fibrils in articular cartilage were studied with a scanning electron microscope, there were no significant morphological differences following a two-hour irrigation period in saline that was temperature controlled to 25°C and 37°C (Cheng et al., 2004). For this reason, testing and hydration performed at room temperature is not believed to have altered the observed changes in native collagen content. Second, this study only captured the changes in collagen content and microstructural damage caused by continuous loading without intermittent rest periods. Data on the time course of collagen synthesis and loading induced cellular processes underlying structural adaptions like calcification would provide additional insights into the mechanisms of CEP injury. In contrast, the *in vitro* design did not afford the analysis of biological processes like remodelling and repair in response to mechanical stimuli. This line of inquiry, however, requires an experimental design that includes a live animal model or culturing techniques. Third, CEP specimens were extracted immediately following the assigned loading protocol. As such, the experimental time exposure was different between control and loading duration groups. Given the results of Cheng et al. (2004), it is unlikely that the maximum 83 minute difference (i.e., between control and 5000 cycle groups) in the current study significantly altered the collagen content. Our research group confirmed the similarity in collagen fluorescence area (type I = 1.01, type II = 1.00)

and fluorescence intensity (type I = 0.99, type II = 1.02) between control specimens and a separate specimen that was exposed to similar hydration states but unloaded for 83 minutes after preconditioning tests.

6.5. Conclusion

In conclusion, the duration of compression loading and the joint posture during cyclic loading had notable effects on fluorescence area (type I and type II collagen) and fluorescence intensity (type II collagen only). The changes to native collagen were supplemented with microstructural voids along the CEP-subchondral bone border (sagittal plane sections), but no evident microstructural changes were observed in the transverse plane sections. Generally, significant changes to collagen fluorescence area (type I and II) were observed earlier in the cyclic loading protocol compared to significant changes in fluorescence intensity (type I and II). The corresponding changes in fluorescence area and void development (sagittal plane) suggests that microstructural damage may precede detectable changes to the density of collagen fibrils. As such, the development of microstructural damage may be responsible for the initial changes to mechanical properties in the central CEP.

CHAPTER 7

Incidence of Compression Induced Microinjury in the Cartilage Endplate of the Spine

Jackie D. Zehr, Joe Quadrilatero, Jack P. Callaghan

Spine, In Press, 2022

Abstract

Objective: This study investigated the incidence of microstructural endplate injuries caused by cyclic compression loading.

Methods: One hundred and fourteen porcine cervical spinal units were examined. All spinal units were exposed to pre-conditioning tests, followed by cyclic compression testing that differed by posture (flexed, neutral), loading duration (1000, 3000, 5000 cycles), and peak compression variation (10%, 20%, 40%). Microstructural injuries were examined via immunofluorescence staining for type I (i.e., subchondral bone) and type II (i.e., hyaline cartilage endplate) collagen. From the 678 acquired images, the incidence of node, avulsion, cartilage microfracture, and circumferential pore microinjuries were determined. The distribution of microinjuries between postures, spinal levels, and vertebrae were evaluated along with the association of lesion size with loading duration and variation.

Results: The incidence of avulsion injuries was significantly greater in caudal endplates (92%, $p = 0.006$). No other injuries differed between vertebrae ($p \geq 0.804$) and no significant differences were observed between spinal units ($p \geq 0.158$). With respect to posture, 100% ($p < 0.001$) and 90% ($p < 0.001$) of avulsion and node injuries, respectively occurred in flexed postures, while 82%

($p < 0.001$) of cartilage microfractures occurred with neutral postures. Loading duration was significantly associated with microinjury lesion size ($p \leq 0.003$).

Conclusions: Mechanical parameters such as posture influence the microinjury pattern in the central CEP. All injury types and their severity were significantly associated with the duration of cyclic compression loading.

7.1. Introduction

Cyclic compression loading associated with occupational lifting is epidemiologically linked to low back injuries (Marras et al., 1995; Marras et al., 1993; Norman et al., 1998). Much of the existing research on overuse low back injury has focused on the intervertebral disc, specifically the structural (Gooyers et al., 2015) and mechanical (Callaghan & McGill, 2001a; Gooyers & Callaghan, 2016; Iatridis, Maclean, & Ryan, 2005; Qasim, Natarajan, An, & Andersson, 2012) adaptations of the annulus fibrosus. Although the intervertebral disc is important, the vertebral endplate profoundly influences load transfer (Bogduk, 2012; S. H. M. Brown et al., 2008) and acts as a mechanically regulated gateway for nutrient transfer (Giers et al., 2017; Rodriguez et al., 2011). Despite its functional and physiological relevance, little is known on how parameters of acute and/or prolonged loading mediate the mechanisms of endplate injuries. Further investigations may provide important insight into the microstructural and biochemical cascade that precedes and may predispose the endplate and/or intervertebral disc to macroscopic failure.

The endplate is a hyaline cartilage juncture between subchondral bone and the intervertebral disc. As the thinnest and weakest element of a vertebra-disc unit (Ferguson & Steffen, 2003), the endplate is vulnerable to mechanical failure (Perey, 1957). Previous investigations on cadaveric lumbar spines have enabled the identification and classification of endplate pathologies along with the prevalence of injury types (Berg-Johansen, Jain, et al., 2018; Y. Wang et al., 2012). These include Schmorl's nodes, fracture lesions, erosion lesions, avulsion, and ossification (Berg-Johansen, Jain, et al., 2018; Y. Wang et al., 2012), which are typically diagnosed in advanced stages of damage using standard radiographical modalities. Despite the ability to diagnose and classify advanced endplate pathologies, there is limited evidence on the

mechanical etiology underlying specific failure patterns. This lack of evidence may, in part, be attributed to the diverse loading history of cadaveric spine tissues. Indeed, endplate pathologies were highly associated with a moderate-high physical loading history (Videman et al., 1990), but the specific loading and/or postural parameters associated with macroscopic and microscopic failure patterns remain unknown.

This study used an immunofluorescence staining approach to determine the incidence of microscopic endplate injuries in response to biofidelic cyclic compression loading (Zehr, Rahman, et al., 2022). The distribution of microinjuries between vertebra (cranial, caudal), spinal level (C3C4, C5C6), and postures (flexed, neutral) were examined. The associations of microinjury area with loading variation (10%, 20%, 40%) and loading duration (1000, 3000, 5000 cycles) were also determined. Vertical endplate deflection in response to joint compression is centrally concentrated (van Dieën, Kingma, et al., 2001); therefore, this study focused on microinjuries to the central endplate region. Given the propensity for microdamage to originate below the endplate surface (Rodriguez et al., 2011), microinjuries were visualized in the sagittal plane. Transverse images were also obtained to examine how cyclic loading influenced the incidence of circumferential damage to the cartilage pores.

Four specific hypotheses were tested. First, the incidence of all microinjuries was hypothesized to be equal between spinal levels and vertebra. Second, poromechanical finite element models of spinal units have demonstrated greater deflection of the central endplate surface when compressed in flexed joint postures (Malandrino et al., 2009). Therefore, microinjury patterns effecting the subchondral bone (node, avulsion) were hypothesized to be more prevalent in spinal units loaded in a flexed joint position. Third, in contrast, cartilage microfractures were hypothesized to be more prevalent in spinal joints that were cyclically loaded in a neutral position.

Fourth, the area of all microinjury types was hypothesized to increase as a function of loading duration.

7.2. Methods

Overview

This study used a multi-colour immunofluorescence procedure to determine the incidence of compression-induced microscopic injury patterns in the central endplate region. FSU loading parameters were the same as Chapter 5. Similar to Chapter 6, endplate tissue from 113 specimens was included in this study and the incidence of four distinct microinjury patterns were determined in the transverse and sagittal planes. From the 678 images, the incidence of circumferential pore microinjuries was determined from transverse plan images, while the incidence of cartilage microfractures, avulsion, and node microinjuries were determined from sagittal plane images. The experimental procedure and tissue handling steps are depicted in Figure 7.2.1.

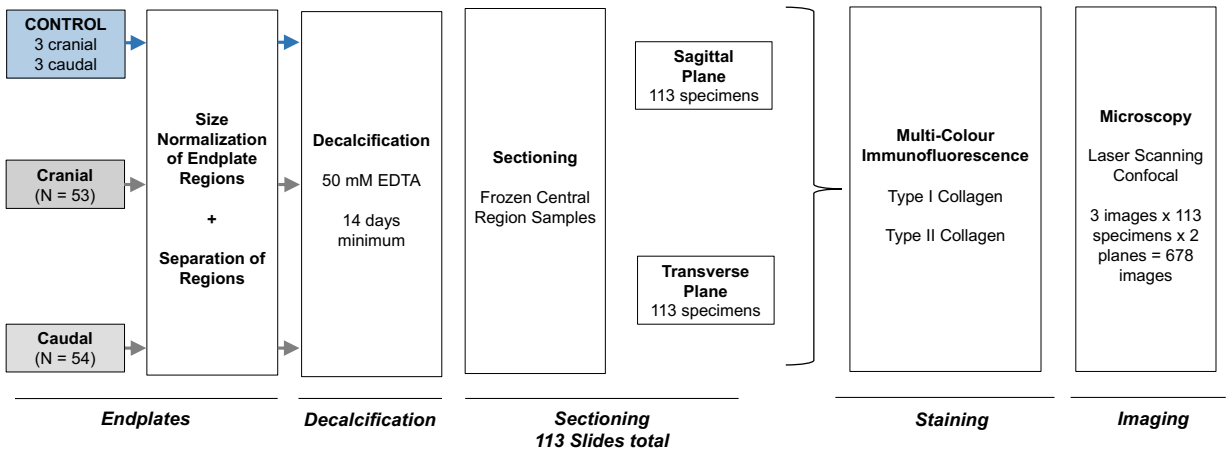

Figure 7.2.1. Schematic of the experimental procedure performed on cyclically loaded central endplate tissue.

Tissue Inclusion & Preparation

The central region of 113 endplates were included in this study. This study was focused on

the central endplate region given its structural vulnerability to fatigue fracture (Grant et al., 2001; van Dieën, Kingma, et al., 2001) and the prevalence of macroscopic endplate fracture effecting the central region (Zehr, Buchman-Pearle, et al., 2020). All 113 endplate specimens underwent post-loading microindentation procedures outlined in Chapter 5. Immediately following the non-destructive microindentation test, the size-normalized and marked central region was extracted and immediately placed in 50 mM ethylenediamimetraactic acid (pH 8.0) for a minimum of 14 days. Samples were stored at 4°C for the decalcification period.

Decalcified tissue was rinsed using phosphate buffered saline, embedded in O.C.T compound, and frozen in liquid nitrogen cooled isopentane. These prepared endplate samples were stored at -80°C for approximately 3 months prior to sectioning. Frozen OCT embedded samples were transferred directly from the -80°C freezer to a temperature-controlled cryostat (-20°C) for sectioning. Serial cryosections in the transverse and sagittal planes were cut to a thickness of 10 μm and placed on Superfrost™ Plus Gold glass microscope slides. Within a specimen, transverse and sagittal plane sections were placed on a single microscope slide; therefore, a total of 113 slides were prepared for staining.

Immunofluorescence Staining

Immunofluorescence analysis performed with primary antibodies against type I and type II collagen (Zehr, Rahman, et al., 2022). This antibody cocktail effectively identified and dissociated the native collagen content of the hyaline cartilage endplate (type II) from the subchondral bone (type I) and has been used to evaluate mechanically induced constitutive and microstructural damage in spine tissues (Zehr, Rahman, et al., 2022).

A laser scanning confocal microscope (Axio Observer Z1 LSM800, Zeiss, Oberkochen, Germany) was used to visualize all prepared slides. Three representative images were taken of

each specimen and in each plane (i.e., a total of 6 images per FSU) using a 20X Plan-Apochromat objective (NA0.8) and ZEN 2.3 System software (Zeiss, Oberkochen, Germany). 488 nm and 561 nm lasers were used with a pinhole size set to 41µm. The master gain for AF 488 and AF 555 channels was 662 V and 650 V, respectively, with a corresponding digital offset of 0 and digital gain of 1.0 in both channels.

Microinjury Classification

A total of 678 images were acquired, totalling 36 images per experimental group, excluding the group consisting of flexed posture, 40% variation, 5000 cycles group (1 macroscopic fracture observed and therefore omitted from all analyses), which contained 30 images. This analysis focused on the incidence of microstructural injuries. In the transverse plane, the presence or loss of cartilage (i.e., type II collagen) around the pores was examined. Compared to the control (Figure 7.2.2A), if the appearance of subchondral bone (i.e., type I collagen) was observed around any pore within the image, a microinjury incidence was recorded. In the sagittal plane images, the incidence of nodes, avulsion between the cartilage and subchondral bone, and microfracture to the endplate were recorded. Compared to the control (Figure 7.2.2B), a node was defined as the formation of a vertical void that extended into the subchondral bone, similar to macroscopic Schmorl's node injuries observed using magnetic resonance imaging (Hamanishi, Kawabata, Yosii, & Tanaka, 1994; Kyere et al., 2012). Nodes that extended into the subchondral bone but did not fully penetrate the endplate surface were also recorded as an incidence. An avulsion was defined as the formation of a structural gap between the cartilage and subchondral bone (Berg-Johansen, Jain, et al., 2018). Lastly, trends of crack and void development in the endplate cartilage were observed in the absence of microstructural damage to the subchondral bone. These incidences were defined as cartilage microfractures. For every microinjury incidence, the area of

microstructural damage/void(s) was determined in ImageJ (Rasband, 1997-2018) and expressed as a percentage of the overall image area.

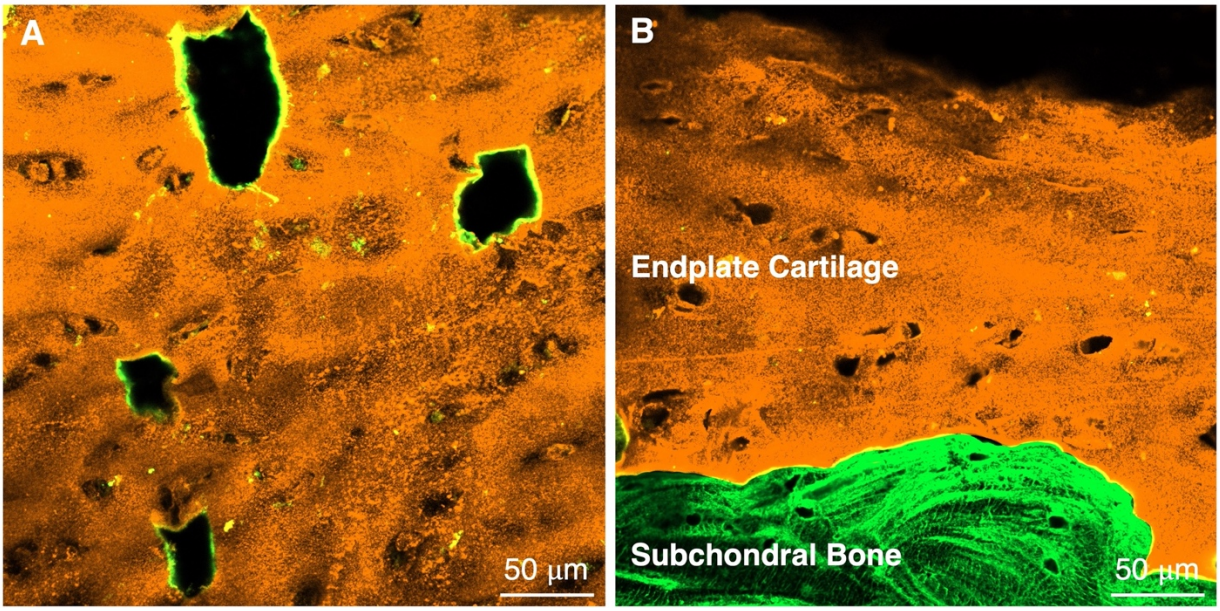

Figure 7.2.2. Control endplate specimens imaged in the transverse (A) and sagittal planes (B). Type I collagen staining (green) of subchondral bone and type II collagen staining (orange) of the hyaline cartilage endplate.

Statistics

Descriptive statistics were used to assess the incidence of microinjury types. Chi-squared (χ^2) tests were further used to compare the prevalence of different microinjuries and their distributions between vertebra (cranial, caudal), spinal level (C3C4, C5C6), and postures (neutral, flexed). Logistic regressions were used to examine the associations between area of microinjuries with loading variation and loading duration. All statistical tests were performed using the R programing language (RStudio Version 3.34, Rstudio Inc, Boston, MA).

7.3. Results

A total of 70 microinjuries were observed in the sagittal plane (node, avulsion, cartilage microfracture) and 40 microinjuries were observed in the transverse plane (pore) (Table 7.3.1). Of the 40 microinjuries observed in the transverse plane, 73% (29) coincided with a microinjury in the sagittal plane.

Distribution of Microstructural Injuries

The total incidence of microinjury was similar between cranial [sagittal: 40% (28); transverse: 53% (21)] and caudal [sagittal: 60% (36); transverse: 47% (19)] endplates. The distribution of avulsion microinjuries significantly differed between vertebra, with 92% (OR = 11.0) occurring in the caudal endplate. The incidence of other microinjuries was not significantly different between vertebrae (Table 7.3.2).

Endplate microinjuries were evenly distributed between C3C4 [sagittal: 49% (34); transverse: 50% (20)] and C5C6 [sagittal: 51% (36); transverse: 50% (20)] spinal units. The types of microinjury did not significantly differ between spinal units (Table 7.3.2).

Similar distributions of microinjuries were observed between flexed [sagittal: 53% (37); transverse: 58% (23)] and neutral [sagittal: 47% (33); transverse: 42% (17)] postures. The incidence of node (90%, OR = 9.0) and avulsion (100%, OR = 12.0) microinjuries were significantly greater in flexed postures than neutral (Table 7.3.2). In contrast, the incidence of cartilage microfractures was significantly greater in neutral postures compared to flexed (82%, OR = 4.4). The incidence of pore injury did not significantly differ between postures (Table 7.3.2).

Association of Endplate Microinjury

When separately examined, significant linear associations were observed between the

lesion area of all microinjury patterns and loading duration (circumferential pore: $R^2 = 0.907$, $p = 0.003$; cartilage microfracture: $R^2 = 0.930$, $p < 0.001$; avulsion: $R^2 = 0.933$, $p < 0.001$; node: $R^2 = 0.995$, $p < 0.001$), but not loading variation (circumferential pore: $R^2 = 0.229$, $p = 0.537$; cartilage microfracture: $R^2 = 0.389$, $p = 0.222$; avulsion: $R^2 = 0.298$, $p = 0.350$; node: $R^2 = 0.315$, $p = 0.411$). The initiation and progression of pore, node, cartilage microfracture, and avulsion microinjuries as a function loading duration are depicted in Figures 7.3.1-7.3.4.

Table 7.3.1. Incidence and prevalence of microstructural injury classifications for each experimental group.

Microinjury Type	Variation	Prevalence	Flexed			Neutral		
			1000	3000	5000	1000	3000	5000
Pore (Transverse)	10%	37%	0	2	5	0	1	3
	20%		0	3	5	0	0	4
	40%		0	2	6	0	3	6
Node	10%	19%	1	2	4	0	0	0
	20%		2	3	3	0	0	1
	40%		0	1	2	0	0	1
Cartilage	10%	35%	0	1	1	1	4	5
	20%		0	1	1	0	5	4
	40%		1	1	1	2	5	5
Avulsion	10%	11%	0	1	1	0	0	0
	20%		1	1	2	0	0	0
	40%		2	2	2	0	0	0

Table 7.3.2. Chi-squared (χ^2) results representing the distribution of microinjuries between vertebra (cranial, caudal), spinal levels (C3C4, C5C6), and postures (flexed, neutral). For a given microinjury type, significant differences between groups ($p < 0.05$) is indicated with an asterisk (*).

Microinjury Type	Vertebra		Spinal Level		Posture	
	χ^2	p	χ^2	p	χ^2	p
Pore (Transverse)	0.040	0.842	0.000	1.000	0.992	0.319
Node	0.061	0.804	0.522	0.457	13.807	$< 0.001^*$
Cartilage	0.041	0.840	1.990	0.158	21.478	$< 0.001^*$
Avulsion	7.594	0.006^*	0.093	0.760	11.344	$< 0.001^*$

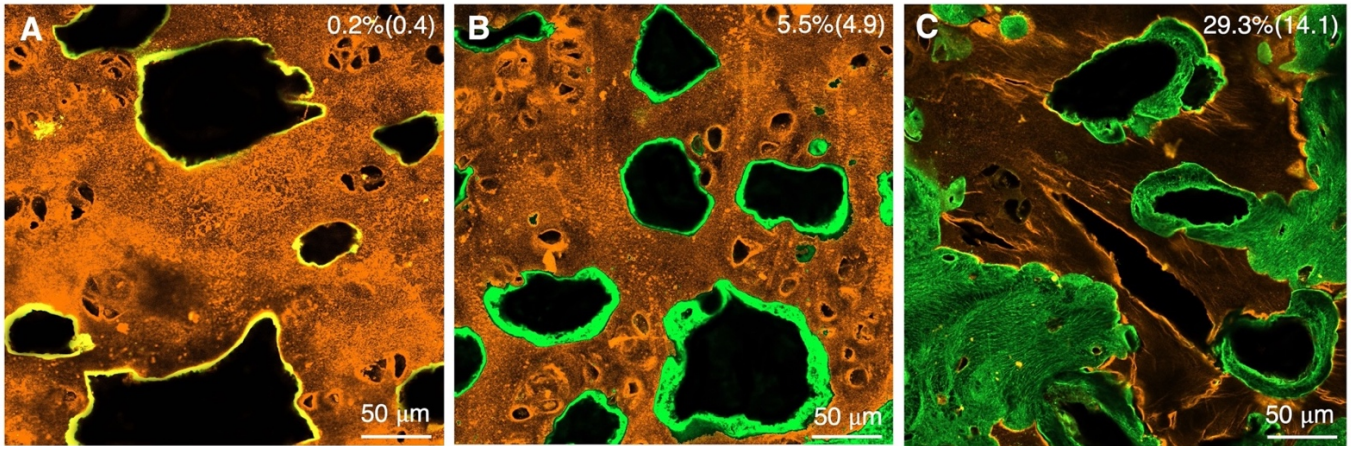

Figure 7.3.1. Representative images of circumferential pore microinjuries following 1000 (A), 3000 (B), and 5000 (C) cyclic compression cycles showing type I collagen (green) and type II collagen (orange) staining. Values placed in the top right corner represent the average (standard deviation) area occupied by circumferential pore damage for each duration.

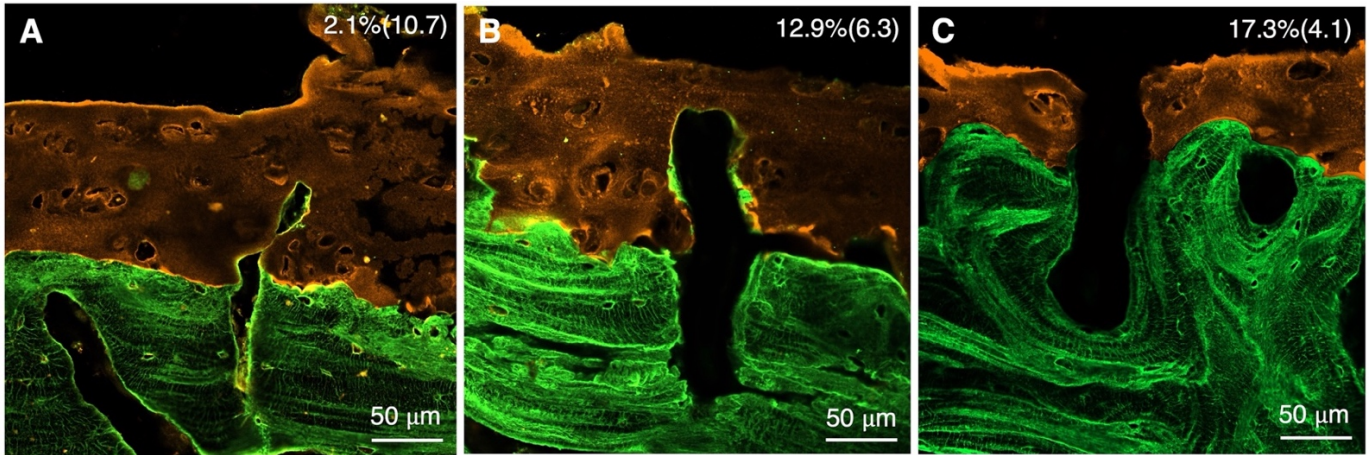

Figure 7.3.2. Representative images of node microinjuries following 1000 (A), 3000 (B), and 5000 (C) cyclic compression cycles showing type I collagen (green) and type II collagen (orange) staining. Values placed in the top right corner represent the average (standard deviation) area occupied by circumferential pore damage for each duration.

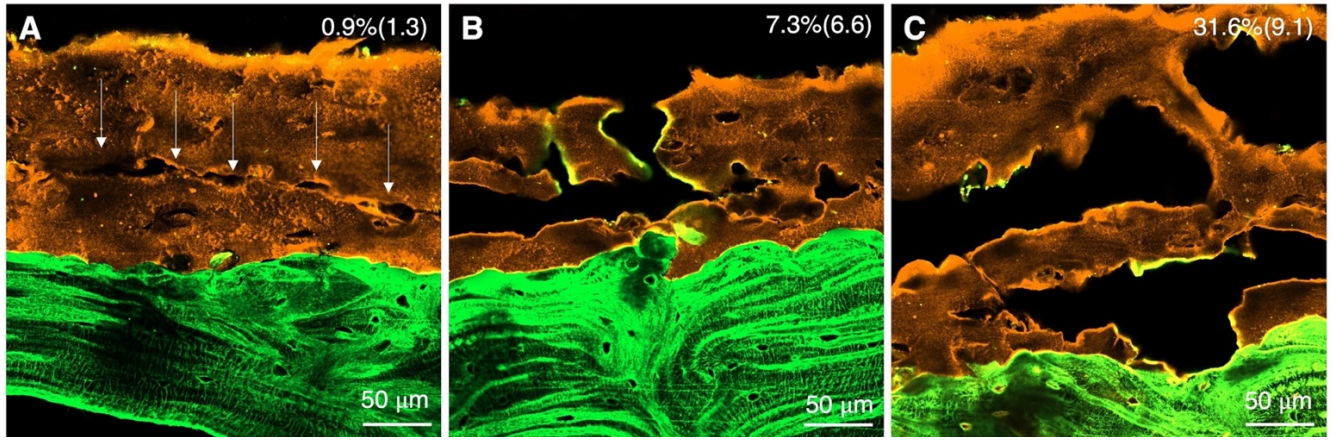

Figure 7.3.3. Representative images of cartilage microfracture following 1000 (A), 3000 (B), and 5000 (C) cyclic compression cycles showing type I collagen (green) and type II collagen (orange) staining. The depicted arrows point to the formation of a crack within the endplate cartilage. Values placed in the top right corner represent the average (standard deviation) area occupied by circumferential pore damage for each duration.

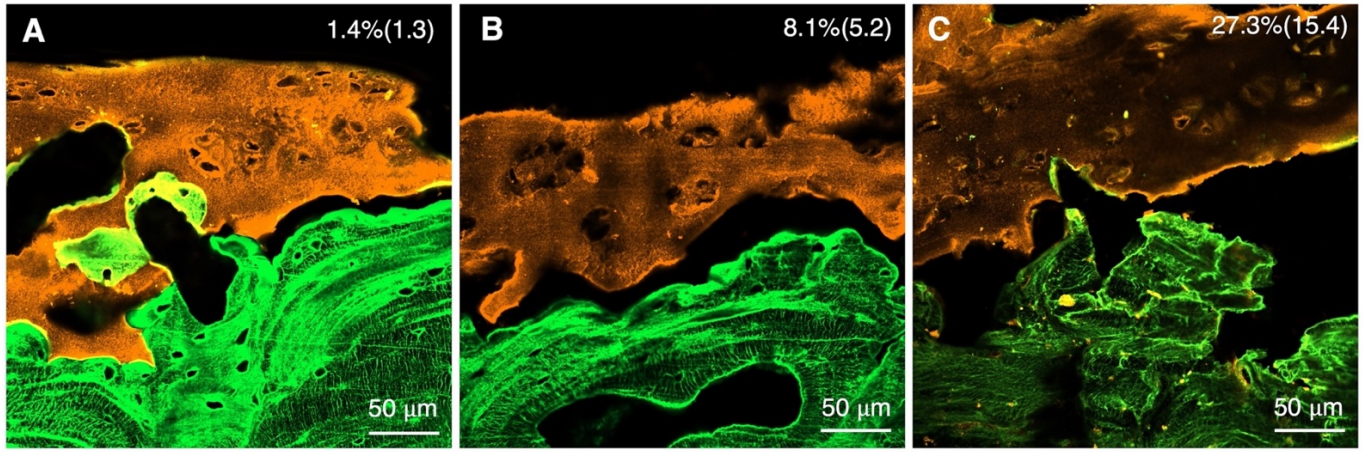

Figure 7.3.4. Representative images of avulsion microinjuries following 1000 (A), 3000 (B), and 5000 (C) cyclic compression cycles showing type I collagen (green) and type II collagen (orange) staining. Values placed in the top right corner represent the average (standard deviation) area occupied by circumferential pore damage for each duration.

7.4. Discussion

This study examined the incidence of endplate microinjury resulting from cyclic compression loading. Microinjury incidence did not significantly differ between spinal levels, and significant differences between vertebra were only observed for avulsion injuries, which occurred in the caudal endplate 92% of the time (Table 7.3.1). This finding partially supports the first study hypothesis. Although joint posture did not appreciably influence the overall incidence of endplate microinjury, the distribution of injury types significantly differed between flexed and neutrally loaded FSUs. The incidence of avulsion (100%) and node (90%) microinjuries were significantly greater with flexed joint postures, while cartilage microfractures were most common in neutral joint postures (82%). Together, these findings support the second and third study hypotheses, respectfully. The incidence of all examined endplate injuries, and their size, had a significant association with loading duration, thereby supporting the fourth study hypothesis. These results collectively demonstrate that, for a low-moderate compression force, the parameters of the cyclic loading can influence the type of microinjury initiation in the central endplate region.

With the exception of avulsion, the distribution of microinjuries to the cranial and caudal endplates was similar in the current study (Table 7.3.1). Existing data on the distribution of endplate injuries between vertebra are mixed. Zhao, Pollintine, Hole, Adams, and Dolan (2009) showed that endplate lesions were more common in the caudal endplate compared to the cranial endplate. In contrast, Y. Wang et al. (2012) showed a similar distribution between cranial and caudal endplates; however, adjacent endplates were frequently affected together. Since the current study included an equal number of cranial and caudal endplates in each experimental group, it is unlikely that the presented findings were affected by the analysis of one endplate per specimen. Although documented strength differences between cranial and caudal endplates do not support

the distribution of node, cartilage and pore microinjuries, this evidence may support the one-sided distribution of avulsion injuries to the caudal endplate (Grant et al., 2001).

The mechanical mechanisms underlying avulsion injuries remain poorly understood. Previous *in vitro* studies on human (Balkovec, Adams, Dolan, & McGill, 2015; Berg-Johansen, Fields, et al., 2018) bone-disc-bone segments demonstrated that annulus-cartilage and bone-cartilage avulsion injuries occurred when exposed to uniaxial tension. These findings suggest that avulsion injuries in the current study were primarily driven by flexion bending, which induces an axial tensile load on the posterior portion of the annulus. As such, it is plausible that cartilage-bone avulsion injuries were initiated in the posterior region (Berg-Johansen, Jain, et al., 2018) and propagated anteriorly via mode 1 loading (i.e., crack opening caused by global stress applied perpendicular to the crack plane). This notion may be supported by the current findings, where the extent of avulsion damage observed in the central region increased as a function of loading duration (Figure 7.3.4). An avulsion mechanism that is dominated by posture is further supported by the frequent coincidence of cartilage-bone avulsion injuries with intervertebral disc herniations (P. Lama et al., 2014; Rajasekaran, Bajaj, Tubaki, Kanna, & Shetty, 2013), which are attributed to low-moderate compression combined with flexion-extension motion (Callaghan & McGill, 2001a).

The observation of node microinjuries in the current study is supported by previous findings indicating a central distribution (81%) of macroscopic Schmorl's nodes (Y. Wang et al., 2012). Although developmental and congenital origins have been speculated (Vernon-Roberts & Pirie, 1977), a chronic overuse injury mechanism is suggested (Y. Wang et al., 2012) and may be demonstrated in the current study by microstructural differences between control and loaded groups (Figure 7.2.1A vs Figure 7.3.2). The strong association of nodes and cartilage

microfractures with posture may, in part, be attributed to poromechanical responses for compression load transfer. For a given compression force, flexed postures increase intradiscal pressure (Schultz et al., 1979; Wilke et al., 1999) and reduce fluid flow through the endplate (Malandrino et al., 2009), thereby inducing greater central endplate deflection compared to neutral (Malandrino et al., 2009). Larger deflections of the compliant cartilage may facilitate greater buckling of the supporting trabecular bone possibly leading to the formation of nodes or structural weaknesses beneath the cartilage surface. The accumulation of damage below the endplate surface has been demonstrated using microcomputed tomography imaging of degenerated cadaveric specimens (Rodriguez et al., 2011). This plausible mechanism for node microinjuries is contrasted by the formation of damage within the cartilage endplate and in the absence of microstructural injury to the subchondral bone, which was more prevalent in neutral postures (Table 7.3.1 and 7.3.2). The evenly distributed load across neutrally positioned joints (Malandrino et al., 2009) may prevent regional stress concentrations on the trabecular bone and therefore isolate fatigue-related microdamage to the cartilage. Future studies are required to directly evaluate how cyclic compression loading influences the constitutive and mechanical properties of the subchondral bone and how this may influence the propensity for node formation and cartilage microinjuries.

Some limitations should be acknowledged. A porcine model was used as a scaled surrogate for the human lumbar spine (Yingling et al., 1999), but the study design was strengthened by the examination of tissue that had similar and healthy initial conditions. Secondary motivations for the study design prevented the application of load until fatigue-failure. This prevented the association between patterns of microscopic and macroscopic endplate damage to be explored. Future studies will aim to bridge this gap.

7.5. Conclusions

In conclusion, parameters of mechanical loading can profoundly influence the type of microinjury experienced by the central endplate region. Significant differences in injury distribution were observed between postures (flexed, neutral) and vertebrae (cranial, caudal). Avulsion and node injuries were significantly more prevalent in flexed postures, while cartilage microfractures were more prevalent in neutral postures. Unlike node, cartilage, and pore injuries, the distribution of avulsion injuries was significantly greater in the caudal endplate. All injury types and their severity were significantly associated with the duration of cyclic compression loading but not the variation in peak compression force.

CHAPTER 8

Experimentally Dissociating the Overuse Mechanisms of Endplate Fracture Lesions and Schmorl's Node Injuries Using the Porcine Cervical Spine Model

Jackie D. Zehr, Michael I. Watson, Jack P. Callaghan

Clinical Biomechanics, 104; 105946, 2023

Abstract

Objectives: Compared to the documented overuse mechanisms of endplate fracture lesions, the cause of Schmorl's node injuries remains unknown, despite existing hypotheses. Therefore, this study aimed to examine and dissociate the overuse injury mechanisms of these spinal pathologies.

Methods: Forty-eight porcine cervical spinal units were included. Spinal units were randomly assigned to groups that differed by initial condition (control, sham, chemical fragility, structural void) and posture (flexed, neutral). Chemical fragility and structural void groups involved a verified 49% reduction in localized infra-endplate trabecular bone strength and removal of central trabecular bone, respectively. All experimental groups were exposed to cyclic compression loading that was normalized to 30% of the predicted tolerance until failure occurred. The cycles to failure were examined using a general linear model and the distribution injury types were examined using chi-squared statistics.

Results: The incidence of fracture lesions and Schmorl's nodes was 31(65%) and 17(35%), respectively. Schmorl's nodes were exclusive to chemical fragility and structural void groups and 88% occurred in the caudal joint endplate ($p = 0.004$). In contrast, 100% of control and sham spinal units sustained fracture lesions, with 100% occurring in the cranial joint endplate ($p < 0.001$).

Spinal units tolerated 665 fewer cycles when cyclically loaded in flexed postures compared to neutral ($p = 0.015$). Furthermore, the chemical fragility and structural void groups tolerated 5318 fewer cycles compared to the control and sham groups ($p < 0.001$).

Conclusions: These findings demonstrate that Schmorl's node and fracture lesion injuries can result from pre-existing differences in the structural integrity of trabecular bone supporting the central endplate..

8.1. Introduction

Schmorl's nodes and fracture lesions are spinal pathologies affecting the cartilage endplate of the lumbar spine. Schmorl's nodes are classically defined by a circular fracture containing regular margins and the vertical intrusion of nucleus pulposus into the adjacent vertebral body (Schmorl & Junghanns, 1971; Seymour et al., 1998; Takahashi et al., 1995). This morphology is distinct from endplate fracture lesions, which are long, irregular in shape, and may or may not involve the intrusion of nucleus pulpous into adjacent vertebrae (Brinckmann et al., 1988; Gallagher et al., 2006; Y. Wang et al., 2012). In post-mortem and medical imaging studies, Schmorl's nodes were documented in 4-30% of individuals (Brayda-Bruno, Albano, Cannella, Galbusera, & Zerbi, 2018; Hamanishi et al., 1994; Mok et al., 2010; Pfirrmann & Resnick, 2001; Y. Wang et al., 2012), while fracture lesions had a prevalence of 7-9% (Brayda-Bruno et al., 2018; Y. Wang et al., 2012). Although both endplate injuries are associated with clinical outcomes like intervertebral disc degeneration and pain reporting (Mok et al., 2010; Williams, Manek, Sambrook, Spector, & Macgreger, 2007), the mechanical pathways leading to these distinct failure patterns remains unknown. Experiments aimed at dissociating these injury mechanisms may provide new insights into their prevention, treatment, and diagnoses.

Endplate fracture lesions have been empirically linked to acute (Gunning et al., 2001; Yingling et al., 1997) and repeated (Brinckmann et al., 1988; Gallagher et al., 2006; Parkinson & Callaghan, 2007b; Zehr, Buchman-Pearle, et al., 2020) compression loading while the etiology of Schmorl's nodes remains a point of contention. Historically, Schmorl's nodes have been speculated to result from compression trauma, developmental disorders, degenerative conditions, and infections (Mok et al., 2010; Peng et al., 2003; N. Zhang et al., 2010). A degenerative condition characterized by local osteonecrosis and/or fragility to the subchondral trabecular bone is a

hypothesized and conceivable mechanism related to progressive overload (Peng et al., 2003). In partial support of this hypothesis, recent *in vitro* research has demonstrated the development of microstructural voids directly beneath the central endplate surface in response to cyclic subthreshold compression, particularly in flexed joint postures (Zehr, Quadrilatero, & Callaghan, 2022a). However, compared to healthy controls, cyclic compression loading did not appreciably alter the organic phase (i.e., collagen) of trabecular bone, suggesting that necrosis and/or fragility may be unrelated to the processes of mechanical fatigue alone (Zehr, Quadrilatero, et al., 2022b). Despite the hypotheses and recent evidence, Schmorl's node injuries have yet to be experimentally reproduced, rendering its mechanism unknown compared to the well-documented cause of fracture lesions.

Therefore, this *in vitro* study aimed to experimentally dissociate the overuse mechanisms of Schmorl's node and fracture lesion injuries. Specifically, the effects of localized trabecular bone integrity and joint posture on endplate failure morphology and joint lifespan were examined in response to subthreshold repeated compression loading. Two specific hypotheses were made. First, considering existing hypotheses for the pathogenesis of Schmorl's nodes (Peng et al., 2003), the high prevalence of fracture lesions in response to cyclic loading applied to initially healthy spinal units (Brinckmann et al., 1988; Gallagher et al., 2006; Parkinson & Callaghan, 2007b; Zehr, Buchman-Pearle, et al., 2020), and the lack of compression-induced damage to the organic phase of trabecular bone (Zehr, Quadrilatero, et al., 2022b), it was hypothesized that Schmorl's nodes would be exclusive to spinal joints that were pre-disposed with trabecular bone fragility and/or structural voids, irrespective of posture. Second, the presence of structurally compromised trabecular bone and flexed joint postures were hypothesized to independently result in significantly fewer tolerated loading cycles.

8.2. Methods

Overview

Prior to cyclic loading, the integrity of the subchondral bone was altered in one of four ways: 1) 49% reduction in compressive strength (chemical fragility); 2) it was structurally removed (structural void); 3) it was negligibly altered via micro drilling (sham); 4) it was unaltered (control). All spinal units were exposed to cyclic compression while positioned in a flexed or neutral posture. Cyclic loading was applied until failure occurred and the morphology of the resulting endplate injuries was classified according to existing criteria. A schematic of the procedure followed in this study is depicted in Figure 8.2.1.

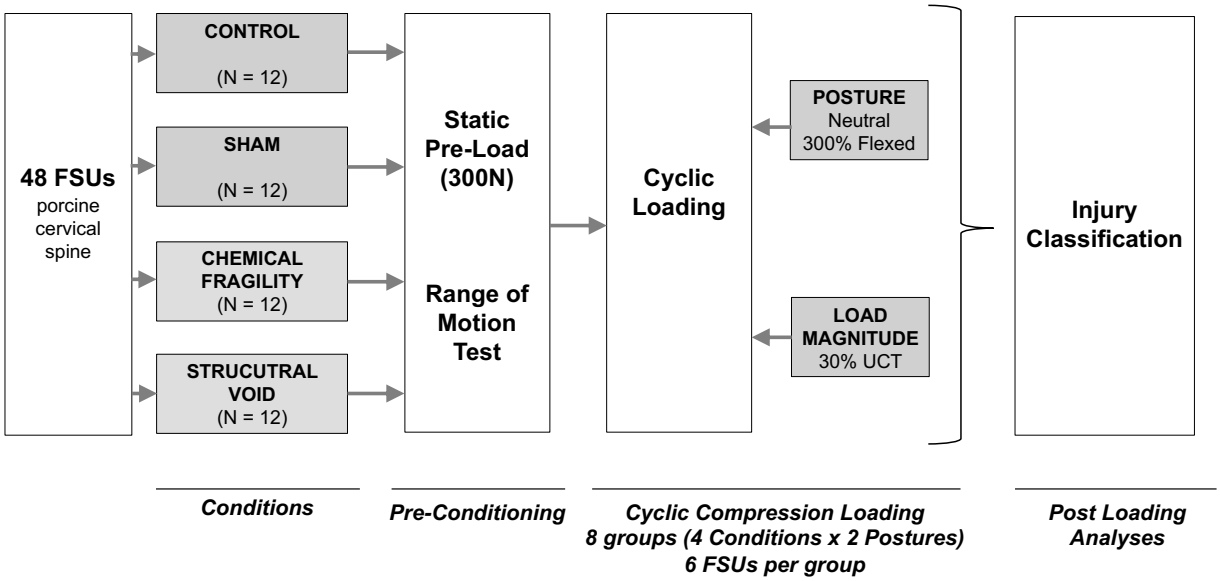

Figure 8.2.1. A schematic of the experimental procedure.

Specimens

Thirty fresh-frozen porcine cervical spines were acquired from an abattoir. All specimens were stored at -20°C and thawed at room temperature for a minimum of 12 hours prior to testing. Once thawed, excess muscle and adipose tissue were dissected away from the osteoligamentous structure. Individual vertebrae (2 C3, 2 C4, 1 C5, 1 C6) were excised from the first six cervical

spine specimens and one vertebra from each cervical spine was randomly selected for inclusion in the experiment conducted to verify chemically induced bone fragility. The C3C4 and C5C6 functional spinal units (FSUs) were excised from the remaining 24 cervical spine specimens for inclusion in the experiment designed to test the effects of trabecular bone fragility and posture on endplate failure morphology. The quality of all exposed intervertebral discs were visually examined and satisfied the grade 1 criteria outlined by the Galante (1967) scale. Therefore, no evident signs of degeneration were present.

Development and Verification of Chemically Induced Fragility

Six vertebrae (2 C3, 2 C4, 1 C5, 1 C6) were included in this analysis, which matches the sample size of all experimental groups. Using a drill press, a 0.3 mm hole was drilled to a depth of 14 mm in the anterior to posterior direction at the epiphyseal plate of the caudal endplate for C3 and C5 vertebra and cranial endplate for C4 and C6 vertebra since these endplates are joint interfacing in the intact FSU (Figure 8.2.2A). The standardized 14 mm depth enabled the chemical agent (6M hydrochloric acid) to be directly administered to the trabecular bone inferior to the central endplate region. A 0.25 mm needle cannula penetrated the 0.3 mm port and was attached to an intravenous line (drop factor = 60 gtt/ml) and a Deltec® 3100 modular micro infusion pump (Figure 8.2.2B). The 6M hydrochloric acid was administered through the intravenous line at a controlled drip rate of 16.67 µl per 5-minute interval, yielding a flow rate of 200 µl/hour. While wrapped in saline soaked gauze, all vertebrae underwent a two-hour drip duration for a total administration volume of 400 µl. A two-hour drip duration was selected based on extensive pilot testing demonstrating an approximate trabecular exposure volume that was greater than 125 mm^3 but less than 512 mm^3. These target volume criteria were selected based on dimensions of Schmorl's node injuries observed in magnetic resonance imaging of the human spine (Hamanishi

et al., 1994) and cadaveric lumbar spine tissue (Y. Wang et al., 2012) and scaled to the dimensions of porcine vertebra (Table X and X). A buffering agent was not used to neutralize residual hydrochloric acid and this decision was based on two factors. First, hydrochloric acid is neutralized with a water-based solution and this reaction generates heat, which may facilitate damage to the cartilage surface and an uncontrolled thermal variable. Second, injecting a basic fluid that does not react with the bone is likely to strengthen the structure, which may offset the acid-induced weakness.

Following the drip exposure, a trabecular bone beam (5 mm anterior-posterior depth, 5 mm medial-lateral depth) was cut from the central region of the vertebral body (including both endplates) using a precision saw (VC-50, LECO Instruments, Mississauga, Canada) (Figure 8.2.2C) and submerged in 0.9% saline to maintain hydration. Two 5 mm × 5 mm × 5 mm trabecular bone cubes were extracted from each beam; one from the exposed region and a paired control from the trabecular bone supporting the opposite endplate within the same vertebra (Figure 8.2.2C and D). Uniaxial ultimate compression testing was performed on control and acid exposed trabecular bone cubes using a serial robot (Yaskawa Motoman, Miamisburg, OH, USA) that had a load cell secured to the end-effector (110516-2, ATI Industrial Automation, Apex, NC, USA) (Figure 8.2.3). Compression force was applied along the marked longitudinal axis (i.e., superior-inferior) at a displacement rate of 0.1 mm/s until failure occurred. Force and vertical position of the end-effector were sampled at a rate of 10 Hz and used to quantify nominal stress and engineering strain. From the obtained stress-strain curves, the apparent modulus, yield stress, and ultimate stress were determined and compared between control and acid exposed specimens.

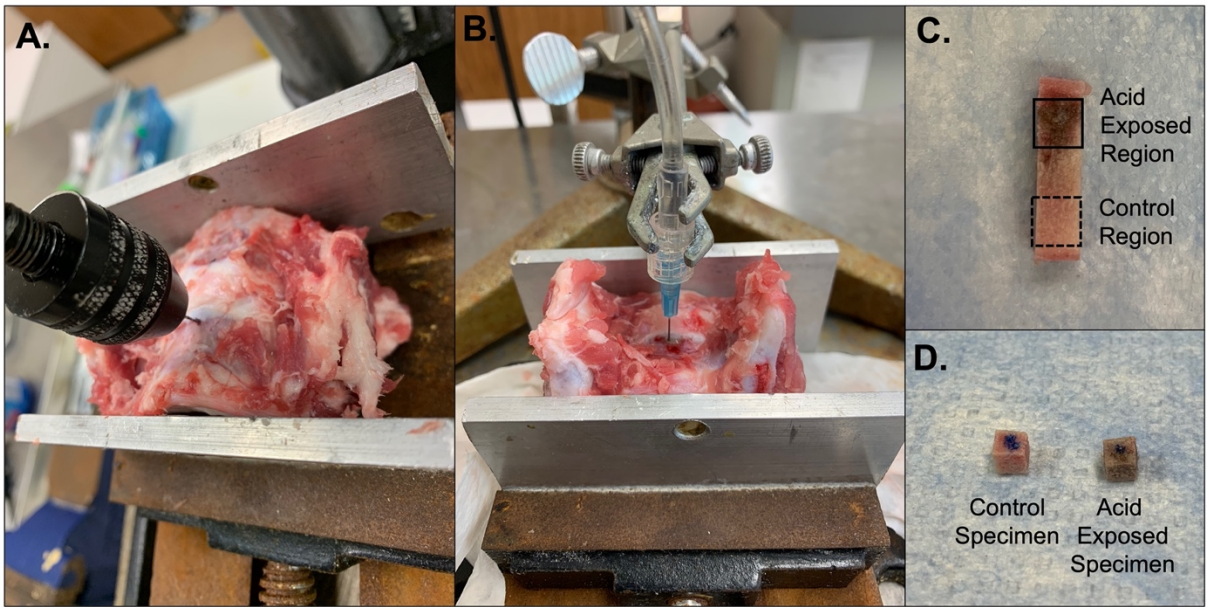

Figure 8.2.2. A) Drilling of the 0.3 mm hole to a standardized depth of 14 mm at the epiphyseal plate. B) 0.25 mm needle used to administer the 6M hydrochloric acid to subchondral bone beneath the central endplate region. C) Bone beam (5 mm anterior-posterior × 5mm medial-lateral) with acid exposed and paired control regions. D) 5 mm × 5 mm × 5mm trabecular bone cubes included in compression testing.

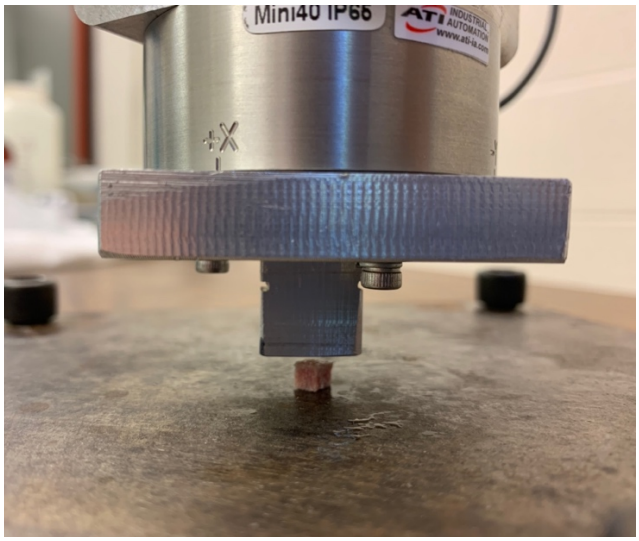

Figure 8.2.3. Experimental setup for the uniaxial compression tests of 5 mm x 5 mm x 5mm trabecular bone cubes.

Apparent modulus (i.e., ratio of stress and strain within the linear elastic region of the stress-strain curve), yield stress (i.e., the stress achieved at the linear limit of the stress-strain curve), and ultimate stress (i.e., maximum stress achieved prior to step-like reduction) quantities

of each specimen are reported in Table 8.2.1 and stress-strain relationships are depicted in Figure 8.2.4. The average ± standard deviation apparent modulus for control and acid exposed specimens was 34.9 ± 2.3 MPa and 34.0 ± 4.7 MPa, respectively. On average, the yield stress was 2.0 MPa (42%) less in acid exposed specimens compared to controls. Furthermore, the two-hour acid exposure resulted in a 2.9 MPa (49%) reduction in ultimate stress. Given the brittle response observed in acid-exposed bone (i.e., similar modulus, minimal plastic deformation, reduced ultimate stress), the procedure for inducing localized trabecular bone fragility was deemed effective and standardized for all experimental testing conducted heron after.

Table 8.2.1. The dimensions and mechanical properties of acid exposed (E0) and paired control (C0) specimens.

	Vertebra	A-P (mm)	M-L (mm)	S-I (mm)	Apparent Modulus (MPa)	Yield Stress (MPa)	Ultimate Stress (MPa)
E01	C6	5.00	5.10	4.92	33.73	3.54	3.59
C01		5.05	4.99	5.03	33.23	5.41	6.32
E02	C3	5.04	5.06	5.14	29.41	2.06	2.07
C02		4.98	4.90	5.01	34.35	5.08	6.23
E03	C4	5.03	4.97	5.09	32.87	2.41	2.45
C03		4.95	4.87	4.97	35.24	4.53	4.58
E04	C5	4.83	4.81	4.98	41.35	3.29	3.97
C04		5.06	4.89	4.91	38.64	4.93	6.63
E05	C3	5.05	5.15	5.09	37.16	3.91	4.56
C05		5.07	5.03	5.05	35.97	4.21	6.39
E06	C4	5.04	5.06	5.03	29.19	1.56	1.62
C06		5.04	5.05	5.07	32.12	4.74	5.59

A-P = anterior-posterior dimensions; M-L = medial-lateral dimensions; S-I = superior inferior dimensions

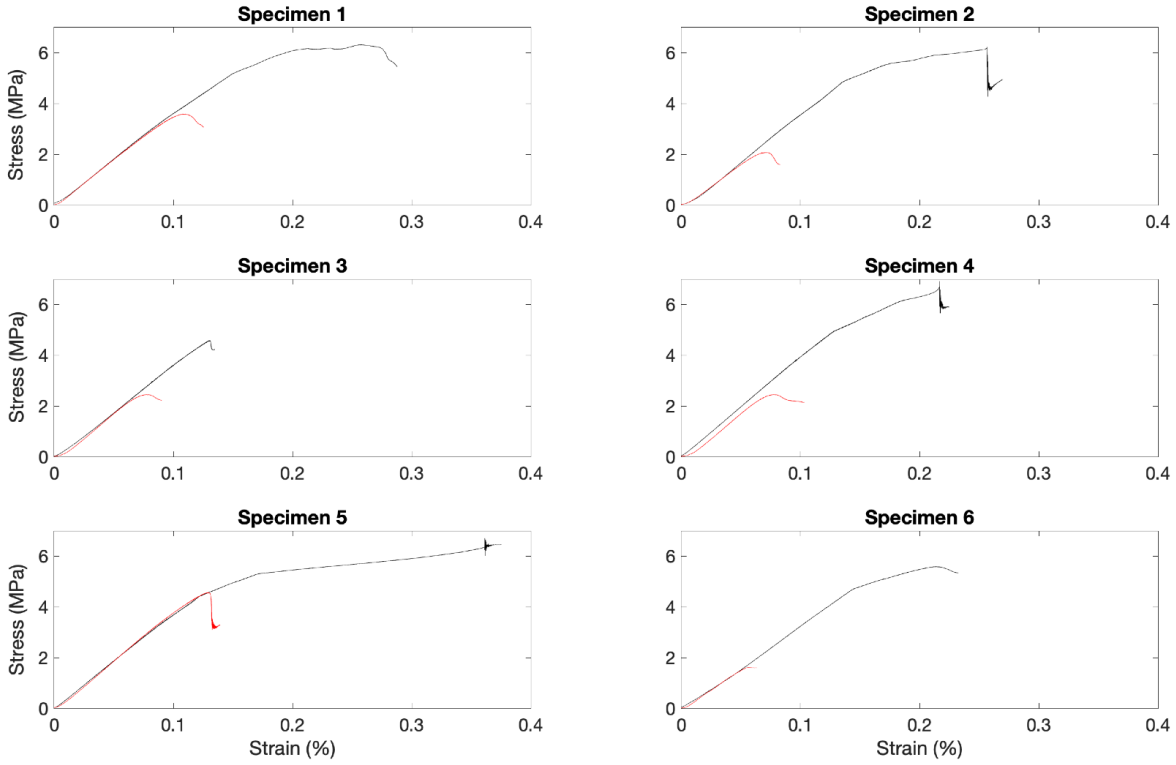

Figure 8.2.4. The nominal stress-engineering strain relationships for each specimen. Red lines represent acid exposed specimens and black lines represent paired controls.

Experimental Preparation and Conditions

After dissection and approval of intervertebral disc quality, width and depth measurements of the exposed endplates were obtained using a digital caliper and used to calculate the surface areas using the equation of an ellipse. The average surface area of the cranial and caudal endplates was input to an existing regression equation for the prediction of joint ultimate compression tolerance (Parkinson et al., 2005), which was later used to normalize the peak compression forces during cyclic testing.

Spinal units were randomly assigned to one of four initial conditions where the integrity of the trabecular bone supporting the central endplate region was uniquely altered. 1) The chemical fragility involved procedures discussed in "*Development and Verification of Chemically Induced*

Fragility." The order that cranial and caudal vertebra underwent the 2-hour drip exposure was randomized between specimens (Figure 8.2.5). This condition specifically tested the effect of pre-existing trabecular bone fragility on endplate failure morphology, which is a proposed but untested mechanism of Schmorl's nodes (Peng et al., 2003). 2) The structural void group involved using a drill press to bore a 5mm hole from the central region of exposed endplates to within 1mm of the joint endplate in the cranial and caudal vertebra (Figure 8.2.5). The 5 mm holes were bored in alignment with the vertebral body orientation and the procedure was X-ray guided (VZW2556RH5, Raymax Medical, Brampton, Canada) to prevent damage to the joint endplate and to ensure depth consistency. Although the structural void model is not fully representative of necrosis and/or void that is observed clinically, it did challenge the hypothesis that structural damage and/or necrosis may predispose the spine to Schmorl's node injuries (Peng et al., 2003). 3) The sham group involved drilling the 0.3 mm by 14 mm port at the epiphyseal plate of the endplates cranial and caudal to the intervertebral disc. A null fluid was not administered, and this group demonstrated that any changes to injury morphology and joint lifespan were not attributed to structural defects caused by micro-drilling. 4) The control group involved no additional dissection or micro-drilling.

Exposed endplates of the cranial and caudal vertebra were mounted to separate aluminum cups using 19-gauge steel wire and nonexothermic dental plaster (Denstone, Southbend, IN). The superior cup was fastened to a flexion-extension carriage that was actuated by a torque motor (T120-106-1K, Sensor Data Technologies, Sterling Heights, MI) and positioned in series to the compression actuator of a material testing system (Model 8872, Instron, Toronto, ON). The inferior cup was bolted to an aluminum base that overlaid a bearing covered surface (Zehr & Callaghan, 2022).

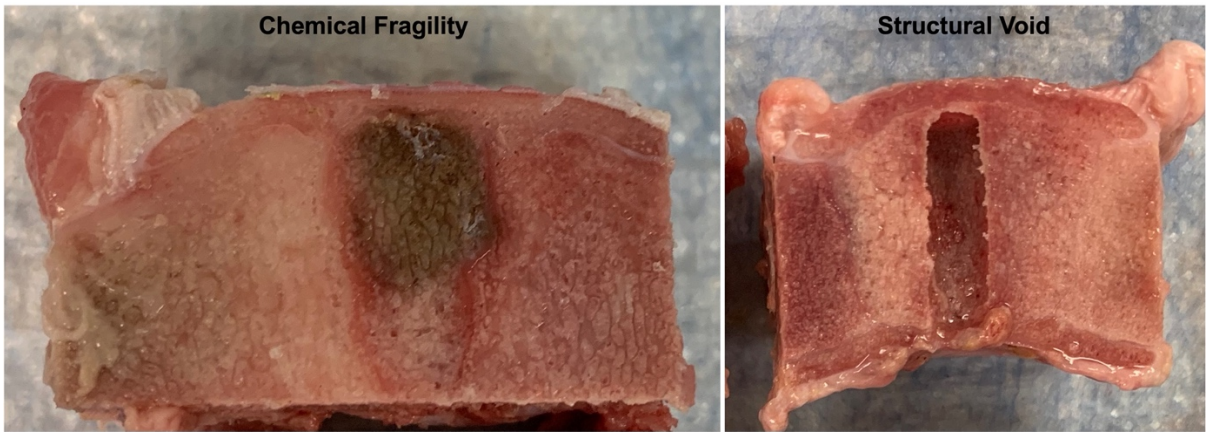

Figure 8.2.5. Representative images of the chemical fragility (left) and structural void (right) conditions within C4 vertebra of a C3C4 spinal unit. The depicted vertebrae have been sectioned in the coronal mid-plane to reveal the chemical fragility exposure and the structural void. Both vertebra within each spinal unit underwent chemical fragility and structural void conditions prior to cyclic compression testing.

Pre-Conditioning & Cyclic Loading

Spinal units were wrapped with saline soaked gauze and received superficial moistening every 20 minutes to prevent dehydration during pre-conditioning and cyclic loading tests. All loading procedures were conducted at room temperature.

First, a 0.3 kN compression force was applied for 15-minutes to counter post-mortem tissue swelling (Callaghan & McGill, 1995). Second, a range-of-motion test was performed to identify the flexion-extension neutral zone. Spinal units were rotated into flexion and then extension at a rate of 0.5 degrees/second until a ±6 Nm moment was reached for a total of four repetitions. Throughout this test, FSUs were exposed to a 0.3 kN compression force and the raw moment and angular position data were sampled at a rate of 25 Hz (Galil Motion Control, Rocklin, CA). The neutral zone limits were determined as the linear boundaries of a fourth-order polynomial fit to the moment-angle data of the final two repetitions (Thompson et al., 2003). A neutral posture was defined as the mid-point between the linear boundaries. A flexed posture was defined as three times the difference between neutral and the linear flexion limit, which is non-destructive and

physiologically achievable during a forward bending or repeated lifting task (Dunk, Kedgley, Jenkyn, & Callaghan, 2009).

FSUs were exposed to cyclic testing while positioned in a flexed or neutral posture. Therefore, eight experimental groups that differed by initial condition (control, sham, chemical fragility, structural void) and posture (flexed, neutral) were examined (i.e., 4 x 2 experimental design). Each experimental group contained six FSUs, with a total of 48 FSUs included in this study. The applied compression waveform represented the force-time profile of lumbar spine joint loading during a lifting task (Gooyers et al., 2018), had a frequency of 1 Hz (Zehr, Buchman-Pearle, et al., 2020), and a peak force that was normalized to 30% of the predicted ultimate compression tolerance. A normalized compression force of 30% approximates the average low back joint loading during a moderate demand repeated lifting task (Gooyers et al., 2018). A bias load of 0.3 kN was further incorporated into the compression waveform to approximate the baseline compression force associated with maintaining the mass of the human trunk in an upright posture. FSUs were cyclically loaded until evidence of macroscopic failure was observed and all compression waveforms were applied using a materials testing system that was operated in load control. The applied compression force and actuator position were continuously sampled at a rate of 50 Hz.

Data and Injury Analysis

Post-loading analyses were conducted on the position-time signal. The cycle at which injury occurred was objectively determined by an precipitous step in vertical position (Brinckmann et al., 1988; Gooyers & Callaghan, 2015; Parkinson & Callaghan, 2009). Following cyclic loading, FSUs were transected through the intervertebral disc for the analysis and classification of macroscopic failure morphology to the cartilaginous endplates. Visual assessments of the facets

and intervertebral disc were also conducted. The annulus and remaining nucleus pulposus tissue were debrided from both endplates. The observed failure morphologies were compared to published criteria for the classification of fracture lesions (Brinckmann et al., 1988; Gallagher et al., 2006) and Schmorl's nodes were defined in accordance to diagnostic medical imaging/injury classification studies (Hamanishi et al., 1994; Kyere et al., 2012; Y. Wang et al., 2012). After classifying the morphology of surface failure, both vertebral bodies were cut in the coronal mid-plane using the precision saw to document evidence of intrusion. Thus, the morphology observed on the endplate surface and evidence of intrusion were collectively used for classification.

Following cyclic loading, FSUs were transected through the intervertebral disc for the analysis and classification of macroscopic failure morphology to the cartilaginous endplates. Visual assessments of the facets and intervertebral disc were also conducted. After classifying the morphology of surface failure, both vertebral bodies were cut in the coronal mid-plane using the precision saw to observe the trabecular bone structure. Endplate fracture lesions were classified in accordance to published criteria (Alessa & Ning, 2018; Callaghan & McGill, 2001b; Callaghan et al., 1999; Gooyers et al., 2018) and the definition of a Schmorl's node aligned with diagnostic medical imaging (Hamanishi et al., 1994; Kyere et al., 2012) and injury classification studies (Y. Wang et al., 2012). That is, specimens with a defined circular fracture together with the vertical intrusion of the nucleus pulpous into the adjacent vertebral body were given the classification of Schmorl's node. Representative surface images of a Schmorl's node and crack fracture lesions are depicted in Figure 8.2.6.

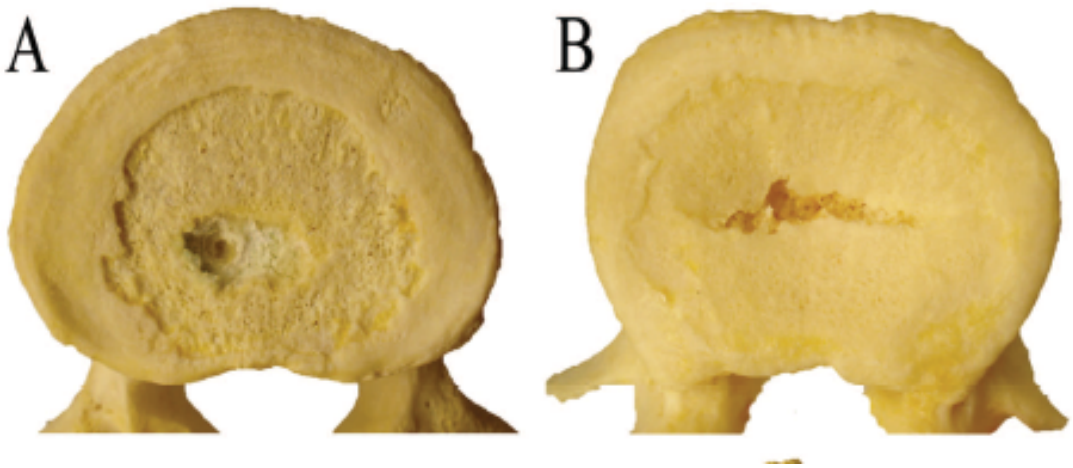

Figure 8.2.6. The types of endplate injuries that were examined in this study. Schmorl's node (A) and crack lesion (B). This image was taken from page 1434 of Wang et al. (2010).

Statistical Analyses

Statistical procedures were conducted using the R programming language (Version 3.34, RStudio Inc, Boston, MA). First, a three-way analysis of variance (ANOVA) test was performed to examine the effects of spinal level (C3C4, C5C6), initial condition (control, sham, chemical fragility, structural void) and posture (neutral, flexed) on endplate surface area. Since endplate area was used to normalize applied compression forces, this test was used to verify the randomization of specimens between experimental groups. Second, a three-way ANOVA test was conducted to evaluate the effects of condition and posture on the number of cycles tolerated until failure. For all ANOVA tests, alpha was set to 0.05 and a Tukey's *post hoc* test was performed with Bonferroni corrections, where applicable. Third, descriptive statistics were used to report the incidence of fracture lesion and Schmorl's node injuries. Chi-squared (χ^2) tests were further used to compare the distributions of injury types between joint endplates (cranial to the intervertebral disc, caudal to the intervertebral disc), spinal levels (C3C4, C5C6), and postures (neutral, flexed).

8.3. Results

Randomization

No significant main effects or interactions were observed for endplate surface area ($p \geq 0.114$). These findings confirm that FSUs assigned to each group were similar in size and therefore experienced similar normalized peak compression forces.

Injury Incidence and Distribution

Representative failure morphologies observed for each group are presented in Figure 8.3.1-8.3.4. The incidence of fracture lesions and Schmorl's node injuries was 31 (65%) and 17 (35%), respectively. Of the observed fracture lesions, 94% were defined by a crack morphology. Fracture lesions were more frequently observed in control (12, 39%) and sham (12, 39%) specimens, compared to chemical fragility (2, 6%) and structural void (5, 16%) groups (Table 8.3.1). In contrast, Schmorl's node injuries were exclusive to specimens pre-disposed with chemical fragility (10, 59%) or a structural void (7, 41%). No observable injuries were observed to intervertebral disc or facets. The distributions of fracture lesion ($\chi = 33.20$, $p < 0.001$) and Schmorl's node ($\chi = 8.27$, $p = 0.004$) injuries were significantly different between vertebra. The incidence of fracture lesions was significantly greater in the cranial vertebra (28, 90%), while a greater incidence of Schmorl's nodes occurred in the caudal vertebra (14, 82%). No significant differences in injury distributions were found between spinal levels [fracture lesions: $\chi = 0.09$, $p = 0.763$; Schmorl's node: $\chi = 0.10$, $p = 0.769$] and postures [fracture lesions: $\chi = 0.784$, $p = 0.376$; Schmorl's node: $\chi = 1.02$, $p = 0.312$].

Table 8.3.1. Incidence of fracture and node injuries to the cranial, caudal, or both endplates of FSUs assigned to each condition.

Failure Type	Condition			
	Control	Sham	Chemical Fragility	Structural Void
Cranial Fracture	11	10	2	5
Caudal Fracture	0	0	0	0
Both Fracture	1	2	0	0
Cranial Node	0	0	0	2
Caudal Node	0	0	9	5
Both Node	0	0	1	0

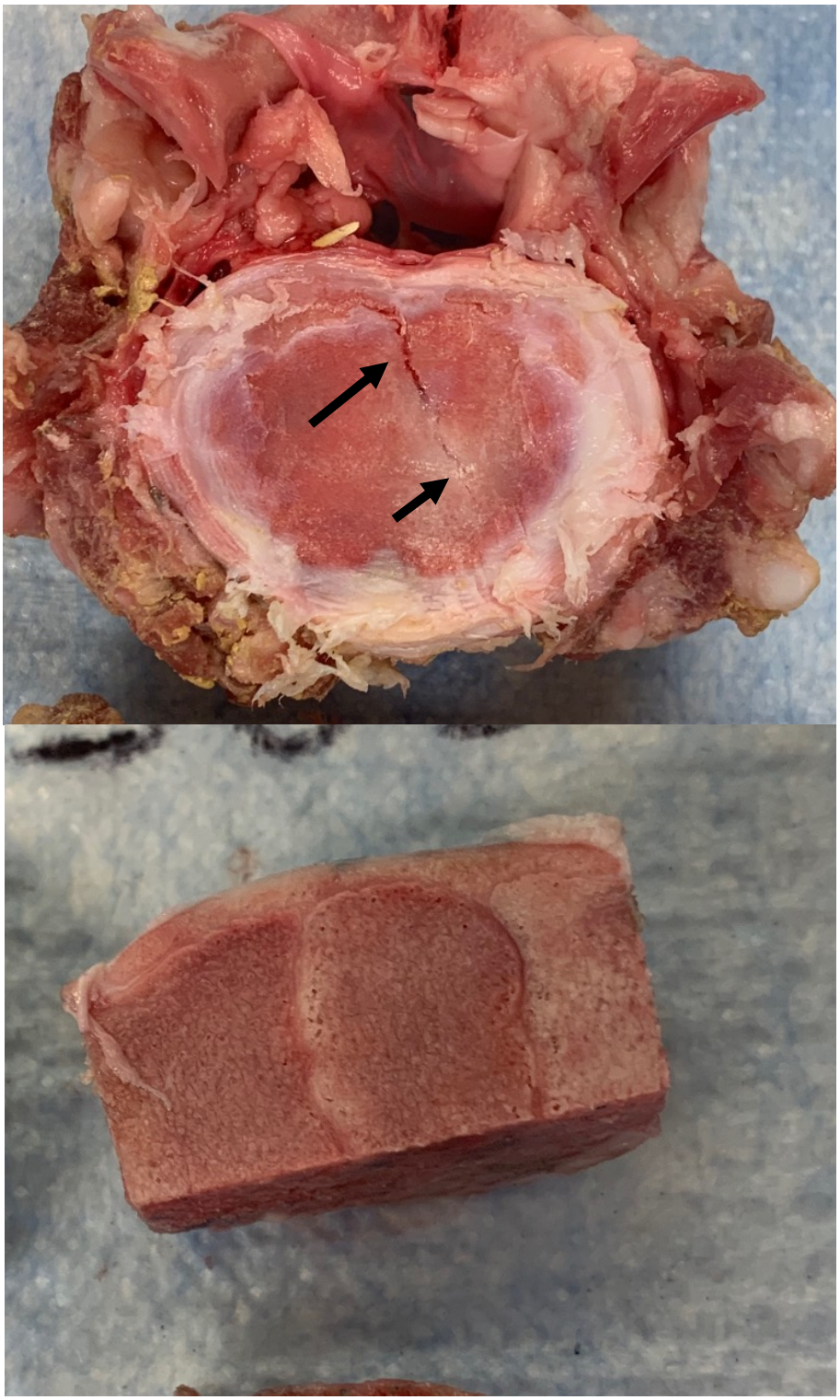

Figure 8.3.1. Representative images of the injury morphology observed in the control condition. The top image was taken in the transverse plane and the bottom image represents a coronal mid-plane section. The depicted injury was classified as a crack fracture lesion.

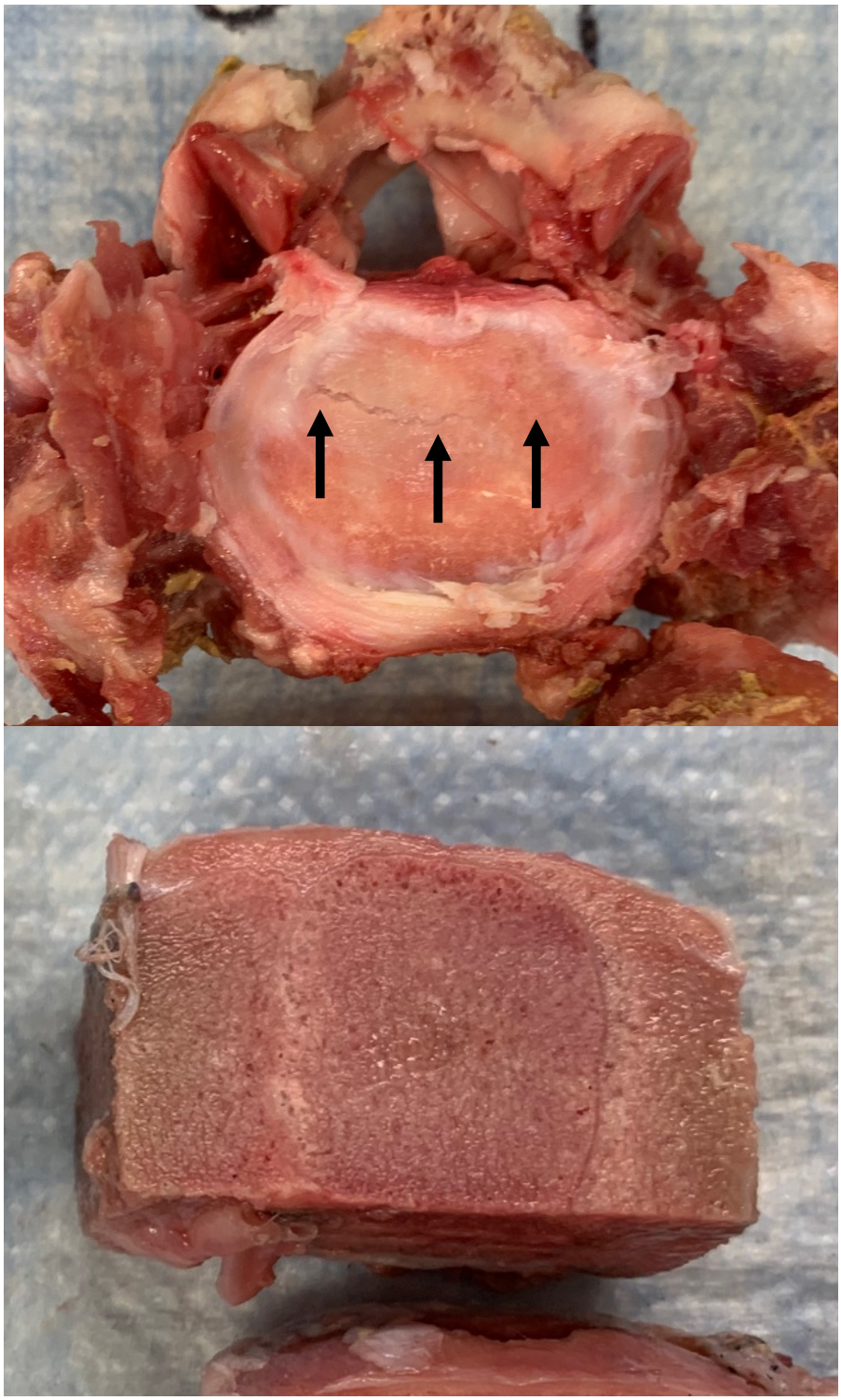

Figure 8.3.2. Representative images of the injury morphology observed in the sham condition. The top image was taken in the transverse plane and the bottom image represents a coronal mid-plane section. The depicted injury was classified as a crack fracture lesion.

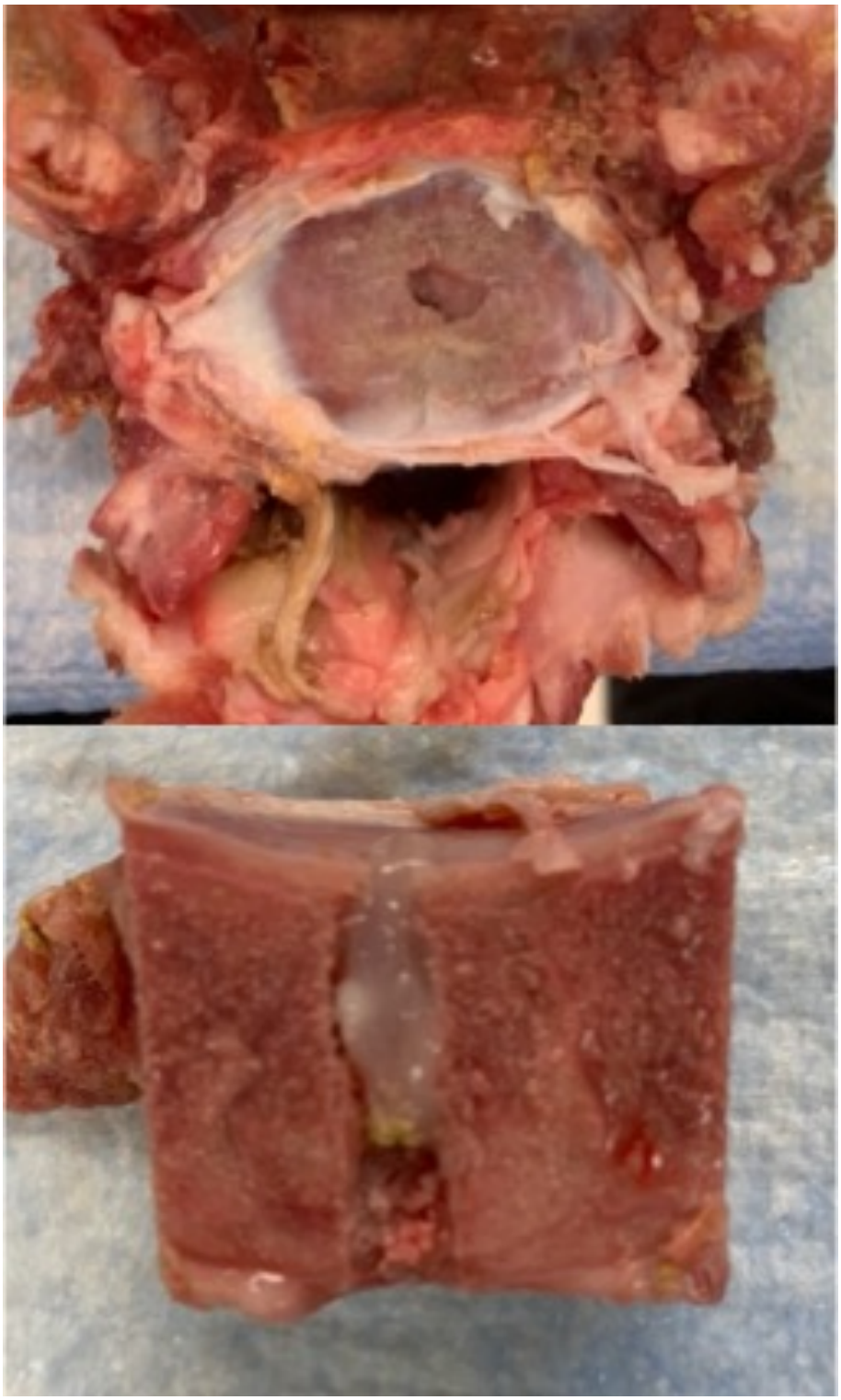

Figure 8.3.3. Representative images of the injury morphology observed in the structural void condition. The top image was taken in the transverse plane and the bottom image represents a coronal mid-plane section. The depicted injury was classified as a Schmorl's node.

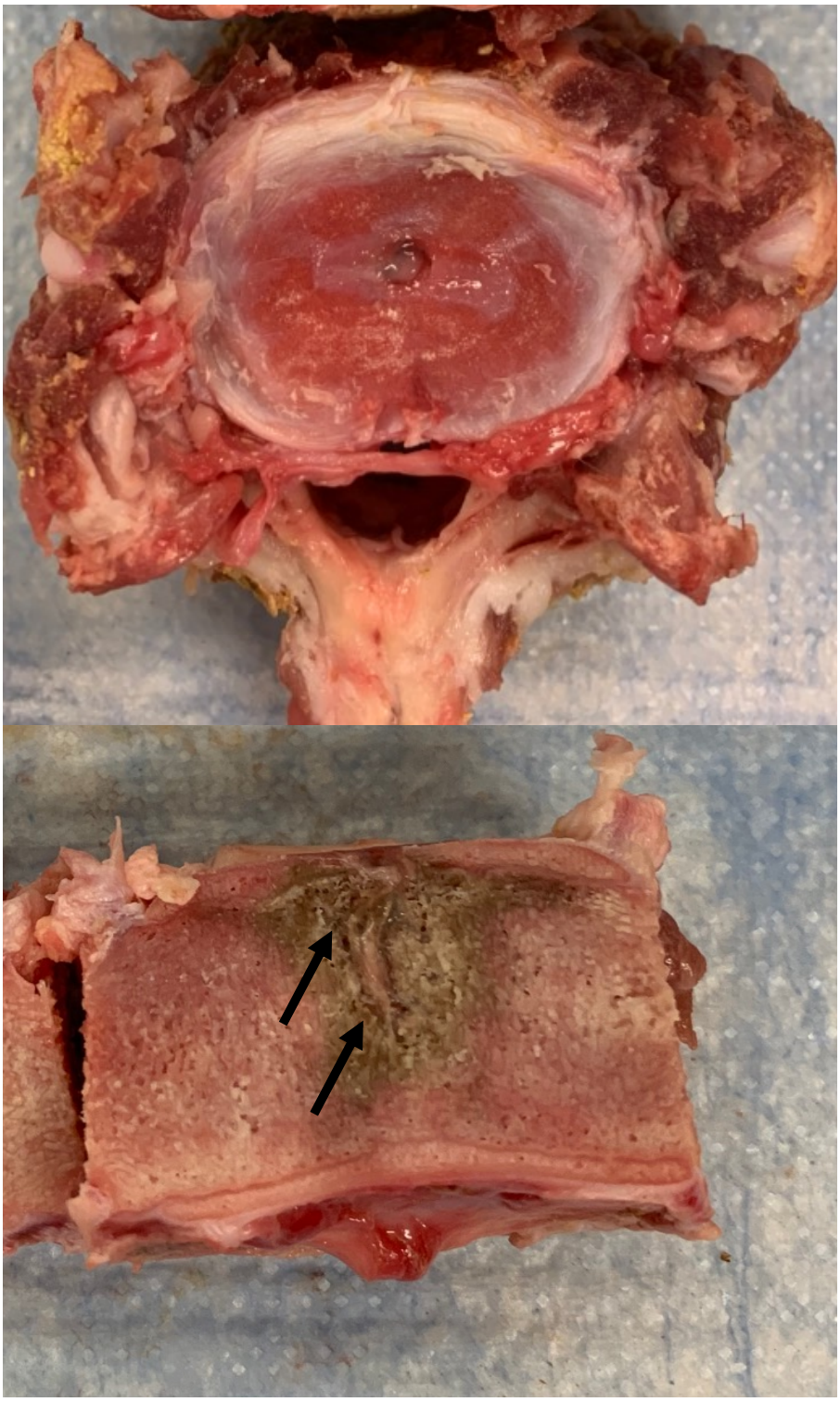

Figure 8.3.4. Representative images of the injury morphology observed in the chemical fragility condition. The top image was taken in the transverse plane and the bottom image represents a coronal mid-plane section. The depicted injury was classified as a Schmorl's node.

Cycles to Failure

Significant main effects of posture ($p = 0.015$) and initial condition ($p < 0.001$) were observed for the number of tolerated cycles. No significant effects of spinal level were observed; therefore, the number of tolerated cycles were collapsed across spinal level. On average, FSUs exposed to cyclic compression while positioned in a flexed posture withstood 665 fewer cycles compared to neutral (Table 8.3.2). With respect to initial condition, the 117-cycle difference between control and sham specimens was not significantly different ($p = 0.989$), confirming that the horizontally drilled port used to administer the hydrochloric acid did not influence the fatigue response. The 288-cycle difference between chemical fragility and structural void groups was also not significant ($p = 0.866$). However, as evidenced in Table 8.3.2, the number of cycles tolerated by control and sham groups were, on average, 5318 cycles greater than chemical fragility and structural void groups ($p < 0.01$).

Table 8.3.2. The average ± standard deviation number of tolerated cycles until failure reported for all experimental groups. Summary values marked with a different superscripted letter were significantly different ($p < 0.05$) within a factor (i.e., Condition, Posture).

	Posture		Summary (Condition)
	Neutral	Flexed	
Control	6467 ± 673	5127 ± 1070	5797 ± 872^{A}
Sham	6395 ±1488	5433 ± 1255	5914 ± 1371^{A}
Chemical Fragility	906 ± 1030	459 ± 289	682 ± 659^{B}
Structural Void	350 ± 36	438 ± 334	394 ± 285^{B}
Summary (Posture)	3530 ± 857^{A}	2864 ± 737^{B}	

8.4. Discussion

This study explored overuse mechanisms of fracture lesions and Schmorl's node injuries. The initial state of the vertebral trabecular bone had a significant effect on endplate failure morphology and the fatigue lifespan of spinal units. The use of 6M hydrochloric acid and the

described method for its administration reduced the localized strength of trabecular bone by 49% (Table 8.2.1, Figure 8.2.4), thereby enabling the effect of pre-existing fragility on failure morphology to be tested. Spinal units predisposed with localized trabecular bone fragility and a centrally positioned structural void resulted in Schmorl's node injuries 59% and 41% of the time, respectively. In contrast, all injuries observed in the control and sham groups were fracture lesions. Furthermore, the chemical fragility and structural void groups tolerated, on average, 5318 fewer loading cycles compared to the control and sham groups. These findings collectively support the study hypotheses and demonstrate that fracture lesions and Schmorl's node injuries result from a difference in the structural integrity of centrally supporting trabecular bone.

Fatigue-failure is defined as the progressive weakening of tissues due to the accumulation of microdamage. In this study, low-moderate compression applied to healthy spinal joints resulted in endplate fracture lesions, irrespective of posture. Therefore, it is likely that the pace of structural and constitutive damage in the hyaline cartilage endplate was similar or outpaced the trabecular bone. This notion is supported by the results of an immunofluorescence analysis, where the reductions to the collagen II content (cartilage endplate) outpaced changes to native type I collagen content (subchondral trabecular bone) under similar cyclic loading conditions (Zehr, Quadrilatero, et al., 2022b). In contrast, Schmorl's nodes appear to occur when trabecular bone damage outpaces that of the cartilage endplate. The infliction of trabecular bone damage is conceivable through two mechanisms. The first mechanism is the accumulation of microcracks caused by high loading or traumatic compression exposures. Under acute loading conditions, Fyhrie and Schaffler (1994) demonstrated a mechanism of failure that was attributed to microscopic cracking of central trabecular elements, with similar cracking patterns and locations (directly beneath the endplate surface) observed during post-mortem analyses of human cadaveric lumbar spines (Wenzel et al.,

1996) and finite element model simulations (Imai, Ohnishi, Bessho, & Nakamura, 2006). Thus, intermittent high compression exposures may initiate and/or accelerate the pace of microcrack accumulation within central trabecular elements. The second mechanism is through physiological factors related to oxidative stress, which have been linked to bone diseases such as osteoporosis (Kimball, Johnson, & Carlson, 2021). Excessive reactive oxygen species have been shown to alter remodelling processes through apoptosis of osteoblasts and osteocytes, thereby impairing the rate of resorption and promoting bone turnover (Domazetovic, Marcucci, Iantomasi, Brandi, & Vincenzini, 2017). Thus, the density of trabecular microcracks may be further exacerbated if spinal tissues are in a state of chronic inflammation. Taken together, it is likely that Schmorl's nodes result from complex interactions between mechanical and physiological factors. Data from the current study suggest that fracture lesions and Schmorl's nodes may occur under submaximal loading conditions; however, the pathways and locations of damage accumulation appear different.

Like in previous research (Callaghan & McGill, 2001a; Gooyers et al., 2015), flexed postures significantly reduced the number of tolerated cycles compared to neutral postures (Table 8.3.2.). This finding also supports the greater reductions in CEP stiffness (Zehr, Barrett, et al., 2022) and accelerated microstructural and constitutive damage (Zehr, Quadrilatero, et al., 2022b) resulting from cyclic loading applied to flexed joint postures. With respect to failure morphology, however, posture did not significantly affect the fracture morphology observed in this study, despite microscopic evidence of node formation in CEPs extracted from spinal joints exposed to cyclic compression while flexed (Zehr, Quadrilatero, et al., 2022a). Thus, while flexed postures may initiate microscopic nodes during subthreshold compression loading, posture appears unrelated to the incidence of macroscopic Schmorl's nodes. A conceivable reason for this is that the microscopic nodes appear to proportionally affect the hyaline cartilage surface and subchondral

bone (Figure 7.3.2), even as the lesion size progresses as a function of loading duration (Zehr, Quadrilatero, et al., 2022a). In contrast, this study demonstrated the need for a secondary mechanical and/or physiological cascade to disproportionately alter the subchondral bone integrity in order for a Schmorl's node to occur under subthreshold compression scenarios.

The endplate geometry together with the structural integrity of trabecular bone is likely to alter the loading modes experienced by the cranial and caudal vertebra. Within a porcine cervical spinal unit, the cranial endplate has a concave geometry, while caudal endplate has a convex geometry (Figure 8.4.1). In a healthy state, the assumed uniform pressure applied to the central endplate region would conceivably generate a radial tensile force on the cranial endplate and a radial compression force on the caudal endplate (Figure 8.4.1). The tensile force experienced by the cranial endplate may render this vertebra vulnerable to crack formation and may explain why fracture lesions were observed in the cranial endplate of all control and sham specimens (Table 8.3.2). In addition to loading mode, a greater prevalence of compression induced cranial endplate fractures was observed by Zhao et al. (2009), and this finding was attributed to a thinner endplate structure and less dense trabecular bone.

In contrast, localized weakness to the supporting trabecular bone is likely to generate a localized tensile force caused by greater central endplate deformation (Figure 8.4.1). Since the cranial vertebra experiences tensile forces prior to the additional structural weakness, the local tensile strain is expected to be greater in the central region of the caudal vertebra. This proposed change in loading mode experienced by the central endplate may explain why 14 of 17 Schmorl's nodes were observed in the caudal vertebra (Table 8.3.2). The distribution (82%) of Schmorl's nodes to the caudal vertebra was greater than the 57-61% prevalence observed in previous injury classification studies (Pfirrmann & Resnick, 2001; Y. Wang et al., 2012), but aligns with the

general notion that the caudal vertebra may be more vulnerable to Schmorl's node injuries. While these explanations are rooted in principles of structural mechanics and supported by anatomical differences (Zhao et al., 2009), further finite element modelling work is required to verify the structural mechanisms and locations of failure in healthy and fragile states.

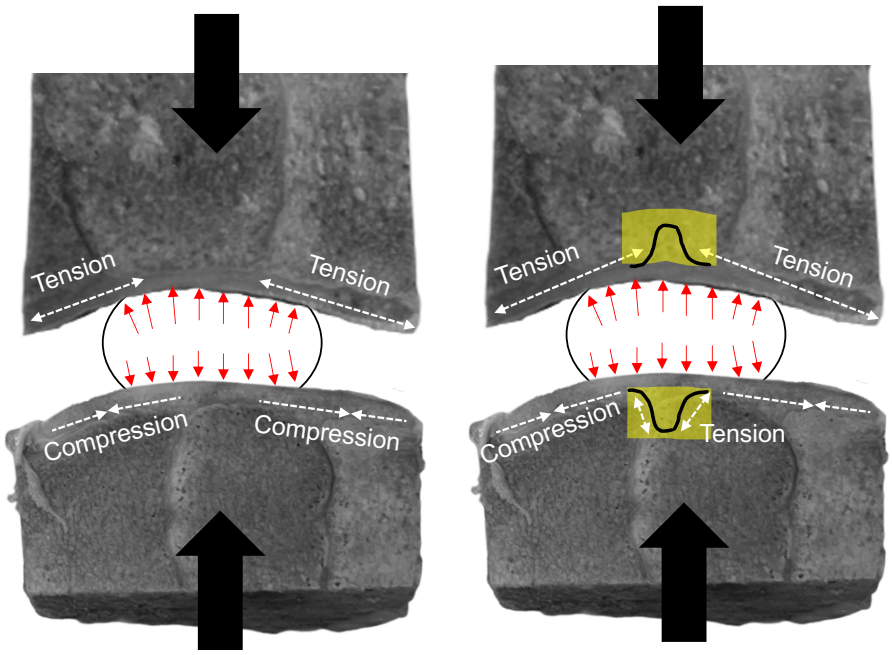

Figure 8.4.1. A schematic of load application and resulting loading modes experienced by endplate tissues. Black arrows = applied compression force; red arrows = assumed uniform pressure applied to the central endplate region by the nucleus pulposus; white arrows = loading mode; yellow highlighting; structural compromise to trabecular bone. The localized tension within the acid exposed region results from nucleus pulposus intrusion.

Some limitations of the current study are acknowledged. First, the surface area and shape of porcine cervical spine endplates are a scaled model of human lumbar spine endplates (Yingling et al., 1999). However, the similarity in concave/convex geometry between porcine and human species is unknown. Geometrical differences may alter the extent to which sub-surface structural compromise influences the loading mode and deformation experienced by the cranial and caudal

joint endplates. Second, the acid exposure was an accelerated model of trabecular bone damage that accumulates overtime due to mechanical exposures and physiological processes. The interactions between mechanical and physiological factors that induce or accelerate trabecular damage within the central vertebrae were not captured in this study and remain largely unknown. Third, post-failure cycles were performed following the precipitous step in vertical position and prior to the 9 mm criteria for load termination. Although the injury severity may have increased during this time, it is unlikely that fracture lesions would have manifested to Schmorl's nodes and vice versa. Fourth, a 49% reduction in ultimate stress was observed in this study with no further attempt to examine the effect of varying trabecular bone strength reductions on failure morphology. Therefore, the minimum reduction in trabecular bone strength that is required to induce a Schmorl's node injury is unknown, but this line of inquiry is a future research direction. Lastly, the mechanism by which hydrochloric acid alters the organic and inorganic phase of trabecular bone is unknown and was beyond the scope of the current study. *In vitro* models of physiological oxidative stress have been applied to cortical bone samples using free radicals generated by the decomposition of hydrogen peroxide (Fiori, 2021). However, this technique required multiple days of hydrogen peroxide exposure, which was impractical for the current study design, and differences in the fracture toughness were not observed (Fiori, 2021). Despite the effectiveness of 6M hydrochloric acid, further work is required to understand the mechanism for reductions in ultimate stress.

8.5. Conclusions

In conclusion, localized strength deficits to trabecular bone supporting the central endplate resulted in Schmorl's node injuries in response to subthreshold loading. This study was first to experimentally generate Schmorl's nodes and the mechanism of fatigue-failure differed from

fracture lesions. Pre-existing structural compromise to the trabecular bone was further associated with a substantial reduction in the number of tolerated loading cycles. Unlike fracture lesions, the occurrence of degenerative Schmorl's nodes appears dependent on the accumulation of mechanical and/or physiological stimuli effecting the integrity of subchondral bone. Future *in vivo* research is required to understand the causes and prevention of trabecular bone fragility in the lumbar spine vertebrae.

CHAPTER 9

Towards the Estimation of Ultimate Compression Tolerance as a Function of Cyclic Compression History: Implications for Lifting-Related Low Back Injury Risk Assessment

Jackie D. Zehr & Jack P. Callaghan

Theoretical Issues in Ergonomics Science, In Press, 2022

Abstract

Objectives: This study aimed to mathematically characterize the ultimate compression tolerance (UCT) as a function of spinal joint posture, loading variation, and loading duration.

Methods: One hundred and fourteen porcine cervical spinal units were tested. Spinal units were randomly assigned to subthreshold cyclic loading groups that differed by joint posture (neutral, flexed), peak loading variation (10%, 20%, 40%), and loading duration (1000, 3000, 5000 cycles). After the assigned conditioning test, UCT testing was performed. Force and actuator position were sampled at 100 Hz.

Results: A three-dimensional relationship between UCT, loading variation, and loading duration was most accurately characterized by a second order polynomial surface (R^2 = 0.644, RMSE = 1.246 kN). However, distinct UCT responses were observed for flexed and neutral postures. A single second-order polynomial most accurately characterized the UCT – loading duration relationship (R^2 = 0.905, RMSE = 0.718 kN) for flexed postures. For neutral joint postures, separate second-order polynomial equations were developed to characterize the UCT – loading duration relationship for each variation group (R^2 = 0.618–0.906, RMSE = 0.617 kN–0.746 kN).

Conclusions: These findings suggest that UCT responses are influenced by joint posture and these data may be used to inform future ergonomic tools for the assessment of low back injury risk during occupational lifting.

9.1. Introduction

Lifting-related low back injury risk is influenced by the interaction of personal and task parameters (Marras, 2000). While physiological and psychosocial risk factors are indeed relevant to low back injury outcomes (K. G. Davis & Heaney, 2000; Garg et al., 2014), many biomechanical investigations have focused on the interaction between joint compression force and repetition (Gallagher & Heberger, 2013; Gooyers et al., 2015), with some including the additional element of loading variation (van Dieën, Dekkers, et al., 2001; Zehr et al., 2019b) or joint posture (Gooyers et al., 2015; Marras et al., 1995; Marras et al., 1993). Compression forces experienced by lumbar spine joints during the performance of occupational lifting are considered sub-threshold, meaning they are less than existing estimates of ultimate compression tolerance (UCT) (Tyson A. C. Beach et al., 2006; Kermit G. Davis, Marras, & Waters, 1998; Fathallah, Marras, & Parnianpour, 1998; Marras, Granata, Davis, Allread, & Jorgensen, 1997; Marras et al., 2006). Therefore, resulting low back injuries have been attributed to a fatigue-failure mechanism (Callaghan & McGill, 2001a; Gallagher & Schall Jr., 2017; Marras, 2000; McGill, 1997). In consideration of the biomechanical risk factors along with the theoretical basis for low back injury causation (i.e., mechanical fatigue), many assessment tools have been developed to aide ergonomists in the estimation of low back injury risk in occupational contexts that require repeated lifting exposures.

Current ergonomic tools for the assessment of low back injury risk include the Lifting Fatigue Failure Tool (LiFFT) (Gallagher et al., 2017), revised NIOSH lifting equations (Waters, Putz-Anderson, Garg, & Fine, 1993), Manual Task Risk Assessment (ManTRA) (Straker, Burgess-Limerick, Pollock, & Egeskov, 2004), Manual Material Handling Assessment Chart (MHAC) (Batish & Singh, 2008), and the Back Exposure Sampling Tool (Back-EST) (Village et al., 2009). These tools similarly aim to assess low back injury risk associated with a given lifting

task design, but they each incorporate different combinations of physical risk factors. These include vertical hand force (Batish & Singh, 2008; Gallagher et al., 2017; Straker et al., 2004; Village et al., 2009; Waters et al., 1993), lifting frequency (Waters et al., 1993), lifting duration (Straker et al., 2004; Waters et al., 1993), repetition (Gallagher et al., 2017; Straker et al., 2004), working posture (Gallagher et al., 2017; Straker et al., 2004; Village et al., 2009; Waters et al., 1993), vibration (Straker et al., 2004), and individual strength (Batish & Singh, 2008). From the various combinations of physical risk factors, estimates of low back joint compression force are typically made with various modeling and prediction approaches, and form the basis for low back injury risk (Gallagher et al., 2017; Village et al., 2009; Waters et al., 1993) and discomfort (Batish & Singh, 2008) assessments. For example, predicted joint compression forces associated with a given task can be referenced to recommended exposure limits (e.g., NIOSH action limit) (Waters et al., 1993) or normalized to existing estimates of the joint UCT to predict the number of compression cycles that a joint can tolerate prior to failure (Gallagher et al., 2017). Collectively, the abovementioned assessment tools have demonstrated that low back injury risk and cumulative tissue damage are dominated by higher compression exposures, even if exponentially fewer repetitions are preformed compared to lower demand lifting tasks.

Theoretically, the potential for low back injury is assessed by the margin of safety; the difference between the applied compression load and the UCT (Marras, 2000; McGill, 1997). In alignment with fatigue-failure theory, the UCT of lumbar spine joints progressively weakens due to the accumulation of microdamage produced by repeated subthreshold compression exposures. Although the joint compression forces have been evaluated with respect to *in vitro* UCT data (Gallagher et al., 2017), these normalizations are limited to a single point in time, typically when the joint is in a healthy state. That is, a normalized compression force of 30% UCT may be initially

considered low risk; however, after *n*th number of loading cycles, it is no longer a 30% UCT force given the progressive reduction in joint UCT. As such, the margin of safety and how it changes during repeated lifting tasks is largely unknown beyond initial loading cycles. Furthermore, spine posture, which is different from working posture, is omitted from all current risk assessment tools, despite strong epidemiological evidence for its association with lifting-related low back injuries (Marras et al., 1995; Marras et al., 1993). Indeed, visual assessments of lumbar spine posture are challenging to obtain during dynamic lifting and squatting tasks without the use of instrumentation (Marras, Fine, Ferguson, & Waters, 1999) and postural estimates are often made with substantive error, even when evaluated by trained clinicians (De Looze, Toussaint, Ensink, Mangnus, & Van Der Beek, 1994; Falk, Aasa, & Berglund, 2021). However, given the relevance of posture to spinal joint mechanics (Gooyers et al., 2012) and fatigue (Gooyers et al., 2015), its effect on the change in UCT, and thus margin of safety of lumbar spine joints should be examined as it relates to risk assessment.

Only in developing mathematical functions that characterize the effect of compression force, repetition, and posture on the lumbar spine UCT can the margin of safety be evaluated based on a given loading history. Due to the lack of quantitative data on cycle-dependent estimates of the UCT in lumbar spine joints, this study aimed to mathematically characterize the UCT based on previously identified interaction effects between compression force, repetition, and joint posture (Zehr, Barrett, et al., 2022). Specifically, an *in vitro* study design was used and data from previous fatigue-failure studies (Zehr, Buchman-Pearle, et al., 2020; Zehr et al., 2019b) informed the applied loading scenario employed in this study. The effect of compression magnitude was probed through variation in the peak compression force (Zehr et al., 2019b), posture was normalized to a percentage of the neutral zone, and repetition was evaluated up to approximately

94% of the joint lifespan (Zehr, Buchman-Pearle, et al., 2020). In alignment with existing parameters that are currently included in risk assessment tools, the relationship between UCT, loading variation, and loading duration was first characterized with a three-dimensional surface. Secondly, the effect of posture was examined, wherein curve-fitting was performed to characterize the UCT–loading duration relationship for cyclic loading performed in flexed and neutrally positioned functional spinal units (FSU).

9.2. Methods

Overview

Using curve fitting approaches, this study mathematically characterized how the UCT changed throughout the joint lifespan as a function of compression loading parameters. Post-loading UCT data obtained from 113 vertebra (Chapter 5) were included in the curve fitting analyses where one three-dimensional surface and four two-dimensional functions were developed. Although additional validation and testing is required prior to implementing the presented results into existing low back risk assessment tools, this study revealed a theoretically justified perspective for the assessment of low back injury risk in occupational contexts. A schematic of the characterization procedures is depicted in Figure 9.2.1.

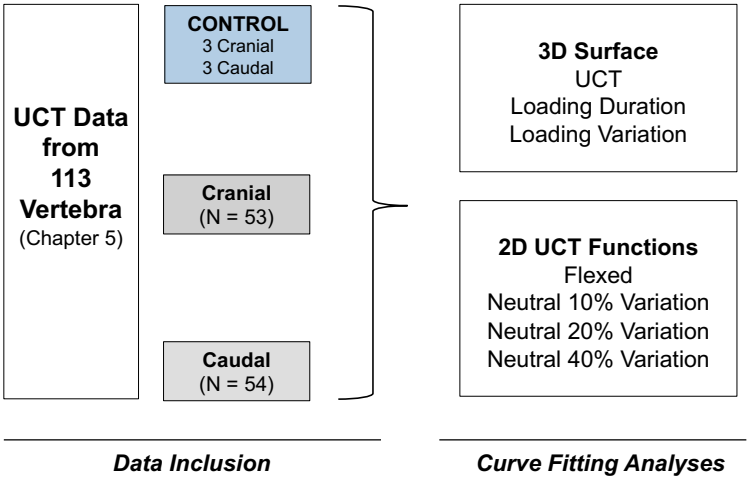

Figure 9.2.1. Schematic of data inclusion and curve fitting approaches used in this study.

Data Inclusion

Data obtained from 113 vertebra were used to characterize the cycle-dependent changes in UCT (Chapter 5). Recall, cyclic compression parameters differed by joint posture (flexed, neutral), variation in peak compression force (10%, 20%, 40%), and loading duration (1000, 3000, 5000 cycles). All loading groups had an average normalized peak compression force of 30% of the predicted UCT, which was obtained using a validated regression equation (Parkinson et al., 2005). Following the prescribed compression paradigm, vertebrae were isolated from the joint and compressed at a rate of 3 kN/s until failure occurred. Raw force and position data were collected at 100 Hz and input into a custom Matlab program (R2020b, The MathWorks Inc., Natick, MA). UCT was determined by a visually apparent step in the force-displacement curve or by a 3.25% drop in the force signal within a 50 ms window (Gunning et al., 2001).

Mathematical Characterization of UCT

First, a three-dimensional surface was constructed to characterize the relationship between UCT, compression variation (i.e., indirectly probes the effect of compression magnitude), and loading duration. This initial analysis was to characterize how UCT is influenced by the

compression force and repetition parameters included in existing cumulative damage models (Batish & Singh, 2008; Gallagher et al., 2017; Straker et al., 2004; Village et al., 2009; Waters et al., 1993) and form the basis for fatigue-failure injuries in the low back (Gallagher & Schall Jr., 2017; Marras, 2000; McGill, 1997). Linear, polynomial (second to fourth order), and sigmoid surfaces were fit to UCT data that were collapsed across postures.

Zehr, Barrett, et al. (2022) reported a three-way interaction between posture, loading variation, and loading duration for UCT. These findings collectively suggest the need to investigate how joint posture effects the UCT as a function of cyclic loading duration. That is, when cyclically loaded in a flexed joint posture, there were no significant differences observed between variation groups within all loading durations. Therefore, the loading variation data were collapsed within each loading duration group to characterize the relationship between UCT and loading duration for flexed conditioning postures. When FSUs were cyclically loaded in a neutral posture, significant UCT differences were observed between loading variation groups after 3000 and 5000 cycles. As such, the relationship between UCT and loading duration was separately characterized for the 10%, 20%, and 40% variation groups for neutral conditioning postures.

To mathematically characterize the relationships that best describe the UCT as a function of loading duration, a scatter plot was constructed containing appropriate data for flexed (i.e., pooled across variation within each duration) and neutral (i.e., separate plots for 10%, 20%, and 40% variation groups) postures. Several curve-fits were attempted including linear, polynomial, exponential, and sigmoid. For polynomial curve-fits, the order was progressively iterated from second to fourth. The equation and order at which there were no further improvements in the root mean square error (RMSE) was selected to represent the relationship between UCT and loading

duration. The correlation coefficient (R^2) was further determined to assess the variance explained by each of the developed equations.

9.3. Results

Compared to linear (RMSE = 1.254 kN) and sigmoid (RMSE =1.262 kN) surfaces, the RMSE was the smallest when a second-order polynomial was used (1.246 kN), with no further improvements with an increase in order. Therefore, the three-dimensional relationship between UCT, loading variation and loading duration was characterized with a second order polynomial surface (Figure 9.3.1), with six resulting coefficients (Table 9.3.1). In Equation 9.3.1, $\boldsymbol{v}$, represents loading variation and is expressed as a percentage of deviation from the mean peak compression force while, $\boldsymbol{d}$, is the number of lifting repetitions performed. The second-order relationship had an R^2 of 0.644, indicating a moderate strength relationship between UCT, loading variation, and loading duration when joint posture was collapsed within each experimental group.

$$UCT(v,d) = A + B(v) + C(d) + D(v^2) + E(d)(v) + F(d^2) \qquad \textbf{Equation 9.3.1}$$

Table 9.3.1. Coefficients (with 95% confidence intervals) corresponding to the variables presented in Equation 9.3.1.

Coefficient	Value
A	10.92 (10.03, 11.80)
B	0.01278 (-0.08397, 0.1095)
C	-9.778×10^{-4} (-1.678×10^{-3}, -2.776×10^{-4})
D	-4.570×10^{-4} (-2.489×10^{-3}, 1.576×10^{-3})
E	-9.748×10^{-6} (-2.061×10^{-5}, 1.116×10^{-6})
F	5.362×10^{-8} (-6.310×10^{-8}, 1.703×10^{-7})

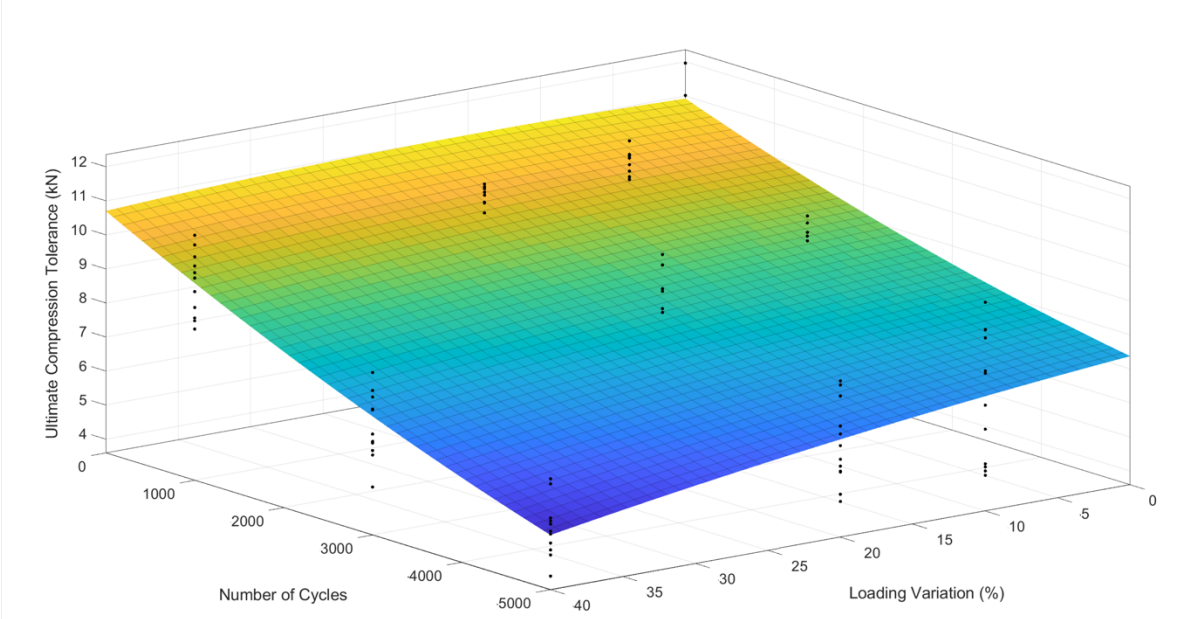

Figure 9.3.1. Three-dimensional surface plot (second-order polynomial) of predicted UCT based on the loading duration and loading variation. The raw data points for each experimental group are represented as filled back circles.

Compared to the polynomial curve-fits, the linear, exponential, and sigmoid functions reproduced the relationship between UCT and loading durations with less accuracy for flexed and neutral posture conditioning groups (Table 9.3.2). As evidenced in Table 9.3.2, a reduction in RMSE was not observed for polynomial functions beyond a second-order. A second-order polynomial function was therefore used to characterize the UCT – loading duration relationship for all relevant flexed and neutral posture conditions (Table 9.3.2). The second-order polynomial equation resulted the production of three coefficients corresponding to those presented in Equation 9.3.2, where ***d*** is the number of lifting repetitions performed. The coefficients for each condition are listed in Table 9.3.3. The resulting second order relationships were moderate to strong in strength (flexed, all variation: $R^2 = 0.905$; neutral, 10% variation: $R^2 = 0.618$; neutral, 20% variation: $R^2 = 0.851$; neutral, 40% variation: $R^2 = 0.906$).

$$UCT(d) = A(d)^2 + B(d) + C$$ **Equation 9.3.2**

Table 9.3.2. UCT root mean square error (kN) for cyclic loading performed in flexion (loading variation collapsed) and neutral (loading variation groups separate) postures.

Posture	Flexed	Neutral		
Variation	ALL	10%	20%	40%
Linear	0.805	0.749	0.666	0.679
Exponential	0.728	0.756	0.699	0.686
Sigmoid	0.862	0.765	0.734	0.745
Polynomial				
Second	0.718	0.746	0.617	0.650
Third	0.718	0.746	0.617	0.650
Fourth	0.718	0.746	0.617	0.650

Table 9.3.3. Coefficients (with 95% confidence intervals) for the second order polynomial equation developed to predict UCT for specific posture and variation conditions.

Posture	Variation	A	B	C
Flexed	ALL	1.415×10^{-7} $(7.601\times10^{-8}, 2.069\times10^{-7})$	-1.829×10^{-3} $(-2.168\times10^{-3}, 1.489\times10^{-3})$	10.79 (10.48, 11.10)
Neutral	10%	-6.357×10^{-8} $(-1.855\times10^{-7}, 5.836\times10^{-8})$	-1.340×10^{-4} $(-7.695\times10^{-4}, 5.015\times10^{-4})$	10.84 (10.26, 11.42)
Neutral	20%	-1.049×10^{-7} $(-2.057\times10^{-7}, -4.127\times10^{-9})$	-1.763×10^{-4} $(-7.017\times10^{-4}, 3.491\times10^{-4})$	10.80 (10.32, 11.28)
Neutral	40%	2.731×10^{-8} $(-8.552\times10^{-8}, 1.401\times10^{-7})$	-1.181×10^{-3} $(-1.769\times10^{-3}, -5.932\times10^{-4})$	11.03 (10.49, 11.57)

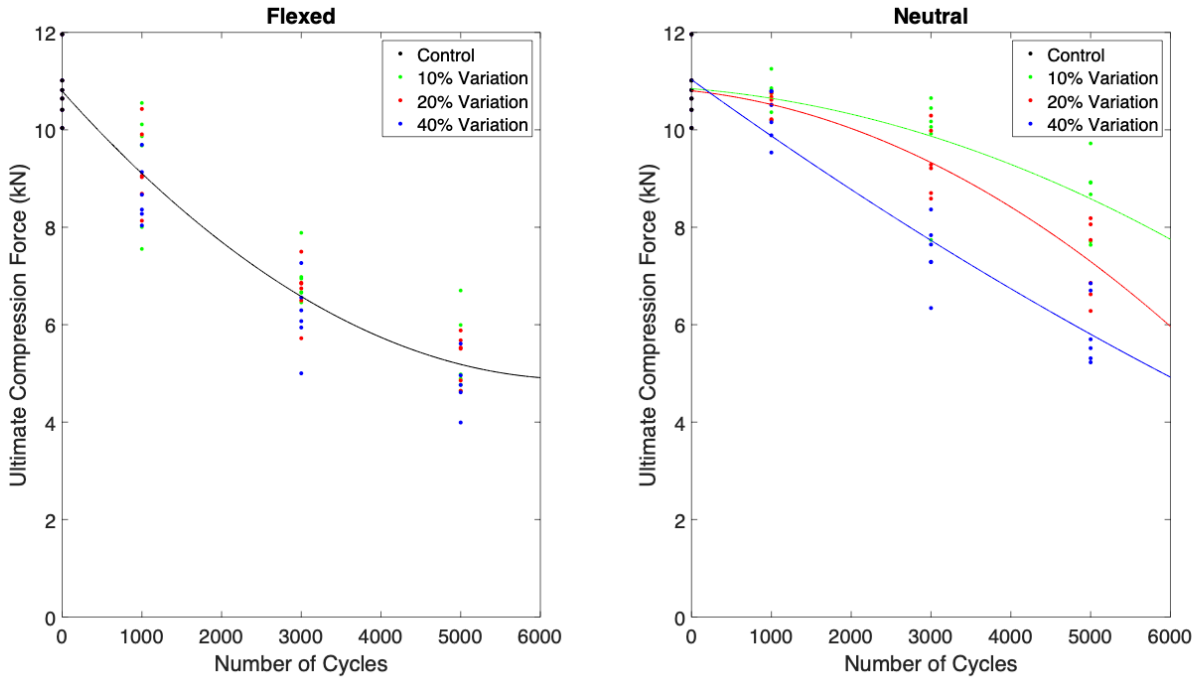

Figure 9.3.2. Mathematical characterizations of the UCT as a function of loading duration for flexed (left) and neutral (right) conditioning postures. The raw data points for each variation condition within a given posture are represented by filled circles.

9.4. Discussion

This study aimed to characterize the relationships between UCT, posture, loading variation, and loading duration. The three-dimensional relationship between UCT, loading duration, and loading variation was nonlinear and characterized with a second-order polynomial surface (R^2 = .644, RMSE = 1.246 kN). The separation of FSU posture during the cyclic compression loading resulted in distinct UCT responses between flexed and neutrally positioned joints (Figure 9.3.2). This resulted in the generation of four – one for flexed postures where loading variation was collapsed within each loading duration and three for neutral postures where separate equations were generated for each loading variation – second-order polynomial equations with moderate (R^2 = 0.618, RMSE = 0.718 kN) to high predictive capacity (R^2 = 0.906, RMSE = 0.650 kN). The

study findings demonstrate an *in vitro* approach for characterizing the UCT and the differences in response as a function of joint posture. These data may be used to inform future ergonomic tools for the assessment of low back margin of safety during repetitive occupational lifting exposures.

The characterization of UCT responses as a function of posture, loading variation, and loading duration enable the margin of safety to be examined. The visually apparent differences in UCT response observed for flexed and neutral postures is inherently reflected in the low back margin of safety estimates. Consider the following examples that compare normalized compression forces and margin of safety estimates using the initial UCT corresponding to the control group (10.81 kN) and cycle-dependent estimates of UCT. It should be noted that the greatest average peak compression force imposed in this study was 4.524 kN (40% variation group), which was used for all assessments and represents the highest risk loading cycles for the same average peak compression force (30% UCT).

The first example will focus on margin of safety estimates for FSUs cyclically loaded in flexed joint postures. Compared to the control group (margin of safety = 6.286 kN), the margin of safety for FSUs cyclically loaded in flexed postures decreased to 4.541 kN (28%), 2.082 kN (67%) and 0.532 kN (92%) after 1000, 3000, and 5000 cycles, respectively (Figure 9.4.1). The 28%, 67%, and 92% reductions in margin of safety are not captured when the peak applied force is subtracted from the initial UCT. Furthermore, the reduction in UCT resulted in higher normalized peak compression forces, which started at 42% (0 cycles) and increased to 52% (1000 cycles), 73% (3000 cycles) and 95% (5000 cycles). At the initially predicted joint lifespan (5311 cycles), the UCT is predicted to be 5.064 kN (0.540 kN margin of safety), which falls within the average error associated with the equation developed for flexed joint postures (RMSE = 0.718 kN) and the average standard deviation for flexed joint postures (0.711 kN).

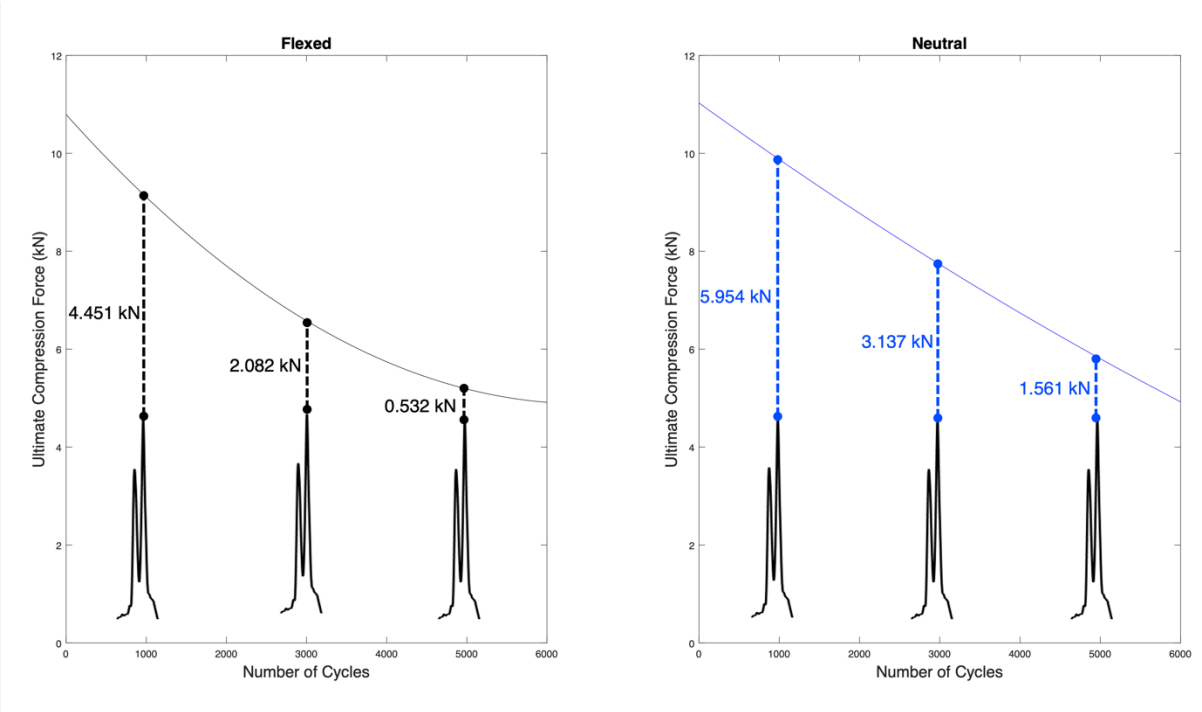

Figure 9.4.1. The decrease in margin of safety for the presented examples: flexed postures (left) and 40% variation with a neutral posture (right). Margin of safety is determined as the difference between the peak applied load and the UCT at 1000, 3000, and 5000 cycles.

The second example will focus on margin of safety estimates for FSUs cyclically loaded in neutral joint postures. Compared to the control group, the margin of safety decreased to 5.954 kN (5%), 3.137 kN (50%) and 1.561 kN (75%) after 1000, 3000, and 5000 cycles, respectively (Figure 9.4.1). Similar to flexed postures, the progressive reduction in UCT yielded higher normalized peak compression forces following 1000 (44% UCT), 3000 (61% UCT), and 5000 (77% UCT) cycles, but to a lesser extent then flexion. Although the peak compression forces are unlikely to exceed the UCT at the predicted lifespan (margin of safety = 0.996 kN), macroscopic failure is expected in approximately 6500 cycles for the average FSU cyclically loaded in neutral and with a 40% variation in compression force. This marginal error may result from the total lifespan being estimated from a previous study that used a slightly higher normalized peak

compression force (40% UCT), which was adjusted based on existing weighting factors to approximate a 30% normalized force (Parkinson & Callaghan, 2007b).

The above examples collectively demonstrate two things: 1) the cycle-dependant reduction in UCT increased normalized compression forces as early as 1000 cycles (2-10%); and 2) flexed postures have a substantive effect on margin of safety with an average difference of 1.164 kN across the lifespan. Recall that normalized joint compression force estimates form the basis of low back injury risk assessment in many ergonomics tools (Gallagher et al., 2017; Village et al., 2009; Waters et al., 1993). The data presented herein together with the theoretical basis of fatigue-failure would suggest that the normalization of estimated compression exposures to a single UCT value may result in the underestimation of low back injury risk, especially as the number of cycles increases. Indeed, within a single workday and industrial worker may perform 450 (1 lift per minute for a 7.5-hour workday) to 4500 (10 lifts per minute for a 7.5 hour work day, which corresponds to the highest repetition in the NIOSH lifting equation with a frequency multiple) lifts per day. The reduction in UCT for the studied loading scenario may appear marginal and range from 9.99 kN (8% decrease) to 10.76 kN (1% decrease) at the lower frequency limit and from 5.43 kN (51% decrease) to 8.95 kN (17% decrease) at the upper frequency limit. However, the time-course of mechanical and biochemical tissue recovery remains largely unknown, and it is likely that overtime, the UCT does not fully recover to the initial condition. Existing estimates of the fatigue lifespan (Gallagher et al., 2017) along with the mathematical characterizations presented herein do not account the time-course of tissue recovery, but future studies will explore this important component.

The observed differences in UCT functions between posture groups and variation groups within a neutral posture are supported by previous *in vitro* findings. First, joint flexion is associated

with the maldistribution of compression forces across the endplate surface (Malandrino et al., 2009) and within the intervertebral disc (Adams, McNally, Chinn, & Dolan, 1994). For a given compression force, joint flexion facilitates a centrally distributed stress concentration, which leads to greater vertical endplate deflection (Malandrino et al., 2009). Greater deflection per loading cycle is likely to accelerate the initiation and progression of microstructural and constitutive damage, which collectively contributes to the weakening of spinal joints. Second, the reduction in UCT associated with higher variation magnitudes in a neutral posture may be explained by existing force weighting factors (Parkinson & Callaghan, 2007b). The developed weighting functions are used to nonlinearly adjust the applied compression force based on the potential for low back injury. That is, random exposures to higher normalized compression forces correspond with a higher weighting factor compared to the average peak force (i.e., 30% UCT) and thus elevate injury potential. This notion is further supported by Zehr et al. (2019b), where a 30% variation resulted in a significant reduction in cyclic lifespan and cumulative load tolerance. These data may explain why the UCT was noticeably less for 20% and 40% variation groups when loaded in a neutral joint posture and beyond 3000% cycles (Figure 9.3.2).

Despite the challenges (Marras et al., 1999) and inaccuracies (De Looze et al., 1994; Falk et al., 2021) associated with visually estimating lumbar spine posture during dynamic lifting tasks, this study has demonstrated the need for its inclusion in low back injury risk assessment tools. The magnitude of joint flexion examined in this study (7.74 to 11.97 degrees from neutral) was indeed extreme but in no way was it unphysiological and infeasible during lifting tasks. That is, if the L5S1 spinal joint contributes to approximately 28% of the total lumbar flexion range-of-motion during a voluntary forward bending task (Dunk et al., 2009), the imposed joint flexion from this study would approximate total lumbar postures that range between 27.6 to 42.7 degrees, which is

well within the ~70 degrees of assumed physiologic range (M. Pearcy, Portek, & Shepherd, 1984). Lumbar flexion of this magnitude has been associated with lifting-related low back disorders in manufacturing contexts (Marras et al., 1995; Marras et al., 1993). Unfortunately, most of this total lumbar posture range is unlikely to be accurately estimated by practitioners, as substantive errors were made at postures less than 34 degrees (Falk et al., 2021). Given the rapid advancements of wearable technology (i.e., inertial measurement units) along with its minimal encumbrance, postural estimates may be more feasible and incorporated into future ergonomics assessments tools for lifting tasks.

The equations to characterize UCT responses were developed using a single normalized mean peak compression magnitude of 30% UCT. This normalized magnitude was intentionally selected to represent internal joint compression during a low-moderate demand occupational lifting tasks (Tyson A. C. Beach et al., 2006; Kermit G. Davis et al., 1998; Fathallah et al., 1998; Marras et al., 1997; Marras et al., 2006). Although beyond the scope of the current study, future investigations may examine and validate the use of existing compression weighting factors to scale the UCT curves for a larger range of normalized compression forces (Parkinson & Callaghan, 2007b). Alternatively, a similar experimental approach may be implemented to determine UCT responses throughout the lifespan for higher demand lifting tasks. UCT trajectories that cover a larger compression range will enable the use of cycle varying UCT estimates for a given cyclic lifespan in ergonomic assessment tools that are currently limited to the fixed estimate of joint tolerance that remains constant regardless of the daily and prior exposures. Additionally, the ability for tool users to predict the UCT resulting from past loading exposures enables the calculation of margin of safety. This additional information can guide load management and the assessment of

risk associated with any compression force, not just the internal load associated with the task indicated by the user.

There were experimental factors that may have contributed to the unexplained variance in UCT responses. First, there is an 11% error associated with the regression equation that was used to predict the UCT based on endplate dimensions (Parkinson et al., 2005). This error in determining the normalized 30% compression force may have translated to variance in the measured UCT. Second, unlike the posture and loading variation factors, the examined durations of cyclic loading were absolute and not normalized to a predicted lifespan of each FSU. Equations for estimating cyclic lifespan exist (Gallagher et al., 2017). However, there are inherent limitations for their application to the current study; namely, a fixed UCT of 6kN, the inclusion of a single compression magnitude, and the exclusion of posture. Therefore, the examined durations likely do not represent the same mechanical state within and between durations. Despite the currently narrow boundaries and unexplained variance of the presented UCT responses, the experimental and theoretical approaches taken in this study emphasized the importance of directly examining the margin of safety as a low back injury risk assessment metric.

A single normalized peak compression force of 30% UCT was used, thereby limiting the broad application of the method. As discussed, weighted adjustments of the presented relationships may be possible based on existing weighting functions (Parkinson & Callaghan, 2007b), but significant validation would be necessary. This study is therefore limited to understanding the effect of a low-moderate compression loading history on the UCT. While limited to low-moderate compression forces, the developed relationships may be useful for understanding the risk associated with performing an abrupt high demand lifting task for a given low demand history. An accelerated *in vitro* injury model was used with no indication of how the spinal joints mechanically

and physiologically recover from rest periods. A porcine animal model was used as a surrogate for the human spine. In addition to the morphological similarities (Yingling et al., 1999) and the appropriate scaling of the compression forces to the specimen-specific endplate surface area (Parkinson et al., 2005), a comparable fatigue response is expected in the human lumbar spine. Furthermore, the average UCT of the control group in this study was 10.81 kN ± 0.69, which is within one standard deviation of the reported UCT values for cadaveric lumbar spine joints excised from male donors between 20 and 29 years of age (Hutton & Adams, 1982). Given the conceivably comparable fatigue response and similar initial UCT values to the cadaveric lumbar spine, a comparable UCT response is expected between species. There are, however, some inevitable differences in generalizing the results to the *in vivo* human lumbar spine. Important differences relate to the exclusion of personal factors (e.g., biological sex, age, spinal levels, and body weight) which have been collectively demonstrated to influence the predicted UCT (Genaidy et al., 1993). While the selected experimental control of factors like age/weight and loading history eliminate the potential for confounding effects to emerge, the findings are less generalizable to a broader population. As such, the generalizability of the presented findings to understand how the UCT response may differ due to combined personal factors is currently limited. Lastly, while the findings support the implementation of a risk assessment approach that directly aligns with the fundamental basis for tissue injury (i.e., applied load exceeds tissue tolerance), the application of data to ergonomic practice require implementation and validation of UCT adjustment factors to enhance injury prevention through ergonomic assessments. This limitation forms a longer-term direction for future studies. That being to develop and incorporate UCT modification factors into tools for risk evaluation of workers. Methodological studies are also needed to quantify lumbar spine posture in the workplace using minimally invasive biomechanical instrumentation. These

posture data would allow the evaluation of UCT modifiers to enhance injury prevention compared with existing risk prediction calculations. This line of inquiry would require a longitudinal study within a cohort of workers, similar to the study completed in Norman et al. (1998). Shorter-term research directions include *in vitro* studies that aim to quantify the UCT throughout the lifespan of joints exposed to wider range of cyclic compression forces. Future multidisciplinary work is also required to understand how the UCT responds to occupationally relevant work:rest ratios. This line of inquiry requires the use live animal models or tissue culturing techniques to probe biomechanical and biochemical processes of tissue damage, recovery, and regeneration.

9.5. Conclusions

In conclusion, this work showed that UCT estimates are greatly influenced by the combination of joint posture, loading variation, and loading duration. While a moderate relationship between UCT, loading variation, and loading duration was observed ($R^2 = 0.644$), the relationship between UCT and loading duration was generally characterized with greater strength when flexed and neutral joint postures were separated. Future work should be conducted to explore the potential for weighting adjustments to scale the UCT responses for a range of physiological compression loading exposures.

CHAPTER 10

General Discussion and Conclusions

10.1. Global Research Contributions

In Chapter 2, the joint compression forces associated with low and high demand occupational lifting tasks were compared to current estimates of ultimate compression tolerance. The compression forces were, in most cases, less than ultimate compression data implying that manual lifting imposed initially subthreshold compression forces on lumbar spine joints. Therefore, it was argued that compression tolerance of lumbar spine tissues must depreciate in response to prior loading cycles (i.e., overuse injury mechanism). However, the cycle-dependent reductions in ultimate compression estimates from the initial state are unknown, thereby preventing true comparisons between applied load and tissue tolerance (i.e., margin of safety) for a given loading history.

The first global objective was to quantify the effect of cyclic compression loading paradigms on the properties and microstructure of the CEP. The results presented in Chapter 5 demonstrated that loading parameters like joint posture and variation in peak compression force can affect the ultimate compression tolerance and regional CEP stiffness for a given loading duration. These changes in joint and tissue properties were explained by data presented in Chapter 6. Although duration-dependent reductions in the native type I and II collagen content were observed, significant reductions compared to the control group were generally not observed until 3000 cycles, which failed to explain the significant reductions in CEP stiffness and joint tolerance that were observed after 1000 cycles, specifically for flexed joint postures. However, the three-way interaction effect detected for sub-surface void development revealed that initial changes to

CEP properties are likely attributed to microstructural void development. Therefore, changes to CEP and joint properties were attributed to a combination of microstructural void development and reductions in native collagen content. That is, microstructural void development was responsible for the initial changes to CEP properties followed by a reduction in native collagen content beyond the midpoint of the lifespan. This pathway appeared accelerated for flexed postures compared to neutral postures.

The second global objective was to examine the effect of cyclic loading parameters on the morphologies of macroscopic and microscopic CEP injury. In Chapter 7, microinjury patterns were largely driven by the joint posture during cyclic loading and the severity of all microinjuries progressed as a function of loading duration. However, the results presented in Chapter 8 did not demonstrate a postural dependency for macroscopic CEP failure morphologies. Irrespective of posture, endplate fracture lesions occurred when cyclic compression was applied to initially healthy spinal units, while Schmorl's nodes were dependent on secondary mechanical and/or physiological cascades that directly alter subchondral bone strength. Given the differing criteria for macroscopic failure morphologies observed in Chapter 8, the microinjury patterns presented in Chapter 7 effectively demonstrate multiple ways to ultimately achieve the same outcome, that being an endplate fracture lesion. Like Schmorl's nodes, fracture lesions can involve the intrusion of the nucleus pulposus into adjacent vertebra (Brinckmann et al., 1988; Gallagher et al., 2006). Since microscopic nodes – that primarily occurred in flexed postures – involved void development within the subchondral bone, intrusion is more conceivable than for example cartilage microfractures – that primarily occurred in neutral postures – where evident subchondral bone damage was not observed (Chapter 7). Given the downstream effects of vertical intrusion on axial joint mechanics (D. Wang et al., 2022), it is possible that joint posture may influence the severity

and functional implications of endplate fracture lesions (i.e., intrusion vs no intrusion); however, this notion has not been experimentally proven.

The third global objective was to characterize the cycle-dependent ultimate compression trajectories in response to acute loading histories. The mathematical characterizations of the ultimate compression tolerance – loading duration relationships were presented in Chapter 9. The second-order polynomial functions are the first depictions of how acute loading histories can differently affect the cycle-dependent ultimate compression response. Although the numerical characterizations in Chapter 9 represent an initial step requiring additional research and validation, the potential for cycle-dependent ultimate compression data to address theoretical knowledge gaps of overuse injury and improve low back injury risk evaluation was demonstrated at a single compression magnitude.

10.2. Specific Research Contributions

Study 1: Indentation Mechanics and Native Collagen Content in the Cartilaginous Endplate: A Comparison Between Porcine Cervical and Human Lumbar Spines

In Chapter 4, the regional indentation mechanics, native collagen content, sub-surface microstructural damage, and cartilage thickness in CEPs from the porcine cervical spine, young human cadaveric spine (19, 33 years), and aged human cadaveric spine were characterized. This study demonstrated a difference in regional loading stiffness (14.33 N/mm), creep displacement (0.043 mm), type I collagen fluorescence intensity (24%), type II collagen fluorescence intensity (58%), sub-surface microstructural void area (1160.5 μm^2), and thickness (0.891 mm) between porcine cervical and young human lumbar CEPs. The indentation mechanics and native collagen content also differed between young and aged human lumbar CEPs. These findings supported the

study hypotheses that indentation mechanics and native collagen content would differ between species (porcine cervical, young human lumbar, aged human lumbar). Despite the mechanical and structural differences observed, this study provided initial data to generally support the usage of porcine cervical CEPs for the study of overuse injury pathways given the affordance of a healthy initial state. An additional contribution to emerge from this study was the visualization of microscopic injury patterns in human lumbar CEPs, specifically avulsion and cartilage microfracture, that were similar to the microinjury patterns observed in porcine cervical CEPs (Chapter 7). These similarities in microinjury patterns may suggest that porcine cervical and human lumbar CEPs may undergo similar overuse injury pathways.

Study 2: Cyclic Loading History Alters the Joint Compression Tolerance and Regional Indentation Responses in The Cartilaginous Endplate

In Chapter 5, the effects of posture, variation in peak compression force, and loading duration on joint compression tolerance, yield force, and regional indentation stiffness were studied. The compression tolerance and yield force were significantly less when loaded in flexed postures compared to neutral, which supported the first study hypothesis. Significant effects of loading variation on joint compression tolerance were only observed when cyclic loading was applied to neutrally positioned joints and after 3000 cycles. Despite higher variation magnitudes eliciting a lower joint compression tolerance after 3000 and 5000 cycles, these findings only partially supported the second study hypothesis; no effect of loading variation was observed for flexed joint postures. Although systematic reductions in compression tolerance were observed as a function of loading duration in flexed postures, this finding did not persist in neutral where a significant reduction was only observed beyond 3000 cycles. This finding only partially supported

the third study hypothesis. As expected, the indentation stiffness of the central CEP region mimicked the ultimate compression response. Collectively, these findings led to the general conclusion and contribution that posture, specifically joint flexion, effectively overrides the effect of loading variability, especially within the central CEP. In the lateral and posterior CEP regions, significant reductions in loading stiffness were only observed after 5000 cycles, therefore supporting the final study hypothesis. Compared to traditional fatigue studies that have examined the effect of loading parameters on the number of tolerated cycles, this study provided novel insight on cycle-dependent changes to joint and CEP properties for a given loading history.

Study 3a: Initiation and Accumulation of Loading Induced Changes to Native Collagen Content and Microstructural Damage in the Cartilage Endplate

In Chapter 6, the effects of posture, variation in peak compression force, and loading duration on the fluorescence area and intensity of type I and II collagen were examined in central CEP tissue. The changes to pore area (transverse plane) and sub-surface void area (sagittal plane) were further examined. In the transverse plane, the fluorescence intensity of type II collagen was dependent on joint posture and loading duration, which did not support the hypothesized interaction. The hypothesis that the fluorescence area of type II collagen would be significantly less in flexed joint postures was supported; however, an effect of loading duration was only observed beyond 3000 cycles, which only partially supported the third study hypothesis. As the area of type II collagen decreased, the type I collagen of the subchondral bone was revealed, but there were no significant differences observed for the fluorescence area and intensity. Despite the damage of type II collagen around the pore perimeter, significant changes to the pore area were not observed.

In the sagittal plane, the fluorescence intensity of type II collagen was also dependent on loading duration and joint posture. Similarly, type II fluorescence intensity was significantly less when joints were cyclically loaded in flexed joint postures and beyond 3000 cycles. Similar trends were observed for the fluorescence area of type I and type II collagen, which did not support the initial hypotheses made. Although appreciable changes in native collagen content were not observed until 3000 cycles, posture, loading variation, and loading duration interacted to affect the area of sub-surface void development. Specifically, a significant increase in void area was observed after 1000 cycles in flexed joint postures, which may explain initial changes to CEP properties observed in Chapter 5.

This study provided novel information on the interaction of microstructural and collagen damage in the central CEP. This study was also first to demonstrate the cycle-dependency of mechanically induced microdamage initiation and the pace of progression. It was generally concluded that similar microdamage pathways were observed for flexed and neutral postures; however, the pace of microdamage accumulation was accelerated in spinal joints loaded in a flexed posture.

Study 3b: Incidence of Compression Induced Microinjuries in the Cartilage Endplate of the Spine

In Chapter 7, the incidence of microstructural injury patterns was quantified. The hypotheses were supported in that incidence of microinjuries involving the subchondral bone (avulsion, node) were significantly greater with flexed joint postures, while the incidence of cartilage microfractures was greater in neutrally positioned joints. It was generally concluded that posture did not affect the incidence of microstructural injury, but it did affect the microinjury pattern. The study hypotheses were further supported by the strong association between

microinjury area and loading duration. Overall, this study provided a direct connection between loading parameters and microinjury pattern. The association of flexed joint postures to microinjuries with greater subchondral bone involvement may suggest a broader dependence of posture on the location and severity of CEP injury.

Study 4: Experimentally Dissociating the Overuse Mechanisms of Endplate Fracture Lesions and Schmorl's Node Injuries Using the Porcine Cervical Spine

In Chapter 8, the effect of trabecular bone integrity and joint posture on macroscopic failure morphology and joint lifespan were examined in response to cyclic compression loading. To do so, a novel approach was developed to induce a 49% reduction in strength to centrally positioned trabecular elements prior cyclic loading. The hypothesis was supported given that spinal units with pre-existing localized trabecular bone fragility (59%) and/or the complete removal of central trabecular elements (41%) failed with a Schmorl's node morphology, irrespective of posture. In contrast, fracture lesions were observed in all control and sham specimens, and the incidence was not affected by posture. Although no significant effect of posture was observed for failure morphology, flexed postures did significantly reduce the joint lifespan compared to neutral postures. Therefore, regardless of initial state, joint flexion appears to accelerate the pace of fatigue failure, irrespective of the initial condition, which aligns with observations made in previous studies (Chapter 5 and 6). This study also that confirmed that while posture can influence the microscopic injury pattern (Chapter 7), it does not appreciably influence the macroscopic failure classification. Instead, the incidence of fracture lesions was attributed to subthreshold compression alone, while occurrence of Schmorl's nodes were attributed to pre-existing deficits in subchondral

bone integrity that are conceivably driven by secondary cascades related mechanical traumas and/or inflammatory disease states.

Study 5: Towards the Estimation of Ultimate Compression Tolerance as a Function of Cyclic Compression Loading History: Implications for Lifting-Related Low Back Injury Risk Assessment

In Chapter 9, mathematical characterizations of the ultimate compression tolerance were presented for a single compression magnitude. Specifically, the relationship between compression tolerance and loading duration was dependent on posture despite both postures being characterized with a second-order polynomial. This study was first to present numerical characterizations of the cycle-dependent ultimate compression tolerance. Although currently limited to a single loading magnitude, this study demonstrated an ultimate compression response that are dependent on the parameters of the acute loading history. The applicability of the findings to ergonomics practice are currently limited. However, with validation and characterization throughout a broader compression magnitude, this paradigm and data may be incorporated into future ergonomic tools for the assessment of low back injury risk.

10.3. Thesis Limitations

In Vitro Study Design

All experimental research was conducted with an *in vitro* study design. Therefore, the biological processes (e.g., cell and enzymatic activity) related to injury and repair were not captured. Short term cyclic loading of isolated and cultured endplate chondrocytes promoted autophagy (Xu et al., 2016) – a self-preservation process where the body recycles parts of damaged cells for repair and regeneration – while long term cyclic (Xu et al., 2016) and static (Kong et al., 2013) loading promoted chondrocyte apoptosis – cell death – and progressive ossification.

Chondrocytes are critical for the maintenance of extracellular matrix constituents and multiple mechanisms for their ossification have been proposed (Han et al., 2018; Sahlman et al., 2001; M. Zhang et al., 2009). The pathways of ossification are important to the study of overuse CEP injury and have implications on the tissue structure, properties, and function.

The use of *in vivo* animal models and cell culturing techniques have enabled the cellular processes of CEP injury to be examined. However, these pathways of cell death and recovery in response to physiologically relevant loading paradigms remain unknown. This knowledge gap is largely attributed to the invasive procedures required to impose controlled joint loading within a rodent spine (Gullbrand et al., 2015) together with the ethical concerns for performing such procedures long-term. Therefore, a strength of the *in vitro* design was the ability to prescribe controlled and relevant compression exposures across the joint lifespan. Although cellular pathways related to CEP injury were not captured, this thesis did provide meaningful data on the relationships between relevant compression paradigms and the accumulation of microstructural and extracellular matrix damage (i.e., collagen). Additional research is required to understand the responses of other extracellular matrix constituents (i.e., proteoglycans, glycosaminoglycans) to dynamic and prolonged compression loading.

Rest and Recovery

Intermittent periods of unloading are important for the growth and remodelling in hyaline cartilage. Given the *in vitro* design, the effect of rest on CEP properties and structure were not examined in this thesis. As evidenced in this thesis, mechanical loading affects the degradation of proteins in the CEP, and these results generally agree with findings obtained from loading tests performed on articular cartilage explants (Hosseini et al., 2013; Otoo, Li, Hart, & Herzog, 2022). However, it has been suggested that the duration of recovery following a period of mechanical

loading affects the synthesis of extracellular matrix proteins more than the load application itself (Sauerland, Raiss, & Steinmeyer, 2003; Steinmeyer, Ackermann, & Raiss, 1997). Additionally, the tissue properties, like the ultimate tolerance, are expected to recover during rest periods (Figure 10.3.1). This recovery of tissue properties is attributed to the biosynthesis of extracellular matrix proteins together viscoelastic properties of hyaline cartilage, although the time-course and extent of rest-induced recovery in the CEP is unknown. Understanding the effect of load:rest ratios on biological and mechanical properties of hyaline cartilage is an important line of inquiry that will be explored in my future research endeavours.

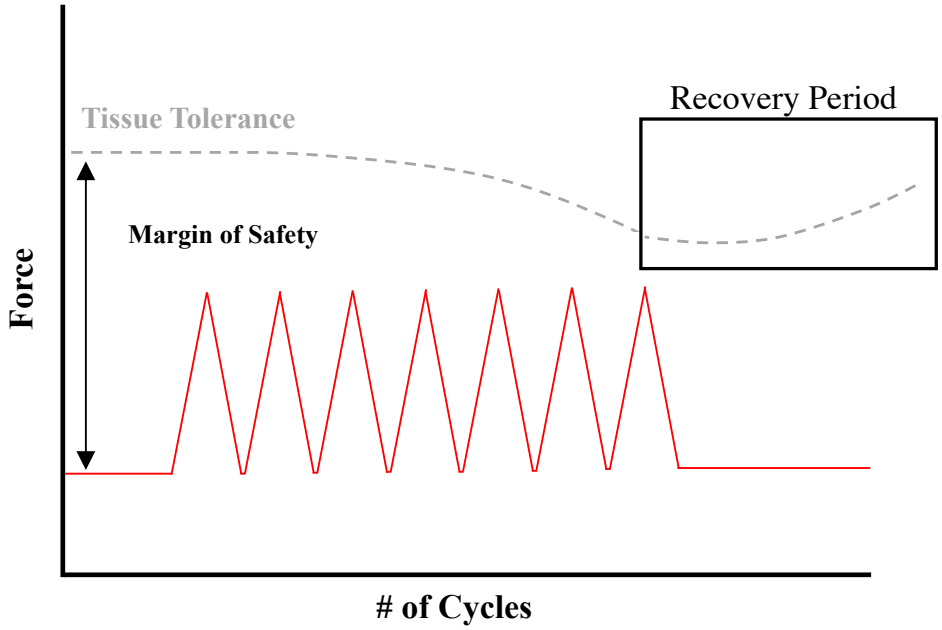

Figure 10.3.1. Relationship between applied compression load (red) and tissue tolerance (grey) as a function of loading cycles and rest. If adequate rest is afforded, the tissue tolerance is expected to increase.

10.4. Overall Conclusions

This thesis demonstrated that joint posture, variation in peak compression force, and loading duration interact to affect the cycle-dependent properties of spinal joints (i.e., ultimate

compression tolerance) and isolated CEP tissue (i.e., loading stiffness). Data obtained from these *in vitro* mechanical tests were used to mathematically characterize the relationships between ultimate compression tolerance and loading duration. The second-order polynomial functions demonstrated the depreciation of ultimate compression tolerance for a given loading history and potential change in low back injury risk. The observed changes to joint and CEP properties were attributed to the development of sub-surface microstructural voids and reductions in native type I and type II collagen content. Despite the interacting effects of loading parameters on the joint and CEP properties, the morphology of microstructural injury was primarily driven by joint posture during cyclic loading. That is, flexed postures resulted in avulsion and node microinjuries, while neutral postures resulted in cartilage microfractures. On a macroscopic level, the failure morphology was less sensitive to posture and attributed to the location/tissue of greatest microscopic damage accumulation. Subthreshold loading alone was shown to facilitate similar microdamage volumes in the cartilage and subchondral bone, which resulted in CEP fracture lesions. Accelerated damage to subchondral bone caused by other mechanical or physiological exposures resulted in Schmorl's nodes when exposed to cyclic compression. Given the limitations associated with the *in vitro* study design, future research should aim to advance *in vivo* experimentation to explore the effects of physiological load:rest ratios on biological and mechanical pathways of CEP damage.

References

Adams, M. A. (1995). Mechanical testing of the spine. An appraisal of methodology, results, and conclusions. *Spine, 20*(19), 2151-2156.

Adams, M. A., Freeman, B. J., Morrison, H. P., Nelson, I. W., & Dolan, P. (2000). Mechanical initiation of intervertebral disc degeneration. *Spine (Phila Pa 1976), 25*(13), 1625-1636.

Adams, M. A., Green, T. P., & Dolan, P. (1994). The strength in anterior bending of lumbar intervertebral discs. *Spine, 19*(19), 2197-2203.

Adams, M. A., & Hutton, W. C. (1980). The effect of posture on the role of apophysial joint in resisiting intervertebral compressive forces. *Journal of Bone and Joint Surgery, 62*, 358-362.

Adams, M. A., & Hutton, W. C. (1982). Prolapsed intervertebral disc. A hyperflexion injury. *Spine, 7*, 184-191.

Adams, M. A., Hutton, W. C., & Stott, J. (1980). The resistance to flexion of the lumbar intervertebral joint. *Spine, 5*, 245-253.

Adams, M. A., McMillan, D. W., Green, T. P., & Dolan, P. (1996). Sustained loading generates stress concentrations in lumbar intervertebral discs. *Spine (Phila Pa 1976), 21*(4), 434-438.

Adams, M. A., McNally, D. S., Chinn, H., & Dolan, K. P. (1994). Posture and the compressive strength of the lumbar spine. *Clinical Biomechanics, 9*(1), 5-14.

Aiyangar, A., Zheng, L., Anderst, W., & Zhang, X. (2017). Instantaneous centers of rotation for lumbar segmental extension in vivo. *Journal of Biomechanics, 52*, 113-121.

Alberton, P., Farkas, Z., Prein, C., Schwarz, J., Li, P., Clausen-Schaumann, H., . . . Aszodi, A. (2019). Aggrecan is critical in maintaining the cartilage matrix biomechanics which in turn influences the correct development of the growth plate. *Osteoarthritis and Cartilage, 27*, S178.

Alekseyev, K., John, A., Malek, A., Lakdawala, M., Verma, N., Southall, C., . . . Ross, M. (2020). Identifying the Most Common CrossFit Injuries in a Variety of Athletes. *Rehabilitation Process and Outcome, 9*, 117957271989706.

Alessa, F., & Ning, X. (2018). Changes of lumbar posture and tissue loading during static trunk bending. *Human Movement Science, 57*, 59-68.

Ángel Rodríguez, M., García-Calleja, P., Terrados, N., Crespo, I., Del Valle, M., & Olmedillas, H. (2022). Injury in CrossFit®: A Systematic Review of Epidemiology and Risk Factors. *The Physician and Sportsmedicine, 50*(1), 3-10.

Antoniou, J., Goudsouzian, N. M., Heathfield, T. F., Winterbottom, N., Steffen, T., Poole, A. R., . . . Alini, M. (1996). The human lumbar endplate. Evidence of changes in biosynthesis and denaturation of the extracellular matrix with growth, maturation, aging, and degeneration. *Spine (Phila Pa 1976), 21*(10), 1153-1161.

Atlas, S. J., & Deyo, R. A. (2001). Evaluating and Managing Acute Low Back Pain in the Primary Care Setting. *Journal of General Internal Medicine, 16*(2), 120-131.

Balkovec, C., Adams, M. A., Dolan, P., & McGill, S. M. (2015). Annulus Fibrosus Can Strip Hyaline Cartilage End Plate from Subchondral Bone: A Study of the Intervertebral Disk in Tension. *Global Spine Journal, 5*(5), 360-365.

Basra, S., Bucklen, B., Muzumdar, A., Khalil, S., & Gudipally, M. (2015). A novel lateral lumbar integrated plate-spacer interbody implant: in vitro biomechanical analysis. *The Spine Journal, 15*(2), 322-328.

Batish, A., & Singh, T. P. (2008). MHAC—An Assessment Tool for Analysing Manual Material Handling Tasks. *International Journal of Occupational Safety and Ergonomics, 14*(2), 223-235.

Beach, T. A. C., Coke, S. K., & Callaghan, J. P. (2006). Upper body kinematic and low-back kinetic responses to precision placement challenges and cognitive distractions during repetitive lifting. *International Journal of Industrial Ergonomics, 36*(7), 637-650.

Beach, T. A. C., Frost, D. M., Zehr, J. D., Howarth, S. J., McGill, S. M., & Callaghan, J. P. (2019). Spine loading during laboratory-simulated fireground operations –Inter-individual variation and method of load quantification. *Ergonomics, 62*(11), 1426-1438.

Bento, T. P. F., Genebra, C. V. D. S., Maciel, N. M., Cornelio, G. P., Simeão, S. F. A. P., & Vitta, A. D. (2020). Low back pain and some associated factors: is there any difference between genders? *Brazilian Journal of Physical Therapy, 24*(1), 79-87.

Berg-Johansen, B., Fields, A. J., Liebenberg, E. C., Li, A., & Lotz, J. C. (2018). Structure-fuction relationships at the human spinal disc-vertebra interface. *Journal of Orthopaedic Research, 36*(1), 192-201.

Berg-Johansen, B., Han, M., Fields, A. J., Liebenberg, E. C., Lim, B. J., Larson, P. E. Z., . . . Lotz, J. C. (2018). Cartilage endplate thickness variation measured by ultrashort Echo-Time MRI is associated with adjacent disc degeneration. *Spine, 43*(10), E592-E600.

Berg-Johansen, B., Jain, D., Liebenberg, E. C., Fields, A. J., Link, T. M., O'Neill, C. W., & Lotz, J. C. (2018). Tidemark Avulsions are a Predominant Form of Endplate Irregularity. *Spine, 43*(16), 1095-1101.

Bian, Q., Jian, A., Xu, X., Kebaish, K., Crane, J. L., Zhang, Z., . . . Cao, X. (2016). Excessive Activation of TGFβ by Spinal Instability Causes Vertebral Endplate Sclerosis. *Science Reports, 3*(6), 27093.

Biggemann, M., Hilweg, D., & Brinckmann, P. (1988). Prediction of compressive strength of vertebral bodies of the lumbar spine by quantitative computed tomography. *Skeletal Radiology, 17*, 264-269.

Bogduk, N. (2012). *Clinical and Radiographical Anatomy of the Lumbar Spine 5th Ed*. Churchill Livingstone: Elsevier Health Sciences.

Bogduk, N., Amevo, B., & Pearcy, M. (1995). A biological basis for instantaneous centres of rotation of the vertebral column. *Proceedings of the Insitution of Mechanical Engineers, 209*(3), 177-183.

Botsford, D. J., Esses, S. I., & Ogilvie-Harris, D. J. (1994). In-vivo diurnal variation in intervertebral disc colume and morphology. *Spine, 19*, 935-940.

Brayda-Bruno, M., Albano, D., Cannella, G., Galbusera, F., & Zerbi, A. (2018). Endplate lesions in the lumbar spine: a novel MRI-based classification scheme and epidemiology in low back pain patients. *European Spine Journal, 27*(11), 2854-2861.

Briar, K. J., & Gregory, D. E. (2023). Combined flexion and compression negatively impact the mechanical integrity of the annulus fibrosus. *European Spine Journal*.

Brinckmann, P., Biggemann, M., & Hilweg, D. (1988). Fatigue failure of human lumbar vertebrae. *Clinical Biomechanics, 3*, S1-S23.

Brinckmann, P., Biggemann, M., & Hilweg, D. (1989). Prediction of compressive strength of human lumbar vertebrae. *Clinical Biomechanics, 4*, Suppl 2 1-27.

Brinckmann, P., Frobin, W., Hierholzer, E., & Horst, M. (1983). Deformation of the vertebral end-plate under axial loading of the spine. *Spine, 8*(8), 851-856.

Brown, M. D., Holmes, D. C., & Heiner, A. D. (2002). Measurement of cadaver lumbar spine motion segment stiffness. *Spine, 27*(9), 918-922.

Brown, M. F., Hukkanen, M. V., McCarthy, I. D., Redfern, D. R., Batten, J. J., Crock, H. V., . . . Polak, J. M. (1997). Sensory and sympathetic innervation of the vertebral endplate in patients with degenerative disc disease. *J Bone Joint Surg Br, 79*(1), 147-153.

Brown, S. H. M., Gregory, D. E., & McGill, S. M. (2008). Vertebral end-plate fractures as a result of high rate pressure loading in the nucleus of the young adult porcine spine. *Journal of Biomechanics, 41*, 122-127.

Busscher, I., van der Beek, A. J., van Dieën, J. H., Kingma, I., Verkerke, G. J., & Veldhuizen, A. G. (2010). In vitro biomechanical characteristics of the spine: A comparison between human and porcine spinal segments. *Spine, 35*(2), 35-42.

Caler, W. E., & Carter, D. R. (1989). Bone creep-fatigue damage accumulation. *Journal of Biomechanics, 22*, 625-635.

Callaghan, J. P., & McGill, S. M. (1995). Frozen storage increases the ultimate compressive load of porcine vertebrae. *Journal of Orthopaedic Research, 13*(5), 809-812.

Callaghan, J. P., & McGill, S. M. (2001a). Intervertebral disc herniation: studies on a porcine model exposed to highly repetitive flexion/extension motion with compressive force. *Clinical Biomechanics, 16*(1), 28-37.

Callaghan, J. P., & McGill, S. M. (2001b). Low back joint loading and kinematics during standing and unsupported sitting. *Ergonomics, 44*(3), 280-294.

Callaghan, J. P., Patla, A. E., & McGill, S. M. (1999). Low back three-dimensional joint forces, kinematics, and kinetics during walking. *Clinical Biomechanics, 14*(3), 203-216.

Campbell, R. (2016). *Patterns of firefighter fireground injuries*. Retrieved from Quincy, MA:

Capowski, J. J., Kylstra, J. A., & Freedman, S. F. (1995). A numeric index based on spatial frequency for the tortuosity of retinal vessels and its application to plus disease in retinopathy of prematurity. *Retina, 15*(6), 490-500.

Carreon, L. Y., Glassman, S. D., D'jurasovic, M., Campbell, M. J., Puno, R. M., Johnson, J. R., & Dimar, J. R. (2009). RhBMP-2 Versus Iliac Crest Bone Graft for Lumbar Spine Fusion in Patients Over 60 Years of Age: A Cost-Utility Study. *Spine, 34*(3), 238-243.

Carter, D. R., & Hayes, W. C. (1976). Fatigue life of compact bone I. Effects of stress amplitude, temperature and density. *Journal of Biomechanics, 9*(1), 27-30.

Cheng, S. C., Jou, I. M., Chern, T. C., Wang, P. H., & Chen, W. C. (2004). The effect of normal saline irrigation at different temperatures on the surface of articular cartilage: an experimental study in the rat. *Arthroscopy, 20*(1), 55-61.

Choi, K., & Goldstein, S. A. (1992). A comparison of the fatigue behavior of human trabecular and cortical bone tissue. *Journal of Biomechanics, 25*(12), 1371-1381.

Cholewicki, J., McGill, S. M., & Norman, R. W. (1991). Lumbar spine loads during the lifting of extremely heavy weights. *Medicine and Science in Sports and Exercise, 23*(10), 1179-1186.

Clague, R. B., & Moore, L. J. (1984). IgG and IgM antibody to native type ii collagen in rheumatoid arthritis serum and synovial fluid evidence for the presence of collagen-anticollagen immune complexes in synovial fluid. *Arthritis & Rheumatism, 27*(12), 1370-1377.

Cripton, P. A., Bruehlmann, S. B., Orr, T. E., Oxland, T. R., & Nolte, L.-P. (2000). In vitro axial preload application during spine flexibility testing: towards reduced apparatus-related artefacts. *Journal of Biomechanics, 33*(12), 1559-1568.

Davis, K. G., & Heaney, C. A. (2000). The relationship between psychosocial work characteristics and low back pain: underlying methodological issues. *Clin Biomech (Bristol, Avon), 15*(6), 389-406.

Davis, K. G., Marras, W. S., & Waters, T. R. (1998). Evaluation of spinal loading during lowering and lifting. *Clinical Biomechanics, 13*(3), 141-152.

De Looze, M. P., Toussaint, H. M., Ensink, J., Mangnus, C., & Van Der Beek, A. J. (1994). The validity of visual observation to assess posture in a laboratory-simulated, manual material handling task. *Ergonomics, 37*(8), 1335-1343.

Dhillon, N., Bass, E. C., & Lotz, J. C. (2001). Effect of frozen storage on the creep behavior of human intervertebral discs. *Spine, 26*(8), 883-888.

Dieleman, J. L., Cao, J., Chapin, A., Chen, C., Li, Z., Liu, A., . . . Murray, C. J. L. (2020). US Health Care Spending by Payer and Health Condition, 1996-2016. *JAMA, 323*(9), 863.

Dolan, P., Earley, M., & Adams, M. A. (1994). Bending and compressive stresses acting on the lumbar spine during lifting activities. *Journal of Biomechanics, 27*(10), 1237-1248.

Domazetovic, V., Marcucci, G., Iantomasi, T., Brandi, M. L., & Vincenzini, M. T. (2017). Oxidative stress in bone remodeling: role of antioxidants. *Clin Cases Miner Bone Metab, 14*(2), 209-216.

Dougherty, G., & Varro, J. (2000). A quantitative index for the measurement of the tortuosity of blood vessels. *Med Eng Phys, 22*(8), 567-574. doi:10.1016/s1350-4533(00)00074-6

Dropkin, J., Moline, J., Power, P. M., & Kim, H. (2015). A qualitative study of health problems, risk factors, and prevention among Emergency Medical Service workers. *Work, 52*(4), 935-951.

Dunk, N. M., Kedgley, A. E., Jenkyn, T. R., & Callaghan, J. P. (2009). Evidence of a pelvis-driven flexion pattern: are the joints of the lower lumbar spine fully flexed in seated postures? *Clin Biomech (Bristol, Avon), 24*(2), 164-168.

Dunlop, R. B., Adams, M. A., & Hutton, W. C. (1984). Disc space narrowing and the lumbar facet joints. *Journal of Bone and Joint Surgery, 66*(5), 706-710.

Englemark, V. E. (1961). *Functionally induced changes in articular cartilage* (F. G. Evans Ed.). Springfield, IL: Charles C Thomas.

Fahey, V., Opeskin, K., Silberstein, M., Anderson, R., & Briggs, C. (1998). The pathogenesis of Schmorl's nodes in relation to acute trauma: An autopsy study. *Spine, 23*(21), 2272-2275.

Falk, J., Aasa, U., & Berglund, L. (2021). How accurate are visual assessments by physical therapists of lumbo-pelvic movements during the squat and deadlift? *Phys Ther Sport, 50*, 195-200.

Fathallah, F. A., Marras, W. S., & Parnianpour, M. (1998). An assessment of complex spinal loads during dynamic lifting tasks. *Spine (Phila Pa 1976), 23*(6), 706-716.

Ferguson, S. J., & Steffen, T. (2003). Biomechanics of the aging spine. *European Spine Journal, 12*(0), S97-S103. doi:10.1007/s00586-003-0621-0

Fields, A. J., Han, M., Krug, R., & Lotz, J. C. (2015). Cartilaginous End Plates: Quantitative MR Imaging with Very Short Echo Times—Orientation Dependence and Correlation with Biochemical Composition. *Radiology, 274*(2), 482-489.

Fields, A. J., Liebenberg, E. C., & Lotz, J. C. (2013). Innervation of pathologies in the lumbar vertebral endplate and intervertebral disc. *The Spine Journal, 14*(3), 513-521.

Fields, A. J., Rodriguez, D., Gary, K. N., Liebenberg, E. C., & Lotz, J. C. (2013). Influence of Biochemical Composition on Endplate Cartilage Tensile Properties in the Human Lumbar Spine. *Journal of Orthopaedic Research, 32*(2), 245-252.

Fiori, C. (2021). *An in vitro model of oxidative damage in bovine cortical bone to induce bone fragility.* (Master of Applied Science). University of Waterloo,

Firminger, C. R., Asmussen, M. J., Cigoja, S., Fletcher, J. R., Nigg, B. M., & Edwards, W. B. (2020). Cumulative metric of tendon load and damage vary discordantly with running speed. *Medicine & Science in Sports & Exercise, In Press*.

Fleck, C., & Eifer, D. (2003). Deformation behaviour and damage accumulation of cortical bone specimens from the equine tibia under cyclic loading. *Journal of Biomechanics, 36*(2), 179-189.

Friedenberg, R., Kalichman, L., Ezra, D., Wacht, O., & Alperovitch-Najenson, D. (2022). Work-related musculoskeletal disorders and injuries among emergency medical technicians and paramedics: A comprehensive narrative review. *Archives of Environmental & Occupational Health, 77*(1), 9-17.

Frobin, W., Brinckmann, P., Leivseth, G., Biggemann, M., & Reikerås, O. (1996). Precision measurement of segmental motion from flexion-extension radiographs of the lumbar spine. *Clinical Biomechanics, 11*(8), 457-465.

Frost, D. M., Beach, T. A., Crosby, I., & McGill, S. M. (2015). Firefighter injuries are not just a fireground problem. *Work, 52*(4), 835-842.

Fung, D. T., Wang, V. M., Laudier, D. M., Shine, J. H., Basta-Pljakic, J., Jepsen, K. J., . . . Flatow, E. L. (2008). Subrupture tendon fatigue damage. *Journal of Orthopaedic Research, 27*(2), 264-273.

Fyhrie, D. P., & Schaffler, M. B. (1994). Failure mechanisms in human vertebral cancellous bone. *Bone, 15*(1), 105-109.

Galante, J. O. (1967). Tensile Properties of the human annulus fibrosus. *Acta Orthopeadica Scandinavia Supplement, 100*, 1-91.

Gallagher, S., & Heberger, J. R. (2013). Examining the Interaction of Force and Repetition on Musculoskeletal Disorder Risk: A Systematic Literature Review. *Human Factors, 55*(1), 108-124.

Gallagher, S., Marras, W., Litsky, A. S., & Burr, D. (2005). Torso flexion loads and the fatigue failure of human lumbosacral motion segments. *Spine, 30*(20), 2265-2273.

Gallagher, S., & Marras, W. S. (2012). Tolerance of the lumbar spine to shear: A review and recommended exposure limits. *Clinical Biomechanics, 27*(10), 973-978.

Gallagher, S., Marras, W. S., Litsky, A. S., & Burr, D. (2006). An exploratory study of loading and morphometric factors associated with specific failure modes in fatigue testing of lumbar motion segments. *Clinical Biomechanics, 21*(3), 228-234.

Gallagher, S., & Schall Jr., M. C. (2017). Musculoskeletal disorders as a fatigue failure process: evidence, implications and research needs. *Ergonomics, 60*(2), 255-269.

Gallagher, S., Sesek, R. F., Schall, M. C., & Huangfu, R. (2017). Development and validation of an easy-to-use risk assessment tool for cumulative low back loading: The Lifting Fatigue Failure Tool (LiFFT). *Applied Ergonomics, 63*, 142-150.

Garg, A., Boda, S., Hegmann, K. T., Moore, J. S., Kapellusch, J. M., Bhoyar, P., . . . Malloy, E. J. (2014). The NIOSH Lifting Equation and Low-Back Pain, Part 1. *Human Factors: The Journal of the Human Factors and Ergonomics Society, 56*(1), 6-28.

Genaidy, A. M., Waly, S. M., Khalil, T. M., & Hidalgo, J. (1993). Spinal compression tolerance limits for the design of manual material handling operations in the workplace. *Ergonomics, 36*(4), 415-434.

Geniady, A. M., Waly, S. M., Khalil, T. M., & Hidalgo, J. (1993). Spinal compression tolerance limits for the design of manual material handling operations in the workplace. *Ergonomics, 36*(4), 415-434.

George, W. T., & Vashishth, D. (2006). Damage mechanisms and failure modes of cortical bone under components of physiological loading. *Journal of Orthopaedic Research, 23*(5), 1047-1053.

Gertzbein, S. D., Seligman, J., Holtby, R., Chan, K. H., Kapasouri, A., Tile, M., & Cruickshank, B. (1985). Centrode patterns and segmental instability in degenerative disc disease. *Spine, 10*(3), 257-261.

Gertzbein, S. D., Seligman, J., Holtby, R., Chan, K. W., Ogston, N., Kapasouri, A., & Tile, M. (1986). Centrode characteristics of the lumbar spine as a function of segmental instability. *Clinical Orthopaedics and Related Research,* (208), 48-51.

Ghanbarian, B., Hunt, A. G., Ewing, R. P., & Sahimi, M. (2013). Tortuosity in Porous Media: A Critical Review. *Soil Science Society of America Journal, 77*(5), 1461-1477.

Giers, M. B., Munter, B. T., Eyster, K. J., Ide, G. D., Newcomb, A. G. U. S., Lehrman, J. N., . . . Theodore, N. (2017). Biomechanical and endplate effects on nutrient transport in the intervertebral disc. *World Neurosurgery, 99*, 395-402.

Gooyers, C. E., Beach, T. A. C., Frost, D. M., Howarth, S. J., & Callaghan, J. P. (2018). Identifying interactive effects of task demands in lifting on estimates of in vivo low back joint loads. *Applied Ergonomics, 67*, 203-210.

Gooyers, C. E., & Callaghan, J. P. (2015). Exploring interactions between force, repetition and posture on intervertebral disc height loss and bulging in isolated porcine cervical functional spinal units from sub-acute-failure magnitudes of cyclic compressive loading. *Journal of Biomechanics, 48*(13), 3701-3708.

Gooyers, C. E., & Callaghan, J. P. (2016). Peak Stress in the Annulus Fibrosus Under Cyclic Biaxial Tensile Loading. *Journal of Biomechanical Engineering, 138*(5), 051006.

Gooyers, C. E., Frost, D. M., McGill, S. M., & Callaghan, J. P. (2013). Partial rupture of the Achilles tendon during a simulated fire ground task: Insights obtained from a case report for the prevention and reporting of musculoskeletal injury. *Clinical Biomechanics, 28*, 436-440.

Gooyers, C. E., McMillan, E. M., Noguchi, M., Quadrilatero, J., & Callaghan, J. P. (2015). Characterizing the combined effects of force, repetition and posture on injury pathways and micro-structural damage in isolated functional spinal units from sub-acute-failure magnitudes of cyclic compressive loading. *Clinical Biomechanics, 30*(9), 953-959.

Gooyers, C. E., McMillan, R. D., Howarth, S. J., & Callaghan, J. P. (2012). The impact of posture and prolonged cyclic compressive loading on vertebral joint mechanics. *Spine, 37*(17), 1023-1029.

Granata, K. P., & Marras, W. S. (1995). An EMG-assisted model of trunk loading during free-style lifting. *Journal of Biomechanics, 28*(1309-1317).

Grant, J. P., Oxland, T. R., & Dvorak, M. F. (2001). Mapping the structural properties of the lumbosacral vertebral endplates. *Spine, 20*(5), 115-1120.

Guilak, F., Meyer, B. C., Ratcliffe, A., & Mow, V. C. (1994). The effects of matrix compression on proteoglycan metabolism in articular cartilage explants. *Osteoarthritis Cartilage, 2*(2),

Guiot, B. H., & Fessler, R. G. (2000). Molecular biology of degenerative disc disease. *Neurosurgery, 47*(5), 1034-1040.

Gullbrand, S. E., Peterson, J., Ahlborn, J., Mastropolo, R., Fricker, A., Roberts, T. T., . . . Ledet, E. H. (2015). ISSLS Prize Winner: Dynamic Loading-Induced Convective Transport Enhances Intervertebral Disc Nutrition. *Spine (Phila Pa 1976), 40*(15), 1158-1164.

Gunning, J. L., Callaghan, J. P., & McGill, S. M. (2001). Spinal posture and prior loading history modulate compressive strength and type of failure in the spine: A biomechanical study using a cervical porcine model. *Clinical Biomechanics, 16*(6), 471-480.

Hamanishi, C., Kawabata, T., Yosii, T., & Tanaka, S. (1994). Schmorl's Nodes on magnetic resonance imaging: Their incidence and clinical relevance. *Spine, 19*(4), 450-453.

Han, Y. C., Ma, B., Guo, S., Yang, M., Li, L. J., Wang, S. J., & Tan, J. (2018). Leptin regulates disc cartilage endplate degeneration and ossification through activation of the MAPK-ERK signalling pathway. *Journal of Cellular and Molecular Medicine, 22*(4), 2098-2109.

Hansson, T. H., Keller, T. S., & Spengler, D. M. (1987). Mechanical behavior of the human lumbar spine II. Fatigue strength during dynamic compressive loading. *Journal of Orthopaedic Research, 5*, 479-487.

Hartvigsen, J., Hancock, M. J., Kongsted, A., Louw, Q., Ferreira, M. L., Genevay, S., . . . Woolf, A. (2018). What low back pain is and why we need to pay attention. *The Lancet, 391*(10137), 2356-2367.

Hauret, K. G., Jones, B. H., Bullock, S. H., Canham-Chervak, M., & Canada, S. (2010). Musculoskeletal Injuries: Description of an Under-Recognized Injury Problem Among Military Personnel. *American Journal of Preventitive Medicine, 38*(61-70).

Heneghan, C. (2002). Characterization of changes in blood vessel width and tortuosity in retinopathy of prematurity using image analysis. *Medical Image Analysis, 6*(4), 407-429.

Hollander, A. P., Heathfield, T. F., Liu, J. J., Pidoux, I., Roughley, P. J., Mort, J. S., & Poole, A. R. (1996). Enhanced denaturation of the ?1(II) chains of type-II collagen in normal adult human intervertebral discs compared with femoral articular cartilage. *Journal of Orthopaedic Research, 14*(1), 61-66.

Holmes, A. D., Hukins, D. W., & Freemont, A. J. (1993). End-plate displacement during compression of lumbar vertebra-disc-vertebra segments and the mechanism of failure. *Spine, 18*(1), 128-135.

Hosseini, S. M., Veldink, M. B., Ito, K., & Van Donkelaar, C. C. (2013). Is collagen fiber damage the cause of early softening in articular cartilage? *Osteoarthritis and Cartilage, 21*(1), 136-143.

Hou, Y., & Luo, Z. (2009). A Study on the Structural Properties of the Lumbar Endplate. *Spine, 34*(12), E427-E433.

Huang, B., Liu, J., Wei, X., Li, S., Xiang, Y., Wu, H., . . . Zhao, F. (2021). Damage to the human lumbar cartilage endplate and its clinical implications. *J Anat, 238*(2), 338-348.

Huang, Y. C., Urban, J. P., & Luk, K. D. (2014). Intervertebral disc regeneration: Do nutrients lead the way? *Nature Reviews Rheumatology, 10*(9), 561-566.

Hutton, W. C., & Adams, M. A. (1982). Can the lumbar spine be crashed in heavy lifting. *Spine, 7*, 586-590.

Hutton, W. C., Cyron, B. M., & Scott, J. R. R. (1979). The compressive strength characteristics of lumbar vertebrae. *Journal of Anatomy, 129*, 753-758.

Iatridis, J. C., Maclean, J. J., & Ryan, D. A. (2005). Mechanical damage to the intervertebral disc annulus fibrosus subjected to tensile loading. *Journal of Biomechanics, 38*(3), 557-565.

Imai, K., Ohnishi, I., Bessho, M., & Nakamura, K. (2006). Nonlinear Finite Element Model Predicts Vertebral Bone Strength and Fracture Site. *Spine, 31*(16), 1789-1794.

Jackman, T. M., Hussein, A. I., Adams, A. M., Makhnejia, K. K., & Morgan, E. F. (2014). Endplate Deflection Is a Defining Feature of Vertebral Fracture and Is Associated With Properties of the Underlying Trabecular Bone. *Journal of Orthopaedic Research, 32*(7), 880-886.

Jackson, A., & Gu, W. (2009). Transport properties of cartilaginous tissues. *Current Rheumatology Reviews, 5*(1), 40.

Jaffe, M., Hammond, W., Tolias, P., & Arinzeh, T. (2012). Assays For Determining Cell Differentiation. In *Characterization of Biomaterials*: Woodhead Publishing

Jager, M., & Luttmann, A. (1989). Biomechanical analysis and assessment of lumbar stress during loading lifting using a dynamic 19 segment human model. *Ergonomics, 32*, 93-112.

James, C. R., Dufek, J. S., & Bates, B. T. (2000). Effects of injury proneness and task difficulty on joint kinetic variability. *Medicine & Science in Sports & Exercise, 32*(11), 1833-1844.

Jennings, B. M., Yoder, L. H., Heiner, S. L., Loan, L. A., & Bingham, M. O. (2008). Soldiers with musculoskeletal injuries. *Journal of Nursing Scholarship, 40*(3), 268-274.

Jin, M., Frank, E. H., Quinn, T. M., Hunziker, E. B., & Grodzinsky, A. J. (2001). Tissue shear deformation stimulates proteoglycan and protein biosynthesis in bovine cartilage explants. *Archives of Biochemistry and Biophysics, 395*(1), 41-48.

Johnson, I., & Spence, M. T. J. (2010). Antibodies, Avidins and Lectins. In *The Molecular Probes Handbook: A Guide to Fluorecent Probes and Labeling Techniques Eleventh Edition*: Life Technologies Corporation.

Kaplan, J. T., Neu, C. P., Drissi, H., Emery, N. C., & Pierce, D. M. (2017). Cyclic loading of human articular cartilage: The transition from compaction to fatigue. *Journal of the Mechanical Behaviour of Biomedical Materials, 65*, 734-742.

Katsavouni, F., Bebetsos, E., Malliou, P., & Beneka, A. (2014). The type and causes of injuries in firefighters. *Archives of Hellenic Medicine, 31*(4), 446-451.

Kawchuk, G. N., Decker, C., Dolan, R., & Carey, J. (2009). Structural health monitoring to detect the presence, location and magnitude of structural damage in cadaveric porcine spines. *Journal of Biomechanics, 42*(2), 109-115.

Kiani, C., Chen, L., Wu, Y. J., Yee, A. J., & Yang, B. B. (2002). Structure and function of aggrecan. *Cell Research, 12*(1), 19-32.

Kim, W. U., Yoo, W. H., Park, W., Kang, Y. M., Kim, S. I., Park, J. H., . . . Kim, H. Y. (2000). IgG antibodies to type II collagen reflect inflammatory activity in patients with rheumatoid arthritis. *J Rheumatol, 27*(3), 575-581.

Kimball, J. S., Johnson, J. P., & Carlson, D. A. (2021). Oxidative Stress and Osteoporosis. *JBJS, 103*(15), 1451-1461.

Klimek, C., Ashbeck, C., Brook, A. J., & Durall, C. (2018). Are Injuries More Common With CrossFit Training Than Other Forms of Exercise? *Journal of Sport Rehabilitation, 27*(3), 295-299.

Kocaoglu, B., Martin, J., Wolf, B., Karahan, M., & Amendola, A. (2011). The effect of irrigation solution at different temperatures on articular cartilage metabolism. *Arthroscopy, 27*(4), 526-531.

Kong, D., Zheng, T., Zhang, M., Wang, D., Du, S., Li, X., . . . Cao, X. (2013). Static Mechanical Stress Induces Apoptosis in Rat Endplate Chondrocytes through MAPK and Mitochondria-Dependent Caspase Activation Signaling Pathways. *PLoS One, 8*(7), e69403.

Krag, M. H., Cohen, M. C., Haugh, L. D., & Pope, M. H. (1990). Body weight change during upright and recumbent posture. *Spine, 15*, 202-207.

Kumar, S. (2001). Theories of musculoskeletal injury causation. *Ergonomics, 44*(1), 17-47.

Kyere, K., Than, K. D., Wang, A. C., Rahman, S. U., Valdivia, J. M., La Marca, F., & Park, P. (2012). Schorl's nodes. *European Spine Journal, 21*, 2115-2121.

Lakstins, K., Arnold, L., Gunsch, G., Flanigan, D., Khan, S., Gadde, N., . . . Purmessur, D. (2020). Characterization of the human intervertebral disc cartilage endplate at the molecular, cell, and tissue levels. *Journal of Orthopaedic Research*.

Lakstins, K., Arnold, L., Gunsch, G., Khan, S., Moore, S., & Purmessur, D. (2020). Characterization of bovine and canine animal model cartilage endplates and comparison to human cartilage endplate structure, matrix composition, and cell phenotype. *JOR SPINE, 3*(4).

Lama, P., Zehra, U., Balkovec, C., Claireaux, H. A., Flower, L., Harding, I. J., . . . Adams, M. A. (2014). Significance of cartilage endplate within herniated disc tissue. *European Spine Journal, 23*(9), 1869-1877.

Lambers, F. M., Bouman, A. R., Tkachenko, E. V., Keaveny, T. M., & Hernandez, C. J. (2014). The effects of tensile-compressive loading mode and microarchitecture on microdamage in human vertebral cancellous bone. *Journal of Biomechanics, 47*(15), 3605-3612.

Leonard, A. K., Loughran, E. A., Klymenko, Y., Liu, Y., Kim, O., Asem, M., . . . Stack, M. S. (2018). Methods for the visualization and analysis of extracellular matrix protein structure and degradation. In (pp. 79-95): Elsevier.

Li, Y. H., Wu, H. L., Li, Z., Li, B. B., Zhu, M., Chen, D., . . . Huang, Y. C. (2022). Species variation in the cartilaginous endplate of the lumbar intervertebral disc. *JOR SPINE, 5*(3), e1218.

Lipps, D. B., Wojtys, E. M., & Ashton-Miller, J. A. (2013). Anterior cruciate ligament fatigue failures in knees subjected to repeated simulated pivot landings. *American Journal of Sports Medicine, 42*(5), 1058-1066.

Lotz, J. C., Fields, A. J., & Liebenberg, E. C. (2013). The role of the vertebral endplate in low back pain. *Global Spine Journal, 3*(3), 153-164.

Lund, T., Nydegger, T., Rathonyi, G., Nolte, L. P., Schlenzka, D., & Oxland, T. R. (2003). Three-dimensional stabilization provided by the external spinal fixator compared to two internal fixation devices: a biomechanical in vitro flexibility study. *Eur Spine J, 12*(5), 474-479.

Maerz, T., Newton, M., Marek, A. A., Planalp, M., & Baker, K. (2018). Dynamic adaptation of vertebral endplate and trabecular bone following annular injury in a rat model of degenerative disc disease. *The Spine Journal, 18*(11), 2091-2101.

Malandrino, A., Planell, J. A., & Lacroix, D. (2009). Statistical factorial analysis on the poroelastic material properties sensitivity of the lumbar intervertebral disc under compression, flexion and axial rotation. *Journal of Biomechanics, 42*(16), 2780-2788.

Mallory, F. B. (1900). A CONTRIBUTION TO STAINING METHODS. *Journal of Experimental Medicine, 5*(1), 15-20.

Marras, W. S. (2000). Occupational low back disorder causation and control. *Ergonomics, 43*(7), 880-902.

Marras, W. S., Fine, L. J., Ferguson, S. A., & Waters, T. R. (1999). The effectiveness of commonly used lifting assessment methods to identify industrial jobs associated with elevated risk of low-back disorders. *Ergonomics, 42*(1), 229-245.

Marras, W. S., Granata, K. P., Davis, K. G., Allread, W. G., & Jorgensen, M. J. (1997). Spine loading and probability of low back disorder risk as a function of box location on a pallet. *Human Factors and Ergonomics in Manufacturing & Service Industries, 6*(4), 323-336.

Marras, W. S., Knapik, J. J., & Ferguson, S. A. (2009). Lumbar spine forces during manoeuvering of ceiling-based and floor-based patient transfer devices. *Ergonomics, 52*(3), 384-397.

Marras, W. S., Lavender, S. A., Leurgans, S. E., Fathallah, F. A., Ferguson, S. A., Allread, W. G., & Rajulu, S. L. (1995). Biomechanical risk factors for occupationally related low back disroders. *Ergonomics, 38*(2), 377-410.

Marras, W. S., Lavender, S. A., Leurgans, S. E., Rajulu, S. L., Allread, W. G., Fathallah, F. A., & Ferguson, S. A. (1993). The Role of Dynamic Three-Dimensional Trunk Motion in Occupationally-Related Low Back Disorders: The Effects of Workplace Factors, Trunk Position, and Trunk Motion Characteristics on Risk of Injury. *Spine, 18*(5), 617-628.

Marras, W. S., Parakkat, J., Chany, A. M., Yang, G., Burr, D., & Lavender, S. A. (2006). Spine loading as a function of lift frequency, exposure duration, and work experience. *Clinical Biomechanics, 21*(4), 345-352.

Martin, J. T., Wesorick, B., Oldweiler, A. B., Kosinski, A. S., Goode, A. P., & Defrate, L. E. (2022). In vivo fluid transport in human intervertebral discs varies by spinal level and disc region. *JOR SPINE, 5*(2).

Martins, D. E., Medeiros, V. P. D., Wajchenberg, M., Paredes-Gamero, E. J., Lima, M., Reginato, R. D., . . . Faloppa, F. (2018). Changes in human intervertebral disc biochemical composition and bony end plates between middle and old age. *PLoS One, 13*(9), e0203932.

Massarwa, E., Aboudi, J., Galbusera, F., Wilke, H. J., & Haj-Ali, R. (2017). A nonlinear micromechanical model for progressive damage of vertebral trabecular bones. *Journal of Mechanics of Materials and Structures, 12*(4), 407-424.

Masuoka, K., Michalek, A. J., Maclean, J. J., Stokes, I. A. F., & Iatridis, J. C. (2007). Different Effects of Static Versus Cyclic Compressive Loading on Rat Intervertebral Disc Height and Water Loss In Vitro. *Spine, 32*(18), 1974-1979.

Mathiassen, S. E. (2006). Diversity and variation in biomechanical exposure: what is it, and why we would like to know. *Applied Ergonomics, 37*(4), 419-427.

Mattei, T. A. (2018). Rope Jumping−Induced Traumatic Compression Fractures: the Underestimated Danger of Repetitive Axial Load Forces. *World Neurosurgery, 113*, 96-97.

McGill, S. M. (1997). The biomechanics of low back injury: implications on current practice in industry and the clinic. *Journal of Biomechanics, 30*(5), 465-475.

McGill, S. M. (2002). *Low Back Disorders 2nd Ed.* Windsor, ON: Human Kinetics.

McGill, S. M., Hughson, R. L., & Parks, K. (2000). Changes in lumbar lordosis modify the role of the extensor muscles. *Clinical Biomechanics, 15*(1), 777-780.

McGill, S. M., & Norman, R. W. (1986). Partitioning of the L4-L5 dynamic moment into disc, ligamentous, and muscular components during lifting. *Spine, 11*(7), 666-678.

McGill, S. M., Norman, R. W., Yingling, V. R., Wells, R. W., & Neumann, P. (1998). *Shear Happens! Suggested Guidelines for Ergonomists to Reduce Risk of Low Back Injury From Shear Loading*. Paper presented at the 30th Annual Conference of the Human Factors Association of Canada, Mississauga, ON.

McInnis, M. M., Olchanski, N., Kemner, J. E., & Goss, T. (2010). PMS17 Budget Impact of New RhBMP-2 Formulation in Patients Undergoing Posterolateral Spinal Fusion Procedures for Degenerative Disc Disease in Randomized Controlled Trial (RCT). *Value Health, 13*(7), A305.

McLachlin, S. D., Beaton, B. J., Sabo, M. T., Gurr, K. R., Bailey, S. I., Bailey, C. S., & Dunning, C. E. (2008). Comparing the fixation of a novel hollow screw versus a conventional solid screw in human sacra under cyclic loading. *Spine, 33*(17), 1870-1875.

McLain, R. F., Yerby, S. A., & Moseley, T. A. (2002). Comparative morphometry of L4 verebrae: comparison of large animal models for the human lumbar spine. *Spine, 27*(8), 200-206.

McMillan, D. W., Garbutt, G., & Adams, M. A. (1996). Effect of sustained loading on the water content of intervertebral discs: implications for disc metabolism. *Annals of the Rheumatic Diseases, 55*(12), 880-887.

McMillan, D. W., McNally, D. S., Garbutt, G., & Adams, M. A. (1996). Stress distributions inside intervertebral discs: the validity of experimental 'stress profilometry'. *Proceedings of the Institution of Mechanical Engineers, 210*, 81-87.

Mimura, M., Panjabi, M. M., Oxland, T. R., Crisco, J. J., Yamamoto, I., & Vasavada, A. (1994). Disc degeneration affects the multidirectional flexibility of the lumbar spine. *Spine, 19*(12), 1371-1380.

Minns, R. J., & Walsh, W. K. (1997). Preliminary design and experimental studies of a novel soft implant for correcting sagittal plane instability in the lumbar spine. *Spine (Phila Pa 1976), 22*(16), 1819-1825; discussion 1826-1817.

Mirzaali, M. J., Libonati, F., Ferrario, D., Rinaudo, L., Messina, C., Ulivieri, F. M., & Cesana, B. M. (2018). Determinants of bone damage: An ex-vivo study on porcine vertebrae. *PloS ONE, 13*(8), e0202210.

Mok, F. P. S., Samartzis, D., Kappinen, J., Luk, K. D., Fong, D. Y. T., & Cheung, K. M. C. (2010). ISSLS Prize Winner: Prevalence, Determinants, and Association of Schmorl Nodes of the Lumbar Spine With Disc Degeneration. A Population-Based Study of 2449 Individuals. *Spine, 35*(21), 1944-1952.

Montalvo, A. M., Shaefer, H., Rodriguez, B., Li, T., Epnere, K., & Myer, G. D. (2017). Retrospective injury epidemiology and risk factors for injury in CrossFit. *Journal of Sports Science and Medicine, 16*(1), 53-59.

Moore, R. J. (2000). The vertebral end-plate: what do we know? *European Spine Journal, 9*, 92-96.

Morisako, T., Nakamae, T., Kamei, N., Tamura, T., Tsuchikawa, Y., Harada, T., . . . Adachi, N. (2022). Development of a rat model with lumbar vertebral endplate lesion. *European Spine Journal, 31*(4), 874-881.

Nemati, R., Rahbar Shahrouzi, J., & Alizadeh, R. (2020). A stochastic approach for predicting tortuosity in porous media via pore network modeling. *Computers and Geotechnics, 120*, 103406.

NIOSH. (1981). *Work practices guide for manual lifting. NIOSH Technical report no. 81-122*. Cincinnati, OH: US Department of Health and Human Services, National Institute for Occupational Safety and Health.

Noguchi, N., Gooyers, C. E., Karakolis, T., Noguchi, K., & Callaghan, J. P. (2016). Is intervertebral disc pressure linked to herniation?: An in-vitro study using a porcine model. *Journal of Biomechanics, 49*, 1824-1830.

Norman, R. W., Wells, R. P., Naumann, P., Frank, J., Shannon, H., & Kerr, M. (1998). A comparison of peak vs. cumulative physical work exposure risk factors for the reporting of low back pain in the automotive industry. *Clinical Biomechanics, 13*(8), 561-573.

Noshchenko, A., Atousa, P., Patel, V. V., Burger, E. L., Baldini, T., & Lu, Y. (2013). Correlation of Vertebral Strength Topography With 3-Dimensional Computed Tomographic Structure. *Spine, 38*(4), 339-349.

Nye, N. S., Pawlak, M. T., Webber, B. J., Tchandja, J. N., & Milner, M. R. (2016). Description and Rate of Musculoskeletal Injuries in Air Force Basic Military Trainees, 2012−2014. *Journal of Athletic Training, 51*(11), 858-865.

O'Callaghan, P., Szarko, M., Wang, Y., & Luo, J. (2018). Effects of bone damage on creep behaviours of human vertebral trabeculae. *Bone, 106*, 204-210.

Ochia, R. S., Inoue, N., Renner, S. M., Lorenz, E. P., Lim, T. H., Andersson, G. B., & An, H. S. (2006). Three-dimensional in vivo measurement of lumbar spine segmental motion. *Spine, 31*(18), 2073-2078.

Oda, H., Matsuzaki, H., Tokuhashi, Y., Wakabayashi, K., Uematsu, Y., & Iwahashi, M. (2004). Degeneration of intervertebral discs due to smoking: experimental assessment in a rat-smoking model. *J Orthop Sci, 9*(2), 135-141.

Ohtori, S., Inoue, G., Ito, T., Koshi, T., Ozawa, T., Doya, H., . . . Takahashi, K. (2006). Tumor necrosis factor-immunoreactive cells and PGP 9.5-immunoreactive nerve fibers in

vertebral endplates of patients with discogenic low back Pain and Modic Type 1 or Type 2 changes on MRI. *Spine (Phila Pa 1976), 31*(9), 1026-1031.

Otoo, B. S., Li, L., Hart, D. A., & Herzog, W. (2022). Development of a Porcine Model to Assess the Effect of In Situ Knee Joint Loading on Site-Specific Cartilage Gene Expression. *Journal of Biomechanical Engineering, 144*(2). doi:10.1115/1.4051922

Oxland, T. R., Panjabi, M. M., Southern, E. P., & Duranceau, J. S. (1991). An anatomic basis for spinal instability: a porcine trauma model. *Journal of Orthopaedic Research, 9*(3), 452-462.

Paietta, R. C., Burger, E. L., & Ferguson, V. L. (2013). Mineralization and collagen orientation throughout aging at the vertebral endplate in the human lumbar spine. *Journal of Structural Biology, 184*(2), 310-320.

Panjabi, M. M. (1988). Biomechanical evaluation of spinal fixation devices: I. A conceptual framework. *Spine, 13*(10), 1129-1134.

Panjabi, M. M. (1992). The stabilizing system of the spine: Part I: Function, dysfunction, adaptation, and enhancement. *Journal of Spinal Disorders, 5*(4), 383-390.

Parkinson, R. J., & Callaghan, J. P. (2007a). Can periods of static loading be used to enhance the resistance of the spine to cumulative compression? *Journal of Biomechanics, 40*, 2944-2952.

Parkinson, R. J., & Callaghan, J. P. (2007b). The role of load magnitude as a modifier of the cumulative load tolerance of porcine cervical spinal units: progress towards a force weighting approach. *Theoretical Issues In Ergonomics Science, 8*(3), 171-184.

Parkinson, R. J., & Callaghan, J. P. (2008). Quantification of the relationship between load magnitude, rest duration and cumulative compressive tolerance of the spine: development of a weighting system for adjustment to a common injury exposure level. *Theoretical Issues In Ergonomics Science, 9*(3), 255-268.

Parkinson, R. J., & Callaghan, J. P. (2009). The role of dynamic flexion in spine injury is altered by increasing dynamic load magnitude. *Clinical Biomechanics, 24*(2), 148-154.

Parkinson, R. J., Durkin, J. L., & Callaghan, J. P. (2005). Estimating the compressive strength of the porcine cervical spine: an examination of the utility of DXA. *Spine, 30*(17), E492-498.

Patel, R. R., Noshchenko, A., Carpenter, R. D., Baldini, T., Frick, C. P., Patel, V. V., & Yakacki, C. M. (2018). Evaluation and Prediction of Human Lumbar Vertebrae Endplate Mechanical Properties Using Indentation and Computed Tomography. *Journal of Biomechanical Engineering, 140*(10), 1010111-1010119.

Patwardhan, A. G., Havey, R. M., Carandang, G., Simonds, J., Voronov, L. I., Ghanayem, A. J., . . . Paxinos, O. (2003). Effect of compressive follower preload on the flexion-extension response of the human lumbar spine. *Journal of Orthopaedic Research, 21*(3), 540-546.

Pauli, C., Whiteside, R., Heras, F. L., Nesic, D., Koziol, J., Grogan, S. P., . . . Lotz, M. K. (2012). Comparison of cartilage histopathology assessment systems on human knee joints at all stages of osteoarthritis development. *Osteoarthritis and Cartilage, 20*(6), 476-485.

Pearcy, M., Portek, I., & Shepherd, J. (1984). Three-dimensional x-ray analysis of normal movement in the lumbar spine. *Spine (Phila Pa 1976), 9*(3), 294-297.

Pearcy, M. J., & Bogduk, N. (1988). Instantaneous axes of rotation of the lumbar intervertebral joints. *Spine, 13*(9), 1033-1041.

Peng, B., Wu, W., Hou, S., Shang, W., WAng, X., & Yang, Y. (2003). The pathogenesis of Schmorl's nodes. *Journal of Bone and Joint Surgery, 85*, 879-882.

Perey, O. (1957). Fracture of the Vertebral End-Plate in the Lumbar Spine: An Experimental Biomechanical Investigation. *Acta Orthopaedica Scandinavica, 28*(sup25), 1-101.

Pfirrmann, C. W., & Resnick, D. (2001). Schmorl nodes of the thoracic and lumbar spine: radiographic-pathologic study of prevalence, characterization, and correlation with degenerative changes of 1,650 spinal levels in 100 cadavers. *Radiology, 219*(2), 368-374.

Porter, R. W., & Adams, M. A. (1989). Physical activity and strength of the lumbar spine. *Spine, 14*, 201-203.

Prairie, J., Plamondon, A., Hegg-Deloye, S., Larouche, D., & Corbeil, P. (2016). Biomechanical risk assessment during field loading of hydraulic stretchers into ambulances. *International Journal of Industrial Ergonomics, 54*, 1-9.

Purcell, P., Tiernan, S., McEvoy, F., & Morris, S. (2015). Strong similarities in the creep and damage behaviour of a synthetic bone model compared to human trabecular bone under compressive cyclic loading. *Journal of the Mechanical Behaviour of Biomedical Materials, 48*, 51-59.

Putzer, M., Ehrlich, I., Rasmussen, J., Gebbeken, N., & Dendorfer, S. (2016). Sensitivity of lumbar spine loading to anatomical parameters. *Journal of Biomechanics, 49*(6), 953-968.

Qasim, M., Natarajan, R. N., An, H. S., & Andersson, G. B. J. (2012). Initiation and progression of mechanical damage in the intervertebral disc under cyclic loading using continuum damage mechanics methodology: A finite element study. *Journal of Biomechanics, 45*(11), 1934-1940.

Rajasekaran, S., Bajaj, N., Tubaki, V., Kanna, R. M., & Shetty, A. P. (2013). ISSLS Prize winner: The anatomy of failure in lumbar disc herniation: an in vivo, multimodal, prospective study of 181 subjects. *Spine (Phila Pa 1976), 38*(17), 1491-1500.

Rasband, W. S. (1997-2018). ImageJ, U. S. *National Institutes of Health, Bethesda, Maryland, USA*.

Reiland, S. (1978). Growth and skeletal development of the pig. *Acta Radiol Suppl, 358*, 15-22.

Roberts, S., Menage, J., Duance, V., Wotton, S., & Ayad, S. (1991). 1991 Volvo Award in basic sciences. Collagen types around the cells of the intervertebral disc and cartilage end plate: an immunolocalization study. *Spine (Phila Pa 1976), 16*(9), 1030-1038.

Roberts, S., Menage, J., & Urban, J. (1989). Biochemical and structural properties of the cartilage end-plate and its relation to the intervertebral disc. *Spine, 14*, 166-174.

Rodriguez, A. G., Rodriguez-Soto, A. E., Burghardt, A. J., Berven, S., Majumdar, S., & Lotz, J. C. (2011). Morphology of the human vertebral endplate. *Journal of Orthopaedic Research, 30*(2), 280-287.

Saadat, E., Lan, H., Majumdar, S., Rempel, D. M., & King, K. B. (2006). The Proteoglycan Metabolism of Mature Bovine Articular Cartilage Explants Superimposed to Continuously Applied Cyclic Mechanical Loading. *Arthritis Research & Therapy, 8*(5), R147.

Sadeghi, H., Espino, D. M., & Shepherd, D. E. T. (2015). Variation in viscoelastic properties of bovine articular cartilage below, up to and above healthy gait-relevant loading frequencies. *Journal of Engineering In Medicine, 229*(2), 115-123.

Sahlman, J., Inkinen, R., Hirvonen, T., Lammi, M. J., Lammi, P. E., Nieminen, J., . . . Puustjärvi, K. (2001). Premature vertebral endplate ossification and mild disc degeneration in mice after inactivation of one allele belonging to the Col2a1 gene for Type II collagen. *Spine (Phila Pa 1976), 26*(23), 2558-2565.

Sauerland, K., Raiss, R. X., & Steinmeyer, J. (2003). Proteoglycan metabolism and viability of articular cartilage explants as modulated by the frequency of intermittent loading. *Osteoarthritis and Cartilage, 11*(5), 343-350.

Schechtman, H., & Bader, D. L. (2002). Fatigue damage of human tendons. *Journal of Biomechanics 35*(3), 347-353.

Schmidt, A. L., Paskoff, G., Shender, B. S., & Bass, C. R. (2012). Risk of lumbar spine injury from cyclic compressive loading. *Spine, 37*(26), 1614-1621.

Schmorl, G., & Junghanns, H. (1971). *The human spine in health and disease*. New York: Grune and Stratton.

Schultz, A. B., Warwick, D. N., Berkson, M. H., & Nachemson, A. L. (1979). Mechanical Properties of Human Lumbar Spine Motion Segments—Part I: Responses in Flexion, Extension, Lateral Bending, and Torsion. *Journal of Biomechanical Engineering, 101*(1), 46-52.

Seymour, R., Williams, L. A., Rees, J. L., Lyons, K., & Lloyd, D. C. (1998). Magnetic resonance imaging of acute intraosseous disc herniation. *Clinical Radiology, 53*, 363-368.

Siewe, J., Rudat, J., Röllinghoff, M., Schlegel, U. J., Eysel, P., & Michael, J. W. P. (2011). Injuries and overuse syndrome in powerlifting. *International Journal of Sports Medicine, 32*(9), 703-711.

Skaggs, D. L., Weidenbaum, M., Iatridis, J. C., Ratcliffe, A., & Mow, V. C. (1994). Regional variation in tensile properties and biochemical composition of the human lumbar anulus fibrosus. *Spine (Phila Pa 1976), 19*(12), 1310-1319.

Smeathers, J. E., & Joanes, D. N. (1988). Dynamic compressive properties of human lumbar intervertebral joints: A comparison between fresh and thawed specimens. *Journal of Biomechanics, 21*(5), 425-433.

Sophia Fox, A. J., Bedi, A., & Rodeo, S. A. (2009). The Basic Science of Articular Cartilage: Structure, Composition, and Function. *Sports Health: A Multidisciplinary Approach, 1*(6), 461-468.

Steinmeyer, J., Ackermann, B., & Raiss, R. X. (1997). Intermittent cyclic loading of cartilage explants modulates fibronectin metabolism. *Osteoarthritis Cartilage, 5*(5), 331-341.

Steinmeyer, J., & Knue, S. (1997). The proteoglycan metabolism of mature bovine articular cartilage explants superimposed to continuously applied cyclic mechanical loading. *Biochem Biophys Res Commun, 240*(1), 216-221.

Straker, L., Burgess-Limerick, R., Pollock, C., & Egeskov, R. (2004). A randomized and controlled trial of a participative ergonomics intervention to reduce injuries associated with manual tasks: physical risk and legislative compliance. *Ergonomics, 47*(2), 166-188.

Szabó, A., & Merks, R. M. H. (2017). Blood vessel tortuosity selects against evolution of aggressive tumor cells in confined tissue environments: A modeling approach. *PLOS Computational Biology, 13*(7), e1005635. doi:10.1371/journal.pcbi.1005635

Takahashi, K., Mitazaki, T., Ohnari, H., Takino, T., & Tomita, K. (1995). Schmorl's nodes and low-back pain: analysis of magnetic resonance imaging findings in symptomatic and asymptomatic individuals. *European Spine Journal, 4*, 56-59.

Tampier, C., Drake, J. D., Callaghan, J. P., & McGill, S. M. (2007). Progressive Disc Herniation: An Investigation of the Mechanism Using Radiologic, Histochemical, and Microscopic Dissection Techniques on a Porcine Model. *Spine, 32*(25), 2869-2874.

Techens, C., Palanca, M., Éltes, P. E., Lazáry, Á., & Cristofolini, L. (2020). Testing the impact of discoplasty on the biomechanics of the intervertebral disc with simulated degeneration: An in vitro study. *Med Eng Phys, 84*, 51-59.

Tencer, A. F., & Ahmed, A. M. (1981). The role of secondary variables in the measurement of the mechanical properties of the lumbar intervertebral joint. *Journal of Biomechanical Engineering, 103*(3), 129-137.

Thompson, R. E., Barker, T. M., & Pearcy, M. J. (2003). Defining the neutral zone of sheep intervertebral joints during dynamic motions: an in vitro study. *Clinical Biomechanics, 18*(2), 89-98.

Thornton, G. M., Schwab, T. D., & Oxland, T. R. (2007). Cyclic loading causes faster rupture and strain rate than static loading in medial collateral ligament at high stress. *Clinical Biomechanics, 22*(8), 932-940.

Tomaszewski, K. A., Saganiak, K., Gładysz, T., & Walocha, J. A. (2015). The biology behind the human intervertebral disc and its endplates. *Folia Morphologica, 74*(2), 157-168.

Urban, J. P., Smith, S., & Fairbank, J. C. (2004). Nutrition of the intervertebral disc. *Spine (Phila Pa 1976), 29*(23), 2700-2709.

van Dieën, J. H., Dekkers, J. J., Groen, V., Toussiant, H. M., & Meijer, O. G. (2001). Within-subject variability in low back load in a repetitively performed, mildly constrained lifting task. *Spine, 26*(15), 1799-1804.

van Dieën, J. H., Kingma, I., Meijer, R., Hänsel, L., & Huiskes, R. (2001). Stress distribution changes in bovine vertebrae just below the endplate after sustained loading. *Clinical Biomechanics, 16*, S135-S142.

van Heeswijk, V. M., Thambyah, A., Robertson, P. A., & Broom, N. D. (2017). Posterolateral Disc Prolapse in Flexion Initiated by Lateral Inner Annular Failure: An Investigation of the Herniation Pathway. *Spine (Phila Pa 1976), 42*(21), 1604-1613.

Vergroesen, P.-P. A., Van Der Veen, A. J., Van Royen, B. J., Kingma, I., & Smit, T. H. (2014). Intradiscal pressure depends on recent loading and correlates with disc height and compressive stiffness. *European Spine Journal, 23*(11), 2359-2368.

Vernon-Roberts, B., & Pirie, C. J. (1977). DEGENERATIVE CHANGES IN THE INTERVERTEBRAL DISCS OF THE LUMBAR SPINE AND THEIR SEQUELAE. *Rheumatology, 16*(1), 13-21.

Videman, T., Nurminen, M., & Troup, J. D. G. (1990). Lumbar spinal pathology in cadaveric material in relation to history of back pain, occupation, and physical loading. *Spine, 15*(8), 728-740.

Village, J., Trask, C., Luong, N., Chow, Y., Johnson, P., Koehoorn, M., & Teschke, K. (2009). Development and evaluation of an observational Back-Exposure Sampling Tool (Back-EST) for work-related back injury risk factors. *Applied Ergonomics, 40*(3), 538-544.

Wade, K. R., Robertson, P. A., & Boroom, N. D. (2011). A fresh look at the nucleus-endplate region: new evidence for significant structural integration. *European Spine Journal, 20*(8), 1225-1232.

Wang, D., Lai, A., Gansau, J., Nasser, P., Lee, Y., Laudier, D. M., & Iatridis, J. C. (2022). Ex vivo biomechanical evaluation of Acute lumbar endplate injury and comparison to annulus fibrosus injury in a rat model. *J Mech Behav Biomed Mater, 131*, 105234.

Wang, X., T., Ker, R. F., & Alexander, R. M. (1995). Fatigue rupture of wallaby tail tendons. *The Journal of Experimental Biology, 198*, 847-852.

Wang, Y., Videman, T., & Battié, M. C. (2012). Lumbar vertebral endplate lesions: Prevalence, classification, and association with age. *Spine, 27*(17), 1432-1439.

Waterman, B. R., Belmont, P. J., & Schoenfeld, A. J. (2012). Low back pain in the united states: Incidence and risk factors for presentation in the emergency setting. *The Spine Journal, 12*(1), 63-70.

Waters, T. R., Putz-Anderson, V., Garg, A., & Fine, L. J. (1993). Revised NIOSH equation for the design and evaluation of manual lifting tasks. *Ergonomics, 36*(7), 749-776.

Weisenthal, B. M., Beck, C. A., Malony, M. D., DeHaven, K. E., & Giordano, B. D. (2014). Injury rate and patterns among CrossFit athletes. *The Orthopaedic Journal of Sports Medicine, 2*(4), 1-7.

Wenzel, T. E., Schaffler, M. B., & Fyhrie, D. P. (1996). In vivo trabecular microcracks in human vertebral bone. *Bone, 19*(2), 89-95.

Wilke, H. J., Claes, L., Schmitt, H., & Wolf, S. (1994). A universal spine tester for in vitro experiments with muscle force simulation. *European Spine Journal, 3*(2), 91-97.

Wilke, H. J., Neef, P., Caimi, M., Hoogland, T., & Claes, L. E. (1999). New in vivo measurements of pressures in the intervertebral disc in daily life. *Spine (Phila Pa 1976), 24*(8), 755-762.

Williams, F. M. K., Manek, N. J., Sambrook, P. N., Spector, T. D., & Macgregor, A. J. (2007). Schmorl's Nodes: Common, Highly Heritable, and Related to Lumbar Disc Disease. *Arthritis & Rheumatism, 57*(5), 885-860.

Wren, T. A., Lindset, D. P., Beaupre, G. S., & Carter, D. R. (2003). Effects of creep and cyclic loading on the mechanical properties and failure of human Achilles tendons. *Ann Biomed Eng, 31*, 710-717.

Wu, Y., Cisewski, C., Wegner, N., Zhao, S., Pellegrini Jr, D., Slate, E. H., & Yao, H. (2016). Region and strain-dependent diffusivities of glucose and lactate in healthy human cartilage endplate. *Journal of Biomechanics, 49*(13), 2756-2762.

Wu, Y., Cisewski, S. E., Sachs, B. L., Pellegrini, J. V. D., Kern, M. J., Slate, E. H., & Yao, H. (2015). The region-dependent biomechanical and biochemical properties of bovine cartilaginous endplate. *Journal of Biomechanics, 48*(12), 3185-3191.

Xu, H. G., Yu, Y. F., Zheng, Q., Zhang, W., Wang, C. D., Zhao, X. Y., . . . Zhang, X. L. (2014). Autophagy protects end plate chondrocytes from intermittent cyclic mechanical tension induced calcification. *Bone, 66*, 232-239.

Xu, H. G., Zheng, Q., Song, J. X., Li, J., Wang, H., Liu, P., . . . Zhang, X. L. (2016). Intermittent cyclic mechanical tension promotes endplate cartilage degeneration via canonical Wnt signaling pathway and E-cadherin/b-catenin complex cross-talk. *Osteoarthritis and Cartilage, 24*(158-168), 158-168.

Yang, M., Xiang, D., Wang, S., & Liu, W. (2022). The Radial Bulging and Axial Strains of Intervertebral Discs during Creep Obtained with the 3D-DIC System. *Biomolecules, 12*(8), 1097.

Yingling, V. R., Callaghan, J. P., & McGill, S. M. (1997). Dynamic loading affects the mechanical properties and failure site of porcine spines. *Clinical Biomechanics, 12*(5), 301-305.

Yingling, V. R., Callaghan, J. P., & McGill, S. M. (1999). The porcine cervical spine as a model of the human lumbar spine: an anatomical, geometric, and functional comparison. *Journal of Spinal Disorders, 12*(5), 415-423.

Yoganandan, N., Umale, S., Stemper, B., & Snyder, B. (2017). Fatigue responses of the human cervical spine intervertebral discs. *Journal of Mechanical Behavior of Biomedical Materials, 29*, 30-38.

Young, B., O'Dowd, G., & Woodford, P. (2014). Basic Tissue Types: Supporting/Connective Tissues. In *Wheater's Functional Histology Sixth Edition*. Philadelphia, PA: Elsevier.

Zehr, J. D., Barrett, J. M., & Callaghan, J. P. (2022). Cyclic loading history alters the joint compression tolerance and regional indentation responses in the cartilaginous endplate. *Journal of the Mechanical Behaviour of Biomedical Materials, 136*, 105542.

Zehr, J. D., Buchman-Pearle, J. M., & Callaghan, J. P. (2020). Joint fatigue-failure: A demonstration of viscoelastic responses to rate and frequency loading parameters using the porcine cervical spine. *Journal of Biomechanics, 113*, 110081.

Zehr, J. D., & Callaghan, J. P. (2022). Reaction forces and flexion-extension moments imposed on functional spinal units with constrained and unconstrained in vitro testing systems. *Journal of Biomechanical Engineering, 144*(5), 054501.

Zehr, J. D., Carnegie, D. R., Welsh, T. N., & Beach, T. A. C. (2020). A comparative analysis of lumbar spine mechanics during barbell- and crate-lifting: implications for occupational lifting task assessments. *International Journal of Occupational Ergonomics and Safety, 26*(1), 1-8.

Zehr, J. D., Howarth, S. J., & Beach, T. A. C. (2018). Using relative phase analyses and vector coding to quantify Pelvis-Thorax coordination during lifting-A methodological investigation. *Journal of Electromyography and Kinesiology, 39*, 104-113.

Zehr, J. D., Quadrilatero, J., & Callaghan, J. P. (2022a). Incidence of compression induced microinjuries in the cartilage endplate of the spine. *Spine, In Press*.

Zehr, J. D., Quadrilatero, J., & Callaghan, J. P. (2022b). Initiation and accumulation of loading induced changes to collagen content and microstructural damage in the cartilaginous endplate *Osteoarthritis & Cartilage, Submitted*.

Zehr, J. D., Rahman, F. A., Callaghan, J. P., & Quadrilatero, J. (2022). Mechanically induced histochemical and structural damage in the annulus fibrosus and cartilaginous endplate: A multi-colour immunofluorescence analysis. *Cell and Tissue Research, 390*(1), 59-70.

Zehr, J. D., Tennant, L. M., & Callaghan, J. P. (2019a). Examining endplate fatigue failure during cyclic compression loading with variable and consistent peak magnitudes using a force weighting adjustment approach: an in vitro study. *Ergonomics, 62*(10), 1339-1348.

Zehr, J. D., Tennant, L. M., & Callaghan, J. P. (2019b). Incorporating loading variability into in vitro injury analyses and its effect on cumulative compression tolerance in porcine cervical spine units. *Journal of Biomechanics, 88*, 48-54.

Zhang, M., Zhou, Q., Liang, Q. Q., Li, C. G., Holz, J. D., Tang, D., . . . Wang, Y. J. (2009). IGF-1 regulation of type II collagen and MMP-13 expression in rat endplate chondrocytes via distinct signaling pathways. *Osteoarthritis and Cartilage, 17*(1), 100-106.

Zhang, N., Li, F. C., Huang, Y. J., Teng, C., & Chen, W. S. (2010). Possible key role of immune system in Schmorl's nodes. *Medical Hypotheses, 74*, 552-554.

Zhang, Y., Lenart, B. A., Lee, J. K., Chen, D., Shi, P., Ren, J., . . . An, H. S. (2014). Histological Features of Endplates of the Mammalian Spine. *Spine, 39*(5), E312-E317.

Zhao, F. D., Pollintine, P., Hole, B. D., Adams, M. A., & Dolan, P. (2009). Vertebral fractures usually affect the cranial endplate because it is thinner and supported by less-dense trabecular bone. *Bone, 44*(2), 372-379.

Zioupos, P., Curr, J. D., & Casinos, A. (2001). Tensile fatigue in bone: are cycles-,or time to failure, or both, more important? *Journal of Theoretical Biology, 210*, 389-399.

Appendix A

Immunofluorescence Staining Batch Calculations

Chapter 3.3.

Table A1. Primary and secondary antibody volumes mixed into each staining batch completed for the work comprising Chapter 3.3.

Specimen	Primary/Secondary	Antibody Reactivity	Antibody Concentration (mg/µl)	Antibody Volume (µl)	Base Volume (µl)	Total Volume (µl)
All	Primary	Type I Collagen Type II Collagen	5 1	2.4 12	585.6	600
	Secondary	Anti-Mouse Anti-Rabbit	2 2	1 1	998	1000

Chapter 4

Table A2. Primary and secondary antibody volumes mixed into each staining batch completed for the work comprising Chapter 4.

Specimen	Primary/Secondary	Antibody Reactivity	Antibody Concentration (mg/µl)	Antibody Volume (µl)	Base Volume (µl)	Total Volume (µl)
Porcine Peripheral	Primary	Type I Collagen Type II Collagen	5 1.14	10 43.85	4946.15	5000
	Secondary	Anti-Mouse Anti-Rabbit	2 2	10 10	4980	5000
H07	Primary	Type I Collagen Type II Collagen	5 1.14	10 43.85	4946.15	5000
	Secondary	Anti-Mouse Anti-Rabbit	2 2	10 10	4980	5000
H08 + H01 L3	Primary	Type I Collagen Type II Collagen	5 1.14	10 43.85	4946.15	5000
	Secondary	Anti-Mouse Anti-Rabbit	2 2	10 10	4980	5000
H01 L4	Primary	Type I Collagen Type II Collagen	5 1.14	10 43.85	4946.15	5000
	Secondary	Anti-Mouse Anti-Rabbit	2 2	10 10	4980	5000

Chapter 6/7

Table A3. Primary and secondary antibody volumes mixed into each staining batch completed for the work comprising Chapter 6 and 7.

Specimen	Primary/Secondary	Antibody Reactivity	Antibody Concentration (mg/µl)	Antibody Volume (µl)	Base Volume (µl)	Total Volume (µl)
1-25	Primary	Type I Collagen Type II Collagen	1 1	50 50	4900	5000
	Secondary	Anti-Mouse Anti-Rabbit	2 2	10 10	4980	5000
26-50	Primary	Type I Collagen Type II Collagen	1 1	50 50	4900	5000
	Secondary	Anti-Mouse Anti-Rabbit	2 2	10 10	4980	5000
51-75	Primary	Type I Collagen Type II Collagen	5 1.14	10 43.85	4946.15	5000
	Secondary	Anti-Mouse Anti-Rabbit	2 2	10 10	4980	5000
76-100	Primary	Type I Collagen Type II Collagen	5 1.14	10 43.85	4946.15	5000
	Secondary	Anti-Mouse Anti-Rabbit	2 2	10 10	4980	5000
101-114	Primary	Type I Collagen Type II Collagen	5 1.14	10 43.85	4946.15	5000
	Secondary	Anti-Mouse Anti-Rabbit	2 2	10 10	4980	5000

Appendix B

Regional and Spinal Level Comparative Data

Table B1. fluorescence intensity, thickness, and void area of endplates extracted from the porcine cervical spine.

Level	Region	Cartilage Thickness (mm)	Void Area (μm^2)
C3	Central	0.194 ± 0.034	85.98 ± 24.30
	Anterior	0.246 ± 0.014	36.05 ± 26.34
	Posterior	0.242 ± 0.049	104.17 ± 76.36
	Lateral	0.205 ± 0.023	46.26 ± 31.25
C4	Central	0.194 ± 0.036	59.63 ± 33.08
	Anterior	0.251 ± 0.031	25.15 ± 15.20
	Posterior	0.241 ± 0.041	109.56 ± 95.10
	Lateral	0.206 ± 0.028	59.23 ± 27.48
C5	Central	0.196 ± 0.045	76.78 ± 56.14
	Anterior	0.251 ± 0.021	19.32 ± 11.30
	Posterior	0.244 ± 0.035	89.01 ± 45.81
	Lateral	0.206 ± 0.034	42.03 ± 40.52
C6	Central	0.195 ± 0.024	62.66 ± 33.50
	Anterior	0.251 ± 0.035	11.63 ± 19.65
	Posterior	0.244 ± 0.039	116.71 ± 19.20
	Lateral	0.206 ± 0.021	49.11 ± 21.20

Table B2. fluorescence intensity, thickness, and void area of endplates extracted from the 33-year-old human cadaveric lumbar spine. All fluorescence values are expressed relative to the same region within the porcine cervical spine.

Level	Region	COL I Fluorescence Intensity (AU)	COL II Fluorescence Intensity (AU)	Cartilage Thickness (mm)	Void Area (μm^2)
L1	Central	0.81 ± 0.09	0.57 ± 0.11	0.845 ± 0.245	3228.24 ± 559.47
	Anterior	0.82 ± 0.21	0.52 ± 0.16	0.938 ± 0.409	104.06 ± 255.16
	Posterior	0.75 ± 0.16	0.59 ± 0.10	0.941 ± 0.365	166.49 ± 194.03
	Lateral	0.83 ± 0.14	0.56 ± 0.11	0.887 ± 0.129	374.61 ± 220.36
L2	Central	0.85 ± 0.06	0.55 ± 0.14	0.887 ± 0.514	312.17 ± 101.88
	Anterior	0.84 ± 0.10	0.54 ± 0.14	1.577 ± 0.489	270.51 ± 212.06
	Posterior	0.85 ± 0.08	0.55 ± 0.12	1.196 ± 0.417	10010.41 ± 977.33
	Lateral	0.86 ± 0.15	0.56 ± 0.13	1.141 ± 0.611	280.96 ± 147.61
L3	Central	0.79 ± 0.07	0.50 ± 0.20	1.022 ± 0.522	1092.61 ± 697.56
	Anterior	0.80 ± 0.09	0.48 ± 0.17	1.438 ± 0.748	5764.82 ± 554.42
	Posterior	0.73 ± 0.11	0.46 ± 0.17	1.274 ± 0.619	1914.67 ± 576.13
	Lateral	0.87 ± 0.14	0.55 ± 0.16	1.174 ± 0.489	457.67 ± 401.25
L4	Central	0.85 ± 0.08	0.54 ± 0.14	0.997 ± 0.374	419.66 ± 501.32
	Anterior	0.84 ± 0.06	0.49 ± 0.16	2.148 ± 0.406	3954.21 ± 661.01
	Posterior	0.83 ± 0.11	0.53 ± 0.09	1.568 ± 0.654	1352.75 ± 784.63
	Lateral	0.84 ± 0.09	0.53 ± 0.10	1.522 ± 0.599	2497.40 ± 814.02

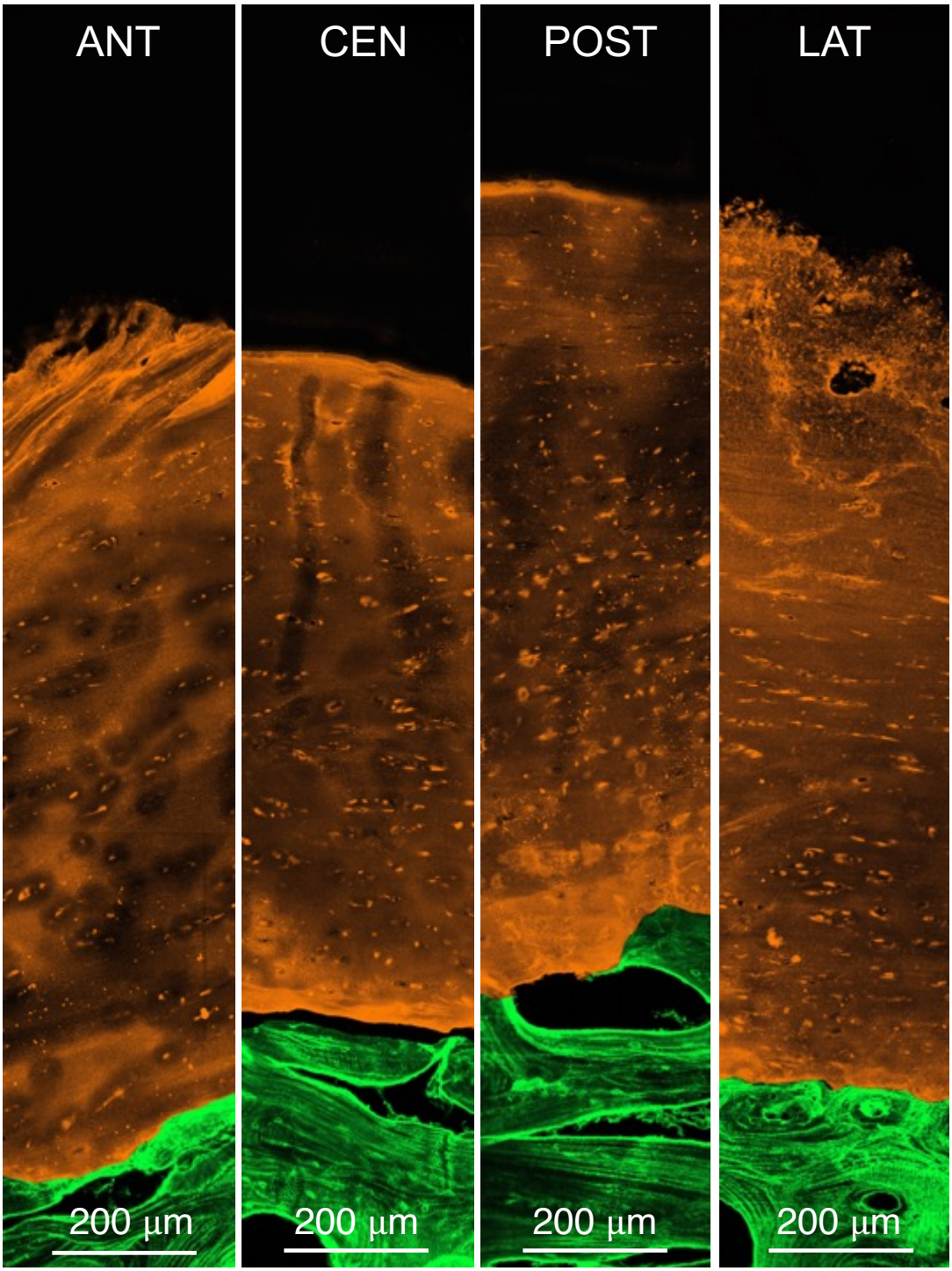

Figure B1. Representative images of the anterior (ANT), central (CEN), posterior (POST), and lateral (LAT) regions of the L1 lumbar spine vertebra (33 years). All images were taken in the sagittal plane. Positive staining is observed for type I (green) and type II (orange) collagen.

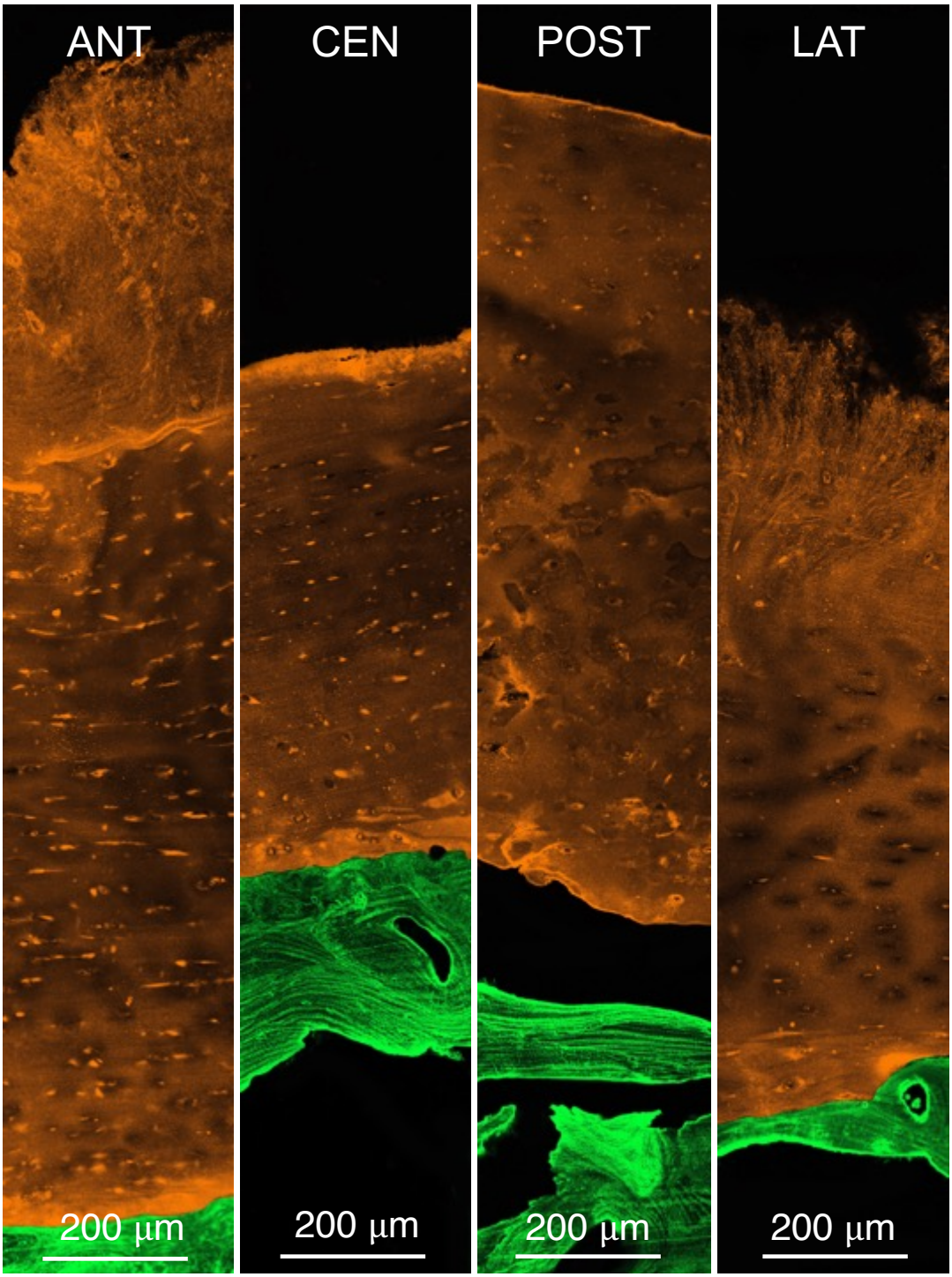

Figure B2. Representative images of the anterior (ANT), central (CEN), posterior (POST), and lateral (LAT) regions of the L2 lumbar spine vertebra (33 years). All images were taken in the sagittal plane. Positive staining is observed for type I (green) and type II (orange) collagen.

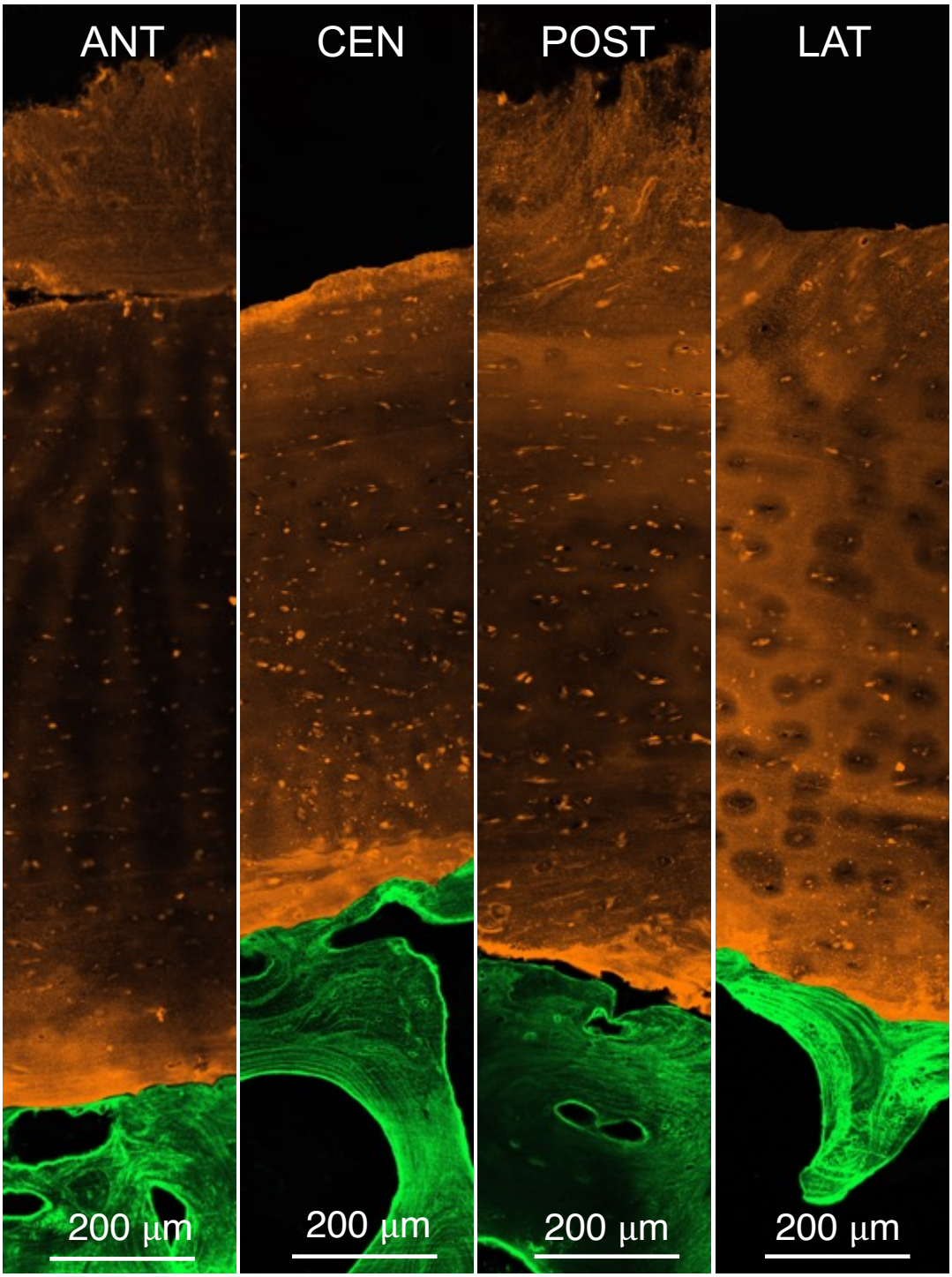

Figure B3. Representative images of the anterior (ANT), central (CEN), posterior (POST), and lateral (LAT) regions of the L3 lumbar spine vertebra (33 years). All images were taken in the sagittal plane. Positive staining is observed for type I (green) and type II (orange) collagen.

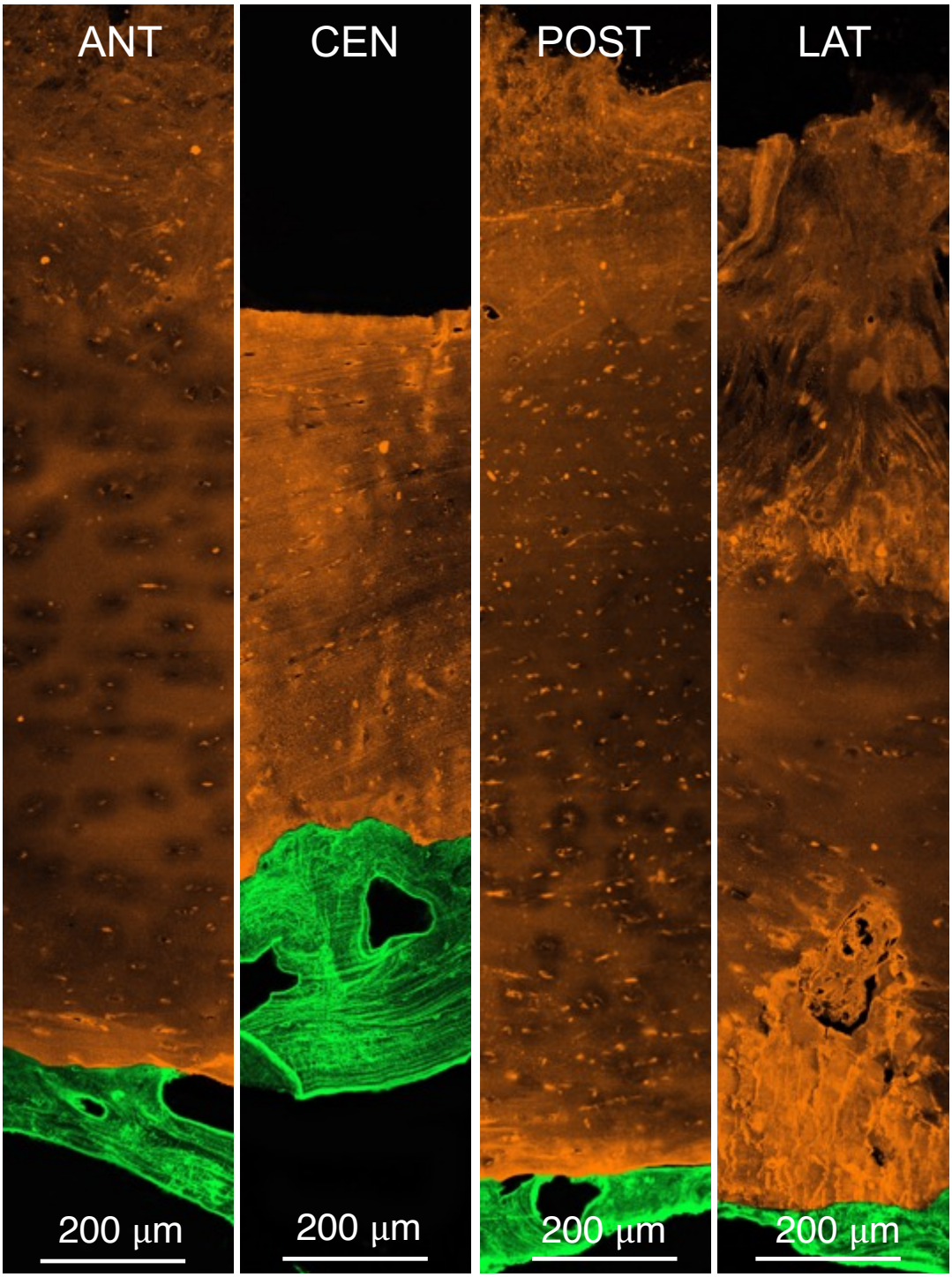

Figure B4. Representative images of the anterior (ANT), central (CEN), posterior (POST), and lateral (LAT) regions of the L4 lumbar spine vertebra (33 years). All images were taken in the sagittal plane. Positive staining is observed for type I (green) and type II (orange) collagen.

Table B3. fluorescence intensity, thickness, and void area of endplates extracted from the 19 year old human cadaveric lumbar spine.

Level	Region	COL I Fluorescence Intensity (AU)	COL II Fluorescence Intensity (AU)	Cartilage Thickness (mm)	Void Area (μm^2)
L1	Central	0.67 ± 0.23	0.31 ± 0.21	0.300 ± 0.111	156.09 ± 117.27
	Anterior	0.71 ± 0.19	0.32 ± 0.17	1.132 ± 0.381	125.87 ± 128.45
	Posterior	0.68 ± 0.04	0.30 ± 0.08	1.083 ± 0.477	998.95 ± 197.84
	Lateral	0.70 ± 0.10	0.30 ± 0.07	1.138 ± 0.416	101.06 ± 113.31
L2	Central	0.64 ± 0.09	0.28 ± 0.13	0.267 ± 0.090	374.61 ± 212.13
	Anterior	0.64 ± 0.11	0.28 ± 0.19	1.122 ± 0.388	301.76 ± 153.33
	Posterior	0.67 ± 0.19	0.31 ± 0.20	1.064 ± 0.323	2164.41 ± 714.28
	Lateral	0.68 ± 0.10	0.30 ± 0.10	1.061 ± 0.428	322.58 ± 129.08
L3	Central	0.65 ± 0.10	0.31 ± 0.02	0.903 ± 0.221	31.21 ± 6.70
	Anterior	0.63 ± 0.21	0.33 ± 0.08	1.164 ± 0.476	72.84 ± 10.43
	Posterior	0.66 ± 0.08	0.29 ± 0.10	1.106 ± 0.525	93.65 ± 9.89
	Lateral	0.65 ± 0.12	0.31 ± 0.17	1.000 ± 0.407	174.58 ± 20.45
L4	Central	0.70 ± 0.08	0.32 ± 0.20	0.890 ± 0.101	67.90 ± 8.78
	Anterior	0.71 ± 0.12	0.35 ± 0.23	0.1139 ± 0.337	101.3 ± 13.33
	Posterior	0.69 ± 0.13	0.28 ± 0.19	0.906 ± 0.245	98.99 ± 15.86
	Lateral	0.71 ± 0.06	0.30 ± 0.19	0.891 ± 0.354	2830.28 ± 450.31
L5	Central	0.68 ± 0.05	0.33 ± 0.02	0.722 ± 0.120	209.32 ± 35.29
	Anterior	0.68 ± 0.10	0.34 ± 0.17	1.612 ± 0.290	114.83 ± 67.60
	Posterior	0.69 ± 0.13	0.29 ± 0.13	1.496 ± 0.338	131.29 ± 48.66
	Lateral	0.67 ± 0.05	0.31 ± 0.19	1.161 ± 0.170	180.90 ± 39.99

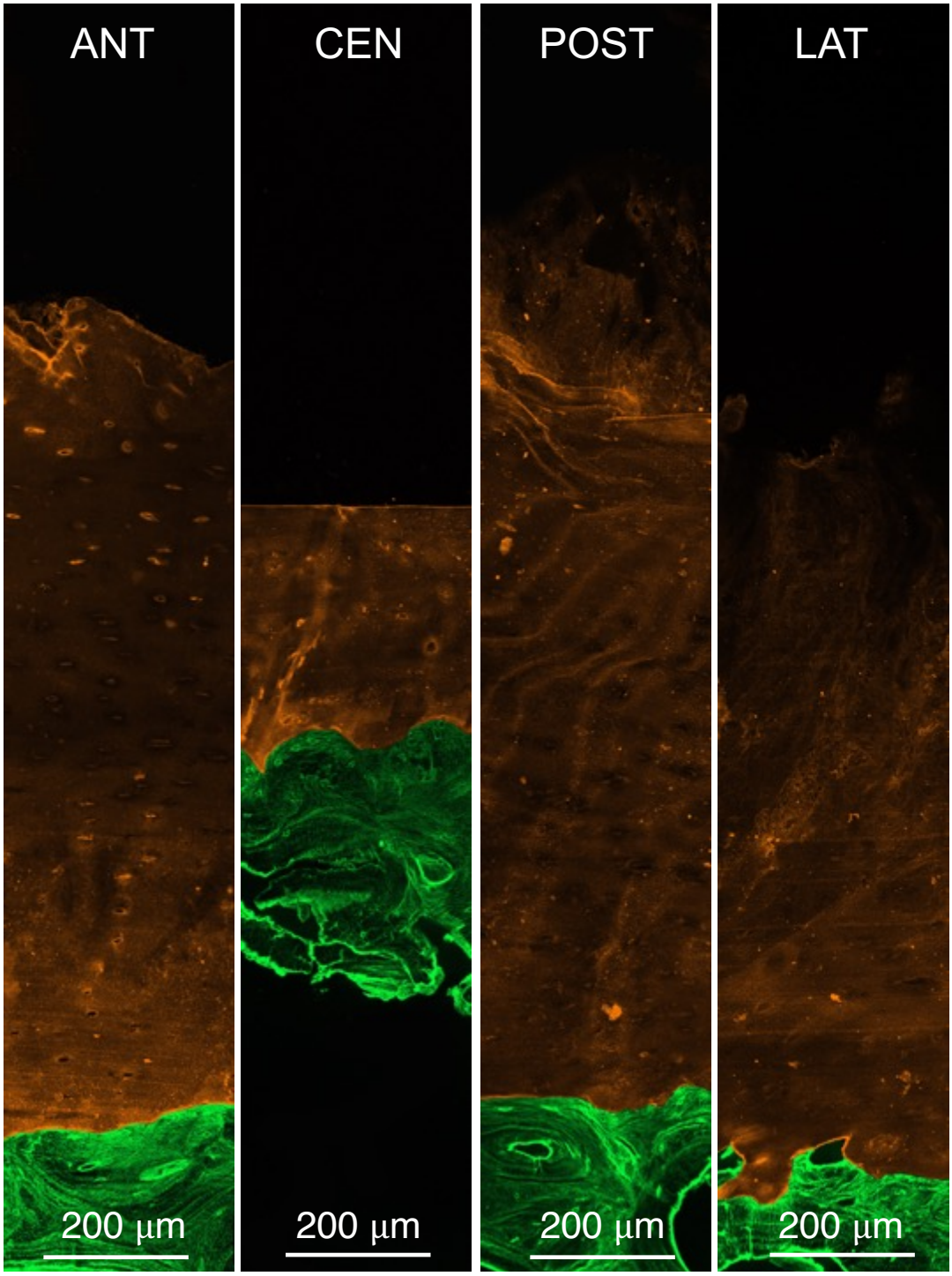

Figure B5. Representative images of the anterior (ANT), central (CEN), posterior (POST), and lateral (LAT) regions of the L1 lumbar spine vertebra (19 years). All images were taken in the sagittal plane. Positive staining is observed for type I (green) and type II (orange) collagen.

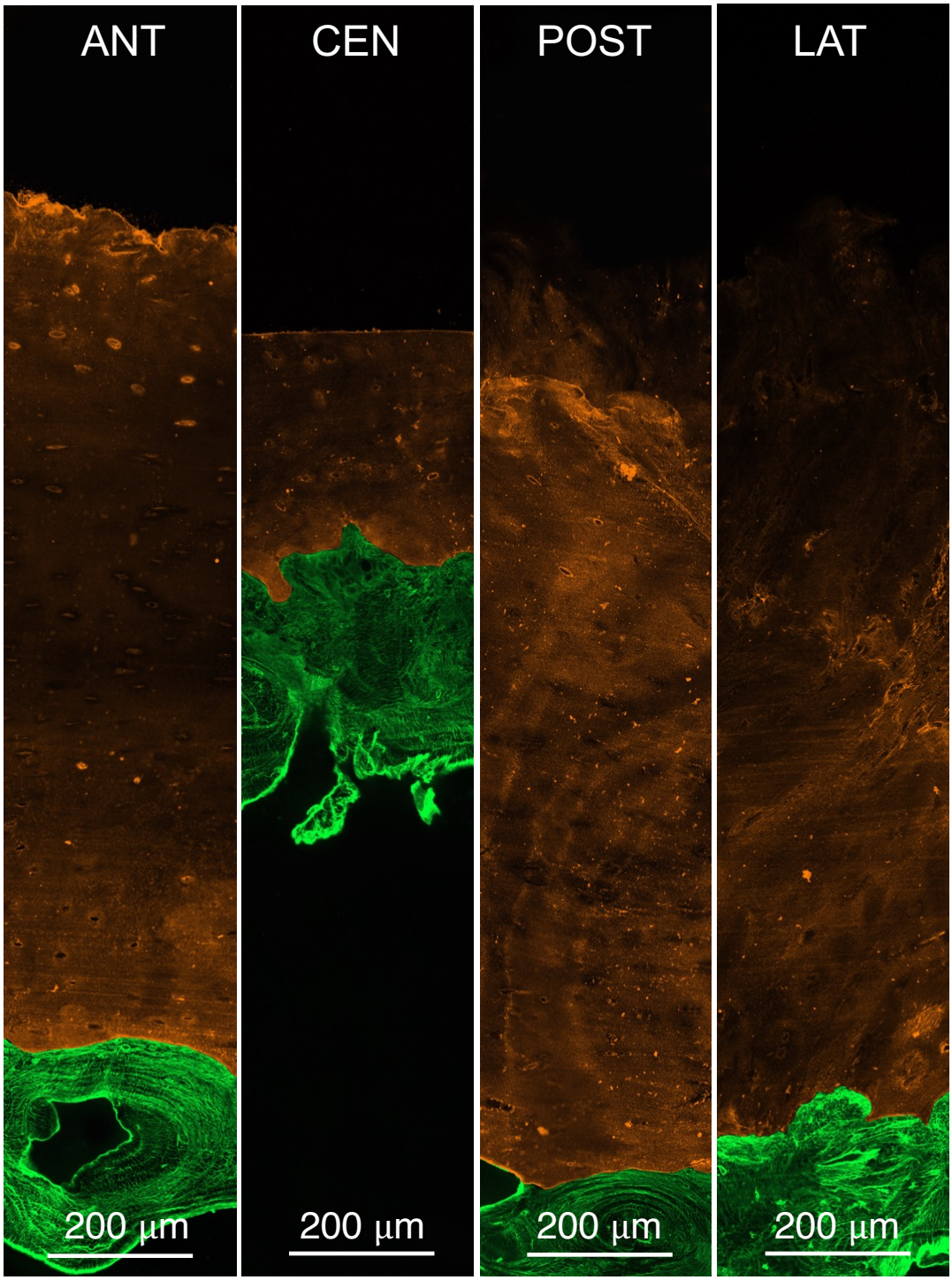

Figure B6. Representative images of the anterior (ANT), central (CEN), posterior (POST), and lateral (LAT) regions of the L2 lumbar spine vertebra (19 years). All images were taken in the sagittal plane. Positive staining is observed for type I (green) and type II (orange) collagen.

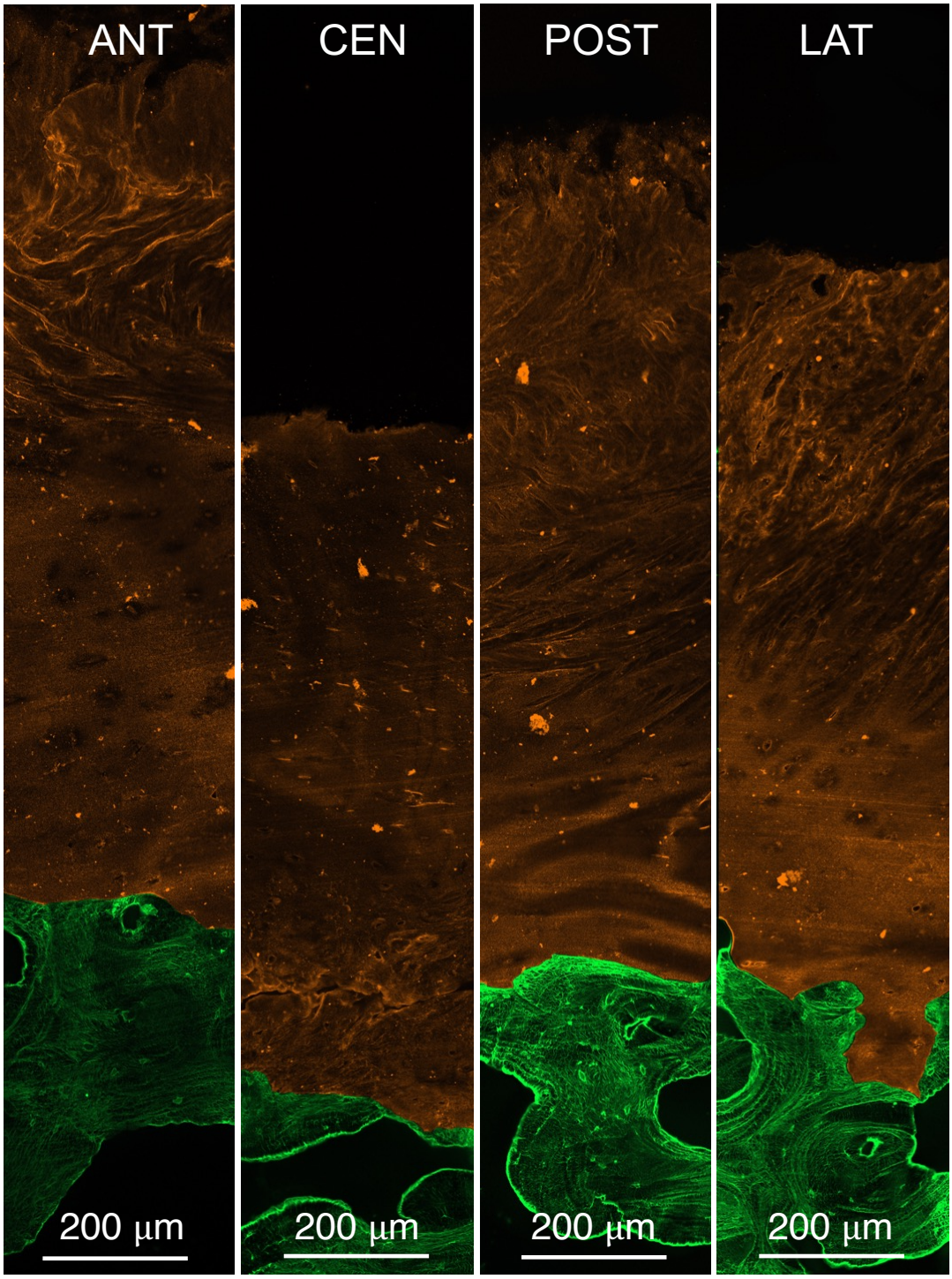

Figure B7. Representative images of the anterior (ANT), central (CEN), posterior (POST), and lateral (LAT) regions of the L3 lumbar spine vertebra (19 years). All images were taken in the sagittal plane. Positive staining is observed for type I (green) and type II (orange) collagen.

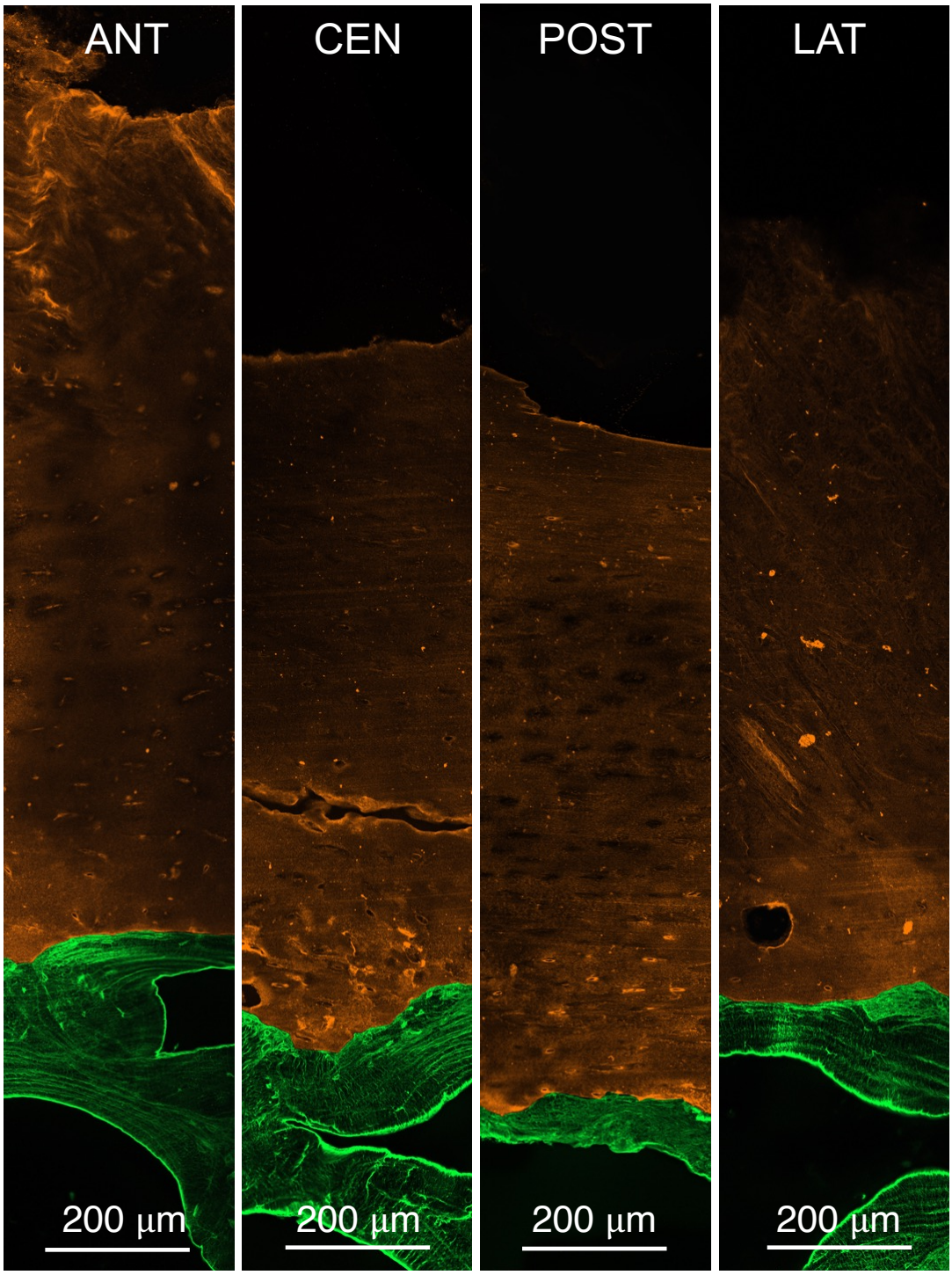

Figure B8. Representative images of the anterior (ANT), central (CEN), posterior (POST), and lateral (LAT) regions of the L4 lumbar spine vertebra (19 years). All images were taken in the sagittal plane. Positive staining is observed for type I (green) and type II (orange) collagen.

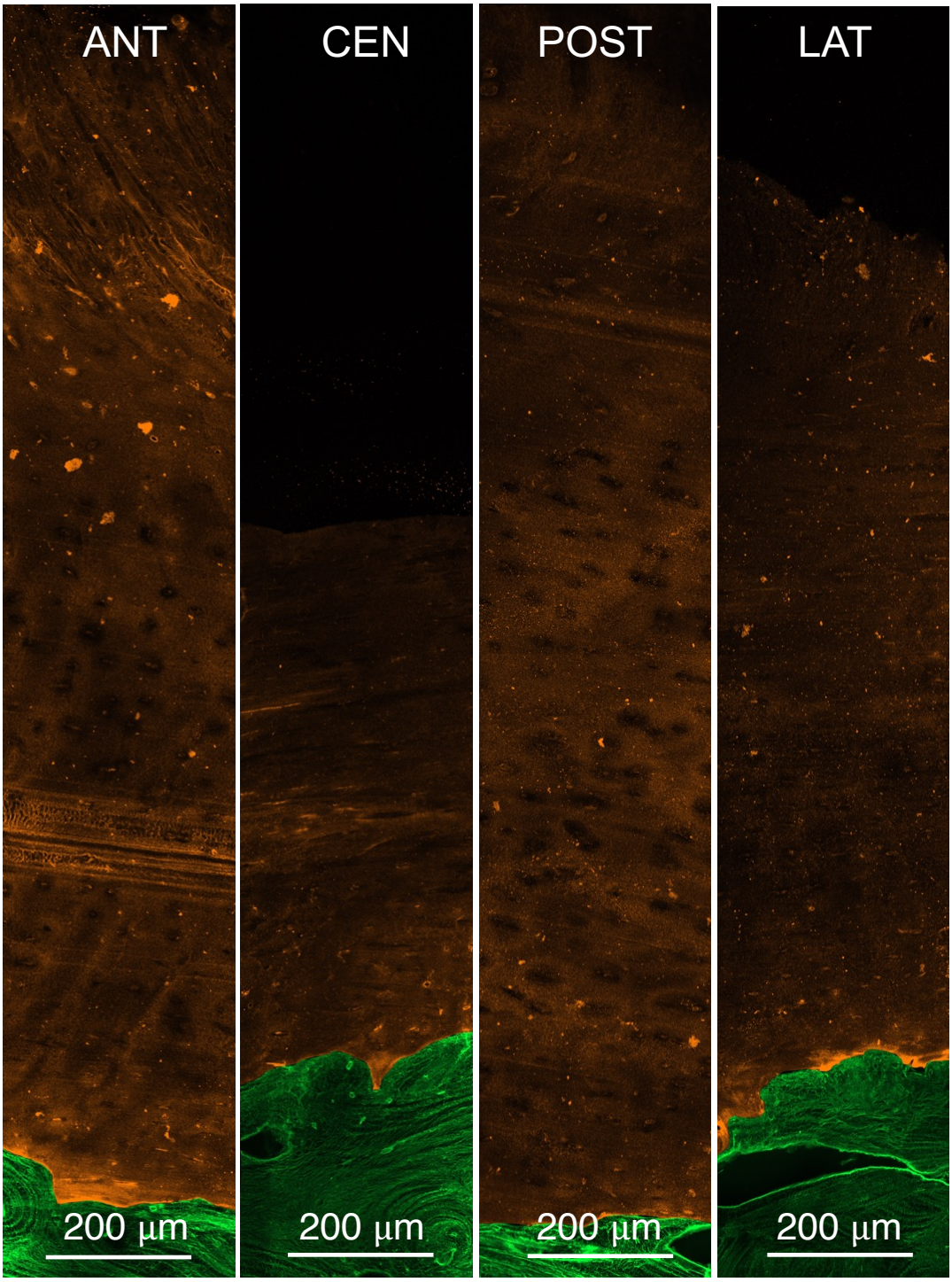

Figure B9. Representative images of the anterior (ANT), central (CEN), posterior (POST), and lateral (LAT) regions of the L5 lumbar spine vertebra (19 years). All images were taken in the sagittal plane. Positive staining is observed for type I (green) and type II (orange) collagen.

Table B4. fluorescence intensity, thickness, and void area of endplates extracted from the 85 year old human cadaveric lumbar spine.

Level	Region	COL I Fluorescence Intensity (AU)	COL II Fluorescence Intensity (AU)	Cartilage Thickness (mm)	Void Area (μm^2)
L3	Central	0.31 ± 0.06	0.14 ± 0.10	0.348 ± 0.056	572.32 ± 97.56
	Anterior	0.34 ± 0.04	0.13 ± 0.04	0.748 ± 0.089	1889.38 ± 58.94
	Posterior	0.33 ± 0.05	0.14 ± 0.05	0.945 ± 0.119	5806.45 ± 324.21
	Lateral	0.30 ± 0.04	0.11 ± 0.06	0.732 ± 0.174	3891.78 ± 257.38
L4	Central	0.36 ± 0.09	0.10 ± 0.07	0.248 ± 0.067	26514.04 ± 978.53
	Anterior	0.30 ± 0.11	0.11 ± 0.02	0.732 ± 0.104	5816.85 ± 564.33
	Posterior	0.15 ± 0.07	0.07 ± 0.05	0.848 ± 0.110	34703.43 ± 713.01
	Lateral	0.32 ± 0.13	0.12 ± 0.05	0.629 ± 0.195	24193.55 ± 914.57

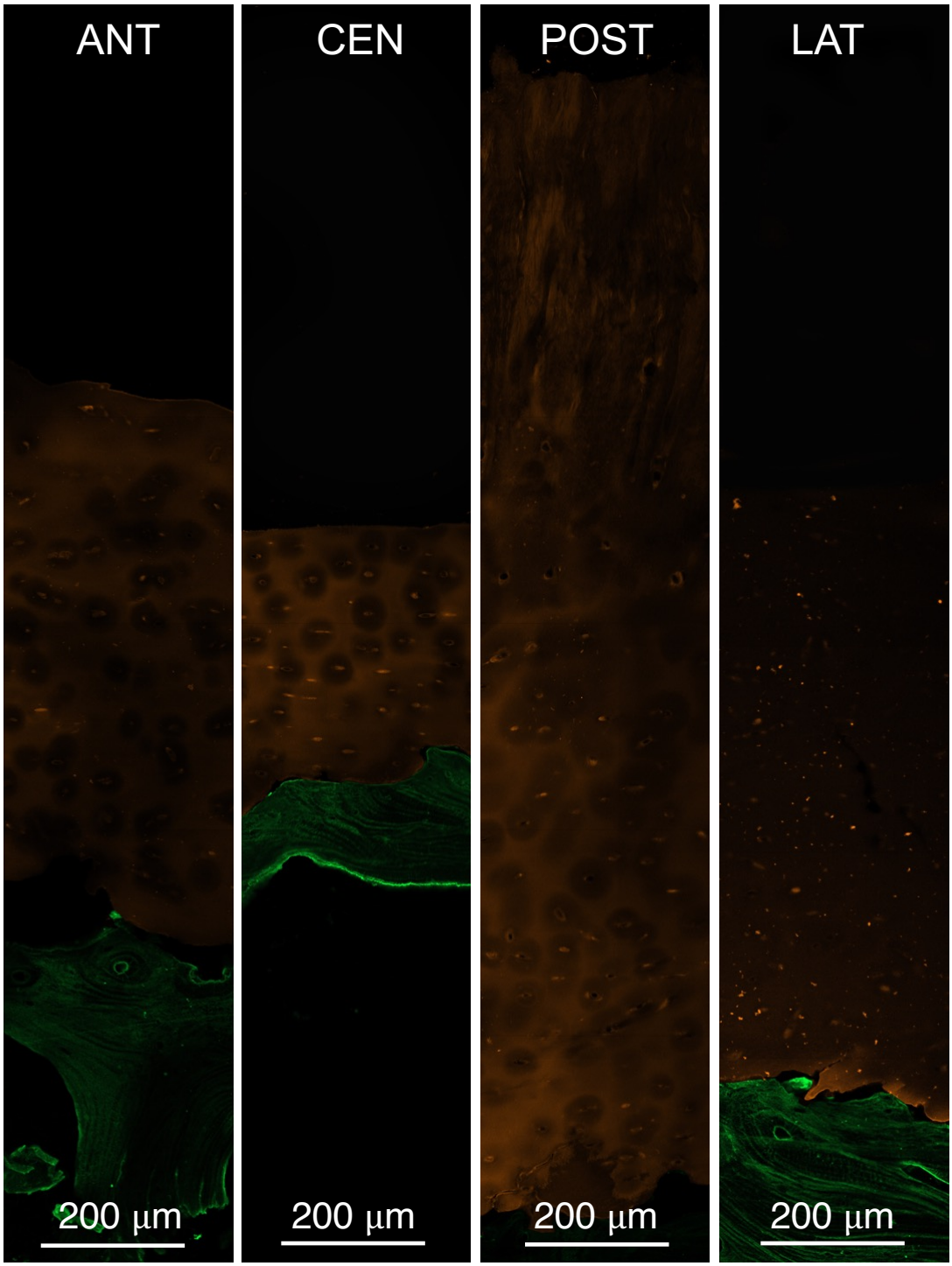

Figure B10. Representative images of the anterior (ANT), central (CEN), posterior (POST), and lateral (LAT) regions of the L3 lumbar spine vertebra (85 years). All images were taken in the sagittal plane. Positive staining is observed for type I (green) and type II (orange) collagen.

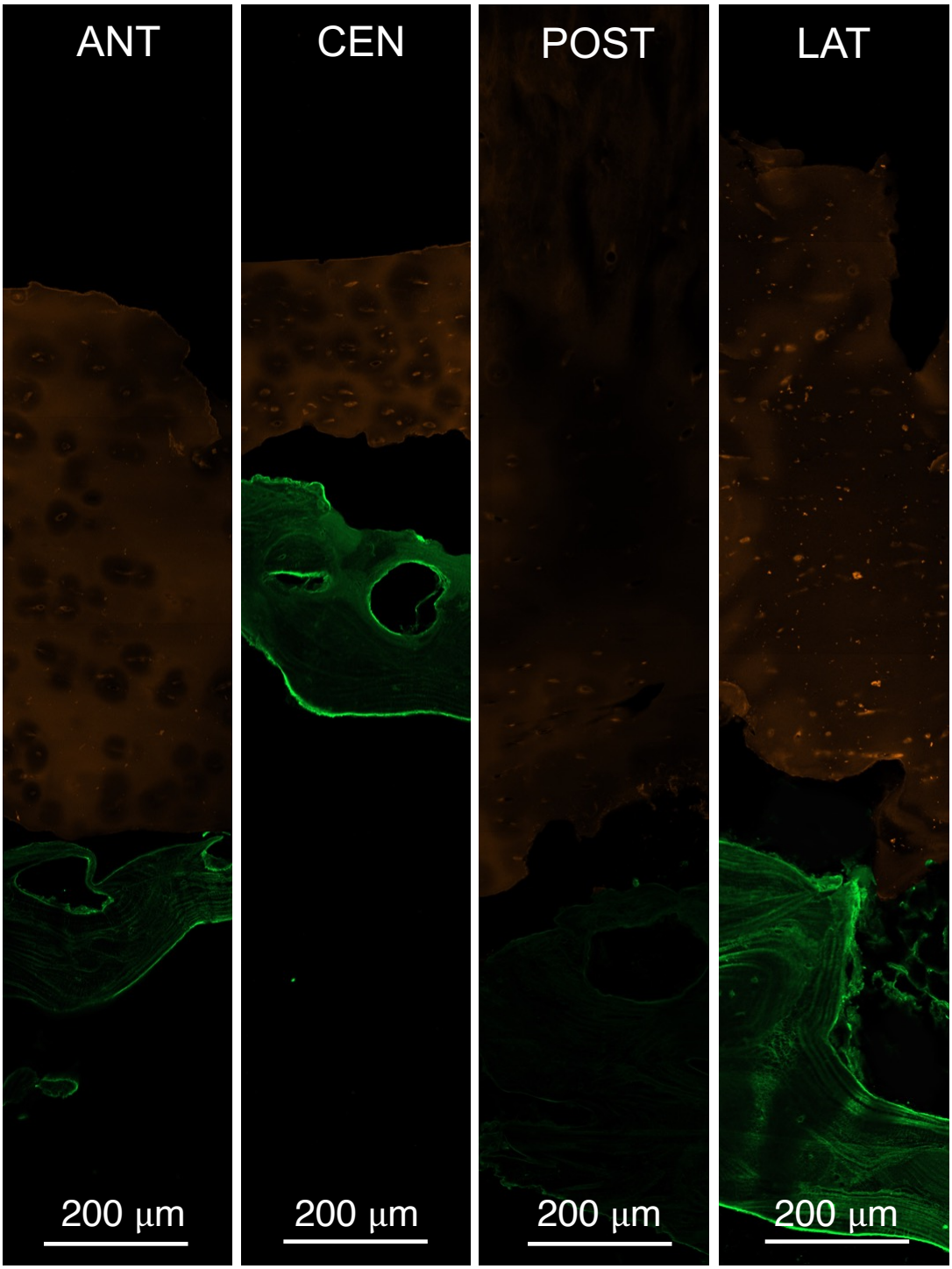

Figure B11. Representative images of the anterior (ANT), central (CEN), posterior (POST), and lateral (LAT) regions of the L4 lumbar spine vertebra (85 years). All images were taken in the sagittal plane. Positive staining is observed for type I (green) and type II (orange) collagen.